

**GAS SENSING CHARACTERISTICS OF WET CHEMICAL
SYNTHESIZED SPINEL FERRITES**

Kalisadhan Mukherjee

GAS SENSING CHARACTERISTICS OF WET CHEMICAL SYNTHESIZED SPINEL FERRITES

*Thesis submitted to the
Indian Institute of Technology, Kharagpur
For award of the degree*

of

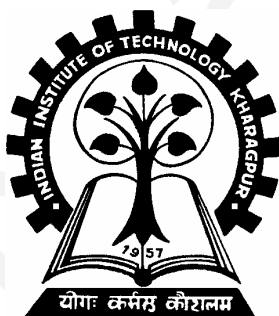
Doctor of Philosophy

By

Kalisadhan Mukherjee

Under the supervision of

Prof. S. B. Majumder



**MATERIALS SCIENCE CENTRE
INDIAN INSTITUTE OF TECHNOLOGY KHARAGPUR
JULY 2012**

© 2012 Kalisadhan Mukherjee. All rights reserved.

Copyright
IIT Kharagpur

Dedicated to My Dear Friend
Late Achin Singha Mahapatra
A Devoted Research Scholar Whose Premature and Sad Demise has
Ended a Life of Utmost Dedication

Copyright
IIT Kharagpur

CERTIFICATE OF APPROVAL

Date: 20.07.2012

Certified that the thesis entitled GAS SENSING CHARACTERISTICS OF WET CHEMICAL SYNTHESIZED SPINEL FERRITES submitted by KALISADHAN MUKHERJEE to Indian Institute of Technology, Kharagpur for the award of the degree of Doctor of Philosophy has been accepted by the external examiners and the student has successfully defended the thesis in the viva-voce examination held today.

Signature

Name: Dr. P. Banerji
(Member of DSC)

Signature

Name: Dr. T. K. Nath
(Member of DSC)

Signature

Name: Prof. S. Ram
(Member of DSC)

Signature

Name: Dr. S. B. Majumder
(Supervisor)

Signature

Name: Prof. Pushan Ayyub
(External Examiner)

Signature

Name:
(Chairman)

Copyright
IIT Kharagpur

DECLARATION

I certify that

- a. The work contained in the thesis is original and has been done by myself under the general supervision of my supervisor.
- b. The work has not been submitted to any other Institute for any degree or diploma.
- c. I have followed the guidelines provided by the Institute in writing the thesis.
- d. I have conformed to the norms and guidelines given in the Ethical Code of Conduct of the Institute.
- e. Whenever I have used materials (data, theoretical analysis, and text) from other sources, I have given due credit to them by citing them in the text of the thesis and giving their details in the references.
- f. Whenever I have quoted written materials from other sources, I have put them under quotation marks and given due credit to the sources by citing them and giving required details in the references.

(Kalisadhan Mukherjee)

Copyright
IIT Kharagpur



**Materials Science Centre
Indian Institute of Technology
Kharagpur-721302**

CERTIFICATE

This is to certify that the thesis entitled **Gas Sensing Characteristics of Wet Chemical Synthesized Spinel Ferrites**, submitted by **Kalisadhan Mukherjee** to Indian Institute of Technology, Kharagpur, is a record of bona fide research work under my supervision and I consider it worthy of consideration for the award of the degree of Doctor of Philosophy of the Institute.

Supervisor

Date:

ACKNOWLEDGEMENTS

I wish to express my sincere gratitude to my supervisor *Dr. S. B. Majumder*, Associate professor, Materials Science Centre, Indian Institute of Technology, Kharagpur, for his meticulous guidance throughout my Ph. D work. His steady inspirations, valuable suggestions, tireless effort, interdisciplinary mindset, analytical observations, and positive thinking motivated me a lot to execute the Ph. D work.

I am obliged to the *Head, Materials Science Centre*, IIT Kharagpur and all the *faculty* and *staff members* of this centre for providing necessary facilities during the research work.

I am appreciative to the members of the Doctoral Scrutiny Committee, *Prof. S Ram* (Materials Science Centre, IIT Kharagpur), *Dr. P. Banerji*, (Materials Science Centre, IIT Kharagpur), *Dr. T. K. Nath* (Dept. of Physics & Meteorology, IIT Kharagpur), for their valuable suggestions.

I would like to acknowledge *Department of Information Technology*, Govt. of India (for project funding) and *Council of Scientific and Industrial Research*, Govt. of India, for providing me the fellowship during my Ph. D.

I would like to thank *Prof. P. Pramanik*, (Department of Chemistry, IIT Kharagpur) for providing me the facilities for the hydrothermal synthesis of ferrite hollow spheres.

I am indebted to my school teacher *Mr. Tarapada Singha Mahapatra* for his constant moral support throughout my journey to higher studies.

I enjoyed every moment in the laboratory and so thankful to my *lab mates* for their cooperative interaction. My special thanks to my entire *friends* who support cheerfully to entertain every episode of ups and downs during research work.

Finally, I absolutely have no idea how to acknowledge my family. It is just enough to mention that without the patience, sacrifice and support from my family I could not complete my Ph. D research work.

Date:

(Kalisadhan Mukherjee)

Copyright
IIT Kharagpur

ABSTRACT

In the present thesis we have developed a generic wet chemical route to synthesize various nano-structured (e.g. nano-particle, thin film, nano-tube, embedded nano-tube, hollow spheres) binary (ZnO), and spinel oxides ($\text{Mg}_{1-x}\text{Zn}_x\text{Fe}_2\text{O}_4$ ($0.0 \leq x \leq 1.0$)). The synthesized oxides are characterized in terms of their phase formation behavior and microstructure evolution characteristics. An automated dynamic flow measurement set up has been fabricated to evaluate the gas sensing characteristics (response %, response/recovery time, stability and cross-selectivity) of the synthesized oxides. We have found that the embedded nano-tube sensing elements exhibit promising gas sensing performance among all the other synthesized nano-structures. Based on Langmuir adsorption isotherm kinetics we have successfully modeled the resistance transients (during response and recovery) and evaluated the relevant kinetic parameters including the activation energies of adsorption and desorption of relevant gases on the sensing elements. A number of interesting features are observed in the recorded resistance/conductance transients of the binary and spinel oxide based nano-structured sensing materials. Some of the prominent features include (i) drift in the base resistance upon repeated response and recovery cycles, causes mainly due to the unsaturated resistance transients during response and recovery, (ii) switching from n to p type conduction behavior of certain nano-structured magnesium zinc ferrite elements, (iii) response and recovery transients with sinusoidal noise etc. We have made an attempt to understand the nature and origin of these features based on our developed hypothesis on the reaction sequence of gas absorption and desorption of the reaction products. We have proposed that the analyses of the resistance transients could be useful to address the selectivity problem of these semiconducting gas sensors. Additionally, we have also adopted feature extraction method of the conductance transients in conjunction with pattern recognition algorithms to investigate the cross-selectivity of $\text{Mg}_{0.5}\text{Zn}_{0.5}\text{Fe}_2\text{O}_4$ sensing elements towards methane, carbon mono oxide and hydrogen gases. Finally, the hydrogen sensing performance of the optimized spinel sensing elements are demonstrated by fabricating a Taguchi-type sensor prototype.

Keywords: Gas sensor, Ferrite, Nano-structuring, Kinetics

Copyright
IIT Kharagpur

LIST OF SYMBOLS AND ABBREVIATIONS

SYMBOLS

FET
SAW
SMO
 R_a
 R_g
 T_{opt}
S
 τ_{res}
 τ_{rec}
IDE
MFC
GPIO
 L_D
 ϵ_o
k
 n_o
 μ
PVA
C.A
E.G
AAO
MFO
MZFO
MZFO-P

MZFO-C

DTA
TGA
FTIR
XRD
FWHM
SEM
TEM
EDS
SAED
BET isotherm
 D_K
 σ
q
 μ_n
 μ_p
 $V_{\dot{O}}$
 $O_{ad-surface}$

ABBREVIATIONS

Field Effect Transistor
Surface Acoustic Wave
Semiconducting Metal Oxide
Resistance of the sensor in air
Resistance of the sensor in reducing gas
Optimized operating temperature
Response (%)
Response time
Recovery time
Inter-digitated Electrode
Mass Flow Controller
General Purpose Interface Bus
Depleted layer width
Static dielectric constant
Boltzmann constant
Total charge carrier concentration
Mobility of charge carrier
Polyvinyl alcohol
Citric acid
Ethylene glycol
Anodized porous alumina template
 $MgFe_2O_4$
 $Mg_{0.5}Zn_{0.5}Fe_2O_4$
 $Mg_{0.5}Zn_{0.5}Fe_2O_4$ nano-particle prepared in
polyvinyl alcohol assisted synthesis route
 $Mg_{0.5}Zn_{0.5}Fe_2O_4$ nano-particle prepared in
modified Pechini route
Differential Thermal Analysis
Thermal Gravimetric Analysis
Fourier Transformed Infra-Red
X-ray diffraction
Full width half maxima
Scanning Electron Microscope
Transmission Electron Microscope
Energy dispersive X-ray spectroscopy
Selected Area Electron Diffractions
Brauner-Emmet-Teller isotherm
Knudsen diffusion constant
Conductivity
Charge of the carrier
Mobility of electron
Mobility of hole
Oxygen vacancy
Physi-adsorbed oxygen

O_{ad}^-	Chemi-adsorbed oxygen
R_{ad}	Physi-adsorbed reducing gas
RO_{ad}	Adsorbed oxidized product of reducing
gas	
RO_{gas}	Desorbed oxidized product of reducing
gas	
$G(t)$	Transient conductance of the sensor
G_0	Initial conductance of the sensor in air
eV_s	Schottky barrier
ZFO	$ZnFe_2O_4$
PVA	Polyvinyl alcohol
k_a	Forward rate constant for the formation of RO_{ad}
k_d	Backward rate constant for the desorption of RO_{ad} in response process
P_{Rgas}	Pressure of reducing gas
S_0	Surface area of the adsorbed gas
N_0	Avogadro's number
K_0	Condensation coefficient of the gas molecules on sensor surface
ν	Frequency of oscillation of adsorbed gas
E_A	Activation energy for the adsorption of gas during response process
E_d	Activation energy for the desorption of gas in response process
Q_1/Q_2	Heat of adsorption in site 1 and site 2
τ	Characteristic response or recovery time
$G(t)_{response}$	Transient conductance change of the sensor during response process
G_0	Conductance of the sensor in air
G_1/G_2	Change in conductance during the adsorption of gases in site 1 and site 2
$\tau_1^{response}/\tau_2^{response}$	Characteristic response time for the adsorption of gas in site 1 and site 2
k_D	Rate constant for the desorption of gas in recovery process
$G(t)_{recovery}$	Transient conductance change of the sensor during response process
G_0'	Conductance of the sensor in reducing
gas	
G_1'/G_2'	Change in conductance during the desorption of oxidized product (RO_{ad}) from site 1 and site 2
$\tau_1^{recovery}/\tau_2^{recovery}$	Characteristic recovery time for the desorption of oxidized product (RO_{ad}) from site 1 and site 2
C_g	Reducing gas concentration
R	Universal gas constant

$F\phi$	Total available sites on the surface
$S(t)$	Transient response of the sensor
S_{\max}	Maximum response of the sensor
τ_{irrev}	Characteristic response time in irreversible response process
T_{\max}	Optimized operating temperature
K	Equilibrium constant for response process
τ_r	Characteristic response time in irreversible response process
D	Diffusion coefficient of gases on sensor surface
D_0	Diffusion pre factor
E_{dif}	Activation energy for the diffusion
$S_G(f)$	Power density spectrum of noise
P	Power
γ	Frequency exponent
f_r	Corner frequency
FFT	Fast Fourier transformation
DWT	Discrete wavelet transformation
DFA	Discriminant factor analysis
PCA	Principal component analysis

Copyright
IIT Kharagpur

LIST OF FIGURES

- Fig. 1.1: Schematic of a typical acoustic wave based gas sensor
- Fig. 1.2: Schematic of a typical MOSFET gas sensor
- Fig. 1.3: Schematic of a typical fibre optics based optical gas sensor
- Fig. 1.4: Schematic of a typical electrochemical gas sensor
- Fig. 1.5: Gas sensing mechanism of semiconducting metal oxide based sensor. The change of band diagram during gas sensing over n-type semiconducting oxide surface is shown in the figure. E_c , E_v , E_f signify the conduction band, valence band and Fermi energy level respectively
- Fig. 1.6: Typical resistance transient of an n-type SMO sensor during detection of reducing gas
- Fig. 1.7: Receptor, transducer and utility function for a typical SMO sensor
- Fig. 1.8: Various types of sensor architectures
- Fig. 2.1: Schematic of the developed gas sensing set-up
- Fig. 2.2: Photograph of (a) developed reactor unit and (b) gas sensing set-up with mass flow controller and temperature control unit
- Fig. 2.3: Summary of the wet chemical routes to synthesize various nano-structured spinel based gas sensing materials
- Fig. 2.4: Flow chart for the synthesis of $Mg_{0.5}Zn_{0.5}Fe_2O_4$ particles by PVA assisted wet chemical route
- Fig. 2.5: Flow chart for the synthesis of $Mg_{0.5}Zn_{0.5}Fe_2O_4$ nano-particles, thin film, embedded and isolated nano tubes by modified Pechini route
- Fig. 2.6: Schematic methodology for the synthesis of embedded and isolated $Mg_{0.5}Zn_{0.5}Fe_2O_4$ nano-tubes
- Fig. 2.7: Formation of embedded nano-tubes in anodized alumina template
- Fig. 2.8: Mechanism of the synthesis of spherical carbon templates
- Fig. 2.9: Flow chart for the synthesis of $Mg_{0.5}Zn_{0.5}Fe_2O_4$ hollow spheres
- Fig. 2.10: Schematic diagram for the formation of $Mg_{0.5}Zn_{0.5}Fe_2O_4$ hollow sphere

- Fig. 2.11: (a) Schematic diagram of a typical X-ray diffractometer (b) photograph of the X-ray diffractometer (Ultima III, Rigaku, Japan) used in the present work
- Fig. 2.12: (a) The experimental (symbol) and refined (solid) X-ray diffractogram patterns of MgFe_2O_4 particles calcined at 300°C for 2 h. The resultant plot after subtracting the experimental and refined spectra and the XRD peak positions for impurity (MgO) and spinel (MgFe_2O_4) phase are marked
- Fig. 2.13: (a) Schematic diagram of a SEM and (b) the photograph of the field emission scanning electron microscope (Supra-40, Carl Zeiss, Germany) used in the present work
- Fig. 2.14: (a) Schematic diagram of a TEM and (b) the photograph of the high resolution transmission electron microscope (JEM 2100, Jeol Ltd., Japan) used in the present work
- Fig. 2.15: Typical linear fit (solid line) of $1/W_a (P_0/P - 1)$ vs P/P_0 experimental data (symbols) from $\text{Mg}_{0.5}\text{Zn}_{0.5}\text{Fe}_2\text{O}_4$ nano-particles synthesized using PVA assisted route
- Fig. 2.16: Typical N_2 adsorption desorption isotherm of $\text{Mg}_{0.5}\text{Zn}_{0.5}\text{Fe}_2\text{O}_4$ nano-particles synthesized using PVA assisted route
- Fig. 2.17: (a) Various types of adsorption-desorption isotherms (b) Various types of hysteresis in type IV isotherms (from Ref. 10)
- Fig. 3.1: FTIR spectra of dried and calcined (a) MgFe_2O_4 and (b) ZnFe_2O_4 powders
- Fig. 3.2: FTIR spectra of $\text{Mg}_{1-x}\text{Zn}_x\text{Fe}_2\text{O}_4$ ($0.0 \leq x \leq 1.0$) particles calcined at 600°C
- Fig. 3.3: X-ray diffractograms of $\text{Mg}_{1-x}\text{Zn}_x\text{Fe}_2\text{O}_4$ ($0.0 \leq x \leq 1.0$) powders calcined at (a) 300°C and (b) 600°C for 2 h in air
- Fig. 3.4: FESEM image of MgFe_2O_4 sensing elements at (a) lower and (b) higher magnifications
- Fig. 3.5: Nitrogen adsorption-desorption isotherm for (a) MgFe_2O_4 and (b) $\text{Mg}_{0.5}\text{Zn}_{0.5}\text{Fe}_2\text{O}_4$ nano-particles calcined at 600°C for 2 h in air
- Fig. 3.6: Resistance transients recorded for $\text{Mg}_{0.5}\text{Zn}_{0.5}\text{Fe}_2\text{O}_4$ sensing element towards the detection of 1660 ppm of (a) H_2 and (b) CO gases at their respective optimized operating temperatures
- Fig. 3.7: Operating temperature dependence of response (%) for $\text{Mg}_{1-x}\text{Zn}_x\text{Fe}_2\text{O}_4$ ($0.0 \leq x \leq 1.0$) sensing elements towards the detection of 1660 ppm of (a) H_2 and (b) CO gases

- Fig. 3.8: Resistance transients recorded for (a) MgFe_2O_4 (b) $\text{Mg}_{0.75}\text{Zn}_{0.25}\text{Fe}_2\text{O}_4$ (c) $\text{Mg}_{0.5}\text{Zn}_{0.5}\text{Fe}_2\text{O}_4$ (d) $\text{Mg}_{0.25}\text{Zn}_{0.75}\text{Fe}_2\text{O}_4$ (e) ZnFe_2O_4 sensing elements towards the detection of various concentration of H_2 gas at their respective optimized operating temperature. The H_2 gas concentration and the respective response (%) are mentioned in the figures
- Fig. 3.9: Response (%) transient for $\text{Mg}_{1-x}\text{Zn}_x\text{Fe}_2\text{O}_4$ ($0.0 \leq x \leq 1.0$) sensing elements in presence of 100 ppm of H_2 measured for finite time (5 min) at their respective optimized operating temperature
- Fig. 3.10: (a) DTA-TGA plot of the $\text{Mg}_{0.5}\text{Zn}_{0.5}\text{Fe}_2\text{O}_4$ gel prepared using modified Pechini route (b) FTIR spectra of $\text{Mg}_{0.5}\text{Zn}_{0.5}\text{Fe}_2\text{O}_4$ gel (prepared using modified Pechini route) and calcined powders
- Fig. 3.11: X-ray diffractograms of the as prepared and calcined (at 300°C and 600°C for 2 h in air) $\text{Mg}_{0.5}\text{Zn}_{0.5}\text{Fe}_2\text{O}_4$ powders. The Rietveld refinement of the X-ray pattern (for calcined powders) are shown as solid line in the figure
- Fig. 3.12: (a) TEM image of the MZFO-C powder calcined at 400°C for 2 h in air (b) FESEM image of the MZFO-C sensor sintered at 600°C for 2 h in air
- Fig. 3.13: Nitrogen adsorption-desorption isotherm for MZFO-C powder calcined at 600°C for 2 h in air
- Fig. 3.14: Operating temperature dependence of H_2 (~ 1660 ppm) sensing response for (a) MZFO-C and (b) MZFO-P sensing elements
- Fig. 3.15: (a) Resistance transients of MZFO-C sensing element in presence of various H_2 gas concentrations (50-1660 ppm) measured at 380°C . (b) Comparison between the response characteristics of MZFO-C and MZFO-P nano-particulate sensing elements towards 100 ppm H_2 gas sensing
- Fig. 3.16: Comparison between the response (%) of MZFO-C and MZFO-P nano-particulate sensors for the detection of various concentrations (50-1660 ppm) of H_2 and CO gases at operating temperature $\sim 380^\circ\text{C}$
- Fig. 3.17: Reproducibility of the gas sensing performance of MZFO-C sensors towards the detection of 500 ppm (a) H_2 and (b) CO gases at an operating temperature $\sim 350^\circ\text{C}$
- Fig. 3.18: Schematic diagram for the formation of PVA-metal ion network during the formation of gel in PVA assisted wet chemical synthesis process
- Fig. 3.19: Schematic diagram for the formation of citric acid-ethylene glycol-metal ion network during the formation of gel in the modified Pechini route
- Fig. 3.20: X-ray diffractograms of bare alumina template and $\text{Mg}_{0.5}\text{Zn}_{0.5}\text{Fe}_2\text{O}_4$ nano-tubes embedded into alumina template

- Fig. 3.21: FESEM image of the isolated $\text{Mg}_{0.5}\text{Zn}_{0.5}\text{Fe}_2\text{O}_4$ nano-tubes (coated on quartz substrates) at (a) low and (b) high magnifications. (c) Hollow nature of a single $\text{Mg}_{0.5}\text{Zn}_{0.5}\text{Fe}_2\text{O}_4$ nano-tube (d) EDS pattern of the $\text{Mg}_{0.5}\text{Zn}_{0.5}\text{Fe}_2\text{O}_4$ nano-tubes
- Fig. 3.22: TEM image of (a) bunch of $\text{Mg}_{0.5}\text{Zn}_{0.5}\text{Fe}_2\text{O}_4$ nano-tubes (b) single $\text{Mg}_{0.5}\text{Zn}_{0.5}\text{Fe}_2\text{O}_4$ nano-tube and (c) SAED pattern of the $\text{Mg}_{0.5}\text{Zn}_{0.5}\text{Fe}_2\text{O}_4$ nano-tube
- Fig. 3.23: Resistance transients of embedded $\text{Mg}_{0.5}\text{Zn}_{0.5}\text{Fe}_2\text{O}_4$ nano-tubes towards H_2 (~ 1660 ppm) sensing measured at (a) 250 °C, (b) 300 °C, (c) 350 °C and (d) 380 °C. The respective operating temperature ($T_{\text{operating}}$), response (S) (%) and H_2 on-off points are marked in the figure
- Fig. 3.24: Resistance transient of isolated $\text{Mg}_{0.5}\text{Zn}_{0.5}\text{Fe}_2\text{O}_4$ nano-tubes towards H_2 (~ 1660 ppm) sensing measured at (a) 250 °C, (b) 300 °C, (c) 350 °C and (d) 380 °C. The respective operating temperature ($T_{\text{operating}}$), response (S) (%) and H_2 on-off points are marked in the figure
- Fig. 3.25: Resistance transients of (a) embedded and (b) isolated $\text{Mg}_{0.5}\text{Zn}_{0.5}\text{Fe}_2\text{O}_4$ nano-tube sensors in presence of various hydrogen concentrations (10-1660 ppm) measured at ~350 °C. The H_2 concentrations and the respective response (S) (%) are mentioned in the figure
- Fig. 3.26: Resistance transients of embedded $\text{Mg}_{0.5}\text{Zn}_{0.5}\text{Fe}_2\text{O}_4$ nano-tube sensor in presence of 1660 ppm of (a) CO and (b) N_2O gases measured at ~350 °C and 380 °C respectively. The respective response (S) (%) are mentioned in the figure
- Fig. 3.27: Resistance transients of isolated $\text{Mg}_{0.5}\text{Zn}_{0.5}\text{Fe}_2\text{O}_4$ nano-tube sensor in presence of (a) CO (~ 250-1660 ppm) and (b) N_2O (~ 1660 ppm) gases measured at ~250 and 300 °C respectively. The respective response (S) (%) are mentioned in the figure
- Fig. 3.28: Schematic of (a) embedded and (b) isolated tube based sensing elements
- Fig. 3.29: Magnified FESEM micrograph of isolated hollow $\text{Mg}_{0.5}\text{Zn}_{0.5}\text{Fe}_2\text{O}_4$ nano-tubes. The micrograph shows that each tube consists of innumerable tiny crystallites
- Fig. 3.30: X-ray diffractograms of $\text{Mg}_{0.5}\text{Zn}_{0.5}\text{Fe}_2\text{O}_4$ thin films annealed at 600 °C for 2 h in air
- Fig. 3.31: Surface morphologies of $\text{Mg}_{0.5}\text{Zn}_{0.5}\text{Fe}_2\text{O}_4$ thin films spun coated on alumina substrates for (a) 8, (b) 15, (c) 30, and (d) 45 times and annealed at 600 °C for 2 h in air. Inset of Fig. 3.31(c) shows the cross sectional morphology of 30 times coated film

- Fig. 3.32: Variation of response (%) of $\text{Mg}_{0.5}\text{Zn}_{0.5}\text{Fe}_2\text{O}_4$ thin films (8, 15, 30 and 45 times coated) towards the detection of 1660 ppm of H_2 gas as a function of operating temperature
- Fig. 3.33: Response transients of $\text{Mg}_{0.5}\text{Zn}_{0.5}\text{Fe}_2\text{O}_4$ films towards the detection of 1660 ppm of H_2 measured at $\sim 250^\circ\text{C}$
- Fig. 3.34: Resistance transient of 15 times coated $\text{Mg}_{0.5}\text{Zn}_{0.5}\text{Fe}_2\text{O}_4$ thin film towards the detection of 20-1660 ppm of H_2 gas measured at $\sim 250^\circ\text{C}$
- Fig. 3.35: Variation of response (%) of 15 times coated $\text{Mg}_{0.5}\text{Zn}_{0.5}\text{Fe}_2\text{O}_4$ thin film in presence of 1660 ppm of H_2 gas as a function of operating temperature. Inset shows the resistance transient recorded during sensing 1660 ppm of CO at 225°C
- Fig. 3.36: FTIR spectra of as dried carbon templates and the calcined $\text{Mg}_{0.5}\text{Zn}_{0.5}\text{Fe}_2\text{O}_4$ hollow spheres (synthesized using spherical carbon template)
- Fig. 3.37: FESEM image of synthesized spherical carbon templates at (a) low and (b) high magnification. The meso-porous surface of the templates are shown in the magnified image
- Fig. 3.38: X-ray diffractogram of $\text{Mg}_{0.5}\text{Zn}_{0.5}\text{Fe}_2\text{O}_4$ hollow spheres calcined at 600°C for 2 h
- Fig. 3.39: (a) FESEM image (b) EDS spectra of the $\text{Mg}_{0.5}\text{Zn}_{0.5}\text{Fe}_2\text{O}_4$ hollow spheres calcined at 600°C for 2 h
- Fig. 3.40: TEM image of (a) the cluster of hollow-spheres, (b) the magnified image of a single hollow-sphere, (c) a partially formed hollow-sphere, and (d) the SAED pattern of these hollow-spheres
- Fig. 3.41: Resistance transients of $\text{Mg}_{0.5}\text{Zn}_{0.5}\text{Fe}_2\text{O}_4$ hollow sphere sensors during H_2 gas sensing (100-1000 ppm). Transients are measured at $\sim 300^\circ\text{C}$.
- Fig. 3.42: Resistance transient of $\text{Mg}_{0.5}\text{Zn}_{0.5}\text{Fe}_2\text{O}_4$ hollow sphere based sensing element during sensing 1660 ppm of (a) N_2O and (b) CH_4 gas at operating temperature $\sim 300^\circ\text{C}$
- Fig. 3.43: Operating temperature dependence response (%) of $\text{Mg}_{0.5}\text{Zn}_{0.5}\text{Fe}_2\text{O}_4$ hollow sphere based sensing element towards the detection of ~ 1660 ppm H_2 , CO , CH_4 and N_2O gases
- Fig. 3.44: Schematic of $\text{Mg}_{0.5}\text{Zn}_{0.5}\text{Fe}_2\text{O}_4$ (a) pellet (b) thin film and (c) embedded nano-tube (d) isolated nano-tube (e) hollow sphere in the form of thick film with respective electrode configuration. The FESEM micrographs of (f) pellet (g) thin film (h) embedded nano-tubes (i) isolated nano-tubes (j) hollow sphere with respective resistance transients corresponding to hydrogen sensing at

different gas concentrations for (k) pellet, (l) thin film and (m) embedded nano-tubes in anodized alumina templates (n) isolated nano-tubes and (o) hollow spheres

Fig. 3.45: (a) Variation of response (%) of $\text{Mg}_{0.5}\text{Zn}_{0.5}\text{Fe}_2\text{O}_4$ based nano-structured sensing elements as a function of operating temperature towards the detection of 1660 ppm of H_2 gas. (b) response transient of $\text{Mg}_{0.5}\text{Zn}_{0.5}\text{Fe}_2\text{O}_4$ based nano-structured sensing elements towards the detection of 100 ppm of H_2 gas

Fig. 4.1: Lennard Jones diagram for non activated gas adsorption

Fig. 4.2: Resistance transient of zinc ferrite sensor at various hydrogen concentrations. Inset shows the SEM micrograph of zinc ferrite sensing element sintered at 600 °C for 2 h in air. Regions with macro and meso-pores are marked in the picture

Fig. 4.3: Surface morphology of MZFO-P sensing element showing macro and mesoporous regions

Fig. 4.4: The response and recovery conductance transients for (a) MgFe_2O_4 (b) $\text{Mg}_{0.5}\text{Zn}_{0.5}\text{Fe}_2\text{O}_4$ and (c) ZnFe_2O_4 sensing elements for H_2 and CO gas sensing (~ 500 ppm) at respective optimized operating temperature. The symbols are experimental data points, and the solid lines correspond the response and recovery, fitted according to Eqn. 4.24 and Eqn. 4.25 respectively

Fig. 4.5: Temperature variation in the (a) response and (b) recovery time constants for MgFe_2O_4 sensor at a fixed H_2 and CO gas concentration (1660 ppm)

Fig. 4.6: Temperature variation in the (a) response and (b) recovery time constants for $\text{Mg}_{0.5}\text{Zn}_{0.5}\text{Fe}_2\text{O}_4$ sensor at a fixed H_2 and CO gas concentration (1660 ppm)

Fig. 4.7: Temperature variation in the (a) response and (b) recovery time constants for ZnFe_2O_4 sensor at a fixed H_2 and CO gas concentration (1660 ppm)

Fig. 4.8: For ZnFe_2O_4 sensor variation of $G_1/(1-G_1)$, $G_2/(1-G_2)$ vs test gas (H_2 and CO) concentration at constant operating temperature (~ 350 °C)

Fig. 4.9: Variation in the response time constants with test gas (H_2 and CO) concentration at constant operating temperature (~ 350 °C)

Fig. 4.10: Typical response and recovery transients of (a) nano-particulate $\text{Mg}_{0.5}\text{Zn}_{0.5}\text{Fe}_2\text{O}_4$, (b) nano-particulate ZnO , for CO sensing in the concentration range 100-1000 ppm (c) embedded $\text{Mg}_{0.5}\text{Zn}_{0.5}\text{Fe}_2\text{O}_4$ nano-tube (in porous alumina), and (d) isolated $\text{Mg}_{0.5}\text{Zn}_{0.5}\text{Fe}_2\text{O}_4$ nano-tube (coated on fused quartz substrate) for H_2 gas sensing in the concentration range between 10-1660 ppm. Figure 4.10 (a) and (b) compare base line drift characteristics. The inset of Fig. 4.10 (b) shows sinusoidal noise behavior. Fig. 4.10 (c) and (d) present typical spike like features in response and recovery transients. The isolated $\text{Mg}_{0.5}\text{Zn}_{0.5}\text{Fe}_2\text{O}_4$ tubes exhibit p-type sensing behavior

- Fig. 4.11: Response and recovery resistance transients of ZnO sensing element recorded for (a) H₂ and (b) CO gas sensing in the concentration range of 100-1000 ppm at operating temperature ~ 380 °C
- Fig. 4.12: Response and recovery resistance transients of Mg_{0.5}Zn_{0.5}Fe₂O₄ (MZFO-P) sensing element recorded for (a) H₂ and (b) CO gas sensing in the concentration range of 100-1000 ppm at operating temperature ~ 380 °C
- Fig. 4.13: Schematic diagram for Langmuir- Hinshelwood reaction mechanism
- Fig. 4.14: For ZnO sensing elements the response transients for (a) H₂ and (b) CO gas sensing. The operating temperature and test gas concentration is kept at ~ 380 °C and 1000 ppm respectively. The solid lines correspond to best fitted curve based on Eqn. 4.39. The inset shows the variation of response time with test gas concentrations
- Fig. 4.15: (a) Response (%) transients of ZnO elements for CO sensing measured at different operating temperatures. The gas concentration is kept fixed ~ 1660 ppm. (b) Response (%) transients of ZnO elements for CO sensing at different gas concentrations. The operating temperature is kept fixed at ~ 380 °C
- Fig. 4.16: The surface morphology of lightly pressed (a) ZnO sensor sintered at 600 °C for 2 h in air (b) The BET adsorption isotherm of ZnO powders calcined at 600 °C for 2 h in air. The corresponding dV (d) vs pore width plots are shown in the inset of respective figure
- Fig. 4.17: Resistance transients for response and recovery during CO gas (~ 1660 ppm) sensing using ZnO sensing elements at different operating temperatures
- Fig. 4.18: Response (%) transients for (a) H₂ and (b) CO gas sensing using Mg_{0.5}Zn_{0.5}Fe₂O₄ (MZFO-P) sensing elements. The gas concentrations are varied in the range of 100-1000 ppm. The operating temperature is kept fixed at ~ 380 °C
- Fig. 4.19: For Mg_{0.5}Zn_{0.5}Fe₂O₄ (MZFO-P) sensing element, the response (%) transient for 1000 ppm CO gas sensing measured at ~ 380 °C. The solid line correspond the best fitted curve based on Eqn. 4.45. The inset shows the variation of response time with test gas (H₂ and CO) concentrations
- Fig. 4.20: Micrograph of Mg_{0.5}Zn_{0.5}Fe₂O₄ (MZFO-P) sensing element sintered at 600 °C for 2 h in air
- Fig. 4.21: Response and recovery transients for Mg_{0.5}Zn_{0.5}Fe₂O₄ (MZFO-C) sensor during detection of 1660 ppm of H₂ at (a) 250 °C, (b) 300 °C, (c) 350 °C and (d) 380 °C
- Fig. 4.22: Schematic of the adsorption sites on the sensing surface

- Fig. 4.23: Conductance transients recorded for (a) H_2 (b) CO (c) CH_4 gas (500 ppm) sensing using $Mg_{0.5}Zn_{0.5}Fe_2O_4$ (MZFO-C) sensing elements at $\sim 350^\circ C$
- Fig. 4.24: The power spectrum of conductance noise for hydrogen, carbon monoxide and methane gas sensing estimated from the respective conductance transients
- Fig. 4.25: Linear fit (dashed line) of log power vs log frequency for hydrogen, carbon monoxide and methane gas sensing. The exponent γ and corner frequency (f_r) is estimated from the linear fit. The low frequency magnitude of power, γ and f_r for H_2 , CO and CH_4 gas sensing is shown at the inset
- Fig. 4.26: Schematic illustration of Category-I [(a) and (b)] and Category-II [(c) and (d)] type spikes (see text)
- Fig. 4.27: Different types of spike recorded for H_2 sensing using $Mg_{0.5}Zn_{0.5}Fe_2O_4$ hollow spheres (a) Category-I and (b) Category-II. The spikes for each category are enlarged in the inset of respective figures
- Fig. 5.1: Schematic of the three level decomposition of the discrete wavelet transformation
- Fig. 5.2: Conductance transients during response and recovery of magnesium zinc ferrite (MZFO-C) particles for 500 ppm (a) hydrogen, (b) carbon monoxide, (c) methane sensing at the operating temperature $\sim 350^\circ C$. Fig. 5.2.(d) shows the temperature variation of response for the sensing of fixed concentration (1660 ppm) of gases
- Fig. 5.3: Schematic of the sequence of the data analyses adopted for the pattern recognition algorithms
- Fig. 5.4: Variation of the amplitude of the Fourier coefficients of 500 ppm methane conductance transient measured at $350^\circ C$. The amplitude is estimated from the real and imaginary part of the Fourier coefficients shown in the inset
- Fig. 5.5: For methane (500 ppm) conductance transient response, the extracted approximate coefficient from discrete wavelet transformation analyses for (a) level 1, (b) level 2, and (c) level 3. The extracted detailed coefficients for (d) level 1, (e) level 2 and (f) level 3
- Fig. 5.6: Principal component analysis using (a) FFT and (b) DWT extraction parameter matrices and discriminant factor analyses using (c) FFT and (d) DWT extraction parameter matrices
- Fig. 5.7: Schematic of the Taguchi type ferrite gas sensing element
- Fig. 5.8: Schematic design of the polymeric casing to hold the Taguchi type ferrite sensor

Fig. 5.9: (a) Photograph of Taguchi type actual $\text{Mg}_{0.5}\text{Zn}_{0.5}\text{Fe}_2\text{O}_4$ sensing element (b) photograph of the actual polymeric casing prepared using injection molding

Fig. 5.10: (a) Schematic of the resistance measurement circuit diagram (b) photograph of the actual resistance measurement circuit developed in our laboratory

Fig. 5.11: Static gas sensing measurement set-up and measurement circuitry developed in our laboratory

Fig. 5.12: Hydrogen sensing performance of Taguchi type $\text{Mg}_{0.5}\text{Zn}_{0.5}\text{Fe}_2\text{O}_4$ sensor in presence of (a) 300 cc (b) 500 cc of 10,000 ppm of H_2 (at $\sim 200^\circ\text{C}$)

Fig. 5.13: Carbon monoxide sensing performance of Taguchi type $\text{Mg}_{0.5}\text{Zn}_{0.5}\text{Fe}_2\text{O}_4$ (MZFO-C) sensor in presence of 500 cc of 10,000 ppm of CO (at $\sim 200^\circ\text{C}$)

Fig. 5.14: Prototype combustible gas sensor using $\text{Mg}_{0.5}\text{Zn}_{0.5}\text{Fe}_2\text{O}_4$ (MZFO-C) sensing element

Copyright
IIT Kharagpur

LIST OF TABLES

- Table-1.1: Application of gas sensors in various purposes
- Table-1.2: Characteristic sensor parameters and their significance
- Table-1.3: Research strategies to improve the performance of SMO sensors
- Table-2.1: Diagnostic tools used for material characterization
- Table-2.2: Refined structural and micro-structural parameters of magnesium ferrite powders calcined at 300 °C for 2 h
- Table-3.1: The refined structural and micro-structural parameters, estimated for $\text{Mg}_{1-x}\text{Zn}_x\text{Fe}_2\text{O}_4$ ($0.0 \leq x \leq 1.0$) powders calcined at 300 °C and 600 °C
- Table-3.2: Comparison of phase purity, crystallite size and lattice parameters of $\text{Mg}_{0.5}\text{Zn}_{0.5}\text{Fe}_2\text{O}_4$ powders prepared using PVA assisted (MZFO-P) and auto-combustion (MZFO-C) synthesis routes
- Table-3.3: Comparison between the H_2 and CO sensing characteristics of $\text{Mg}_{1-x}\text{Zn}_x\text{Fe}_2\text{O}_4$ ($0.0 \leq x \leq 1.0$) nano-particulate sensing elements
- Table-3.4: Summary of the carrier inversion characteristics reported in literature
- Table-3.5: Values of response (%), response and recovery times estimated from the resistance transients of 15 and 30 times coated films during the detection of 20-1000 ppm of H_2 gas at operating temperature ~ 250 °C
- Table-3.6: Comparison of the H_2 sensing characteristics among the synthesized $\text{Mg}_{0.5}\text{Zn}_{0.5}\text{Fe}_2\text{O}_4$ sensing elements and conventional binary oxide based sensors
- Table-3.7: Comparison of H_2 sensing characteristics of various cubic spinel ferrites with the synthesized $\text{Mg}_{1-x}\text{Zn}_x\text{Fe}_2\text{O}_4$ ($0.0 \leq x \leq 1.0$) based sensing elements
- Table-4.1: Fitted parameters for the response kinetics for H_2 and CO (~ 500 ppm) gas sensing using MgFe_2O_4 , $\text{Mg}_{0.5}\text{Zn}_{0.5}\text{Fe}_2\text{O}_4$ and ZnFe_2O_4 sensing elements
- Table-4.2: Fitted parameters for the recovery kinetics for H_2 and CO (~ 500 ppm) gas sensing using MgFe_2O_4 , $\text{Mg}_{0.5}\text{Zn}_{0.5}\text{Fe}_2\text{O}_4$ and ZnFe_2O_4 sensing elements
- Table-4.3: Estimated activation energies (both for site 1 and site 2) for adsorption and desorption during H_2 and CO gas sensing using ferrite sensing elements
- Table-4.4: Estimated activation energies for adsorption desorption, b and β values for hydrogen and carbon monoxide sensing using zinc ferrite sensing element

Table-4.5: Overview of the reversible and irreversible type gas sensing reported in various types of gas sensing materials. (The abbreviated terms mentioned in the table are: DMMP- dimethyl methylphosphonate; TTF–TCNQ- Tetrathiafulvalene tetracyano- quinodimethane; m-CNT- multiwall carbon nano-tubes; Ppy- polypyrrole)

Table-4.6: Overview of the noisy resistance transients observed for variety of gas sensors during detection of various test gases

Table-4.7: Overview of the spike like features reported for various sensing materials during the detection of a variety of test gases

CONTENTS

Title Page	i
Declaration	v
Certificate by the Supervisor	vii
Acknowledgement	ix
Abstract	xi
List of Symbols and Abbreviations	xiii
List of Figures	xvii
List of Tables	xvii
Contents	xxix
Chapter-1: INTRODUCTION	1
1.1 Preamble	1
1.2. Solid State Gas Sensors	2
1.3. Semiconducting Metal Oxide Gas Sensors: Principle of Operation	6
1.4. Factors Influence the Gas Sensing Performance of a SMO Gas Sensor	8
1.5. Sensor Architecture	11
1.6. Measurement of the Gas Sensing Characteristics	13
1.7. Brief Literature Review on Semiconducting Oxide Gas Sensors	13
1.8. Statement of the Problem	17
1.9. Objective	18
1.10. Organization of the Thesis	19
Reference	21
Chapter-2: EXPERIMENTAL	27
2.1. Introduction	27
2.2. Fabrication of an Automated Gas Sensing Set-up	27
2.2.1. Gas Delivery Unit	28
2.2.2. Reactor Unit	30
2.2.3. Automated Process Control and Data Acquisition	31

2.3. Sensor Material Synthesis: Importance of the Nano-structured Oxides	31
2.3.1. PVA Assisted Sol Gel Method to Prepare $(\text{Mg}_{1-x}\text{Zn}_x)\text{Fe}_2\text{O}_4$ ($0.0 \leq x \leq 1.0$) Nano- particles	35
2.3.2. Synthesis of $\text{Mg}_{0.5}\text{Zn}_{0.5}\text{Fe}_2\text{O}_4$ Nano-particles, Thin Films and Nano-tubes by Modified Pechini Route	36
2.3.3. Hydrothermal Synthesis of $\text{Mg}_{0.5}\text{Zn}_{0.5}\text{Fe}_2\text{O}_4$ Hollow Spheres	40
2.4. Characterization of Synthesized Materials	42
2.4.1. Differential Thermal Analyses (DTA) and Thermal Gravimetric Analysis (TGA)	43
2.4.2. Fourier Transformed Infra-Red (FTIR) Spectra	43
2.4.3. X-ray Diffraction	44
2.4.4. Electron Microscopy	47
2.4.5. BET: Analysis of Surface Area and Pore Size Distribution	51
2.5. Fabrication of Sensing Elements and Gas Sensing Measurements	54
Reference	55
Chapter-3: PHASE FORMATION BEHAVIOR, MICRO-STRUCTURE EVALUATION AND GAS SENSING CHARACTERISTICS OF NANO-STRUCTURED FERRITE MATERIALS	57
3.1. Introduction	57
3.2. Experimental	59
3.3. Phase Formation Behavior, Surface Morphology and Gas Sensing Characteristics of $\text{Mg}_{1-x}\text{Zn}_x\text{Fe}_2\text{O}_4$ ($0.0 \leq x \leq 1.0$) Nano-particles Prepared Using PVA Assisted Wet Chemical Route	60
3.3.1. FTIR Analyses	60
3.3.2. Phase Formation Behavior	61
3.3.3. Surface Morphology	63
3.3.4. Pore-size and Pore-size Distribution	64
3.3.5. Gas Sensing Characteristics of $\text{Mg}_{1-x}\text{Zn}_x\text{Fe}_2\text{O}_4$ ($0.0 \leq x \leq 1.0$) Nano-particulate Sensors	65

3.4. Phase Formation Behavior, Surface Morphology and Gas Sensing Characteristics of $\text{Mg}_{0.5}\text{Zn}_{0.5}\text{Fe}_2\text{O}_4$ Nano-particles Prepared Using Modified Pechini route	70
3.4.1. Thermal and FTIR Analyses	71
3.4.2. Phase Formation Behavior	72
3.4.3. Surface Morphology	73
3.4.4. Pore-size and Pore-size Distribution	74
3.4.5. Comparison between the Gas Sensing Characteristics of $\text{Mg}_{0.5}\text{Zn}_{0.5}\text{Fe}_2\text{O}_4$ Nano-particles Synthesized Using PVA Assisted and Modified Pechini Based Chemical Routes	75
3.5. Structural, Micro-structural and Gas Sensing Characteristics of $\text{Mg}_{0.5}\text{Zn}_{0.5}\text{Fe}_2\text{O}_4$ Nano-tubes	82
3.5.1. Phase Formation Behavior	82
3.5.2. Surface Morphology	82
3.5.3. Gas Sensing Characteristics of $\text{Mg}_{0.5}\text{Zn}_{0.5}\text{Fe}_2\text{O}_4$ Nano-tubes	84
3.5.3.1. Origin of 'n' and 'p' type conduction in embedded and isolated $\text{Mg}_{0.5}\text{Zn}_{0.5}\text{Fe}_2\text{O}_4$ nano-tubes: Effect of surface morphology	88
3.6. Structural, Micro-structural and Gas Sensing Characteristics of $\text{Mg}_{0.5}\text{Zn}_{0.5}\text{Fe}_2\text{O}_4$ Thin Films	92
3.6.1. Structure and Surface Morphology of $\text{Mg}_{0.5}\text{Zn}_{0.5}\text{Fe}_2\text{O}_4$ Thin Films	92
3.6.2. Gas Sensing Characteristics of $\text{Mg}_{0.5}\text{Zn}_{0.5}\text{Fe}_2\text{O}_4$ Thin Films	94
3.7. Structural, Micro-structural and Gas Sensing Characteristics of $\text{Mg}_{0.5}\text{Zn}_{0.5}\text{Fe}_2\text{O}_4$ Hollow Spheres	97
3.7.1. FTIR Analyses and Surface Morphology of the Carbon Templates	98
3.7.2. Structural and Micro-structural Characteristics of $\text{Mg}_{0.5}\text{Zn}_{0.5}\text{Fe}_2\text{O}_4$ Hollow Spheres	99
3.7.3. Gas Sensing Characteristics of $\text{Mg}_{0.5}\text{Zn}_{0.5}\text{Fe}_2\text{O}_4$ Hollow Spheres	101
3.8. Pros and Cons of the Gas Sensing Characteristics of Tailor Made Spinel Nano-structures	103
3.9. Summary and Conclusions	109
Reference	110

Chapter-4: KINETIC ANALYSES OF RESISTANCE/ CONDUCTANCE TRANSIENTS OF FERRITE SENSING ELEMENTS	115
4.1. Introduction	115
4.2. Salient Features of Gas-Solid Interaction during Gas Sensing	116
4.3. Experimental	120
4.4. Modeling the Conductance Transients during Response and Recovery	120
4.4.1. Derivation of the Response and Recovery Conductance Transients Based on Langmuir Adsorption Isotherm	122
4.4.2. Non-Linear Fitting of Response and Recovery Transients	125
4.4.3. Variation of the Response and Recovery Time Constants with Sensor Operating Temperatures	127
4.4.4. Variation of the Estimated Fitted Parameters with Test Gas Concentration: Addressing the selectivity issue	131
4.5. Characteristic features observed in resistance transients	134
4.5.1. Investigations on the Irreversible and Reversible Type Gas Sensing in Oxide Gas Sensors	136
4.5.1.1. Mechanism of irreversible gas sensing	140
4.5.1.2. Mechanism of reversible gas sensing	145
4.5.2. Periodic Undulation of the Resistance Transients during Response and Recovery	149
4.5.3. Spike-Like Features in Resistance Transients	155
4.6. Summary and Conclusions	158
Reference	161

Chapter-5: CROSS SELECTIVITY OF MAGNESIUM ZINC FERRITE SENSING ELEMENT: USE OF PATTERN RECOGNITION TECHNIQUES (PART-I) and DEVELOPMENT OF PROTOTYPE MAGNESIUM ZINC FERRITE COMBUSTIBLE GAS SENSOR (PART-II)	165
5.1. Introduction	165
PART-I	167
5.2. Feature Extraction and Pattern Recognition Methods	167
5.2.1. Feature Extraction Technique	167
5.2.2. Pattern Recognition Algorithm	169
5.3. Experimental	171
5.4. Results and Discussion	172
5.4.1. Feature Extraction from the Conductance Transients	173
5.4.2. Pattern Recognition: Addressing the Selectivity of $Mg_{0.5}Zn_{0.5}Fe_2O_4$ Sensors	175
PART-II	178
5.5. Development and Performance of a Taguchi Type $Mg_{0.5}Zn_{0.5}Fe_2O_4$ Sensor Prototype	178
5.5.2. Resistance Measurement Circuitry	180
5.5.3. Evaluation of the Gas Sensing Characteristics	181
5.5.4. Packaging of the Prototype Ferrite Gas Sensor	183
5.6. Summary and Conclusions	184
Reference	186
Chapter-6: SUMMARY AND CONCLUSIONS	187
6.1. Summary of the Thesis Work	187
6.2. Conclusive Remarks	188
6.3. Highlights of the Thesis Work	192
6.4. Scope for Further Research	194
APPENDIX	195
Appendix-1:	195
Appendix-2:	197
Appendix-3:	198

Copyright
IIT Kharagpur

Chapter-1

INTRODUCTION

1.1. Preamble

Gas sensors play an important role in industrial, medical, environmental, and domestic applications for monitoring toxic and flammable gases [1]. The interaction between the test gas and the sensing surface can be detected by the measurements of change in resistance, capacitance, work function, mass, optical characteristics etc. The specific applications of gas sensors are tabulated in Table 1.1.

Table-1.1: Application of gas sensors in various purposes

Application area	Purpose of gas sensing
Indoor air quality monitoring	Cooking gas leakage monitoring, air quality control, monitoring heat ventilation and air conditioning (HVAC) system
Human safety	Inflammable and toxic gas detection, smoke detection, hydrogen detection in aerospace, methane leak detection, detection of explosive materials
Food industries	Monitoring microbial, fungal attack of food, packaging quality control
Automobile industries	Fuel to oxygen ratio determination, car ventilation system control, NO _x detection, HVAC control
Health care	Breath analysis, disease detection,

The present chapter provides a brief introduction about various types of solid state gas sensors, their working principles and the field of applications. The relative merits and demerits of these gas sensors are compared with metal oxide based semiconducting gas

sensors. Next we have described the factors responsible to achieve good sensing characteristics of semiconducting chemi-resistors. The state of the art metal oxide based gas sensors are reviewed and some of the outstanding issues regarding the synthesis, microstructure engineering and performance of these metal oxides have been highlighted. Based on the literature review we have made the statement of problem and identified the objective of the present research and relevant plan of the thesis work.

1.2. Solid State Gas Sensors

In the last few decades, the demands for highly efficient gas sensors, together with the challenge to detect the toxic gases in harsh environment have invoked the development of various types of solid state gas sensors. These solid state gas sensors include acoustic wave gas sensors, field effect transistor (FET) gas sensors, optical fiber gas sensors, electrochemical gas sensors, chemi-resistive gas sensors etc. The sensing principle, type of sensing elements and application field of these gas sensors are briefly discussed as follows.

Acoustic wave gas sensors: In these devices organic based gas sensing thin films are coated on piezoelectric (lithium niobate, ZnO, quartz) substrates. The schematic of a typical surface acoustic wave (SAW) gas sensor has been shown in **Fig. 1.1**.

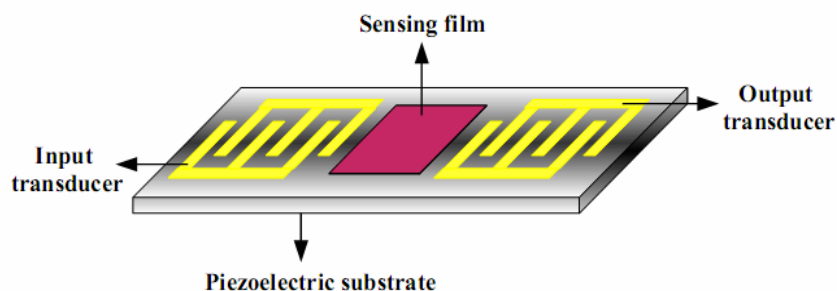


Fig. 1.1: Schematic of a typical acoustic wave based gas sensor

As shown in the figure, the sensing element is placed between two inter-digitated electrodes which act as input and output transducer respectively. When an ac signal is applied to the input transducer of the sensor, a surface acoustic wave (SAW) propagates through the piezoelectric substrate and the resulting signal is recorded in output

transducer. When the device is exposed to any test gas environment, due to gas adsorption, the mass of the sensing film is changed. As a result the frequency, amplitude and phase of the SAW are altered. The changes of these parameters usually vary linearly with the test gas concentration. Depending on the nature of gas sensitive layer (deposited over piezoelectric substrates) SAW based gas sensors can detect a variety of gases (e.g. alcohol, hydrocarbon etc). However these sensors suffer from poor signal to noise performance (as these are operated at high frequencies) and the circuitry required to operate these sensors are complex and expensive [2-3].

Metal-oxide-semiconductor field effect transistor (MOSFET) gas sensors: The architecture of a typical MOSFET sensor is shown in Fig. 1.2. Usually these sensors consist with a catalytic metal (e.g. Pd, Pt), an insulator (SiO_2) and a semiconductor (Si). The catalytic metal layer (used as a gate) is used as gas sensing element and three contacts (source contact, drain contact and gate contact) are used to transmit the signal. The source contact allows current in, drain contact allows current out and a gate contact regulates the current through the transistor.

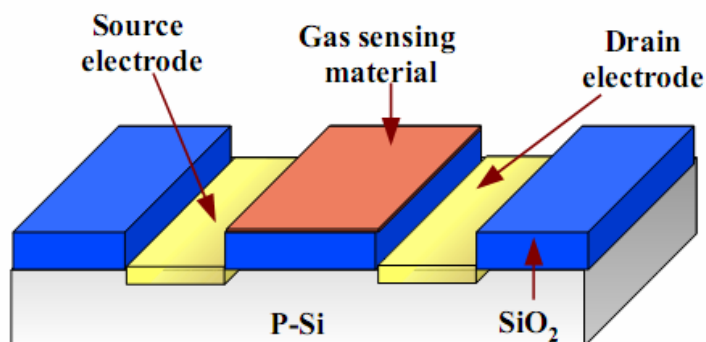


Fig. 1.2: Schematic of a typical MOSFET gas sensor

When a voltage is applied on gate and drain contact an electric field is generated. Upon interaction of gases with the metal gate, the electric field and current through the sensor are changed. The change of the current (through the sensor) is actually due to the variation of work function of the metal and the oxide surface in presence of gas. The performance of MOSFET-based sensors depends on operating temperature and composition of the catalytic metal. MOSFET gas sensors are usually produced by micro-

fabrication technique and thus the reproducibility of these sensors are good and can be incorporated in small volume. However the serious drawback of these sensors is the variation of sensitivity and selectivity with the flow rate of gases which limits their hand held use. These sensors are mostly used to detect H_2 gas [4-5].

Optical gas sensors: In optical sensors the target gas interacts with a sensing layer (usually polymers) and changes the optical properties (viz. index of refraction, absorption coefficient, etc) of the sensing element [1, 6]. The change of optical characteristics of the sensor is specific for particular gas type. The schematic diagram of a fibre optic cable based optical sensor has been shown in Fig. 1.3. As compared to other gas sensors, the optical sensors are not influenced by electro-magnetic interferences and yield faster response. These sensors function well in harsh environment. Additionally, by combining it with standard optical telecom fibres and integrated optics, it is possible to fabricate optical remote gas sensing systems. However, the associated electronics and software for these sensors would be complex in nature and expensive. The sensors often exhibit poor lifetime due to photo-bleaching.

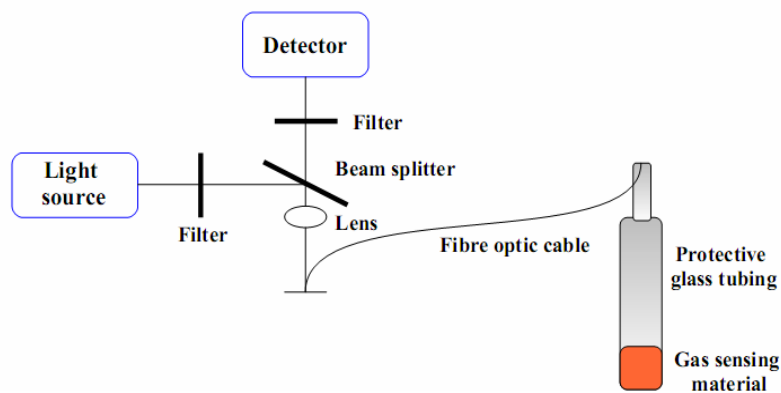


Fig. 1.3: Schematic of a typical fibre optics based optical gas sensor

Electrochemical gas sensors: In an electrochemical gas sensor the test gases are either oxidized or reduced in the anode or cathode surface respectively [1, 7]. These reactions on the electrode surfaces change the internal potential of the electrochemical sensors. Fig.1.4 shows the schematic of a typical electrochemical gas sensor. The performance of an electrochemical sensor is directly related to the concentration or partial pressure of the test gas. Depending on whether the output of the sensor is an open circuit voltage or current, the electrochemical gas sensors is classified as potentiometric or

amperometric sensors respectively. Potentiometric gas sensors are widely used as oxygen sensors (λ -sensors) for monitoring the air/fuel ratio in automotive combustion engines. For an automotive combustion engine, the partial pressure of oxygen in the exhaust gas is measured with respect to oxygen partial pressure of ambient air and thus the air to fuel ratio is determined. Usually ZrO_2 stabilized with Y_2O_3 is commonly used solid electrolyte for such applications. Amperometric sensors are usually operated by applying an external high voltage that electrochemically drives certain electrode reaction to maintain a zero oxygen concentration at the cathodic surface. The performance of an amperometric oxygen sensor is determined by the current response due to the diffusion of oxygen from cathode to anode.

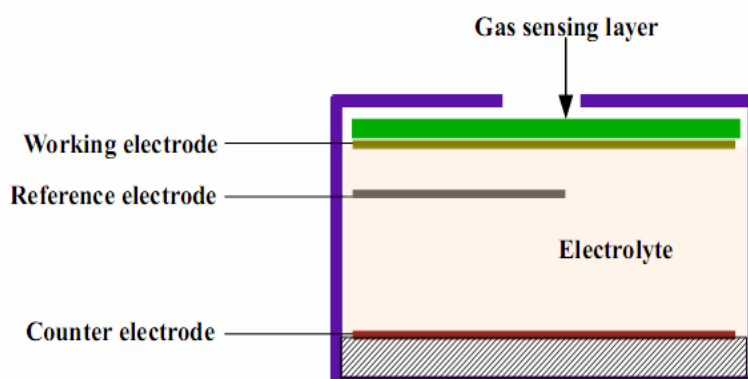


Fig. 1.4: Schematic of a typical electrochemical gas sensor

Chemi-resistive gas sensors: The operation principle of chemi-resistive sensors is based on the variation in resistance/ conductance of the element when these are exposed to target gas atmosphere. A variety of materials (polymeric/ metal oxide/ polymer-metal oxide composite/ carbon nano-tube) are used as sensing materials for these chemi-resistive sensors [8-12]. Polymers (e.g. polypyrrole, polythiophene etc) are often used for low temperature applications. However for high temperature applications metal oxide (e.g. SnO_2 , ZnO , WO_3 etc) are preferred. The mechanisms that lead to the resistance/ conductance variation of these sensors (in presence of reducing or oxidizing gases) are different for polymeric and metal oxide based sensors; however, the architecture of these chemi-resistive sensors is almost similar. Usually, to measure the resistance (or voltage output across a known resistor) of these sensors, inter-digitated or two parallel electrodes are deposited over sensing element. For metal oxide based sensor a heating element is

required to activate the material for sensing. The polymer based sensors exhibit reasonable sensitivity towards polar compounds, but these are very much sensitive towards humidity and do not very useful for long term applications [13]. The metal oxide based sensors are attractive due to their low cost, high sensitivity, long term stability, and compatibility with simple resistance detection electronic circuitry. However, the poor selectivity (towards a specific gas) as well as higher operating temperature sometimes limits their adaptability in different industrial and domestic applications [14-15].

The use of above mentioned solid state gas sensors is directed by their cost, ease of operation and specific application field. Among all the gas sensing materials, semiconducting metal oxide (SMO) based resistive gas sensors (e.g. SnO_2 , ZnO , WO_3 etc) have been extensively studied due to their lower cost, ease of synthesis and simplicity in use. In the following sections the operating principles and factors influence the sensing performance of these SMO based gas sensors are described in details.

1.3. Semiconducting Metal Oxide Gas Sensors: Principle of Operation

The principle of semiconducting metal oxide (SMO) sensor is based on the resistance change of the sensing element with the variation of reducing/oxidizing test gas concentration. The atoms on SMO surface lattice sites do not satisfy all their bonds leading to surface excess dangling bonds with lower coordination number. At elevated temperature, these dangling bonds produce surface active sites for the chemi-adsorption of oxygen. Although the actual gas sensing mechanism over SMO sensor is complicated and not fully understood, the simplified version of the sensing mechanism as reported in several literatures is presented sequentially in Fig. 1.5. As shown in the figure, when a SMO sensing element is heated beyond room temperature oxygen is chemi-adsorbed on the sensor surface. The chemi-adsorption of oxygen over SMO surface forms electron depleted layers which eventually act as potential barrier for grain to grain electron migration on the sensing surface. Exposure to a reducing gas (such as H_2 , CO) leads the surface reaction with the chemi-adsorbed oxygen resulting to the release of electrons to the conduction band of oxide sensor (shown in the band diagram in Fig. 1.5). In case of an n-type SMO, release of electrons to the conduction band increases the number of main charge carriers which decreases the sensor resistance.

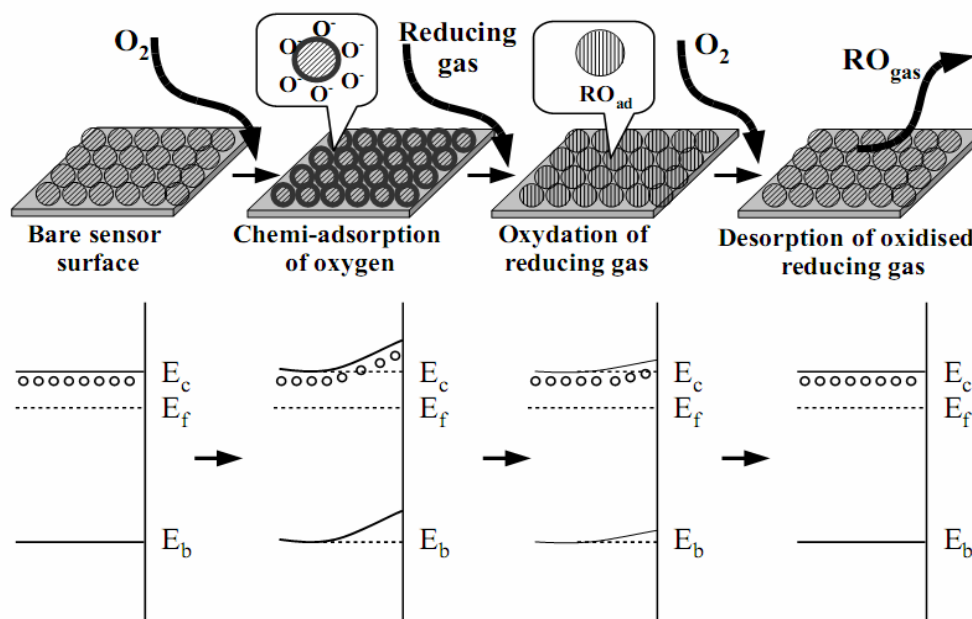


Fig. 1.5: Gas sensing mechanism of semiconducting metal oxide based sensor. The change of band diagram during gas sensing over n-type semiconducting oxide surface is shown in the figure. E_c , E_b , E_f signify the conduction band, valence band and Fermi energy level respectively

Since for a p-type material, holes are the majority charge carriers; the released electrons recombine with the holes, resulting an increase of sensor resistance. So irrespective of the n or p type oxide, the resistance of the sensor in air (R_a) changes in exposure to a reducing gas finally to attain steady state value (R_g). For an n-type SMO sensor, the

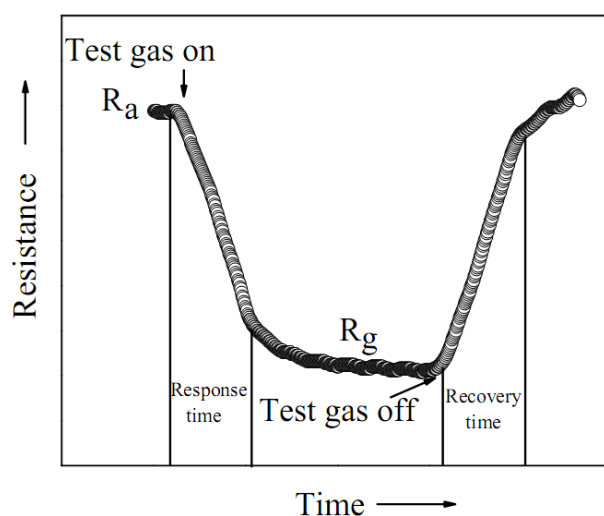


Fig. 1.6: Typical resistance transient of an n-type SMO sensor during detection of reducing gas

typical resistance transient recorded during the detection of reducing gas is shown in Fig. 1.6. The parameters (extracted from the corresponding resistance transients) and their significance which demonstrates the performance of a SMO sensor has been described in Table-1.2.

Table-1.2: Characteristic sensor parameters and their significance

Sensor parameters	Significance
Response (S) (%)	$(R_a - R_g)/R_a$ % or R_a/R_g where R_a and R_g is the resistance of the sensor in presence of air and test gas respectively
Selectivity	Maximum response to a particular gas over other test gases
Optimized operating temperature (T_{opt}) ($^{\circ}\text{C}$)	The temperature at which sensor shows maximum response
Response time (τ_{res}) (s)	Time required to attain about 63 % of the total resistance (/output voltage) change during response process
Recovery time (τ_{rec}) (s)	Time required to attain about 63 % of the total resistance (/output voltage) change during recovery process
Response range	The minimum and maximum gas concentration can be detected by a sensing element
Stability	Minimal variation of the base resistance (measured in ambient condition) after repeated response-recovery cycles
Ageing (days)	Identical gas sensing performance of the sensing element after left idle for long time.

1.4. Factors Influence the Gas Sensing Performance of a SMO Gas Sensor

The gas sensing performance of a SMO based sensor is influenced by the *receptor*, *transducer*, and *utility* functions of the sensing element. These functions are illustrated schematically in Fig. 1.7. The structure of the sensing elements at different length scales influence these functions. The *receptor* function is influenced by the crystallite size of the semiconducting oxide. At elevated temperature oxygen ions are chemi-adsorbed on these crystallites forming a charge depleted layer. The receptor function decides how the sensing surface interacts with the gas environment during the response and recovery. The *transducer* function, on the other hand, controls the flow of charge carriers between the

electrodes. Finally, the *utility* function controls the diffusion of gases during the response and recovery of the sensors.

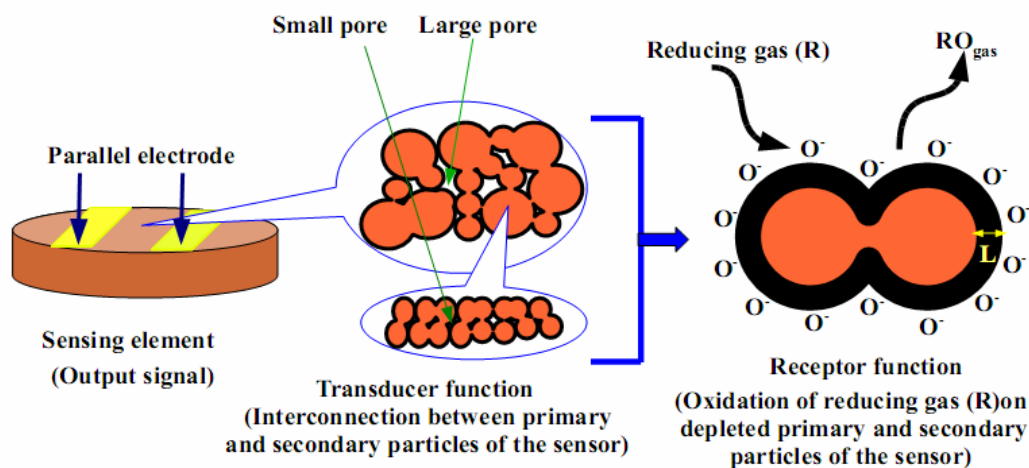


Fig. 1.7: Receptor, transducer and utility function for a typical SMO sensor

The key parameters that control the *receptor* function of the sensor include its composition, nature of metal-oxygen bonding, specific surface area, porosity, and crystallite size. The *transducer* function is influenced by the grain to grain contact and phase purity of the sensing element. The composition of the sensing element and the nature (ionic/ covalent) of the metal-oxygen bond influence the defect chemistry which in turn changes the nature of surface dangling bonds of the sensing elements [16-18]. The surface area, nature of porosity, grain size, grain to grain contact of a sensing element are dependent on the synthesis condition of sensor material and the methodology to fabricate the sensing element. As shown schematically in Fig. 1.7, when the nano-particulate based sensing materials are loosely compacted in the form of circular pellet and sintered at relatively lower temperature, the sensor surface possesses a complex porous structure. The nano-particulate sensors consist of loosely sintered secondary particles termed as grains [19-20]. The secondary particles consist of number of tiny primary particles (alternatively termed as crystallites). Generally the dimensions of pores between the secondary particles are in the order of microns (termed as macro-pores), whereas those in between the primary particles are in the order of nanometers (< 50 nm) (termed as meso-pores). When the sensor is aged at elevated temperature, oxygen gas is diffused through

both the macro (corresponds to molecular diffusion) and meso-porous (corresponds to Knudsen diffusion) regions and these regions are charge depleted due to the chemi-adsorption of oxygen. During gas sensing the test gases diffuse through macro and meso-porous regions and react with the chemi-adsorbed oxygen. The diffusion of gases through the meso-porous regions is known to play important role during the reducing gas sensing using SMO based sensing elements [20-22]. The magnitude of conductance change (upon its exposure to reducing gases) depends on the depth of the depleted layer; and beyond this layer the sensor material is considered inactive towards gas sensing. It is reported that when the grain size (D) of the sensing material is equal to twice of the depletion layer thickness (L), it becomes fully depleted. Therefore, when the grain size becomes larger than twice the depletion layer thickness, it becomes partially depleted [21]. Maximum response is achieved when the grains are fully depleted. It is therefore obvious that in order to yield maximum response, the crystallite size should be in the order of twice of the depletion layer width. For a variety of oxide gas sensors, the depletion layer width has been calculated to be in the range of 3-10 nm. Therefore, in order to yield maximum response, the particle size of the sensing materials should be in the range of 6-20 nm. Additionally, the pore size and pore size distribution of these nano-crystalline sensing element should be conducive to easier diffusion of oxygen, test gas and their reaction product. Meso-porous sensing surfaces yield improved gas sensing performance.

The presence of electrically insulating impurity phase(s), precipitated during the synthesis of multi-component oxides [23], impede the movement of the charge carriers during electrical conduction. Presence of impurity phase(s), therefore, deteriorates the gas sensing performance of multi-component oxide sensors.

The gas sensing response of SMO based sensors can also be markedly improved using porous nano-structured sensing elements with various geometries [24-27]. For a fixed electrode separation, the nano-structured electrodes usually yield higher resistance, however, the operating temperature (corresponds to highest sensitivity) is grossly reduced than its bulk counterpart. The first factor demands larger drive voltage whereas the later is conducive to lower heater voltage and thus these two factors has a competitive effect in favor to increase/reduce the operating power of the sensor with a nano-structured sensing element.

The selectivity of a sensor towards a specific gas sensing can be improved by adding suitable noble metals. These noble metals form a porous coating on the oxide particles yielding a core-shell type structure. The selectivity towards a specific gas is believed to be due to catalytic effect rendered by the added noble metal atoms.

1.5. Sensor Architecture

Figure 1.8 shows various types of sensor architectures used for gas sensing using SMO based sensing materials. To evaluate the gas sensing performance the ceramic powders are pressed in the form of circular pellets (Fig. 1.8(a)). The pellets are sintered at lower temperature to maintain the porous structure and retard the particle growth. The sintering temperature is sufficient enough to yield neck formation between particles (for efficient transduction) and sufficient handling strength. As shown in the figure, two parallel electrode stripes are either painted or vacuum deposited for electrical contacts. Such palletized sensing elements are not used in any commercial sensor.

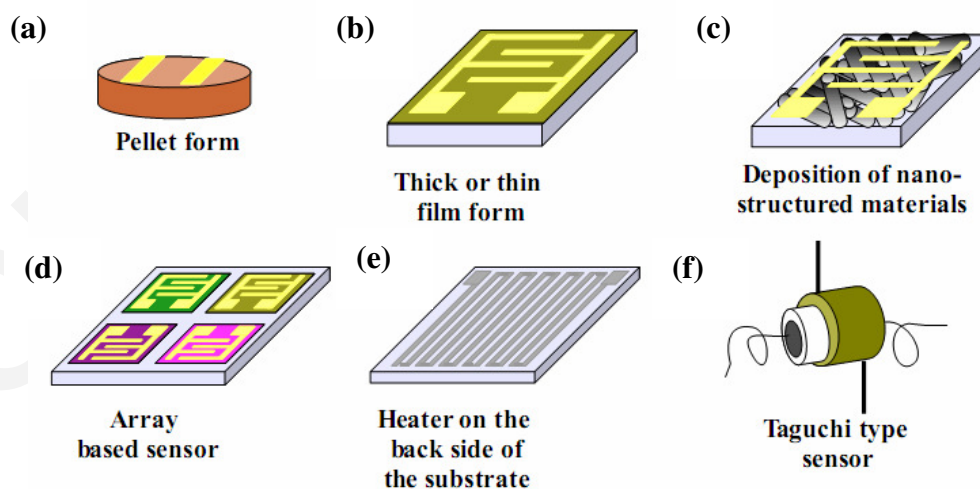


Fig. 1.8: Various types of sensor architectures

In commercial gas sensors either a Taguchi type (Fig. 1.8(f)) or thin/thick film type (Fig. 1.8(b)) sensing elements are used. To fabricate a Taguchi type sensing element, the sensing materials (in the form of powder) are suspended in an organic binder (PVDF-NMP solution). The suspension is coated on a hollow alumina tube (see Fig. 1.8(f)). The coated layer is dried in a vacuum oven and sintered at lower temperature to yield a porous

layer. A nichrome heater is inserted into the hollow alumina tube to heat the sensor surface for oxygen chemi-adsorption during the gas sensing. Finally the sensing layer is coated with Ag/Au conducting paste for taking out the electrical contacts.

For the thin film architecture, the sensing elements are deposited on thermally conducting but electrically insulating substrate (alumina, fused quartz, mica) using spin/dip coating or physical/chemical vapor deposition techniques. Thick films are usually deposited by tape casting or screen print techniques. These films are sintered at relatively lower temperature to ensure the porous structure and minimal grain growth of the sensing materials. As shown in Fig. 1.8(b), IDE electrodes are sputter deposited on the deposited film. The IDE structure ensures lower surface resistance between the contacts. At the back of the substrate, metal IDE is sputter deposited to act as a heater (see Fig. 1.8(e)). By controlling the heater voltage one can control the surface temperature of the sensing elements.

Figure 1.8(c) shows the sensing elements with nano-tube type sensing elements. As described in details in Chapter-2, using wet chemical routes, one can synthesize a variety of nano-structured sensing elements directly on top of the underlying ceramic substrates. As mentioned earlier, the back surface of the substrate is coated with IDE metals which act as a heater. Such nano-structured sensing elements yield efficient gas sensing performance; however, to the best of our knowledge, these are not yet commercially available.

SMO based sensors usually have poor selectivity towards a specific gas. As mentioned in the preceding section, by suitable noble metal doping the cross-selectivity can be grossly minimized. In other words, the response of a SMO sensor may be maximized for a particular gas sensing. Several such selective sensors can be deposited on a single substrate to form a sensor array. Figure 1.8(d) shows the schematic of a typical sensor array comprising 4 such selective sensors. As shown in Fig. 1.8(d), each of these sensors is coated with IDE electrodes to measure individual resistance/conductance transients. By comparing the response one can identify a specific gas type. In the following section we have described the details of different types of gas sensing measurements.

1.6. Measurement of the Gas Sensing Characteristics

Generally two types of measurement protocols, namely *static* and *dynamic*, are adopted to evaluate the gas sensing characteristics of SMO sensors [28-29]. In *static* method the sensors are kept in closed chamber and the sensor temperature is increased from room temperature to required operating temperature. The sensor is aged at the operating temperature for a long time until it attains a constant resistance value. After attaining a fixed sensor resistance in air (R_a) a test gas is injected into the closed chamber. Depending on the volume of the closed chamber (/ dilution of the test gas), the test gas ultimately reaches to the sensor surface and react with the chemi-adsorbed oxygen to decrease/ increase (depending on the n/p type SMO) the sensor resistance finally to attain a constant resistance value in test gas atmosphere (R_g). The sensor is usually recovered to its initial state by opening the chamber in ambient air or by applying vacuum.

In *dynamic* method the sensors are kept in a chamber with continuous flow of gases which leads higher flux density of gases over the sensing surface. At elevated temperature (sensor operating temperature) first the sensor is allowed to be exposed in a continuous flow of air (usually controlled by mass flow controllers) to attain a constant base resistance in air. After achieving a fixed sensor resistance in air (R_a) a calculated amount of test / carrier gas mixture is passed through the chamber with same flow rate until it attains a fixed resistance (R_g). Generally the sensor recovery is attained by flushing the sensor with the flow of air.

1.7. Brief Literature Review on Semiconducting Oxide Gas Sensors

Change of the surface resistance upon gas-solid interaction is first discovered by Bielanski et. al. and Seiyama et. al. [30-31]. Based on this phenomenon Taguchi made SnO_2 based commercial gas sensor to detect flammable/explosive gases [32]. Now-a-days there are a number of companies manufacture SMO based gas sensors. Among them Figaro (<http://www.figarosensor.com/>) and FIS (<http://www.fisinc.co.jp/>) are considered to be the market leader.

As outlined earlier, the sensing performance of SMO based sensors are governed by three key parameters namely receptor, transducer, and utility functions. It is important to develop low cost SMO based sensors to detect low concentration test gas at lower

operating temperature. These sensors should exhibit quick response and recovery characteristics with marginal drift in base resistance after prolonged operation. Several strategies are adopted to improve the gas sensing performance of SMO gas sensors. The focus of these research issues and adopted strategies are tabulated in Table-1.3.

Table-1.3: Research strategies to improve the performance of SMO sensors

Research issues	Adopted strategies	Ref.
Investigate the gas sensing characteristics of a variety of multi-functional oxide ceramics	Apart from the conventional metal oxides (SnO_2 , ZnO , WO_3 etc), the gas sensing performance of various perovskite, cubic spinel and pyrochlore materials are investigated. Some of these oxides exhibit selective response for a particular gas type.	[12,33-37]
Effect of oxygen and cation vacancy concentration on the gas sensing characteristics	Metal oxide doped with aliovalent dopants. The gas sensing characteristics are correlated with defect concentration and band gap energies.	[16,17,38-41]
Process induced structural modification of the sensing materials and correlate structure with gas sensing characteristics.	Phase pure, meso-porous oxides with large specific surface area are synthesized by various wet chemical and hydrothermal routes.	[42-46]
Gas sensing characteristics of nano-structured oxide sensor-Marked improvement of the sensing characteristics due to size effect.	Various oxides in the form of nano-tube, nano-wire, nano-belts, nano-ribbon, thin film, hollow spheres etc have been synthesized by wet chemical route and PVD routes. Gas detection in ppb level is reported for some nano-structured oxides.	[9,25-27,47-51]
Surface modification of oxide sensors to improve the cross-selectivity	Surface coating of the oxide particles with noble metals to form core-shell structure. The noble metal dissociates certain molecular gas into active atomic form resulting significant improvement in response characteristics.	[52-53]
Improved sensing through engineered sensor architecture.	Engineered surface morphology of sensing element; improving the electrode and heater configuration for thin/thick film sensors; improving the electronic circuit module for detecting the minute resistance change.	[54-55]

Reviewing the literature reports summarized in Table-1.3, it is apparent that major research efforts are directed to improve the basic sensing characteristics of SMO based sensors. Indeed, quick response-recovery and ppb level sensing are achieved in nano-structured SMO sensors. Unfortunately, optimized operating temperature for these sensors still remain quite high ($> 250\text{ }^{\circ}\text{C}$) and cross-selectivity still remains a major research issue.

Various strategies have been adopted to address the cross-selectivity issue. These include modulation of sensor operating temperature [56], use of filter [57], surface modification of the sensing elements using noble metals [52-53] etc.

Inspecting the resistance/conductance transients during the response and recovery of SMO based sensing elements; a number of interesting features are noted. These features include the drift in the base resistance [58-59], appearance of sinusoidal noise [60-61], and sporadic spikes [9, 62]. In some cases, n to p type conductivity switching is also reported [63-64]. Through the analyses of noise spectra the selectivity issue of SMO based sensors has been addressed [9]. These features are quite generic for a variety of SMO based sensing elements used to detect various test gases; however, limited effort has so far been made to understand the underlying mechanism controlling the occurrence of such features in the transient spectra.

The literature review presented above can be summarized as follows. The interaction between the test gas and the sensing surface can be detected by the measurements of change in resistance, capacitance, work function, mass, optical characteristics etc. Various sensing materials (covalent semiconductors, semiconducting metal oxides, solid electrolytes, polymers etc) in the form of a porous thick or thin film and a variety of measurement techniques have been utilized to characterize the gas-solid interaction. Among all the gas sensing materials, semiconducting metal oxide based resistive gas sensors have been extensively studied due to their lower cost, ease of production and simplicity in use. Binary oxides such as SnO_2 , In_2O_3 , WO_3 etc are used as conventional gas sensing materials. The binary oxides have poor selectivity towards various reducing gases. As an effective alternative to these binary oxides various spinel ferrites reported not only to have excellent gas sensitivity but also some of them exhibit reasonably good selectivity to a specific gas environment [65-68]. Both for these conventional as well as

spinel oxides, gas sensing response can be markedly improved using porous nano-structured sensors of various geometries. For a fixed electrode separation, the nano-structured electrodes usually yield higher resistance, however, the operating temperature (corresponds to highest sensitivity) is grossly reduced than its bulk counterpart. The first factor demands larger drive voltage whereas the later is conducive to lower heater voltage and thus these two factors has a competitive effect in favor to increase/reduce the operating power of the sensor with a nano-structured sensing element.

As compared to these porous nano-structured electrodes, partially sintered block of sensors possesses far more complex (porous) structures. The later can be think of consisting loosely sintered secondary particles (termed as grains) whereas each of these secondary particles consist number of tiny primary particles (termed as crystallites). The dimensions of pores between the secondary particles are in the order of microns (macro-pores), whereas that in between the primary particles is in the order of nanometers (meso-pores). It is obvious that the gas diffusion through the macro-pores (molecular diffusion) is much more rapid than the diffusion of gas through meso-pores (Knudsen diffusion) [21]. It is apparent that reduction of the crystallite size (in the order of twice the depletion layer thickness) as well as increase of the size of meso-pores would increase the sensitivity of the gas sensor [20-21]. Therefore, in order to develop highly sensitive gas sensors the adoptive strategy should be to synthesize the gas sensing material at lower process temperature (to yield smaller crystallite size) and also sinter them at low temperature to yield sufficient handling strength as well as macro-porous structure. Two different measurement protocols, namely *static* and *dynamic*, have been adopted to estimate the sensing characteristics of synthesized materials in the form of bulk, thin film or nano-structured porous electrodes.

The sensing response of the sensors is usually measured in the equilibrium condition (noting the resistance values when the chemi-adsorption of oxygen is complete (R_a) and test gas reacts completely with the absorbed oxygen (R_g)) using either the relation $S = R_a/R_g$ or $(R_a - R_g)/R_a$. Since the gas sensing mechanism involves surface oxidation/reduction, electron exchange and desorption of the reaction product, the dynamics of these process is completely overlooked when the sensor characteristics is estimated from the equilibrium conditions [48-50]. In order to measure the kinetics of

response and recovery, dynamic measurement protocol needs to be adopted. Although a few theoretical and experimental works in this direction have been reported in the literature, most of these works are based on conventional oxides [69], hetero-contacts [70] or polymer based sensors [71] and to the best of our knowledge, the analyses of response of recovery kinetics of ferrite based sensors have not been studied.

1.8. Statement of the Problem

Viewing in light of the above, we felt that there is a growing need to identify sensing materials (alternate to existing binary oxides) which are selective to toxic and inflammable gases. Ferrites are demonstrated to be efficient gas sensing materials and many of them exhibit pronounced selectivity towards specific gases. Therefore, there exists a growing need to investigate the gas sensing performance of non-conventional ceramic oxides in order to achieve improved gas response, selectivity and lower operating temperature.

Recently it has been reported that the gas sensing performance as well as the selectivity of many of these oxides are markedly improved in nano-structured morphologies. Therefore, the synthesis and gas sensing characteristics of the nano-structured oxides need to be systematically investigated by varying the test gas concentration and operating temperatures.

Since the gas sensing mechanism in oxide semiconductors involve surface oxidation, electron exchange and desorption of the reaction product; the kinetics of response and recovery characteristics of these sensors need to be investigated. Through these analyses the activation energies for gas adsorption and desorption processes may be estimated from the respective thermally activated kinetic process. Since each gas, depending on its reactivity, size of the gas molecules etc has characteristic activation energies for adsorption and desorption, kinetic analyses of resistance transients during response and recovery might give valuable insight towards their selectivity when exposed to various types of reducing gas environments.

In case of discrete binary semiconducting oxide gas sensors, cross-selectivity remains one of the major research issues that often lead to false alarm. To improve the selectivity of these discrete binary oxide sensors various research approaches namely temperature programming, surface sensitization using catalysts, use of filters etc has been attempted. To address the selectivity issue, we felt that in addition to the kinetic analysis of the resistance/conductance transient during gas sensing; feature extraction method of the conductance transients in conjunction with pattern recognition algorithms may be considered as a viable tool to investigate the cross-selectivity of the sensor elements towards various reducing gases.

Most of the literature reports on gas sensing materials are based on laboratory research. The performance of the synthesized sensing materials in a real time sensor may be markedly different. In order to evaluate the sensing performance of the optimized sensing materials for practical applications, development of prototype gas sensor with allied electronic circuit module needs to be developed. The performance of the sensor prototype would reflect the true performance of the developed gas sensor materials.

1.9. Objective

The specific objective of present thesis is as follows:

- Development of a soft solution processing route to synthesize binary (e.g. ZnO) and quaternary oxide [e. g. $\text{Mg}_{1-x}\text{Zn}_x\text{Fe}_2\text{O}_4$ ($0.0 \leq x \leq 1.0$)] nano-structures in the form of nano-powders (0-d), nano-tubes (1-d), thin films (2-d), embedded nano-tubes in anodized alumina templates, and hollow spheres.
- Development of an automated, dynamic volume gas sensing set up to measure the resistance changes of the sensing elements as a function of gas concentration and operating temperatures. The gas sensing set up would have three major components namely gas delivery system, reactor and resistance measurement unit.
- Characterize the phase formation behavior, microstructure of the synthesized nano-structured oxides. Evaluation of their gas sensing characteristics in terms of response (%), response/recovery time, stability and selectivity.

- Investigate the kinetics of the response as well as recovery behavior through the analysis of respective conductance transients. Modeling the conductance transients to understand the underlying physics of the gas-solid interactions operative in the synthesized nano-structured sensing materials.
- Use of pattern recognition techniques to address the cross-selectivity issue of the synthesized sensing materials. Fabrication of a static test box chamber, prototype sensing elements and electronic circuit module to test the gas sensing performance of the process optimized sensing materials.

1.10. Organization of the Thesis

The thesis work is divided into six chapters as detailed below.

Chapter-1 provides a brief introduction about various types of solid state gas sensors, their working principles and the field of applications. We have described the factors responsible to achieve good gas sensing characteristics of semiconducting chemi-resistors. The state of the art metal oxide based gas sensors are reviewed and some of the outstanding issues regarding the synthesis, microstructure engineering and performance of these metal oxides have been highlighted. Based on the literature review we have made the statement of problem and identified the objectives of the present research and relevant plan of the thesis work.

Chapter-2 begins with the description of the salient features of the design and development of an automated dynamic gas sensing measurement set up. For control and automated data acquisition we have interfaced the mass flow controllers and an electrometer with a personal computer using Labview 8.5 software. In the next section we have described the wet chemical synthesis of nano-structured oxides in the form of nano-powders, nano-tubes, thin film, embedded nano-tube in porous alumina template, and hollow spheres. In the subsequent sections we have introduced the characterization tools used in the present study. For each of these characterization tools, the working principle, details of the instrumentation, sample preparation, characterization conditions and data analyses procedures have been described sequentially.

Chapter-3 deals with the phase formation behavior, surface morphology and gas sensing characteristics of nano-structured (nano-powders, nano-tubes, thin film, embedded nano-tube in porous alumina template, and hollow spheres) $\text{Mg}_{1-x}\text{Zn}_x\text{Fe}_2\text{O}_4$ (MZFO) ($0.0 \leq x \leq 1.0$) sensing elements.

Chapter-4 deals with the analyses of resistance/conductance transients during the response and recovery of gas sensing measurements. The chapter begins with a preamble on the salient features of such transient analyses. The kinetics of conductance transients (during gas sensing and recovery) has been modeled using Langmuir adsorption isotherm. A number of interesting features are observed in the recorded resistance transients of the binary and spinel oxide based nano-structured sensing materials. Some of the prominent identified features include (i) drift in the base resistance upon repeated response and recovery cycles, causes mainly due to the unsaturated resistance transients during response and recovery, (ii) switching from n to p type conduction behavior of certain nano-structured magnesium zinc ferrite elements, (iii) response and recovery transients with sinusoidal noise (iv) occurrence of 'spike' like features in the resistance transients. In the remaining part of Chapter-4, we have made an attempt to understand the nature and origin of these features based on our developed hypothesis on the reaction sequence of gas absorption and desorption of the reaction products.

Chapter-5 begins with the feature extraction method of the conductance transients in conjunction with pattern recognition algorithms to investigate the cross-selectivity of $\text{Mg}_{0.5}\text{Zn}_{0.5}\text{Fe}_2\text{O}_4$ sensing elements towards methane, carbon mono oxide and hydrogen gases. The remaining part of Chapter-5 describes the fabrication details and hydrogen sensing characteristics of a Taguchi type sensor made using optimized magnesium zinc ferrite nano-particles.

Chapter-6 highlights the important conclusions derived from the present study and also suggest the scope of further works.

Reference

- [1] Capone, S., Forleo, A., Francioso, L., Rella, R., Siciliano, P., Spadavecchia, J., Presicce, D.S. and Taurino, A.M. (2003), Solid State Gas Sensors: State of the Art and Future Activities, *Journal of Optoelectronics and Advanced Materials*, Vol. 5, pp.1335-1348.
- [2] Hoummady, M., Campitelli, A. and Wlodarski, W. (1997), *Acoustic Wave Sensors: Design, Sensing Mechanisms and Applications*, Smart Materials and Structures, Vol. 6, pp. 647-657.
- [3] Sadek, A.Z., Wlodarski, W., Shin, K., Kaner, R.B. and Kalantarzadeh, K. (2006), A Layered Surface Acoustic Wave Gas Sensor Based on a Polyaniline/ In_2O_3 Nanofibre Composite, *Nanotechnology*, Vol.17, pp. 4488-4492.
- [4] Arshak, K., Moore, E., Lyons, G.M., Harris, J. and Clifford, S. (2004), A Review of Gas Sensors Employed in Electronic Nose Applications, *Sensor Review*, Vol. 24, pp. 181-198.
- [5] Liao, L., Zhang, Z., Yan, B., Zheng, Z., Bao, Q.L., Wu, T., Li, C.M., Shen, Z.X., Zhang, J.X., Gong, H., Li, J.C. and Yu, T. (2009), Multifunctional CuO Nanowire Devices: p-type Field Effect Transistors and CO Gas Sensors, *Nanotechnology*, Vol. 20, pp. 085203 (6pp).
- [6] Soller, B.R. (1994), Design of Intravascular Fiber Optic Blood Gas Sensors, *IEEE Engineering Medicine and Biology*, Vol. June/ July, pp. 327-335.
- [7] Moseley, P.T., (1997), Solid State Gas Sensors, *Measurement and Science Technology*, Vol. 8, pp. 223-237.
- [8] Gong, J., Sun, J. and Chen, Q. (2008), Micromachined Sol-Gel Carbon Nanotube/ SnO_2 Nanocomposite Hydrogen Sensor, *Sensors and Actuators B*, Vol.130, pp. 829-835.
- [9] Tan, Y., Li, C., Wang, Y., Tang, J. and Ouyang, X. (2008), Fast-Response and High Sensitivity Gas Sensors Based on SnO_2 Hollow Spheres, *Thin Solid Films*, Vol. 516, pp. 7840-7843.
- [10] Wu, R.J., Huang, Y.C., Yu, M.R., Lin, T.H. and Hung, S.L. (2008), Application of m-CNTs/ NaClO_4 /Ppy to a Fast Response Room Working Temperature Ethanol Sensor, *Sensors and Actuators B*, Vol. 134, pp. 213-218.
- [11] Hong, L., Li, Y. and Yang, M. (2010), Fabrication and Ammonia Gas Sensing of Palladium/Polypyrrole Nanocomposite, *Sensors and Actuators B*, Vol.145, pp. 25-31.
- [12] Eranna, G., Joshi, B.C., Runthala, D.P. and Gupta, R.P. (2004), Oxide Materials for Development of Integrated Gas Sensors-A Comprehensive Review, *Critical Reviews in Solid State and Materials Sciences*, Vol. 29, pp.111-188.
- [13] Cole, M., Olivieri, N., Guzman, J.G. and Gardner, J.W. (2003), Parametric Model of a Polymeric Chemoresistor for Use in Smart Sensor Design and Simulation, *Microelectronics Journal*, Vol. 34, pp. 865-875.

- [14] Tomchenko, A.A., Harmer, G.P., Marquis, B.T. and Allen, J.W. (2003), Semiconducting Metal Oxide Sensor Array for the Selective Detection of Combustion Gases, *Sensors and Actuators B*, Vol. 93, pp.126-134.
- [15] Gomri, S., Seguin, J.L. and Aguir, K. (2005), Modeling on Oxygen Chemisorption-Induced Noise in Metallic Oxide Gas Sensors, *Sensors and Actuators B*, Vol.107, pp. 722-729.
- [16] Batzill, M., and Diebold, U. (2007), Surface Studies of Gas Sensing Metal Oxides, *Physical Chemistry Chemical Physics*, Vol. 9, pp. 2307–2318.
- [17] Ahn, M.W., Park, K.S., Heo, J.H., Park, J.G., Kim, D.W., Choi, K.J., Lee, J.H. and Hong, S.H. (2008), Gas Sensing Properties of Defect-Controlled ZnO-Nanowire Gas Sensor, *Applied Physics Letters*, Vol. 93, pp. 263103 (3).
- [18] Korotcenkov, G. (2007), Metal Oxides for Solid-State Gas Sensors: What Determines Our Choice?, *Materials Science and Engineering B*, Vol. 139, pp. 1-23.
- [19] Yamazoe, N. and Shimanoe, K. (2009) Receptor Function and Response of Semiconductor Gas Sensor, *Journal of Sensors*, Article ID. 875704 (21).
- [20] Yamazoe, N., Sakai, G. and Shimanoe, K. (2003), Oxide Semiconductor Gas Sensors, *Catalysis Surveys from Asia*, Vol. 7, pp. 63-75.
- [21] Tiemann, M. (2007), Porous Metal Oxides as Gas Sensors, *Chemistry-A European Journal*, Vol. 13, pp. 8376-8388.
- [22] Sakai, G., Matsunaga, N., Shimanoe, K. and Yamazoe, N. (2001), Theory of Gas Diffusion Controlled Sensitivity for Thin Film Semiconductor Gas Sensor, *Sensors and Actuators B*, Vol. 80, pp. 125-131.
- [23] Rao, C.N.R., Vanitha, P.V. and Cheetham, A.K. (2003), Phase Separation in Metal Oxides, *Chemistry-A European Journal*, Vol. 9, pp. 828-836.
- [24] Kolmakov, A. and Moskovits, M. (2004), Chemical Sensing and Catalysis by One Dimensional Metal-oxide Nanostructures, *Annual Review of Materials Research*, Vol. 34, pp.151-180.
- [25] Lee, J.H. (2009), Gas Sensors Using Hierarchical and Hollow Oxide Nanostructures: Overview, *Sensors and Actuators B*, Vol.140, pp. 319-336.
- [26] Gerlitza, R.A., Benkstein, K.D., Lahr, D.L., Hertz, J.L., Montgomery, C.B., Bonevich, J.E., Semancik, S. and Tarlov, M.J. (2009), Fabrication and Gas Sensing Performance of Parallel Assemblies of Metal Oxide Nanotubes Supported by Porous Aluminum Oxide Membranes, *Sensors and Actuators B*, Vol.136, pp. 257-264.
- [27] Deb, B., Desai, S., Sumanasekera G.U. and Sunkara, M.K. (2007), Gas Sensing Behaviour of Mat Like Networked Tungsten Oxide Nanowire Thin Films, *Nanotechnology*, Vol.18, pp. 285501 (7).

-
- [28] Maziarz, W. and Pisarkiewicz, T. (2008), Gas Sensors in a Dynamic Operation Mode, *Measurement Science and Technology*, Vol.19, pp. 055205 (7).
- [29] Jain, G.H. and Patil, L.A. (2006), Gas Sensing Properties of Cu and Cr Activated BST Thick Films, *Bulletin of Materials Science*, Vol. 29, pp. 403-411.
- [30] Bielanski, A., Deren, J. and Haber, J. (1957), The Electric Conductivity and Catalytic Activity of Semiconducting Oxide Catalysts, *Nature*, Vol.179, pp. 668-669.
- [31] Seiyama, T., Kato, A., Fujiishi, K. and Nagatani, M. (1962), A New Detector for Gaseous Components Using Semiconductive Thin Films, *Analytical Chemistry*, Vol. 34, 1502-1503.
- [32] N. Taguchi, (1971), Gas Detecting Device, U.S.Patent, 3,631,436.
- [33] Comini, E. (2006), Metal Oxide Nano Crystals for Gas Sensing, *Analytica Chimica Acta*, Vol. 568, pp. 28-40.
- [34] Zakrzewska, K. (2001), Mixed Oxides as Gas Sensors, *Thin Solid Films*, Vol. 391, pp. 229-238.
- [35] Xiangfeng, C., Dongli, J. and Chenmou, Z. (2007), The Preparation and Gas-Sensing Properties of NiFe_2O_4 Nanocubes and Nanorods, *Sensors and Actuators B*, Vol.123, pp.793-797.
- [36] Biswas, S.K., Pramanik, P. (2008), Studies on the Gas Sensing Behaviour of Nanosized CuNb_2O_6 towards Ammonia, Hydrogen and Liquefied Petroleum Gas, *Sensors and Actuators B*, Vol.133, pp. 449-455.
- [37] Chaudhari, G.N., Jagtap, S.V., Gedam, N.N., Pawar, M.J. and Sangawar V.S. (2009), Sol-Gel Synthesized Semiconducting $\text{LaCo}_{0.8}\text{Fe}_{0.2}\text{O}_3$ -Based Powder for Thick Film NH_3 Gas Sensor, *Talanta*, Vol. 78 pp. 1136-1140.
- [38] Han, N., Chai, L., Wang, Q., Tian, Y., Deng, P. and Chen, Y. (2010), Evaluating the Doping Effect of Fe, Ti and Sn on Gas Sensing Property of ZnO, *Sensors and Actuators B*, Vol.147, pp. 525-530.
- [39] Sahay, P.P. and Nath, R.K. (2008), Al-Doped Zinc Oxide Thin Films for Liquid Petroleum Gas (LPG) Sensors, *Sensors and Actuators B*, Vol. 133, pp. 222-227.
- [40] Ruiz, A.M., Cornet, A., Shimanoe, K., Morante, J.R. and Yamazoe, N. (2005), Transition Metals (Co, Cu) as Additives on Hydrothermally Treated TiO_2 for Gas Sensing, *Sensors and Actuators B*, Vol.109, pp. 7-12.
- [41] Korotcenkov, G., Boris, I., Cornet, A., Rodriguez, J., Cirera, A., Golovanov, V., Lychkovsky, Y. and Karkotsky, G. (2007), The Influence of Additives on Gas Sensing and Structural Properties of In_2O_3 -Based Ceramics, *Sensors and Actuators B*, Vol. 120, pp. 657-664.

-
- [42] Benkstein, K.D. and Semancik, S. (2006), Mesoporous Nanoparticle TiO_2 Thin Films for Conductometric Gas Sensing on Microhotplate Platforms, *Sensors and Actuators B*, Vol. 113, pp. 445-453.
- [43] Ghosh, A., Sharma, R., Ghule, A., Taur, V.S., Joshi, R.A., Desale, D.J., Gudage, Y.G., Jadhav, K.M. and Han, S.H. (2010), Low Temperature LPG Sensing Properties of Wet Chemically Grown Zinc Oxide Nanoparticle thin film, *Sensors and Actuators B*, Vol.146, pp. 69-74.
- [44] Jun, J.H., Yun, J., Cho, K., Hwang, I.S., Lee, J.H. and Kim, S. (2009), Necked ZnO Nanoparticle Based NO_2 Sensors with High and Fast Response, *Sensors and Actuators B*, Vol.140, pp. 412-417.
- [45] Rella, R., Spadavecchia, J., Manera, M.G., Capone, S., Taurino, A., Martino, M. Caricato, A.P. and Tunno, T. (2007), Acetone and Ethanol Solid-State Gas Sensors Based on TiO_2 Nanoparticles Thin Film Deposited by Matrix Assisted Pulsed Laser Evaporation, *Sensors and Actuators B*, Vol. 127, pp. 426-431.
- [46] Senguttuvana, T.D., Srivastava, V., Tawal, J.S., Mishra, M., Srivastava, S. and Jain, K. (2010), Gas Sensing Properties of Nanocrystalline Tungsten Oxide Synthesized by Acid Precipitation Method, *Sensors and Actuators B*, Vol.150, pp. 384-388.
- [47] Seo, M.H., Yuasa, M., Kida, T., Huh, J.S., Shimanoe, K. and Yamazoe, N. (2009), Gas Sensing Characteristics and Porosity Control of Nanostructured Films Composed of TiO_2 Nanotubes, *Sensors and Actuators B*, Vol. 137, pp. 513-520.
- [48] Kolmakov, A., Klenov, D.O., Lilach, Y., Stemmer, S. and Moskovits, M. (2005), Enhanced Gas Sensing by Individual SnO_2 Nanowires and Nanobelts Functionalized with Pd Catalyst Particles, *Nano Letters*, Vol. 5, pp.667-673.
- [49] Huang, J. and Wan, Q. (2009), Gas Sensors Based on Semiconducting Metal Oxide One-Dimensional Nanostructures, *Sensors*, Vol.9, pp. 9903-9924.
- [50] Zhang, H., Wu, J., Zhai, C., Du, N., Ma, X. and Yang, D. (2007), From ZnO Nanorods to 3D Hollow Microhemispheres: Solvothermal Synthesis, Photoluminescence and Gas Sensor Properties, *Nanotechnology*, Vol.18, pp. 455604 (7)
- [51] Wang, X., Zhang, M., Liu, J., Luo, T. and Qian, Y. (2009), Shape and Phase Controlled Synthesis of In_2O_3 with Various Morphologies and Their Gas Sensing Properties, *Sensors and Actuators B*, Vol. 137, pp. 103-110.
- [52] Ramgir, N.S., Hwang, Y.K., Jhung, S.H., Mulla, I.S. and Chang, J.S. (2006), Effect of Pt Concentration on the Physiochemical Properties and CO Sensing Activity of Meso Structured SnO_2 , *Sensors and actuators B*, Vol. 114, pp. 275-282.
- [53] Choi, J.K., Hwang, I.S., Kim, S.J., Park, J.S., Park, S.S., Jeong, U., Kang, Y.C., Lee, J.H., (2010), Design of Selective Gas Sensors Using Electrospun Pd-Doped SnO_2 Hollow Nanofibers, *Sensors and Actuators B*, Vol.150, pp.191-199.
- [54] Cadena, G.J., Riu, J. and Rius, F.X. (2007), Gas Sensors Based on Nanostructured Materials, *The Analyst*, Vol. 132, pp.1083-1099.
-

-
- [55] Gong, J.S., and Chen, J.Q. (2008), Micromachined Sol-Gel Carbon Nanotube/SnO₂ Nanocomposite Hydrogen Sensor, *Sensors and Actuators B*, Vol. 130, pp. 829-835.
- [56] Fort, A., Gregorkiewicz, M., Machetti, N., Rocchi, S., Serrano, B., Tondi, L., Ulivieri, N., Vignoli, V., Faglia, G. and Comini, E. (2002), Selectivity Enhancement of SnO₂ Sensors by means of Operating Temperature Modulation, *Thin Solid Films*, Vol. 418, pp. 2-8.
- [57] Mann, D.P., Paraskeva, T., Pratt, K.F.E., Parkin, I.P. and Williams, D.E. (2005), Metal Oxide Semiconductor Gas Sensors Utilizing a Cr-Zeolite Catalytic Layer for Improved Selectivity, *Measurement Science and Technology*, Vol.16, pp. 1193-1200.
- [58] Tison, Y., Stolojan, V., Watts, P.C.P., Cox, D.C., Chen, G.Y. and Silva, S.R.P. (2007), Gas Sensing Properties of Vapour-Deposited Tungsten Oxide Nanostructures, *Microscopy of Semiconducting Materials*, Vol.120, pp. 281-284.
- [59] Rothschild, A., Edelman, F., Komem, Y. and Cosandey, F. (2000), Sensing Behavior of TiO₂ Thin Films Exposed to Air at Low Temperatures, *Sensors and Actuators B*, Vol. 67, pp. 282-289.
- [60] Nakata, S., Kato, Y., Kaneda, Y. and Yoshikawa, K. (1996), Rhythmic Chemical Reaction of CO on the Surface of a SnO₂ Gas Sensor, *Applied Surface Science*, Vol.103, pp. 369-376.
- [61] Yin, X.M., Li, C.C, Zhang, M., Hao, Q.Y., Liu S., Li, Q.H., Chen, L.B. and Wang, T.H.(2009), SnO₂ Monolayer Porous Hollow Spheres as a Gas Sensor, *Nanotechnology*, Vol. 20, pp. 455503 (6).
- [62] Li, Y., Trinchì, A., Wlodarski, W., Galatsis, K. and Kalantarzadeh, K. (2003), Investigation of the Oxygen Gas Sensing Performance of Ga₂O₃ Thin Films with Different Dopants, *Sensors and Actuators B*, Vol. 93, pp. 431-434.
- [63] Gurlo, A., Barsan, N., Oprea, A., Sahm, M., Sahm, T. and Weimar, U. (2004), An n-to p-type Conductivity Transition Induced by Oxygen Adsorption on α -Fe₂O₃, *Applied Physics Letters*, Vol. 85, pp. 2280-2282.
- [64] Kim, D., Rothschild, A., Lee, B.H., Kim, D.Y., Jo, S.M. and Tuller, H.L. (2006) Ultrasensitive Chemiresistors Based on Electrospun TiO₂ Nanofibers, *Nano Letters*, Vol. 6, pp. 2009-2013.
- [65] Zhu, H., Gu, X., Zuo, D., Wang, Z., Wang, N. and Yao, K. (2008), Microemulsion Based Synthesis of Porous Zinc Ferrite Nanorods and its Application in a Room-Temperature Ethanol Sensor, *Nanotechnology*, Vol. 19, pp. 405503 (5).
- [66] Kamble, R.B. and Mathe, V. L. (2008), Nanocrystalline Nickel Ferrite Thick Film as an Efficient Gas Sensor at Room Temperature, *Sensors and Actuators B*, Vol. 131, pp. 205-209.
-

-
- [67] Jiao, Z., Wu, M., Gu, J. and Qin, Z. (2003), Preparation and Gas-Sensing Characteristics of Nanocrystalline Spinel Zinc Ferrite Thin Films, IEEE Sensors Journal, Vol. 3, pp. 435-438.
- [68] Zhang, G., Li, C., Cheng, F. and Chen, J. (2007), ZnFe₂O₄ Tubes: Synthesis and Application to Gas Sensors with High Sensitivity and Low-Energy Consumption, Sensors and Actuators B, Vol.120, pp. 403-410.
- [69] Korotcenkov, G., Ivanov, M., Blinov, I., Stetter, J.R. (2007), Kinetics of Indium Oxide-based Thin Film Gas Sensor Response: The Role of “Redox” and Adsorption/Desorption Processes in Gas Sensing Effects, Thin Solid Films, Vol. 515, pp.3987-3996.
- [70] Aygun, S. and Cann, D. (2005), Response Kinetics of Doped CuO/ZnO Heterocontacts, The Journal of Physical Chemistry B, Vol.109, pp. 7878-7882.
- [71] Hu, H., Trejo, M., Nicho, M.E., Saniger, J.M. and Valenzuela, A.G. (2002), Adsorption Kinetics of Optochemical NH₃ Gas Sensing with Semiconductor Polyaniline Films, Sensors and Actuators B., Vol. 82, pp.14-23.
- Copyright © Kharaadpur

Chapter-2

EXPERIMENTAL

2.1. Introduction

The present chapter is devoted to describe the details of the experimental procedures carried out in the present thesis work. The chapter begins with the description of the salient features of the design and development of an automated dynamic gas sensing measurement set up. In the next section we have described the wet chemical synthesis of nano-structured oxides in the form of nano-powders, nano-tubes, thin film, embedded nano-tube in porous alumina template and hollow spheres. In the subsequent sections we have introduced the characterization tools used in the present study. For each of these characterization tools, the working principle, details of the instrumentation, sample preparation, characterization conditions and data analyses procedures have been described sequentially.

2.2. Fabrication of an Automated Gas Sensing Set-up

As already described in Chapter-1, for the measurement of gas sensing characteristics of the semiconducting metal oxide (SMO) based sensor generally two different measurement protocols (namely static and dynamic) are adopted. To evaluate the gas sensing characteristics of the synthesized materials we have adopted dynamic measurement protocols. We have designed and fabricated a dynamic volume gas sensing

measurement set-up. The schematic of the integrated gas sensing measurement set up is shown in Fig. 2.1. As shown in the figure the set-up mainly consists with three sub-units. The first one is a gas delivery unit, the second one is a reactor unit equipped with temperature control unit and third one is a (resistance) measurement unit. The brief description of these sub units are briefly described as follows.

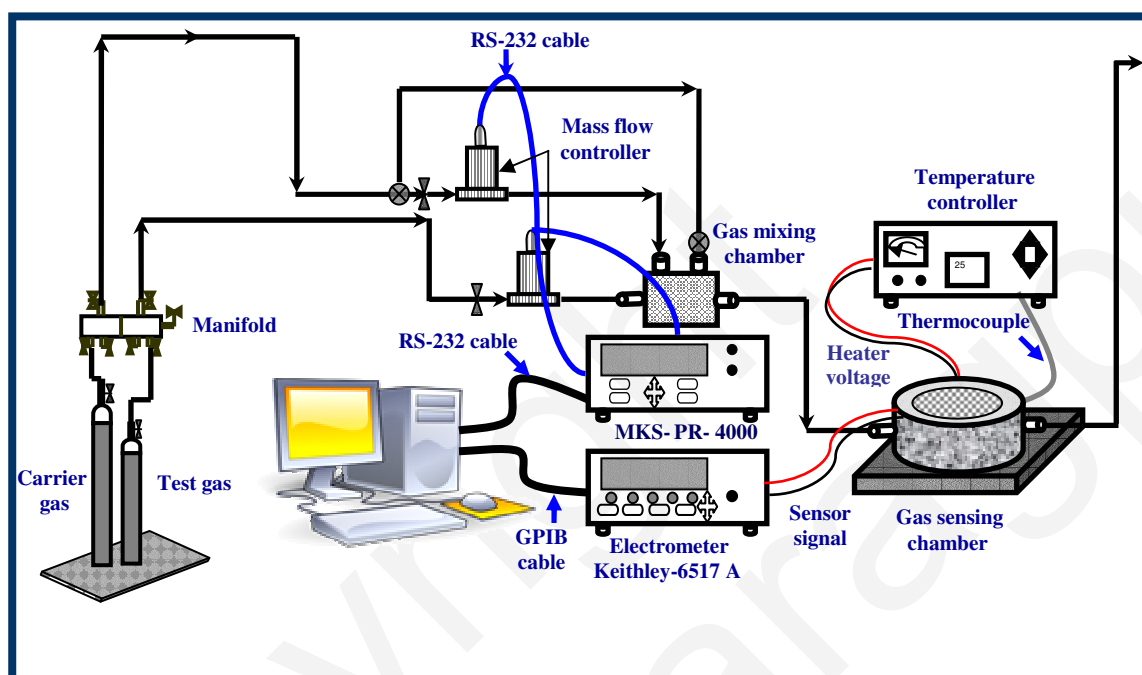


Fig. 2.1: Schematic of the developed gas sensing set-up

2.2.1. Gas Delivery Unit

The gas delivery unit consists of a manifold, pipe lines made out of SS304 stainless steel, electro-magnetic/ needle valves, mass flow controllers (MFCs) (M100B, MKS instruments, USA) and a gas mixing chamber. The carrier (air) and test gases (e.g. hydrogen, carbon monoxide, methane and nitrous oxide) are connected from the gas cylinders to the gas delivery unit through the manifold. The manifold, equipped with several needle valves, is designed to simultaneously deliver the carrier gas and single/ mixture of test gases. In the present work, however, only one type of test gas is delivered with the carrier gas. As shown in Fig. 2.1, the carrier gas (air), controlled by an electro-magnetic valve can be introduced in the gas mixing chamber either directly (flushing

line) or through the carrier gas MFC (0-500 sccm) (for dilution of test gas for sensing measurement). Needle valves are installed in appropriate positions that allow the user to use the carrier gas either for flushing or diluting the test gas for sensing measurement. Thus, as shown in Fig. 2.1, for flushing, the needle valve prior to the MFC for carrier gas should be closed, whereas the needle valve prior to the gas mixing chamber should be opened so that the air can flush the gas sensing chamber and exhausts. For the dilution of test gas, air should flow through the mass flow controller and the valve (for direct air flushing) prior to the gas mixing chamber should be closed. The test gas, controlled by an electromagnetic valve, is fed to the gas mixing chamber through another MFC (0-20 sccm). Both these two MFCs (for air and test gas) are controlled by a dual channel programmable control unit (PR-4000, MKS instrument, USA). The stainless steel made gas mixing chamber is designed to make the gas flow turbulent inside which ensures homogeneous mixing of test and carrier gas. As shown in the figure, after mixing, the mixed gas is directly fed to the reactor unit and goes out through the exhaust line. The mixed gas concentration inside the reactor chamber is controlled by varying the flow rates of carrier and test gases using the following relation [1].

$$C_{\text{mixed gas}} = C_{\text{test gas}} \times (V_{\text{test gas}} / [V_{\text{carrier gas}} + V_{\text{test gas}}]) \quad (2.1)$$

Where C_{mixed} is the required test gas concentration, $C_{\text{test gas}}$ is the concentration of test gas in the cylinder, $V_{\text{test gas}}$ and $V_{\text{carrier gas}}$ are the flow rates of the test and carrier gas respectively. Premixed gas bottles (already diluted in nitrogen to 10000 ppm unless stated otherwise) and commercial air is used as test and carrier gas respectively. As an example when the $V_{\text{test gas}}$ and $V_{\text{carrier gas}}$ are maintained at 5 and 495 sccm respectively, then using $C_{\text{test gas}} \sim 10000$ ppm, $C_{\text{mixed gas}}$ is estimated to be 100 ppm. Similarly, by controlling the test and carrier gas flow rate in a calculative way, the desired mixed gas concentration can be achieved. Using the appropriate valves and mass flow controllers, the environment inside the reactor unit can easily be switched back and forth between air and diluted test gas. In such dynamic flow sensing unit the test gas concentration remains unaltered during the gas sensing measurements. Next we describe the details of the reactor unit used for gas sensing measurements.

2.2.2. Reactor Unit

The stainless steel made reactor unit (without the top lid) is shown in Fig. 2.2 (a). The reactor unit has a temperature controlled thermal stage to heat the sensor material. The heater unit is both thermally and electrically insulated from the body of the reactor. A separate temperature controller unit is also custom build to precisely control the temperature of the sensor. The reactor has a gas inlet and outlet port and it is also equipped with additional feed-through to take out the electrical connection for (i) the heater, (ii) thermocouple and (iii) electrical signal. Two gold coated silver made contact

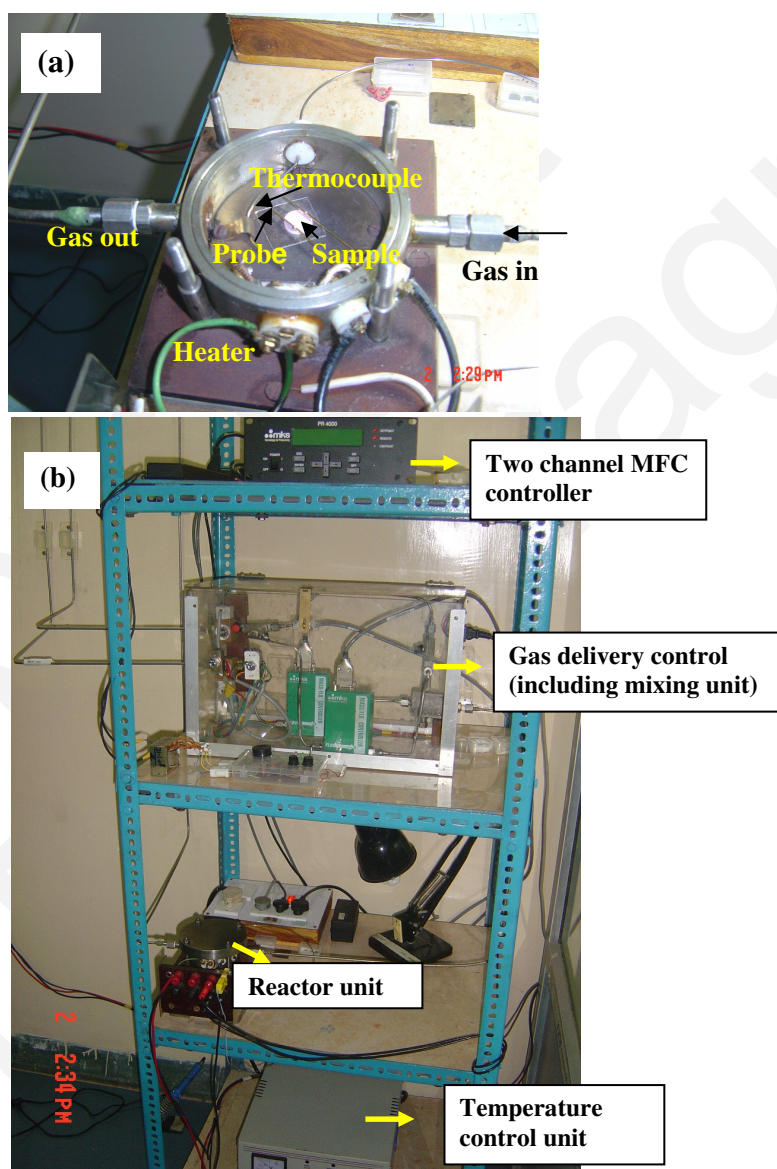


Fig. 2.2: Photograph of (a) developed reactor unit and (b) gas sensing set-up with mass flow controller and temperature control unit

probes are fitted to the reactor unit for electrical measurements. The unit is stationed on a stable steel platform. In Fig. 2.2(a), a sensor material under test, heater base, thermocouple position and one of the three feed-through are shown for illustration. The actual photograph of the partial gas sensing set up is shown in Fig. 2.2(b).

2.2.3. Automated Process Control and Data Acquisition

The mass flow controllers and resistance measurement unit (6517A, Keithley Instruments, USA) are controlled by a PC through RS 232 and GPIB interface respectively using Labview 8.5 (National Instruments, USA) software. The temperature of the thermal stage is controlled manually using a temperature control unit. One of the major aims of this thesis work is to develop a fully automated gas sensor measurement unit. A dedicated personal computer equipped with a GPIB card and Labview 8.5 software is used to control the gas flow, measure the resistance of the sensor material as a function of temperature (for a known concentration of test gas in the reactor unit) or a function of test gas concentration keeping the operating temperature fixed, store the acquire data (/plot real-time) for further analyses. The details of Labview VI, developed for this purpose is described in Appendix-1. In the subsequent sections we have described the experimental procedure to synthesize the sensing materials using wet chemical synthesis route and the techniques adopted to characterize the synthesized materials.

2.3. Sensor Material Synthesis: Importance of the Nano-structured Oxides

As mentioned in Chapter-1, the present work has been focused to evaluate the gas sensing characteristics of the spinel ferrite based sensing elements. As compared to the binary metal oxide based gas sensors (e.g. SnO_2 , ZnO , WO_3 etc) the gas sensing performance of spinel ferrites are relatively less studied. Ferrites are known for their important magnetic, magneto-resistive and magneto-optical characteristics. For these applications highly sintered dense ferrites are required. On the other hand for gas sensing purpose porous and loosely sintered ferrite sensing elements are desired. The gas sensing performance of the ferrite particles are significantly influenced by their surface to volume ratio, particle size, morphology as well as intra-particle porosity. Ferrites could be synthesized in nano-regime with ordered as well as random pore structure. Such

structures are expected to enhance the sensor performance through the so called "size effect" as well as the increase the surface area available for the gas adsorption. From literature review it is apparent that the majority of the research activities are confined to the development of fast responding, sensitive and highly selective gas sensor using conventional transition metal oxides and therefore efforts seeking any alternative sensing materials are grossly neglected. In this regard, apart from the traditional metal oxides (e.g. ZnO), our research will explore the performance of certain spinel oxide as gas sensing material. The salient features of the executed work are elaborated below.

The synthesized oxides are targeted to detect minor concentrations of potentially hazardous gases in air with fixed oxygen partial pressure. Two major issues in such gas sensing materials are the detection of these gas concentrations at ppm level (gas response) and also the detection of a specific gas in a mixed gas environment (gas selectivity). In the following text we have elaborated why the nano-structured oxides is expected to enhance both the response as well as the selectivity of the minority gas sensors.

The performance of the gas sensor (in terms of response (S)) is related to the change in the carrier concentration and the depleted space charge region (Debye length L_D) through the relation

$$S = \Delta G / G_0 = (\Delta n / n_0) \cdot L_D \quad (2.2)$$

where ΔG is the change in conductance with respect to the initial conductance G_0 , Δn is the change in carrier concentration, The Debye length (L_D) can be expressed as

$$L_D = (\epsilon_0 kT / n_0 e^2)^{1/2} \quad (2.3)$$

where ϵ_0 is the static dielectric constant, n_0 is the total carrier concentration, e is the carrier charge, k is the Boltzmann constant and T is the temperature. To increase the sensor response, larger Debye length and larger change in carrier concentration is required upon oxygen chemi-adsorption. Empirically, maximum response is achieved when L_D is comparable to the particle size (in nano-regime). Additionally, in case of nano-size particles, lower n_0 is achieved as almost all the carriers are trapped in the surface states and few are thermally activated and available for conduction. This would

increase L_D and eventually the sensor response (S) towards the detection of gases. The response (S) is directly related to the reduction of particle size broadly in two ways: first as the particle size is roughly twice the surface space charge region then sensor response is maximized [2]. Secondly with the reduced particle size, specific surface area is enormously increased and when the size is in nano order, a large fraction of the atoms are present at the surface with structure and property significantly different from the bulk. Thus for the particle size in the range of 5-50 nm the response characteristics of the sensors could be significantly improved [3]. Apart from the micro-structural change, aliovalent substitution/(s) is also another effective mean to enhance the sensor performance. Doping controlled sensing performance is envisaged through the modification of the carrier concentration (n_0) and mobility (μ) [4].

The particle size effect is not fully realized when conventional sensor electrode synthesis is adopted. As for example, screen printing is routinely adopted to deposit sensor materials (such as SnO_2 , TiO_2 etc). It is however very challenging to control the rheological properties of sensor material, organic medium and binder, to maintain a homogeneous dispersion of the particles in the slurry avoiding agglomeration. In the present work, synthesis of nano-structured electrode is explored to delineate the microstructure effect. Synthesis of meso-porous as well as ordered nano-pillar growth of the ferrite gas sensing materials is attempted to investigate the said size effect. Clearly in these nano-structured materials the problem of particle agglomeration will be avoided to delineate the true size effect which so far could not be established unequivocally although their positive effect towards the enhancement of the sensor response (S) is well known [5]. The additional nano-structure includes the synthesis of discrete nano-tubes of the gas-sensing materials. The dimension of nano-tube is of the order (~ 200 nm). However, the nano-tube is spun coated on the substrate and hence percolations of electrons are through interconnected tubes. On the other hand, for nano-pillar percolations of electrons are through the tubes in Z direction. Particulate coating is performed using slurry where by suitable rheology control a homogeneous dispersion of particles is already achieved.

Apart from increasing the sensor response (S), reduction of particle size yield smaller response time. The reduction in response time is related to the surface area enhancement of the nano-particle which in turn is expected to be reduced further in case of nano-

structured electrodes with ordered porosity. The effect can be systematically studied by synthesizing sensor materials in the form of nano-tube (well dispersed in the slurry) (1d), meso-porous film (2d) and structured nano-pillar (3d). During high temperature operation of the sensor, the problem of particle/grain growth and coalescence is expected to be marginal both in random (meso-porous film) as well as ordered (nano-pillar growth) nano-structured films.

The most challenging part of the thesis work is to establish the sensor selectivity for specific gases. As mentioned in Chapter-1, the sensor selectivity for most of the instances is achieved by enhancing the gas adsorption or promoting specific chemical reactions via catalytic or electronic effects by using dopants, surface modification method etc [6-7]. The specific effect of the nano-structuring towards the selectivity of a specific reducing gas remains virtually unknown. In general selectivity is dependent on many parameters, such as gas adsorption and co-adsorption mechanisms, surface reaction kinetics, electron transfer to or from the conduction band of the semiconductor. The cross selectivity issue of the synthesized spinel oxides is described later in Chapter-4 and 5.

Solution based synthesis routes are attractive to synthesize tailor made nano-structures of electro-ceramics in simple and cost effective way.

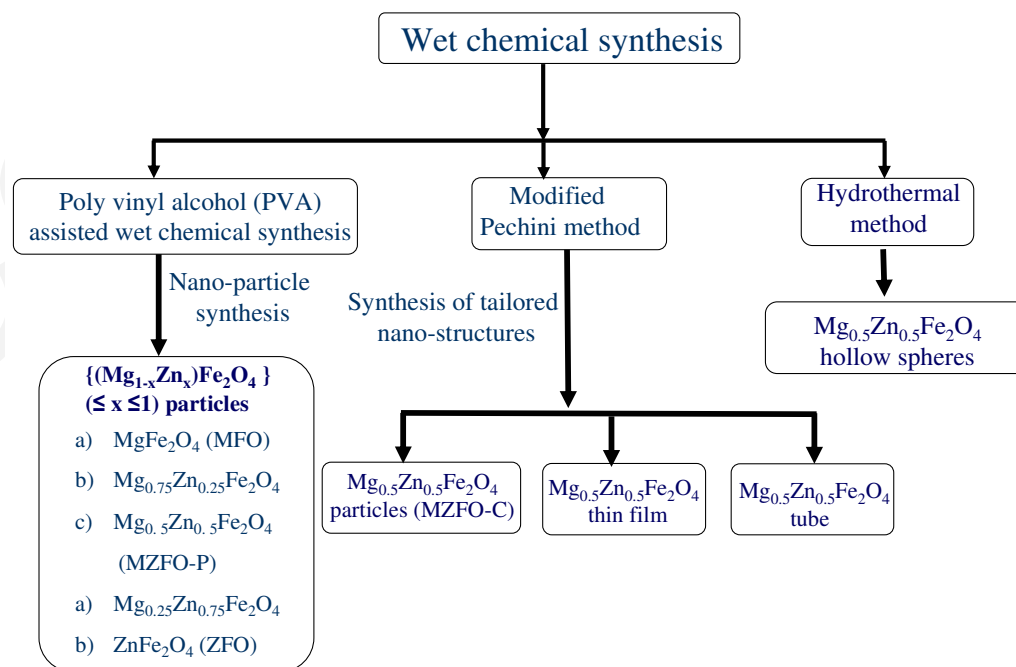


Fig. 2.3: Summary of the wet chemical routes to synthesize various nano-structured spinel based gas sensing materials

In the present work we have devised low temperature, cost effective, wet chemical process to synthesize nano-structured ferrite based sensing materials in a variety of forms. Fig. 2.3 summarizes the wet chemical synthesis schemes adopted to synthesize magnesium zinc spinel ferrites in the form of nano-particle, nano-tube, embedded nano-tube, thin film and hollow spheres. Polyvinyl alcohol assisted chemical synthesis, citrate assisted Pechini route and hydrothermal route are adopted to synthesize these nano-structured oxides. Apart from that an acetate salt based wet chemical route is adopted to synthesize zinc oxide nano-particles for gas sensing purpose. Each of these synthesis routes are described in the following subsections.

2.3.1. PVA Assisted Sol Gel Method to Prepare $(\text{Mg}_{1-x}\text{Zn}_x)\text{Fe}_2\text{O}_4$ ($0.0 \leq x \leq 1.0$) Nano-particles

We have synthesized $(\text{Mg}_{1-x}\text{Zn}_x)\text{Fe}_2\text{O}_4$ ($0.0 \leq x \leq 1.0$) solid solutions using a simple, economic PVA assisted wet chemical synthesis route. Hydrated salts of magnesium acetate ($\text{Mg}(\text{CH}_3\text{COO})_2 \cdot 4\text{H}_2\text{O}$), zinc acetate ($\text{Zn}(\text{CH}_3\text{COO})_2 \cdot 2\text{H}_2\text{O}$) and iron nitrate ($\text{Fe}(\text{NO}_3)_3 \cdot 9\text{H}_2\text{O}$) are used as precursor materials. Typical flow chart for $\text{Mg}_{0.5}\text{Zn}_{0.5}\text{Fe}_2\text{O}_4$

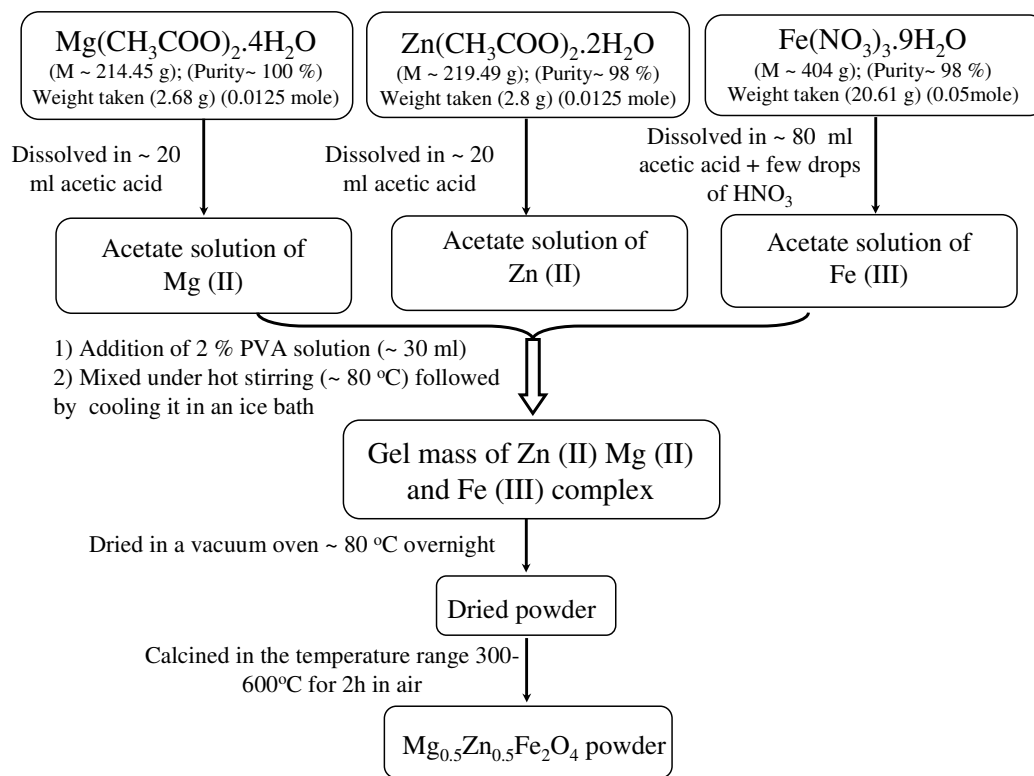


Fig. 2.4: Flow chart for the synthesis of $\text{Mg}_{0.5}\text{Zn}_{0.5}\text{Fe}_2\text{O}_4$ particles by PVA assisted wet chemical route

particle synthesis is shown in Fig. 2.4. Stoichiometric amount of these precursor materials are first dissolved in hot acetic acid through continuous stirring. A 2% PVA solution is added into the mixed precursor solution (in 1:0.25 volume ratios) and the resultant precursor is heated $\sim 80^\circ\text{C}$ for 24 hours followed by cooling it in an ice bath to form a gelled mass. The gel is dried in a vacuum oven kept about 80°C overnight to form dried powders. The dried powders are further calcined in a temperature range $300\text{--}600^\circ\text{C}$ in air for crystallization into spinel ferrite phase. Similar process is followed to synthesize other compositions.

2.3.2. Synthesis of $\text{Mg}_{0.5}\text{Zn}_{0.5}\text{Fe}_2\text{O}_4$ Nano-particles, Thin Films and Nano-tubes by Modified Pechini Route

Particle synthesis: We have prepared magnesium zinc ferrite ($\text{Mg}_{0.5}\text{Zn}_{0.5}\text{Fe}_2\text{O}_4$) precursor sol using a modified Pechini process. Nitrate salts of magnesium, zinc and iron are used as precursor materials. The precursor salts (Mg, Zn and Fe nitrate in 1: 1: 4 mole ratios) are first dissolved in distilled water through continuous stirring. Then the aqueous solution of citric acid (C.A) (C.A: total cation (mole) ~ 1.5) and ethylene glycol (E.G) (E.G: C.A (mole) ~ 3) are added to the mixed precursor solution to form a polymeric-metal cation network. Citric acid (consisting with three carboxyl groups and one hydroxyl group) is a weak acid and easily decomposes in aqueous solution to its conjugate base which acts as chelating agent to trap the cations of precursor materials. In this process cations are first bonded by citric acid followed by a temperature assisted hydrolysis reaction of citric acid with ethylene glycol to form an internal ester linkage. The complex precursor is stirred for 4 h at 80°C and finally cooled down to room temperature to prepare the $\text{Mg}_{0.5}\text{Zn}_{0.5}\text{Fe}_2\text{O}_4$ sol. The sol thus prepared is used to synthesize $\text{Mg}_{0.5}\text{Zn}_{0.5}\text{Fe}_2\text{O}_4$ nano-particles, thin films, and nano-tubes. The flowchart of these synthesis procedures is shown in Fig. 2.5. In order to synthesize $\text{Mg}_{0.5}\text{Zn}_{0.5}\text{Fe}_2\text{O}_4$ nano-particles, the sol is dried for few hours at 120°C to evaporate the liquid content and to produce a gelled mass. The gel is heated at 140°C until the auto combustion is initiated. This combustion process includes the decomposition and auto-combustion of gel followed by the formation of dried $\text{Mg}_{0.5}\text{Zn}_{0.5}\text{Fe}_2\text{O}_4$ particles.

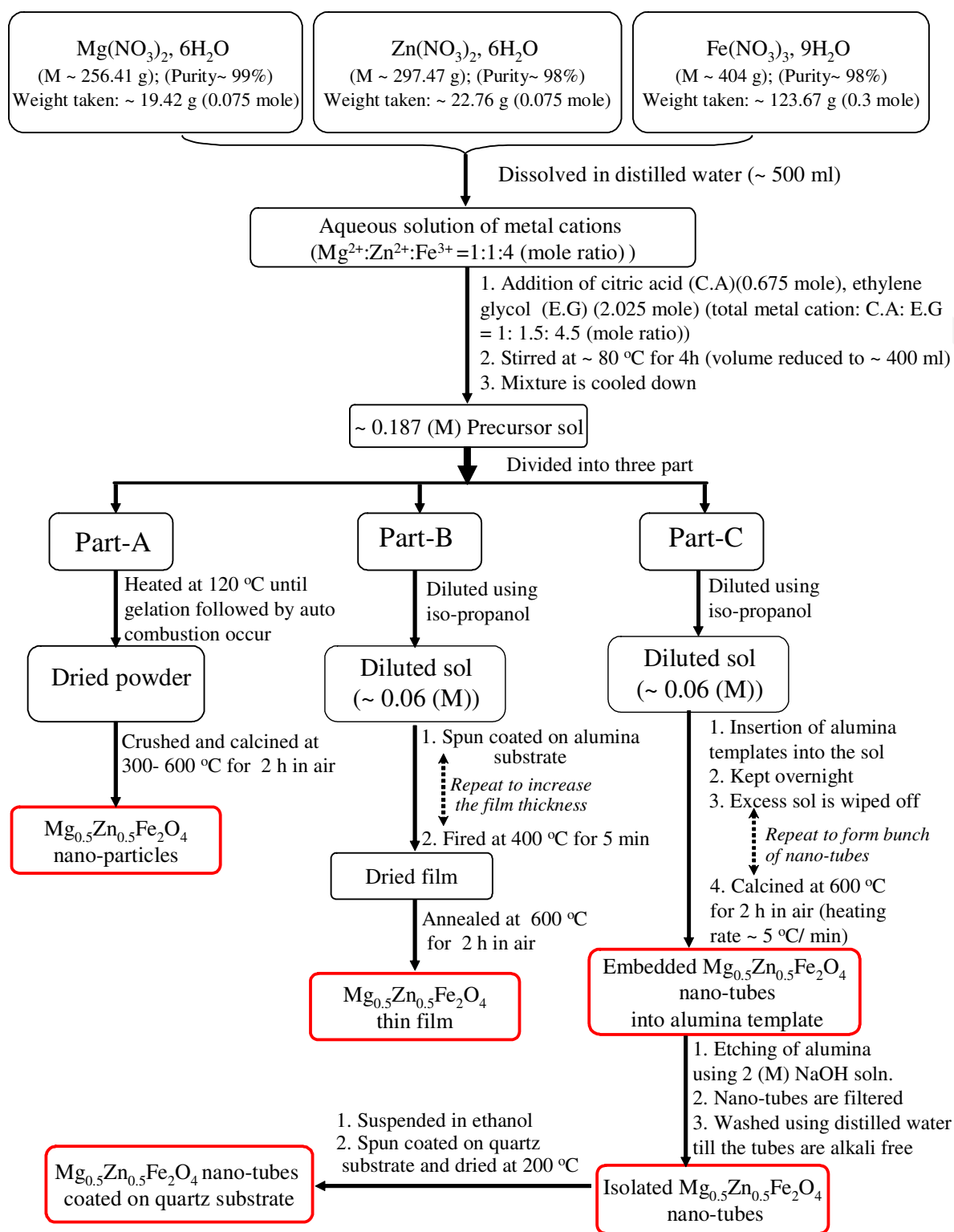


Fig. 2.5: Flow chart for the synthesis of $\text{Mg}_{0.5}\text{Zn}_{0.5}\text{Fe}_2\text{O}_4$ nano-particles, thin film, embedded and isolated nano tubes by modified Pechini route

The auto combustion is considered as a thermally induced redox reaction in which the carboxyl groups acts as reducing agent and nitrate ion (NO_3^-) plays the role of oxidant [8]. Citric acid and ethylene glycol serve the role of organic fuel in this auto combustion process. Since the process is completed within a very short period, the particle size of the synthesized ferrite powders remains in the nano-size region.

Thin film synthesis: For the synthesis of $\text{Mg}_{0.5}\text{Zn}_{0.5}\text{Fe}_2\text{O}_4$ thin film, the complex precursor sol is directly spun coated on alumina substrate. We have prepared films of different thickness (e.g. by coating for 8, 15, 30 and 45 times) by varying the no. of coating and firing cycles. Prior to the coating the alumina substrates are cleaned using sonication in methanol and acetone. The films are spun coated each time at 4000 rpm for 30 s using a spin coating unit. Just after deposition, the film is inserted into a preheated furnace (kept at 400°C) for 5 min and then quenched to room temperature. The coating and firing cycles are repeated to increase the film thickness. After final coating and firing cycle the film is annealed at 600°C for 2 h in air and cooled down to room temperature by normal furnace cooling.

Synthesis of embedded and isolated nano-tubes: In order to synthesize embedded and isolated nano-tubes from the $\text{Mg}_{0.5}\text{Zn}_{0.5}\text{Fe}_2\text{O}_4$ precursor sol we have used anodized porous alumina (AAO) template assisted synthesis route. The sequential processing steps for the preparation of isolated $\text{Mg}_{0.5}\text{Zn}_{0.5}\text{Fe}_2\text{O}_4$ nano-tubes from the precursor sol (prepared using modified Pechini route) have been illustrated schematically in Fig. 2.6. For the preparation of embedded nano-tubes (into alumina template), the porous alumina templates (Whatmann, $50\ \mu\text{m}$ thick, $200\ \text{nm}$ pore size) are first dipped into

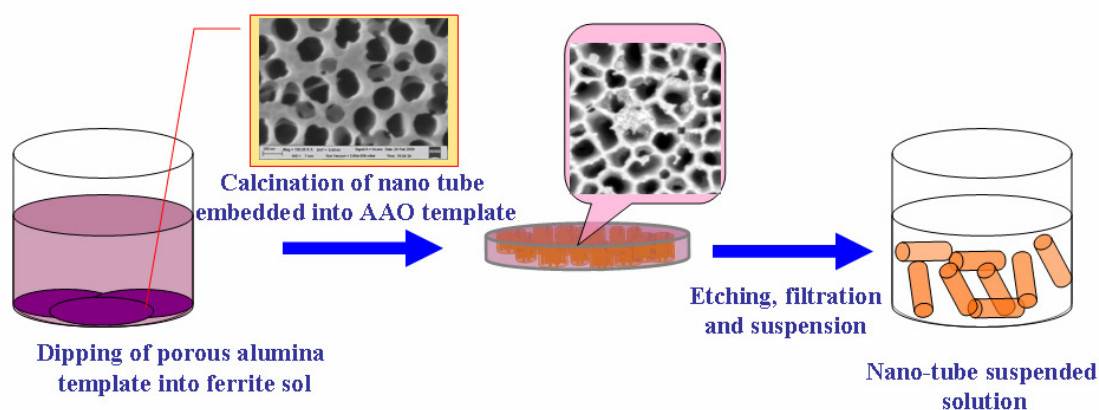


Fig. 2.6: Schematic methodology for the synthesis of embedded and isolated $\text{Mg}_{0.5}\text{Zn}_{0.5}\text{Fe}_2\text{O}_4$ nano-tubes

$\text{Mg}_{0.5}\text{Zn}_{0.5}\text{Fe}_2\text{O}_4$ precursor sol for extended period. Due to the capillary suction, the sol inserts into the pores. The excess sol on the surface of the template is wiped off using lint-free tissue paper and calcined at $600\text{ }^\circ\text{C}$ for 2 h in air for the simultaneous removal of organic residue and crystallization of $\text{Mg}_{0.5}\text{Zn}_{0.5}\text{Fe}_2\text{O}_4$ tubes inside the template pores. A typical heating rate $\sim 5\text{ }^\circ\text{C min}^{-1}$ is used for calcination. The dipping and calcination steps are repeated for couple of times to obtain bunch of nano-tubes inside the templates. Due to multiple dipping and calcination treatment the $\text{Mg}_{0.5}\text{Zn}_{0.5}\text{Fe}_2\text{O}_4$ nano-tubes are crystallized in the pores of the alumina templates. To synthesize isolated tubes the alumina templates are dissolved in 2 (M) NaOH solution, dispersing the crystallized $\text{Mg}_{0.5}\text{Zn}_{0.5}\text{Fe}_2\text{O}_4$ nano-tubes inside the pores. The resultant suspension is filtered off and washed several times with de-ionized water to remove NaOH. Finally the nano-tubes are further dispersed in ethanol and the resultant suspension is directly spun coated on fused quartz substrate to make nano-tube sensing elements. The plausible mechanism of the formation of $\text{Mg}_{0.5}\text{Zn}_{0.5}\text{Fe}_2\text{O}_4$ nano-tubes is described in Fig. 2.7. During the calcination process the infiltrated sol inside the template pores are quickly transformed into gel followed by removal of organic residues and simultaneous release of gases. During calcination, the gel mass are crystallized along the pore wall of the alumina template to form the tubes. The FESEM micrograph of AAO template and embedded nano-tubes are shown in Fig. 2.7.

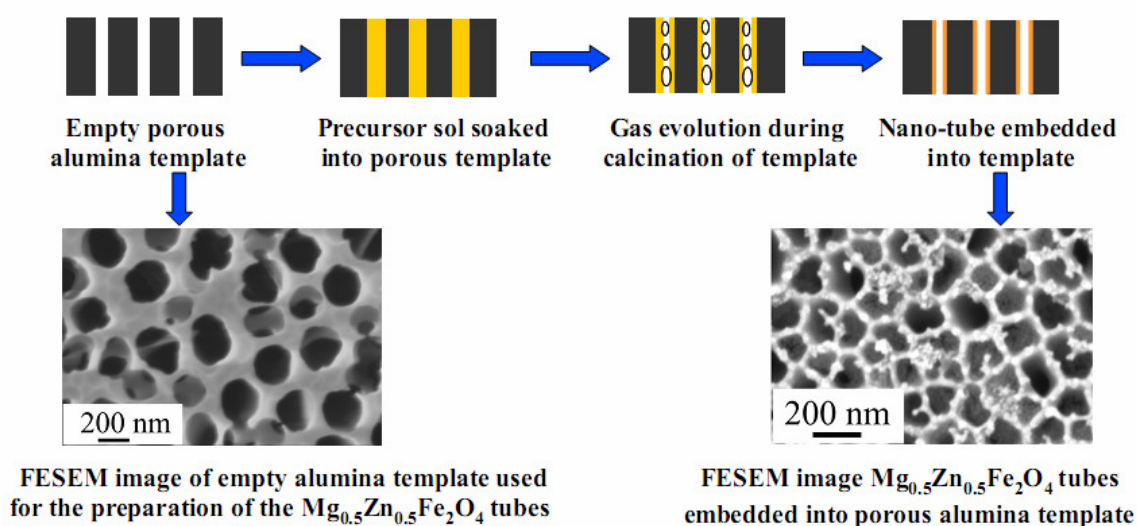


Fig. 2.7: Formation of embedded nano-tubes in anodized alumina template

2.3.3. Hydrothermal Synthesis of $\text{Mg}_{0.5}\text{Zn}_{0.5}\text{Fe}_2\text{O}_4$ Hollow Spheres

For the synthesis of $\text{Mg}_{0.5}\text{Zn}_{0.5}\text{Fe}_2\text{O}_4$ hollow spheres we have adopted spherical carbon template assisted hydrothermal synthesis route. The spherical carbon templates are prepared using the hydrothermal reaction of dextrose solution. For the preparation of carbon templates the dextrose is first dissolved in distilled water. Dextrose i. e. dextrorotatory glucose is the most abundant form of glucose in nature and easily soluble in water. The aqueous solution of dextrose is transferred to a teflon-lined stainless steel autoclave, sealed and maintained at 180°C for 9 h. After cooling the mixture to room temperature we obtain black-brown precipitates. The precipitates are then washed and filtered with ethanol and distilled water several times and dried in oven at $\sim 60^\circ\text{C}$ for 5h to obtain the carbon spheres. The prepared carbon spheres are used as core template to synthesize hollow $\text{Mg}_{0.5}\text{Zn}_{0.5}\text{Fe}_2\text{O}_4$ spheres. The plausible mechanism of the hydrothermal synthesis of carbon spheres has been illustrated in Fig. 2.8. As demonstrated in the figure, in the first step, in the aqueous solution, dextrose (under hydrothermal condition at high temperature) polymerize through condensation of water molecule. The formation of polymer between the pyranose forms (dextrose is generally stable in cyclic pyranose form in aqueous solution) of dextrose molecules lead to a carbonization reaction during prolonged heating in autoclave. The carbonization reaction is an exothermic in nature and at critical point initiates nucleation reaction [9]. The nuclei grow uniformly to form carbon core sphere by diffusion of polymeric solutes toward the

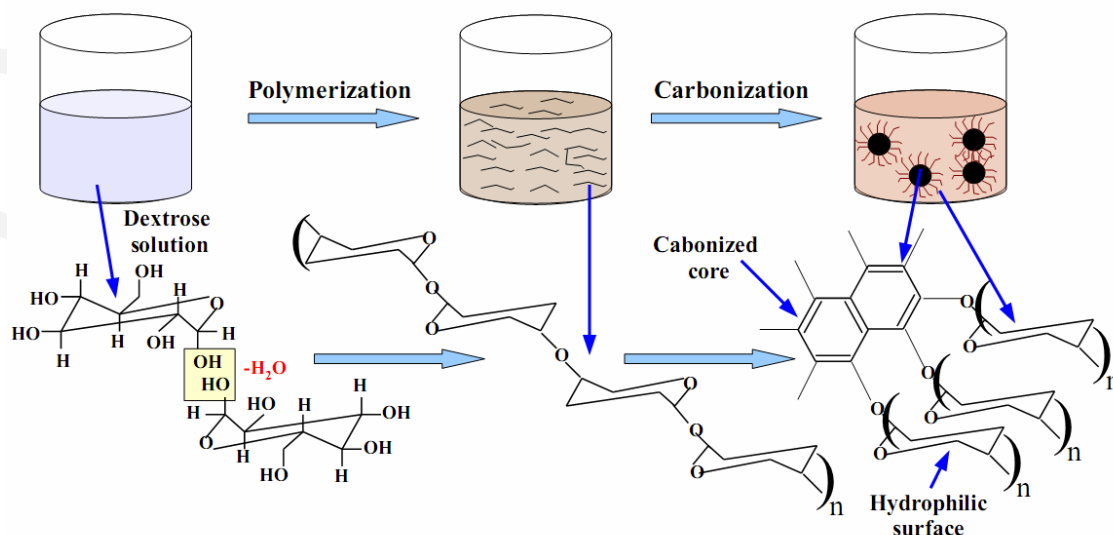


Fig. 2.8: Mechanism of the synthesis of spherical carbon templates

sphere surfaces. The surface of the spheres (consisting of OH and C=O groups) is hydrophilic in nature. Being hydrophilic in nature, these carbon spheres can form bond with the metal cations dissolved in aqueous solution. The flow diagram for the hydrothermal synthesis of $\text{Mg}_{0.5}\text{Zn}_{0.5}\text{Fe}_2\text{O}_4$ hollow spheres using the hydrothermally prepared carbon spheres is shown in Fig. 2.9.

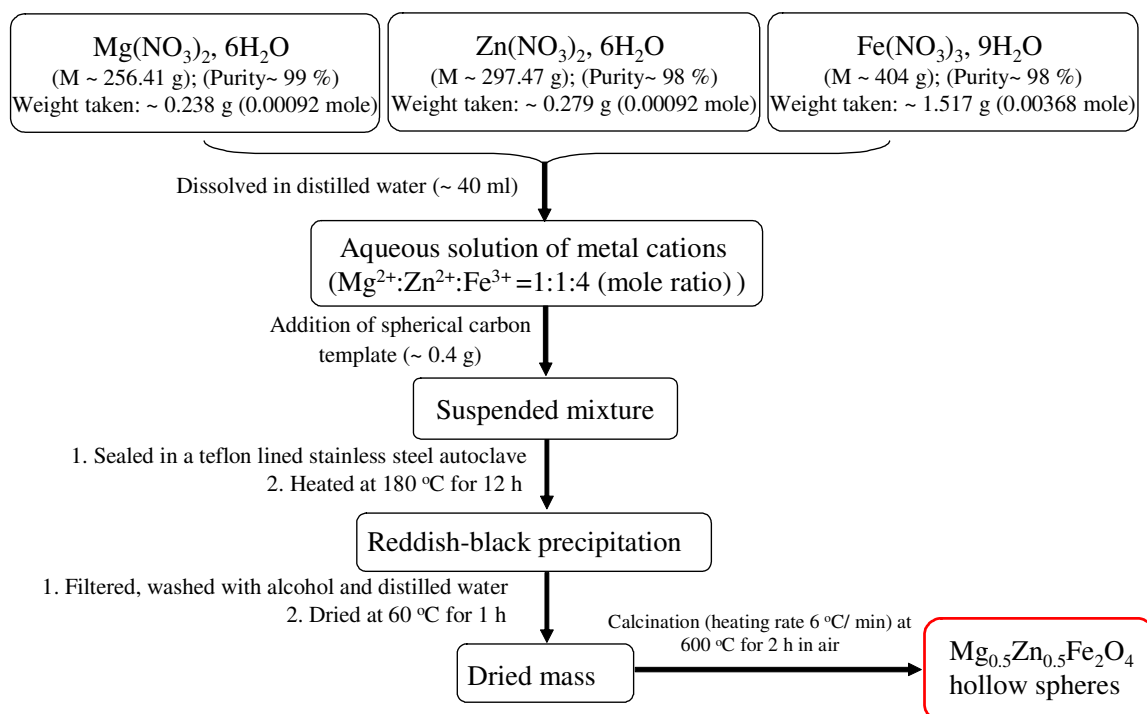


Fig. 2.9: Flow chart for the synthesis of $\text{Mg}_{0.5}\text{Zn}_{0.5}\text{Fe}_2\text{O}_4$ hollow spheres

For the preparation of hollow $\text{Mg}_{0.5}\text{Zn}_{0.5}\text{Fe}_2\text{O}_4$ spheres using the spherical carbon templates first the hydrated nitrate salts of Mg (II), Zn (II) and Fe (III) precursor cations are dissolved in distilled water. The spherical carbon templates are then mixed with the aqueous precursor solution and ultra-sonicated for 30 mins to form uniform template suspension. The mixture is then transferred to a teflon lined stainless steel autoclave and heated at 180 °C for 12 h. After cooling the mixture we have gotten a reddish brown precipitate. The precipitate is washed repeatedly with ethanol and water and dried in oven at 60 °C for 2 h. The dried precipitate is then calcined at 600 °C for 2 h (maintaining a

heating rate $\sim 6\text{ }^{\circ}\text{C}/\text{min}$) to obtain the $\text{Mg}_{0.5}\text{Zn}_{0.5}\text{Fe}_2\text{O}_4$ hollow spheres. The mechanism of hollow sphere synthesis is shown schematically in Fig. 2.10.

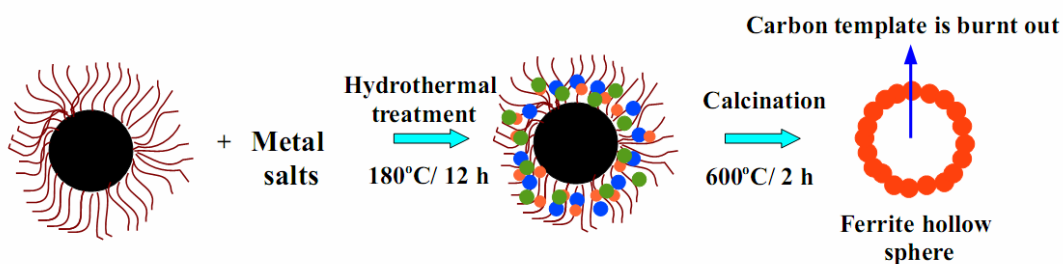


Fig. 2.10: Schematic diagram for the formation of $\text{Mg}_{0.5}\text{Zn}_{0.5}\text{Fe}_2\text{O}_4$ hollow sphere

2.4. Characterization of Synthesized Materials

The characteristics of gel derived powders and the phase formation behavior, micro-structure and the pore size distribution of the calcined powders are characterized by using a variety of diagnostic tools as listed in Table-2.1. In the following section we have briefly discussed the operation principle and the measurement procedures of all the above characterization tools.

Table-2.1: Diagnostic tools used for material characterization

Sample characterization	Diagnostic tools used
Thermal and infra-red analyses of gel derived powder	Differential thermal analyses (DTA), thermo-gravimetric analyses (TGA), Fourier transformed infra-red (FTIR) spectroscopy
Phase formation behavior	X-ray diffraction and Rietveld refinement of X-ray diffractogram
Micro-structure	Scanning and transmission electron microscopy
Surface area, pore size and pore size distribution	Brunauer–Emmett–Teller (BET) adsorption-desorption analyzer

2.4.1. Differential Thermal Analyses (DTA) and Thermal Gravimetric Analysis (TGA)

The thermal decomposition of $\text{Mg}_{0.5}\text{Zn}_{0.5}\text{Fe}_2\text{O}_4$ gel prepared using modified Pechini method is characterized using DTA in conjunction to TGA analysis (Perkin Elmer Pyris Diamond TG-DTA, USA). DTA is a thermo-analytic technique in which the material (under study) and an inert (no transformations in the temperature range of interest) reference are subjected to the same heating programme. When the samples undergo a transformation, it will either absorb (endothermic) or release (exothermic) heat. The endothermic and exothermic reaction will decrease or increase the temperature of the sample. The recorded temperature difference (ΔT) between the sample and reference are plotted with the variation of operating temperature. In TGA the total weight loss and the rate of weight loss of the sample (due to decomposition of the material) are measured with the variation of sample temperature. Thus DTA in conjunction to TGA characterize the thermal profile for weight loss of the sample and identify the corresponding thermal process (exothermic/ endothermic). Now-a-days, the DTA and TGA techniques are mostly incorporated in a single instrument which provides the mass loss and thermal information simultaneously. The sample and the reference are kept in two sample holder connected to a back to back thermocouple in a furnace. The voltage difference (or in terms of temperature change) between the samples and reference are recorded. To study the thermal decomposition of the $\text{Mg}_{0.5}\text{Zn}_{0.5}\text{Fe}_2\text{O}_4$ gel, α -alumina powder is used as reference and the furnace temperature is raised from room temperature to 750°C at $10^\circ\text{C min}^{-1}$ in presence of air. For thermo-gravimetry a micro-balance is attached to the sample crucible to measure the weight loss with the increase in temperature.

2.4.2. Fourier Transformed Infra-Red (FTIR) Spectra

The formation of metal oxygen bond and removal of organic and other phases with the increase of calcination temperature of the $\text{Mg}_{1-x}\text{Zn}_x\text{Fe}_2\text{O}_4$ ($0 \leq x \leq 1$) particles have been investigated using a FTIR spectrometer (Nexus- 870, Thermo Nicolet Corp., USA). The synthesized carbon sphere templates (to prepare the ferrite hollow sphere) are also characterized using the FTIR spectra. In FTIR spectrometer, the IR radiations from an IR

source are passed through the sample and the amount of energy adsorbed/ transmitted is recorded by suitable detector and is guided through an interferometer where a Fourier transform is performed on the output signal. For the measurement of FTIR spectra the sample is first grinded with dry KBr using mortar pestle and pellet (13 mm diameter, 0.3 mm thick) is prepared for IR characterization. The pellets are exposed to IR radiation in the spectrometer. Infrared spectra uniquely characterize the bonding type of the molecules and for each type of bonding it produces characteristic absorption bands.

2.4.3. X-ray Diffraction

X-ray diffraction (XRD) is a powerful technique to determine the crystal structure and to estimate various structural parameters (e.g. phase purity, volume fraction of the desired phase, crystallite size, lattice parameter, micro-strain, cation distribution etc.) of a crystalline material. When a monochromatic X-ray (electromagnetic radiation) of wavelength λ incident on a sample, it is diffracted by the atoms of the crystalline material. When an X-ray of suitable wave length (in the order of inter-planner distance of two atomic layers (d)) is diffracted from the atoms of a crystalline material, it follows the well known Bragg's relation

$$n\lambda = 2d \sin \theta \quad (2.4)$$

where n is an integer (for monochromatic X-ray, $n=1$), λ is the wavelength of the X-ray and θ is the angle of incidence of X-ray on the sample.

In the X-ray diffraction technique, the intensity of the diffracted beam is plotted with the Bragg's angle (2θ). The value of the inter-planner distance (d) and lattice parameter of the studied sample is estimated to confirm its crystal structure. The schematic of a typical XRD instrument and the photograph of the XRD instrument (Ultima-III, Rigaku, Japan) used in the present study are shown in Fig. 2.11 (a) and (b) respectively. An XRD instrument is equipped with an X-ray generator, sample holder and an X-ray detector. In the X-ray generator a tungsten filament (cathode) and a desired target metal (e.g. Cu) (anode) is kept in a sealed glass tube under vacuum. The filament is heated at high temperature by applying high voltage to emit electrons. The emitted electrons interact with the anode and produce X-rays. The produced X-rays are filtered (For Cu target Ni-

filter is used) to emit monochromatic X-ray radiation. During the process the anode material is cooled by passing cooled water using a chiller unit. The produced monochromatic X-ray is then incident on an aligned specimen (under investigation) and diffracted from the atoms of the specimen. The diffracted X-ray beam is detected and the diffractogram is stored in the computer attached to the instrument. In the present study most of the X-ray diffraction patterns are recorded using CuK_α radiation (few samples are characterized using CoK_α radiation) in 2θ range 20-80 degree at a scanning rate 3 degree min^{-1} . During the operation of the instrument, the accelerating voltage and current is kept 40 kV and 30 mA respectively.

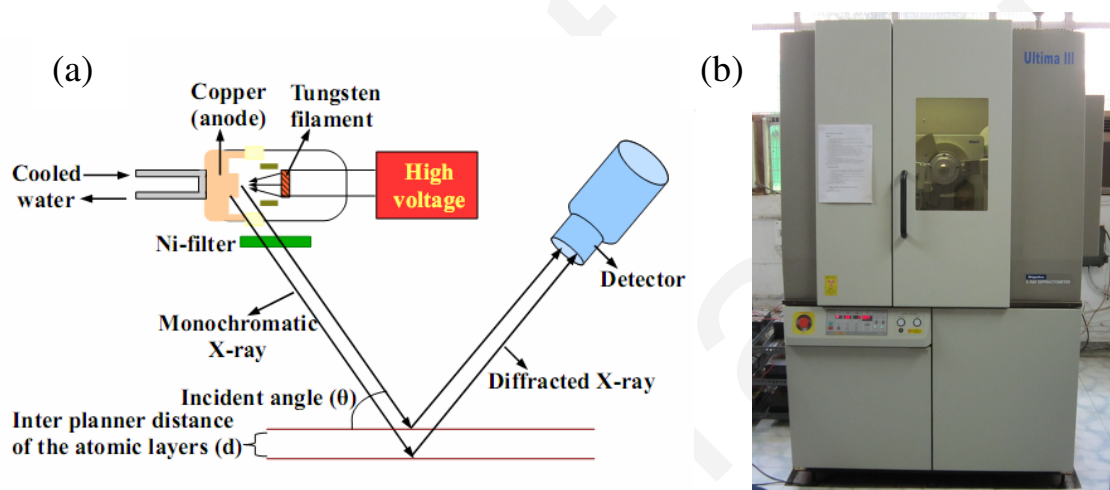


Fig. 2.11: (a) Schematic diagram of a typical X-ray diffractometer (b) photograph of the X-ray diffractometer (Ultima III, Rigaku, Japan) used in the present work

Rietveld refinement of the X-ray diffractogram: To quantify the structural and micro-structural parameters, for selected samples we have performed Rietveld refinement of the X-ray diffractograms of $\text{Mg}_{1-x}\text{Zn}_x\text{Fe}_2\text{O}_4$ ($0.0 \leq x \leq 1.0$) based sensing materials using a free Rietveld refinement program MAUD [<http://www.ing.unitn.it/~maud/>]. The program refines structural parameters such as lattice parameters, atomic positions and occupancies simultaneously with the micro-structural parameters including crystallite size and r.m.s strain. For all structural refinements we have fitted the background with a five degree polynomial and an asymmetric pseudo-Voigt function used to fit the XRD peaks. The constraints of the structural refinements are as follows: each cation site is

assumed to be fully occupied and the ratio of the summation of the atomic fractions of the constituent atoms in tetrahedral and octahedral sites equal to 1: 2 and overall charge neutrality of the material is maintained. Assuming the broadening of the diffraction peaks is mainly due to crystallite size and root mean square strain (the instrumental broadening is subtracted from the measured XRD) in the crystallites; these micro-structural parameters are also refined by the program. The quality of the agreement between

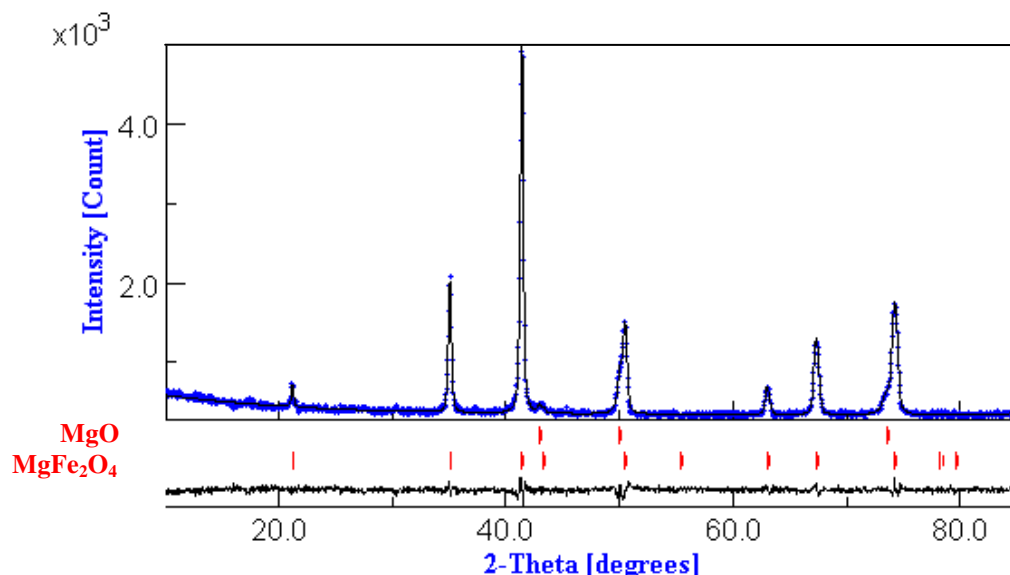


Fig. 2.12: (a) The experimental (symbol) and refined (solid) X-ray diffractogram patterns of MgFe_2O_4 particles calcined at 300 °C for 2 h. The resultant plot after subtracting the experimental and refined spectra and the XRD peak positions for impurity (MgO) and spinel (MgFe_2O_4) phase are marked

Table-2.2: Refined structural and micro-structural parameters of magnesium ferrite powders calcined at 300 °C for 2 h

Magnesium ferrite MgFe_2O_4 (MFO)	Refined composition $(\text{Mg}_{0.14}\text{Fe}_{0.86})_{\text{T}}(\text{Mg}_{0.86}\text{Fe}_{1.14})_{\text{O}}\text{O}_4$				
Phase(s) present	Statistical parameters				
MgFe_2O_4 cubic spinel (Fd-3m) 82 wt%	R_{wp} : 5.6 % ; R_{p} : 4.87 %				
MgO cubic (Fm-3m) 18 wt%	R_{wbp} : 4.47 % ; R_{pb} : 4.23 %				
Calcination temperature 300 °C					
Refined parameters (MgFe_2O_4)	Atomic coordinates				
Lattice parameter (Å) 8.38 (0.0014)	Atom	x	y	z	$\beta(\text{\AA}^2)$
Rms microstrain 0.0017%	Mg_{T}	0.125	0.125	0.125	1.21
Crystallite size (nm) 81.7 (2.09)	Fe_{T}	0.125	0.125	0.125	1.21
Density (gm/cc) 4.49 gm/cc	Mg_{O}	0.5	0.5	0.5	0.37
Refined parameters (MgO)	Fe_{O}	0.5	0.5	0.5	0.37
Lattice parameter (Å) 4.23 (0.0011)	O	0.255	0.255	0.255	0.713
Crystallite size (nm) 145 (9.9)					

observed and calculated profiles are evaluated by weighted residual factor (R_{wp}), expected weighted profile factor (R_{exp}), goodness of fit indicator (GOF), reduced chi-square (G_oF squared) and Bragg factor (R_B) [The mathematical expression for these statistical functions may be found in the manual of the program MAUD]. As a thumb rule GOF value close to 1 (usually in between 1.1 to 1.3) is a good indicator of the convergence of this least squared fitting procedure. If the material under investigation is not phase pure, the volume fraction of each phase is also calculated by the program from the refined scale factor, formula unit per unit cell, atomic weight of the formula unit and volume of the unit cell. A typical refinement plot for $MgFe_2O_4$ particles, calcined at 300 °C for 2 h, is shown in Fig. 2.12. The refined composition, structural and micro-structural parameters (i.e phase, volume fraction, lattice parameter, r.m.s micro-strain, and crystallite size) as well as the statistical fitting parameters for MFO powder calcined at 300 °C for 2 h is tabulated in Table-2.2.

2.4.4. Electron Microscopy

Electron microscopy has been used to characterize the surface morphology and composition of the synthesized nano-structured gas sensing materials. The principle of electron microscopy is based on the fact to focus electron beam on to a small part of the sample kept in vacuum, and detect the output signals originate during the interaction of electrons with the sample. In the electron microscope, the electrons emit from the cathode are accelerated using a very high voltage. According to the de Broglie relation ($\lambda = h/p$ where h is a Planck's constant and p is the momentum of the electron) the wavelength of electron will be lower for the electrons with higher momentum. Thus by manipulating the momentum of the electrons, the resolution of the microscope is adjusted. Depending on the momentum of the electrons (depends on the acceleration voltage and its functioning); the electron microscopes are usually classified into two types: scanning electron microscope (SEM) and transmission electron microscope (TEM).

Scanning electron microscope (SEM): In a SEM, the electrons are usually accelerated by applying the voltage ranges 1-50 kV. The schematic diagram of a SEM and the commercial instrument (Supra-40, Carl Zeiss, Germany) used in the present study are shown in Fig. 2.13 (a) and (b) respectively. As shown in the schematic diagram, a

SEM is equipped with an electron gun (to generate electrons), two electromagnetic lenses (to focus the electron beam on the sample), scanning coils (to scan the electron beam over the sample), sample chamber (to keep the sample) and detectors (to detect the output signals). All these components are kept inside a vacuum chamber. There are two types of electron gun: thermionic and field emission type. In a thermionic gun usually the electrons are emitted from a bent tungsten filament (withstand high temperature without melting) that acts as cathode. In the field emission scanning electron microscope (FESEM), the electrons are emitted from a sharp tip by applying a high electric field. The electrons produced by field emission are larger in amount than the thermionic produced electrons. The electrons emitted from the electron gun are accelerated by applying a high electric potential. In order to focus the electrons into a finely adjusted focused beam, the electromagnetic lenses are used. The scanning of the electron beam over the sample surface is controlled by deflecting the electron beam using a scanning coil. The electrons produced by field emission are larger in amount than the thermionic produced electrons. The electrons emitted from the electron gun are accelerated by applying a high electric potential. In order to focus the electrons into a finely adjusted focused beam, the electromagnetic lenses are used. The scanning of the electron beam over the sample surface is controlled by deflecting the electron beam using a scanning coil.

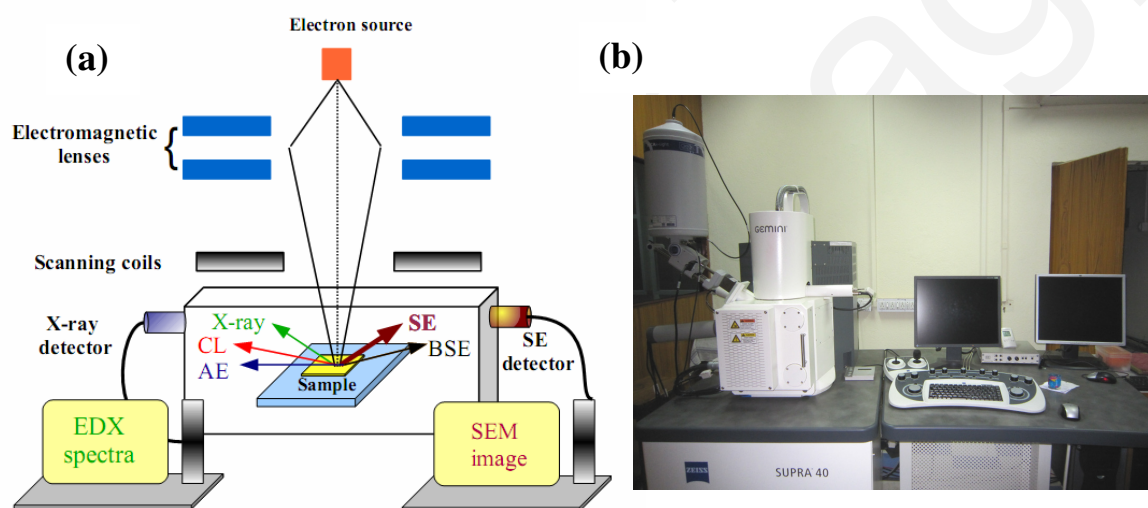


Fig. 2.13: (a) Schematic diagram of a SEM and (b) the photograph of the field emission scanning electron microscope (Supra-40, Carl Zeiss, Germany) used in the present work

When an energetic electron beam strikes on the surface of a specimen, a number of different phenomena may occur. The most probable incident is the liberation of electrons from outer shell orbital of the specimen atoms. These knocked out outer shell electrons are termed as secondary electrons (SE). Since a large amount of secondary electrons are produced, the detection of secondary electrons is most common in the SEM. Sometimes

the incident electrons may collide with the nucleus of the sample atom resulting bounce back of the high energetic electrons, known as backscattered electrons (BSE). These BSE electrons produce brighter region (in the image) for the atoms with higher atomic number. In the SEM, usually the SEs are identified in the detector and used for the production of image. The images can be directly stored in the SEM microscope in digital format. Besides the emission of SE and BSEs, the incident electrons again may collide with the inner shell electron of the sample atom and produces X-rays and Auger electrons (AE). The generated X-ray and AEs are unique to each element type and thus can be used for the elemental detection of the sample. In the electron microscopy the elemental detection using an X-ray detector is known as energy dispersive X-ray spectroscopy (EDS). During the interaction of the electrons beam with the sample surface light (in ultraviolet, visible and infra red region) is also emitted. The emission of light is known as catho-luminescence (CL). Thus in addition to provide the information of sample topography, detection of BSE, EDS, AE could provide additional information on impurity phase and elemental composition of the sample. In the present work we have characterized the synthesized materials using SE image and EDS elemental detection. Before micro-structure evaluation, the insulating samples are gold coated using a dc sputter coating unit.

Transmission electron microscopy (TEM): As the name suggests in this electron microscopy technique the electrons are passed through the sample. The samples (thin film/ powders etc) should therefore be made very thin or well dispersed nano-particle suspension should be investigated. Usually the samples (thin films/ pellets) are thinned (to make them electron transparent) by dimpling followed by ion beam thinning and jet polishing. Samples such as nano-particles, nano-tubes are first well dispersed in low boiling solvent (usually ethanol) using an ultrasonic bath. The well dispersed suspension is then deposited on a carbon coated copper grid using a micro-pipette and kept overnight in vacuum desiccators for solvent evaporation. In TEM, the voltage (200-300 kV) used to accelerate the electrons is much higher than the SEM. The high energetic focused electron beam pass through a thin sample. The de Broglie wavelength of such high energetic electrons are very short and thus as compared to the SEM, detailed features in the samples are detected with higher resolution. The working principle of TEM is more

or less similar to that of a SEM. The schematic diagram of a typical TEM and the photograph of the TEM instrument (JEM 2100, Jeol Ltd., Japan) used for the characterizations of the synthesized materials are shown in Fig. 2.14 (a) and (b) respectively.

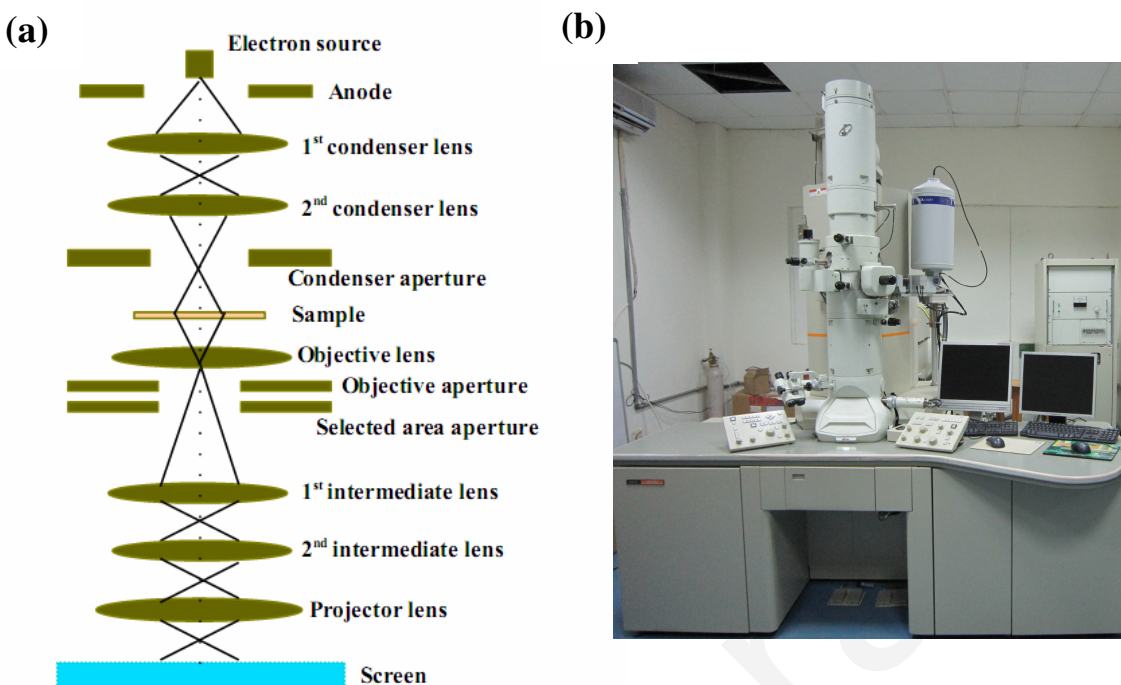


Fig. 2.14: (a) Schematic diagram of a TEM and (b) the photograph of the high resolution transmission electron microscope (JEM 2100, Jeol Ltd., Japan) used in the present work

Similar to the SEM, an electron gun is located at the top of the TEM column. The electron beam is focused to the column by using condenser lenses 1 and 2 and a condenser aperture (that removes high angle defocused electrons). The focused electron beam strikes the specimen and parts of it are transmitted. The transmitted electrons are then focused by the objective lens into an image. The TEM imaging system is used either for image projection or selected area diffraction pattern projection. These two projections are controlled by using the objective and selected area apertures. During the image projection mode, the objective aperture is adjusted to enhance the contrast of the image by blocking the high-angle diffracted electrons. For recording the diffraction pattern projection the selected area aperture is adjusted to capture the interaction of the electrons with the ordered arrangement of atoms in the sample. During the image projection the

transmitted electrons are passed through the intermediate and projector lenses before it strike to the fluorescent screen.

The transmission of the electrons through the sample is inversely proportional to the thickness of the sample. Therefore the dark and lighter regions of a TEM image correspond to the thicker and thinner part of the sample respectively. For recording the pattern projection when the incident electrons are deflected (without any energy loss) due to their interaction with the sample (with regular arrangement of atoms) these follow Bragg's law of diffractions. The deflected electrons are focused using magnetic lenses to form a pattern of diffraction spots which are used to identify the crystalline nature of the sample. This mode of operation is known as selected area electron diffractions (SAED). Besides providing the information about imaging and crystallinity of the material one can obtain the compositional information using the TEM. Similar to the SEM, (when the incident electrons strike the sample) as discussed earlier usual phenomenon (SE, BSE, AE, EDX, CL) are observed in TEM as well. These are used to detect impurity phase, sample composition etc.

2.4.5. BET: Analysis of Surface Area and Pore Size Distribution

In the present work the phenomenon of the physical adsorption of nitrogen gas (by varying the partial pressure of nitrogen) on the synthesized materials ($\text{Mg}_{1-x}\text{Zn}_x\text{Fe}_2\text{O}_4$ ($0 \leq x \leq 1$)) is utilized to estimate their specific surface area. The physical adsorption of N_2 over the samples follows the Brauner-Emmet-Teller (BET) adsorption isotherm theory which is represented as follows:

$$1/\{W_a(P_0/P) - 1\} = 1/W_m C + \{(C-1)/W_m C\}(P/P_0) \quad (2.5)$$

where P: absolute pressure, P_0 : saturation pressure, W_a : adsorbed weight of N_2 gas at equilibrium, W_m : weight of the monolayer adsorbed gas and C is a constant. During the monolayer-multilayer adsorption of N_2 over the sample, $1/W_a(P_0/P - 1)$ vs P/P_0 results a straight line usually in the range $0.05 \leq P/P_0 \leq 0.35$. From the slope $((C-1)/W_m C)$ and intercept $(1/W_m C)$ of the plot, and knowing precisely the weight of the sample taken (W_s) one can easily estimate the specific surface of the sample (S_{sp}) using the following relation

$$S_{sp} = (W_m \times N \times A_{cs}) / (M \times W_s) \quad (2.6)$$

where N is Avogadro number, A_{cs} is the area covered by one molecule of N_2 gas (16.2 \AA^2 at 77K).

One typical example for the estimation of specific surface area of $Mg_{0.5}Zn_{0.5}Fe_2O_4$ nano-particles (prepared using PVA assisted route) is described as follows.

For this sample Fig. 2.15 shows a typical $1/W_a (P_0/P - 1)$ vs P/P_0 plot and the linear fit (solid line). The weight of the sample is $\sim 0.0638 \text{ g}$ and P/P_0 is kept in the range $0.05 \leq P/P_0 \leq 0.35$. From the slope (122.0039) and intercept (2.63317) of the linear fit the estimated surface area (using Eqn. 2.6) is estimated to be $\sim 28 \text{ m}^2\text{g}^{-1}$.

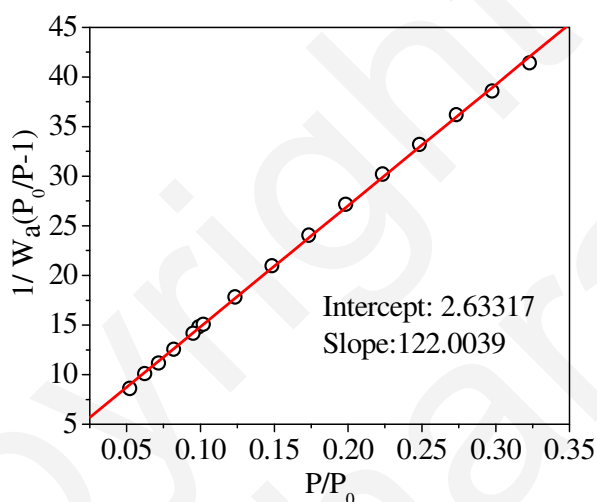


Fig. 2.15: Typical linear fit (solid line) of $1/W_a (P_0/P - 1)$ vs P/P_0 experimental data (symbols) from $Mg_{0.5}Zn_{0.5}Fe_2O_4$ nano-particles synthesized using PVA assisted route

The BET instrument (Autosorb-1, Quantachrome Instruments, USA) typically consists of a gas supply unit, a gas flow regulator, a vacuum pump, sample holder, temperature controller unit and a Dewar flask. The sample holder is usually made with U-shaped glass tube to allow smooth gas flow. To record the N_2 adsorption-desorption isotherm, the samples are first kept in the glass tube container (pre tared) and degassed at high temperature ($\sim 300 \text{ }^\circ\text{C}$) for 4-5 h to get rid of the adsorbed moisture. After degassing the tube (with sample) is again weighed precisely to note the exact weight of the sample. The sample container is then connected to the BET analysis chamber and the measurement is started by cooling down and evacuating the system. After cooling at liquid N_2 temperature, the sample is exposed to nitrogen by varying the nitrogen pressure.

During the adsorption of N_2 over the sample, the chamber pressure remains constant. As soon as the surface is covered completely in N_2 , the chamber pressure increases. When the chamber pressure is reached to atmospheric pressure, the procedure is repeated in reverse mode (desorption of N_2). After the completion of the cycle, nitrogen comes out from the sample and the pressure is measured after equilibrium.

Fig. 2.16 shows a typical N_2 adsorption-desorption isotherm of $Mg_{0.5}Zn_{0.5}Fe_2O_4$ nano-particles (prepared using PVA assisted route).

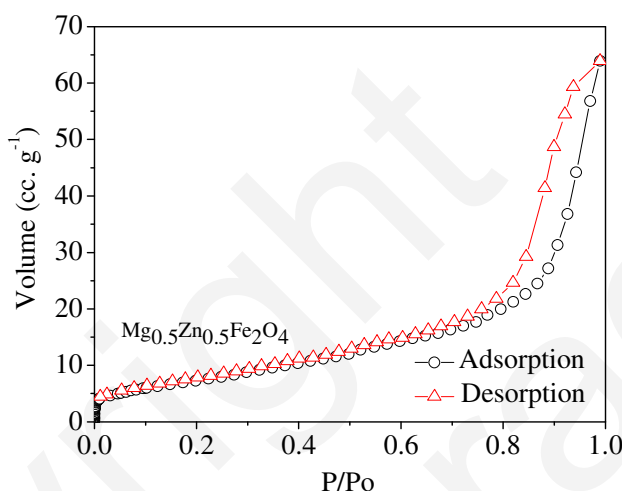


Fig. 2.16: Typical N_2 adsorption desorption isotherm of $Mg_{0.5}Zn_{0.5}Fe_2O_4$ nano-particles synthesized using PVA assisted route

The N_2 adsorption desorption isotherm of the materials provides the information about the nature of pore (micro, meso and macro porous) and porosity distribution of the sample under investigation. According to IUPAC the isotherms are grouped into six types as shown in Fig. 2.17(a) [10]. Among these isotherms, the type IV isotherm is common for meso-porous (preferable for gas sensing applications) materials.

The hysteresis loop (in the type IV isotherm) arises due to the capillary condensation of gases in the meso-pores. The other types of isotherms also represent some basic adsorption-desorption characteristics over porous (micro, meso and macro porous) sample and described in details in the IUPAC recommendation [10].

Depending on the hysteresis nature, type IV isotherms are again classified in 4 classes (H1, H2, H3 and H4). These isotherms are shown in Fig. 2.17(b). The detail of these hysteresis loops found in the adsorption-desorption isotherms are described elsewhere [10]. As shown in Fig. 2.16 the N_2 adsorption desorption isotherm of $Mg_{0.5}Zn_{0.5}Fe_2O_4$

nano-particle corresponds to type IV isotherm with H1 hysteresis which supports the meso-porous nature of $\text{Mg}_{0.5}\text{Zn}_{0.5}\text{Fe}_2\text{O}_4$ nano-particle.

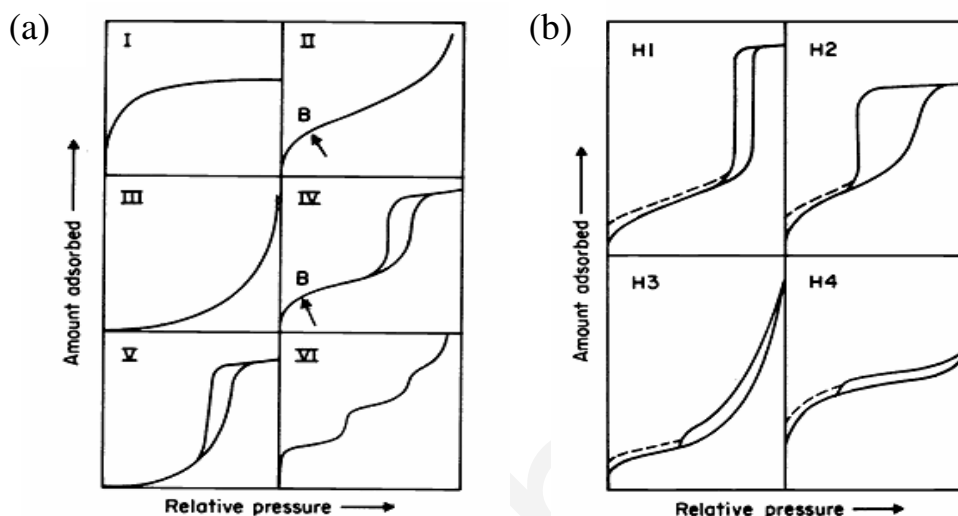


Fig. 2.17: (a) Various types of adsorption-desorption isotherms (b) Various types of hysteresis in type IV isotherms (from Ref. 10)

The fabrication of sensing elements using the synthesized nano-structured oxides and brief details of the gas sensing measurements are described in the next section.

2.5. Fabrication of Sensing Elements and Gas Sensing Measurements

For measuring the gas sensing characteristics of the nano-particulate sensors, the synthesized $(\text{Mg}_{1-x}\text{Zn}_x)\text{Fe}_2\text{O}_4$ ($0.0 \leq x \leq 1.0$) nano-particles (calcined at 300°C) are mixed with few drops of 10% PVA solution as binder and pressed in the form of thin circular discs (~ thickness $100\ \mu\text{m}$ and diameter $\sim 12\ \text{mm}$) using a hydraulic press. The pellets are sintered in a two step process, first one at 400°C for 1 h for the removal of organics followed by sintering at 600°C for 2 h in air. The above heat treatment ensures minimal particle growth, necking between particles, sufficient handling strength and porous nature of the sensing element. After sintering the surface of the pellets are polished using a velvet cloth.

For the electrical measurements, one of the surfaces of the sensing elements are sputter coated with planar gold stripes of 7mm length, 3 mm wide and separated from each other by 4mm.

For the measurement of gas sensing characteristics of $\text{Mg}_{0.5}\text{Zn}_{0.5}\text{Fe}_2\text{O}_4$ thin films (grown on alumina substrate by spin coating technique using the $\text{Mg}_{0.5}\text{Zn}_{0.5}\text{Fe}_2\text{O}_4$ sol prepared through Pechini method), the surface of the film are sputter coated with inter-digitated gold electrode using a shadow mask.

To measure the resistance change of the embedded $\text{Mg}_{0.5}\text{Zn}_{0.5}\text{Fe}_2\text{O}_4$ nano-tubes (crystallized inside the pores of the anodized alumina) parallel plate geometry has been used. Both the faces of the anodized alumina template (embedded with $\text{Mg}_{0.5}\text{Zn}_{0.5}\text{Fe}_2\text{O}_4$ nano-tubes) are sputter coated with thin gold film. During the gold coating the disks are kept inclined about 15 degree so that the metal coating partially coats the exposed surface.

To measure the gas sensing performance of the isolated $\text{Mg}_{0.5}\text{Zn}_{0.5}\text{Fe}_2\text{O}_4$ nano-tubes and hollow spheres, these are coated on quartz substrate (using PVA as binder). After coating the sensing elements are heat treated at 400 °C for 1 h to remove the organics. To measure the resistance change of the sensing elements, inter-digitated gold electrode is sputter coated on the nano-tube and hollow sphere film using inter-digitated mask.

The response (S) of the sensor, response and recovery time and the stability of the sensing elements are characterized using the dynamic volume gas sensing measurement unit described in details in Sec. 2.2.

The architecture of these sensing elements and the details of the gas sensing measurements are described in Chapter-3.

Reference

- [1] Mukhejee, K. and Majumder, S.B., (2009), Analyses of Response and Recovery Kinetics of Zinc Ferrite as Hydrogen Gas Sensor, *Journal of Applied Physics*, Vol.106, pp. 064912 (9).
- [2] Hu, Y., Tan, O.K., Cao, W. and Zhu, W. (2004), Oxygen Sensing Properties of Fe Doped-SrTiO₃ Powders Obtained by Self-Propagating High Temperature Synthesis and Treated by Ball Milling, *Ceramic International*, Vol.33, pp.1819-1822.
- [3] Akbar, S., Dutta, P. and Lee, C. (2006), High Temperature Ceramic Gas Sensors: A Review, *International Journal of Applied Ceramic Technology*, Vol. 3, pp-302-311.
- [4] Jia, L., Cai, W. and Wang, H. (2010), Metal Ion Doped SnO₂ Ordered Porous Films and Their Strong Gas Sensing Selectivity, *Applied Physics Letters*, Vol. 96, pp. 103115 (3).
- [5] Zhang, G.Y., Guo, B. and Chen, J. (2006), MCo₂O₄ (M = Ni, Cu, Zn) Nanotubes: Template Synthesis and Application in Gas Sensors, *Sensors and Actuators B*, Vol. 114, pp. 402-409.
- [6] Penza, M., Martucci, C. and Cassano, G. (1998), NO_x Gas Sensing Characteristics of WO₃ Thin Films Activated by Noble Metals (Pd, Pt, Au) Layers, *Sensors and actuators B*, Vol. 50, pp. 52-59.
- [7] Mann, D.P., Paraskeva, T., Pratt, K.F.E., Parkin, I.P. and Williams, D.E. (2005), Metal Oxide Semiconductor Gas Sensors Utilizing a Cr-Zeolite Catalytic Layer for Improved Selectivity, *Measurement Science and Technology*, Vol.16, pp.1193-1200.
- [8] Purohit, R.D. and Tyagi, A.K. (2002), Auto-Ignition Synthesis of Nanocrystalline BaTi₄O₉ Powder, *Journal of Materials Chemistry*, Vol. 12, pp. 312-316.
- [9] Sun, X. and Li, Y. (2004) Colloidal Carbon Spheres and Their Core/Shell Structures with Noble-Metal Nanoparticles, *Angewandte Chemie International Edition*, Vol. 43, pp. 597-601.
- [10] Sing, K.S.W., Everett, D.H., Haul, R.A.W., Moscou, L., Pierotti, R.A., Rouquerol, J. and Siemieniowska, T. (1985), Reporting Physisorption Data for Gas/ Solid Systems with Special Reference to the Determination of Surface Area and Porosity, *Pure and Applied Chemistry*, Vol. 57, pp. 603-619.

Chapter-3

PHASE FORMATION BEHAVIOR, MICRO-STRUCTURE EVALUATION AND GAS SENSING CHARACTERISTICS OF NANO-STRUCTURED FERRITE MATERIALS

3.1. Introduction

There is growing demand of gas sensors from industrial, automotive, clinical, environment monitoring as well as domestic sectors to sense a wide variety of gases including toxic, combustible, organic, cooking vapors etc. A gas sensor is primarily characterized by four key performance parameters: sensitivity, selectivity, stability and low response time [1]. The commercial gas sensor materials are restricted mainly to limited number of elemental oxide semiconductors namely ZnO, SnO₂, TiO₂, WO₃, Fe₂O₃ etc. The major research activities in these areas are limited to improve the gas sensing characteristics by modifying materials, device design and electrical signal analysis [2-5]. Limited attention has therefore been paid to search alternative gas sensing materials. The binary oxides have poor selectivity towards various reducing gases. As an effective alternative to these binary oxides various spinel ferrites are reported not only to have excellent gas sensitivity but also some of them exhibit reasonably good selectivity towards a specific gas sensing [6-8]. High throughput solution based material synthesis technique would be an effective alternative to accelerate the search of alternative material as it allows combinatorial material synthesis and thereby a number of potential materials can be evaluated in terms of their effectiveness for gas sensing applications [9].

The improved performance of the gas sensors is directly related to their exposed surface volume and therefore sensors made using high surface area nano-powders often exhibits dramatically improved gas sensing performance [10-11]. The majority of the nano-materials are tested in thick film form synthesized by screen-printing technique. Proper control of the grain size of these thick film sensors remains one of the major research issues. The thick film devices must be heated to sufficiently high temperature for film integrity as well as grain-to-grain connectivity. At the same time the processing temperature should not be too high so that rapid grain growth takes place with rapid decrease of the open porosity. The gas sensing reaction takes place well above the room temperature; therefore, the stability of nano-crystalline thick film sensor (grain growth during sensor operation) also remains one of the major research issues.

The stability problem, mentioned above, can be partially circumvented by fabricating nano-structured sensor materials using template based synthesis. In recent days considerable effort has been focused on the use of a template into which the sensor material can be assembled. Block copolymers, latex spheres, water in emulsions, polystyrene particles, anodized alumina etc can be used as template [12-15]. As for example, using two-dimensional array of polystyrene micro-sphere as a template, synthesis of hollow hemi-spheres of TiO_2 film has been reported [13] which is used as CO and ethanol sensor. Using anodic aluminum oxide membrane MCo_2O_4 ($\text{M} = \text{Ni}, \text{Cu}, \text{Zn}$) nano-tubes are synthesized which are used to sense ethanol and SO_2 [16]. These reports clearly demonstrate the superior gas sensing performance of these nano-structured films. Viewing in the light of the above reports the present research work aims to execute an in depth study on nano-structured oxide electrodes and evaluate the gas sensing performance of certain non-conventional oxide materials as gas sensors.

As reviewed in details in Chapter-1, the gas sensing characteristics of the ferrite based sensing elements are significantly influenced by the phase purity, particle/ grain size, surface area, porous nature of the sensing materials. The experimental results on the phase formation, micro-structural and gas sensing characteristics the synthesized ferrite based sensor materials are described as itemized below:

- Phase formation behavior, surface morphology and gas sensing characteristics of $\text{Mg}_{1-x}\text{Zn}_x\text{Fe}_2\text{O}_4$ ($0.0 \leq x \leq 1.0$) nano-particles prepared using PVA assisted wet chemical route.
- Comparison between the phase formation behavior, micro-structure and gas sensing characteristics of $\text{Mg}_{0.5}\text{Zn}_{0.5}\text{Fe}_2\text{O}_4$ nano-particles synthesized using PVA assisted wet chemical and a modified Pechini based auto-combustion routes.
- Investigations on the phase formation behavior, surface morphology and gas sensing characteristics of nano-structured (thin film, embedded nano-tube into porous alumina template, isolated nano-tubes and hollow-sphere) $\text{Mg}_{0.5}\text{Zn}_{0.5}\text{Fe}_2\text{O}_4$ sensors.

3.2. Experimental

In the present work we have adopted two different wet chemical routes (namely PVA assisted and auto-combustion) to synthesize $\text{Mg}_{1-x}\text{Zn}_x\text{Fe}_2\text{O}_4$ ($0.0 \leq x \leq 1.0$) particles. The details synthesis procedures are described in Chapter-2. From the precursor sol prepared by modified Pechini process we have synthesized $\text{Mg}_{0.5}\text{Zn}_{0.5}\text{Fe}_2\text{O}_4$ sensing materials in the form of nano-tubes (embedded in anodized alumina template and isolated quoted on fused quartz substrates), and thin film form. Additionally $\text{Mg}_{0.5}\text{Zn}_{0.5}\text{Fe}_2\text{O}_4$ hollow-spheres are also synthesized by hydrothermal route. The details of these material syntheses are described in Chapter-2.

The precursor sol is characterized by thermal analyses (DTA and TGA of gel derived powders). The heating schedule of these oxides is optimized based on the thermal analyses results. The phase formation behavior is characterized by X-ray diffraction techniques. The pore-size, pore-size distribution and specific surface area of the synthesized nano-particles are estimated from nitrogen adsorption isotherm analyses. The porous bulk, thin film, and nano-structured sensing elements are characterized by scanning electron as well as transmission electron microscopy with selected area electron diffraction analyses wherever appropriate. The gas sensing performances of these materials are characterized by dc resistance measurements as detailed in preceding chapter. From the measured dc resistance of the sensing element in air (R_a) and in test gas environment (R_g), the response (S) is estimated using the following relations:

$$S(\%) = \{(R_a - R_g) / R_a\} \% \quad (3.1) \quad \text{for 'n' type sensing element}$$

$$S(\%) = \{(R_g - R_a) / R_g\} \% \quad (3.2) \quad \text{for 'p' type sensing element}$$

3.3. Phase Formation Behavior, Surface Morphology and Gas Sensing Characteristics of $\text{Mg}_{1-x}\text{Zn}_x\text{Fe}_2\text{O}_4$ ($0.0 \leq x \leq 1.0$) Nano-particles Prepared Using PVA Assisted Wet Chemical Route

3.3.1. FTIR Analyses

Typical FTIR spectra of dried as well as calcined (upto 600 °C) MgFe_2O_4 (MFO) and ZnFe_2O_4 (ZFO) powders has been shown in Fig. 3.1(a) and (b) respectively. Note that the modes due to the organics and other impurities (C-O, C=O, O-H) of as dried powders are completely removed and a low frequency mode (due to M-O bond formation) emerges in

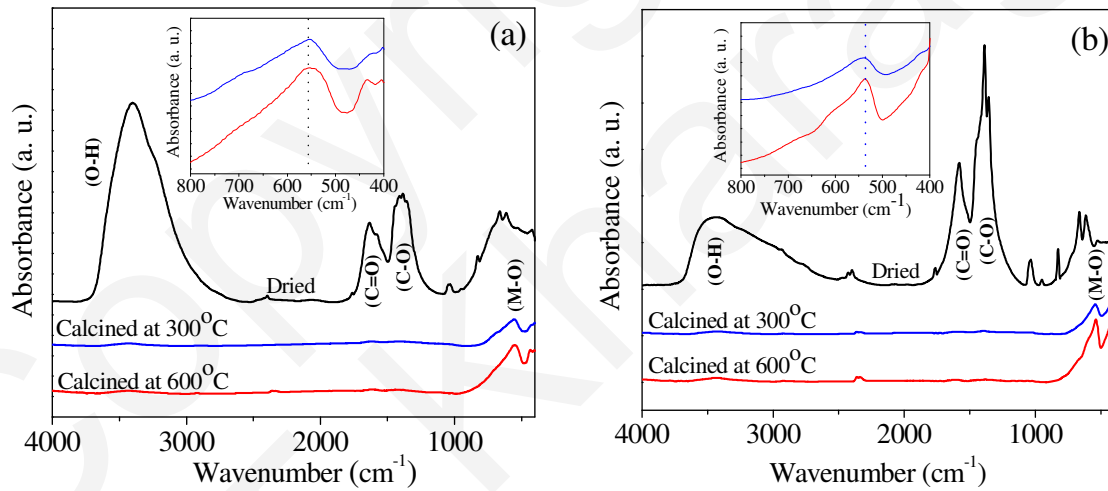


Fig. 3.1: FTIR spectra of dried and calcined (a) MgFe_2O_4 and (b) ZnFe_2O_4 powders

powders calcined at 300 °C. As shown in the inset of Fig. 3.1(a) and (b), the mode frequencies for metal-oxygen (M-O) bonds are almost invariant to the calcination temperature. For MgFe_2O_4 , the prominent M-O IR vibration modes are reported to be at 565 (ν_2) and 406 cm^{-1} (ν_1). For ZnFe_2O_4 , these modes are reported to be at 555 (ν_2) and 393 cm^{-1} (ν_1) [17]. In spinel ferrites cations are located in tetrahedral and octahedral voids. As reported for several spinel structures [18-19], any shift of the M-O mode

frequencies is indicative to the cation disorder in the tetrahedral and octahedral voids. The cation disorder may increase with the increase in calcination temperature resulting appreciable change in M-O bond length as well as vibration frequencies. From the FTIR spectra of MFO and ZFO particles it is apparent that the mode frequencies for tetrahedral cation/(s) are almost invariant to the calcination temperature. This suggests minimal cation disorder in these ferrites.

However, interesting variation of the M-O mode frequency is observed when we compare FTIR spectra of $\text{Mg}_{1-x}\text{Zn}_x\text{Fe}_2\text{O}_4$ ($0.0 \leq x \leq 1.0$) solid solutions, calcined at identical temperatures. Thus, Fig. 3.2 shows the FTIR spectra of $\text{Mg}_{1-x}\text{Zn}_x\text{Fe}_2\text{O}_4$ ($0.0 \leq x \leq 1.0$) particles calcined at 600 °C. Note that as the Zn contents in the solid solution are increased the tetrahedral mode frequency is shifted to lower wavenumber. This is expected as Zn has higher atomic mass as compared to Mg ion in a specific crystallographic lattice site. The results presented above indicate that the synthesized ferrite particles are free from any organic moieties with minimal cation disorder.

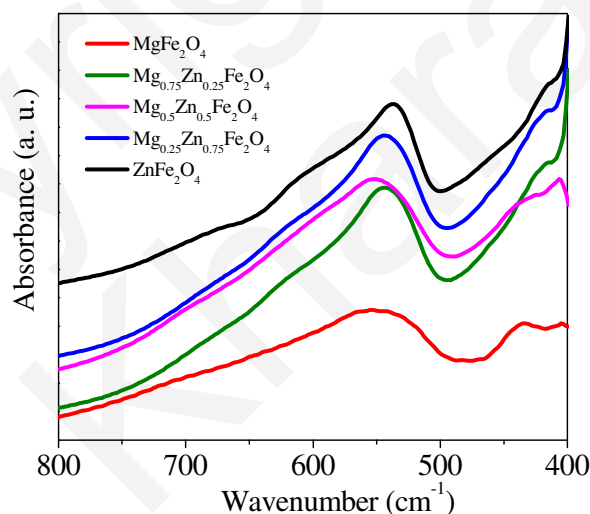


Fig. 3.2: FTIR spectra of $\text{Mg}_{1-x}\text{Zn}_x\text{Fe}_2\text{O}_4$ ($0.0 \leq x \leq 1.0$) particles calcined at 600 °C

3.3.2. Phase Formation Behavior

Fig. 3.3 (a) and (b) shows the X-ray diffractograms of $\text{Mg}_{1-x}\text{Zn}_x\text{Fe}_2\text{O}_4$ ($0.0 \leq x \leq 1.0$) powders calcined at 300 and 600 °C respectively. All these powders crystallize into cubic spinel structure at a temperature as low as 300 °C. At lower calcination temperature, with the desired cubic spinel phase, MgO and ZnO co-exist as impurity phase in Mg and Zn

rich ferrite compositions respectively. On the other hand, when the calcination temperature is raised to $\sim 600^\circ\text{C}$, (especially in Mg rich compositions) $\alpha\text{-Fe}_2\text{O}_3$ coexists as impurity phase with the desired cubic spinel phase. It is interesting to note that among all these compositions only $\text{Mg}_{0.5}\text{Zn}_{0.5}\text{Fe}_2\text{O}_4$ powders, calcined at 300°C , are phase pure in nature. Comparing the FWHM of the XRD pattern of $\text{Mg}_{0.5}\text{Zn}_{0.5}\text{Fe}_2\text{O}_4$ powders calcined at different temperatures, it is apparent that lower the calcination temperature smaller is the crystallite size. For efficient gas sensing characteristics semiconducting oxides with smaller crystallite size is preferred.

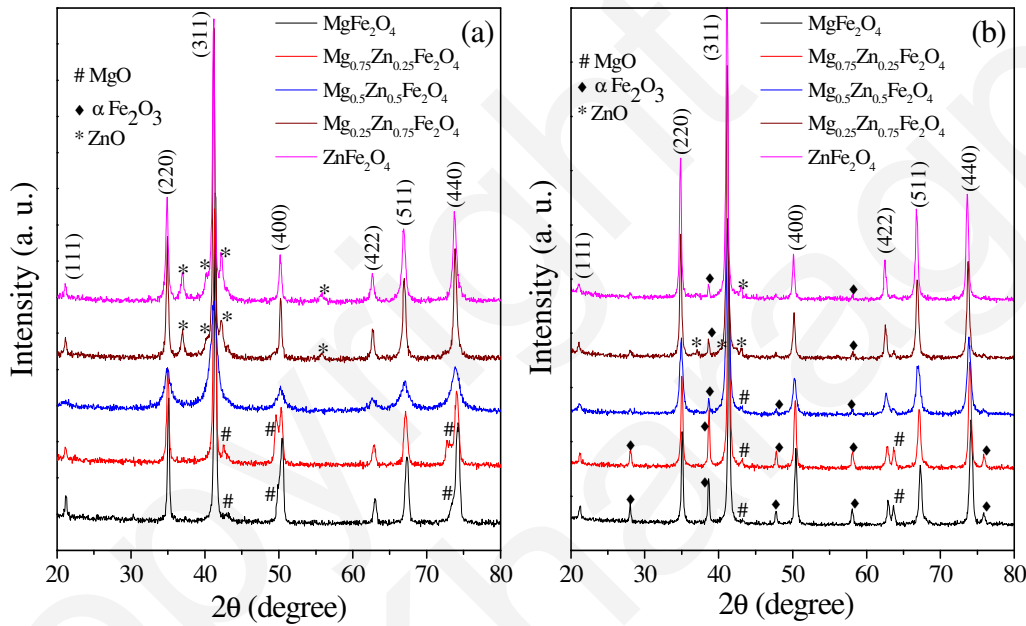


Fig. 3.3: X-ray diffractograms of $\text{Mg}_{1-x}\text{Zn}_x\text{Fe}_2\text{O}_4$ ($0.0 \leq x \leq 1.0$) powders calcined at (a) 300°C and (b) 600°C for 2 h in air

To quantify structural and micro-structural parameters, we have performed Rietveld refinement of the X-ray diffractograms of the $\text{Mg}_{1-x}\text{Zn}_x\text{Fe}_2\text{O}_4$ ($0.0 \leq x \leq 1.0$) particles using the Rietveld refinement program MAUD [<http://www.ing.unitn.it/~maud/>]. As an example, the typical X-ray Rietveld refinement plot of MFO powder calcined at 300°C has already been presented in Chapter-2. The refined structural and micro-structural parameters, estimated for $\text{Mg}_{1-x}\text{Zn}_x\text{Fe}_2\text{O}_4$ ($0.0 \leq x \leq 1.0$) powders calcined at 300°C and 600°C is tabulated in Table-3.1.

As shown in Table-3.1, among all the studied composition of $\text{Mg}_{1-x}\text{Zn}_x\text{Fe}_2\text{O}_4$ ($0.0 \leq x \leq 1.0$), $\text{Mg}_{0.5}\text{Zn}_{0.5}\text{Fe}_2\text{O}_4$ particles have smallest crystallite size. The lattice parameter is increased with the increase in calcination temperature (300 to 600 °C) as well as with the increase in Zn contents in MgFe_2O_4 lattice. Within the experimental error, the crystallite sizes of all the $\text{Mg}_{1-x}\text{Zn}_x\text{Fe}_2\text{O}_4$ ($0.0 \leq x \leq 1.0$) compositions are found to increase with the increase in calcination temperature.

Table-3.1: The refined structural and micro-structural parameters, estimated for $\text{Mg}_{1-x}\text{Zn}_x\text{Fe}_2\text{O}_4$ ($0.0 \leq x \leq 1.0$) powders calcined at 300 °C and 600 °C

Material	Phase (%)		Crystallite size (nm)		Lattice parameter	
	(Spinel: impurity)				(Å)	
	300 °C	600 °C	300 °C	600 °C	300 °C	600 °C
MgFe_2O_4	82: 18	78: 22	70	84	8.384	8.387
$\text{Mg}_{0.75}\text{Zn}_{0.25}\text{Fe}_2\text{O}_4$	65: 35	55: 45	39	63	8.412	8.415
$\text{Mg}_{0.5}\text{Zn}_{0.5}\text{Fe}_2\text{O}_4$	100: 00	62: 38	11	21	8.418	8.426
$\text{Mg}_{0.25}\text{Zn}_{0.75}\text{Fe}_2\text{O}_4$	90: 10	61: 39	85	97	8.429	8.441
ZnFe_2O_4	93: 07	97: 03	38	45	8.433	8.450

3.3.3. Surface Morphology

The synthesized nano-particles are pressed in the form of circular pellet and loosely sintered at ~ 600 °C for 2 h. The surface morphology of the loosely sintered $\text{Mg}_{1-x}\text{Zn}_x\text{Fe}_2\text{O}_4$ ($0.0 \leq x \leq 1.0$) pellets is investigated using a field emission scanning electron microscope. Fig. 3.4(a) shows the typical micrograph of MgFe_2O_4 sensing element sintered at 600 °C for 2 h. As shown in Fig. 3.4(a), the individual nano-crystalline MFO particles are agglomerated to yield a porous sensing surface. As envisaged in the micrograph, the nano-crystalline MFO particles (termed as primary particle) are sintered to form relatively bigger grains. Neck formation among these bigger grains is clearly visible. The magnified image of one such bigger grains are shown separately in Fig. 3.4(b). Inspecting Fig. 3.4(a) and (b), the porous region in the sensing surface can be classified into two types: the first type between the bigger particles are termed as macro-porous region, whereas the second type within the individual bigger grains are termed as meso-porous regions. According to the IUPAC nomenclature, larger pores (with average

size more than 50 nm) is termed as macro-pore, whereas those in the size range between 2-50 nm are termed as meso-pores [20]. During gas sensing test gas can diffuse through these macro and meso porous regions and the respective diffusion is termed as molecular and Knudsen diffusion respectively. Similar meso and macro-porous morphologies are also observed in ZFO and $\text{Mg}_{1-x}\text{Zn}_x\text{Fe}_2\text{O}_4$ ($0.0 \leq x \leq 1.0$) (MZFO) solid solution based sensor surfaces. These surface morphologies have been described later in the subsequent chapters as appropriate.

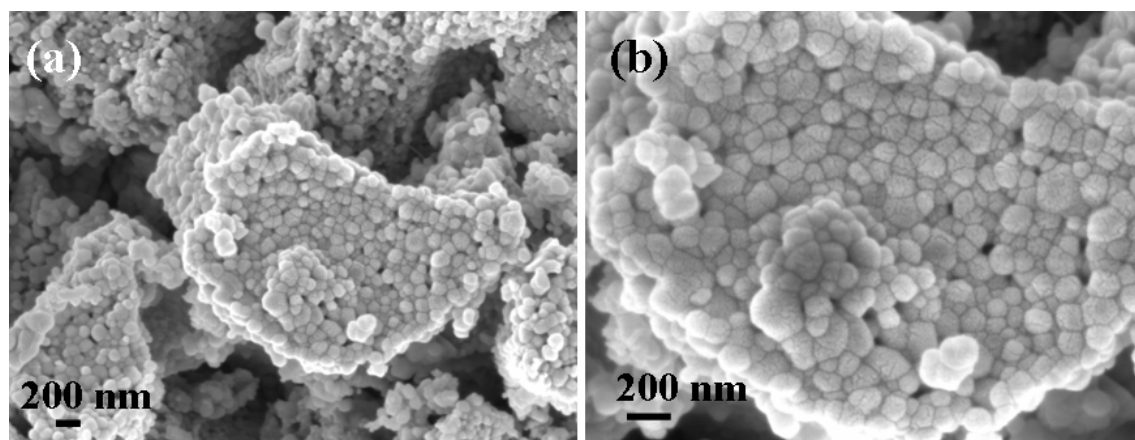


Fig. 3.4: FESEM image of MgFe_2O_4 sensing elements at (a) lower and (b) higher magnifications

3.3.4. Pore-size and Pore-size Distribution

The pore-size, pore-size distribution and specific surface area of MgFe_2O_4 , $\text{Mg}_{0.5}\text{Zn}_{0.5}\text{Fe}_2\text{O}_4$ and ZnFe_2O_4 particles (calcined at 600°C for 2 h) are estimated using by nitrogen adsorption isotherm measured at liquid nitrogen temperature. The BET adsorption-desorption isotherms of MgFe_2O_4 and $\text{Mg}_{0.5}\text{Zn}_{0.5}\text{Fe}_2\text{O}_4$ particles are shown in Fig. 3.5(a) and (b) respectively. Both these isotherms exhibit hysteresis and according to IUPAC they are classified as type- IV isotherms [20]. Type-IV isotherms are known to be associated with capillary condensation in meso-pores. As shown in the inset of Fig. 3.5(a), MgFe_2O_4 particles, have narrower size distribution of meso-pores and their hysteresis is classified as H4 type. In contrast, for $\text{Mg}_{0.5}\text{Zn}_{0.5}\text{Fe}_2\text{O}_4$ (MZFO-P) particles, the adsorption-desorption branches are nearly vertical and almost parallel over higher range of gas pressure (P/P_0) (Fig. 3.5(b)). The hysteresis is classified as H1 type. The inset of Fig. 3.5(b) shows that the MZFO-P particles have wider size distribution of

meso-pores as compared to MFO particles shown in the inset of Fig. 3.5(a). From the BET isotherms the surface area of MgFe_2O_4 , $\text{Mg}_{0.5}\text{Zn}_{0.5}\text{Fe}_2\text{O}_4$ and ZnFe_2O_4 particles are estimated to be 166, 28 and $50 \text{ m}^2\text{g}^{-1}$ respectively.

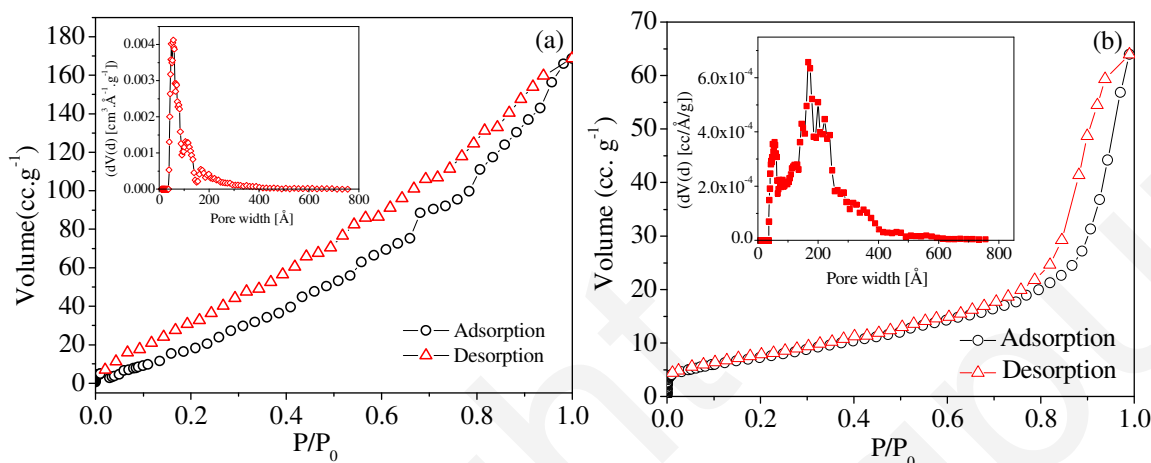


Fig. 3.5: Nitrogen adsorption-desorption isotherm for (a) MgFe_2O_4 and (b) $\text{Mg}_{0.5}\text{Zn}_{0.5}\text{Fe}_2\text{O}_4$ nano-particles calcined at 600°C for 2 h in air

3.3.5. Gas Sensing Characteristics of $\text{Mg}_{1-x}\text{Zn}_x\text{Fe}_2\text{O}_4$ ($0.0 \leq x \leq 1.0$) Nano-particulate Sensors

We have studied the hydrogen and carbon monoxide gas sensing characteristics of nano-particulate $\text{Mg}_{1-x}\text{Zn}_x\text{Fe}_2\text{O}_4$ ($0.0 \leq x \leq 1.0$) sensing elements sintered at 600°C . During the gas sensing measurements the gas concentration is varied from 50-1660 ppm and the sensor operating temperatures are kept in the range between 250 - 380°C . Figure 3.6 shows the typical resistance transients recorded for $\text{Mg}_{0.5}\text{Zn}_{0.5}\text{Fe}_2\text{O}_4$ sensing element towards (a) H_2 and (b) CO gas sensing. The test gas concentration for each case is kept ~ 1660 ppm. As shown in the figure, the test gas is detected through the reduction of sensor resistance, whereas up on recovery the base resistance is regained. The response (S) percentage is estimated through the relation $S = [(R_a - R_g)/R_a] \%$, where R_a and R_g are the sensor resistance measured in air and test gas respectively. Minimal base-line drift is observed when the sensing element is switched back and forth between air and test gas environment.

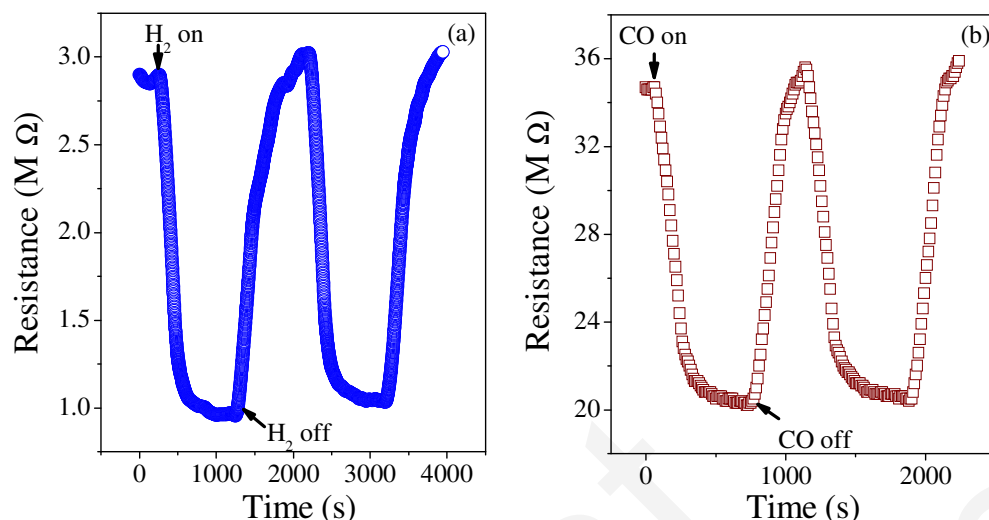


Fig. 3.6: Resistance transients recorded for $\text{Mg}_{0.5}\text{Zn}_{0.5}\text{Fe}_2\text{O}_4$ sensing element towards the detection of 1660 ppm of (a) H_2 and (b) CO gases at their respective optimized operating temperatures

We have measured the *temperature dependence* of the response of $\text{Mg}_{1-x}\text{Zn}_x\text{Fe}_2\text{O}_4$ ($0.0 \leq x \leq 1.0$) sensing elements used to detect H_2 and CO gases. The test gas concentration is kept ~ 1660 ppm. For all these sensors, resistance transients are measured in the operating temperature range between 250 – 380 $^{\circ}\text{C}$ and the corresponding response in each case is estimated. The results are presented in Fig. 3.7 in the form of histograms for (a) H_2 and (b) CO gas sensing. As shown in the figure, irrespective of the operating temperatures, all these ferrite compositions exhibit reasonable good response towards H_2 and CO gas sensing. However, they have better response towards H_2 gas sensing. Also for all these compositions, response is increased up to a specific operating temperature and beyond this temperature (termed as optimized operating temperature, T_{opt}) response is found to decreased. In other words, for each of this gas, T_{opt} is dependent on the ferrite compositions. As for example, for $\text{Mg}_{0.5}\text{Zn}_{0.5}\text{Fe}_2\text{O}_4$ sensing H_2 and CO gases, T_{opt} is estimated to be ~ 380 $^{\circ}\text{C}$ and 300 $^{\circ}\text{C}$ respectively. Similar behavior (existence of optimized operating temperatures corresponding to the maximum response towards a specific gas) has also been reported for a variety of SMO sensors [21-22]. The following physical mechanisms are invoked to explain the observed behavior.

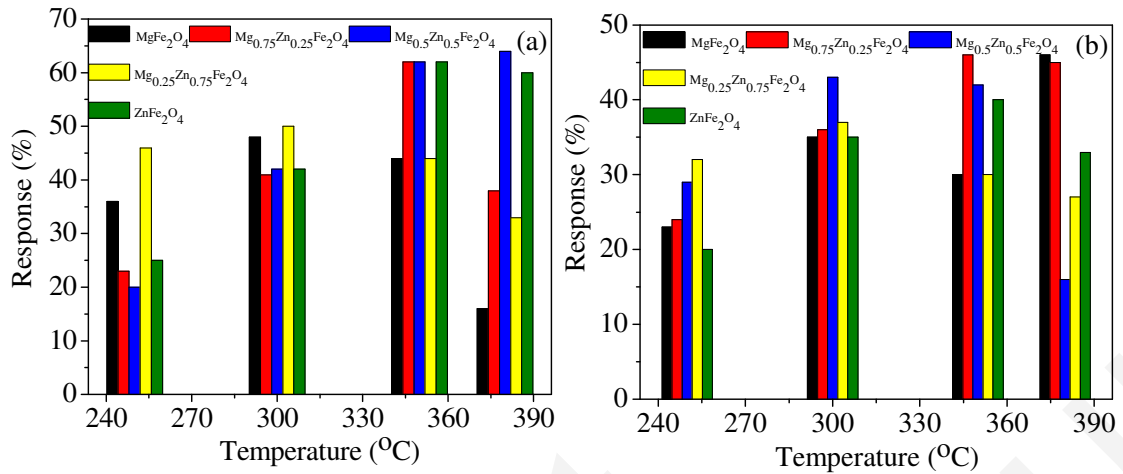


Fig. 3.7: Operating temperature dependence of response (%) for $\text{Mg}_{1-x}\text{Zn}_x\text{Fe}_2\text{O}_4$ ($0.0 \leq x \leq 1.0$) sensing elements towards the detection of 1660 ppm of (a) H_2 and (b) CO gases

With the increase of surface temperature chemisorptions of oxygen species is increased which eventually leads to increased response with temperature. The reduction of response at higher temperature is explained to be due to the increased desorption rates of oxygen at the sensor surface. The behavior can also be explained using the depletion layer width (L_D) concept. For the semiconducting material the charge carrier concentration (n_0) (and therefore the conductance) increases with the increase in temperature. The depletion layer width (L_D), carrier concentration (n_0) and response (S) is related according the following relations [23]

$$L_D = (\epsilon_0 kT / n_0 e^2)^{1/2} \quad (3.3)$$

$$S = (\Delta n / n_0) \times L_D \quad (3.4)$$

where ϵ_0 is the static dielectric constant, n_0 is the total carrier concentration, e is the carrier charge, k is the Boltzmann constant, T is the absolute temperature, and Δn is the change in the carrier concentration. From these equations it is apparent that till T_{opt} , S increases as $\Delta n/n_0$ is increased. Beyond T_{opt} , the response is reduced due to the decrease in depletion layer width due to significant increase of total carrier concentration.

We have measured the *concentration dependence* of the response of $\text{Mg}_{1-x}\text{Zn}_x\text{Fe}_2\text{O}_4$ ($0.0 \leq x \leq 1.0$) sensing elements for H_2 gas sensing. The resistance transients for hydrogen gas sensing in the concentration range between 100-1660 ppm are shown in Fig. 3.8(a)-(e). The optimized sensor operating temperature (T_{opt}) and the estimated response percent for each gas concentration is marked in the respective figure.

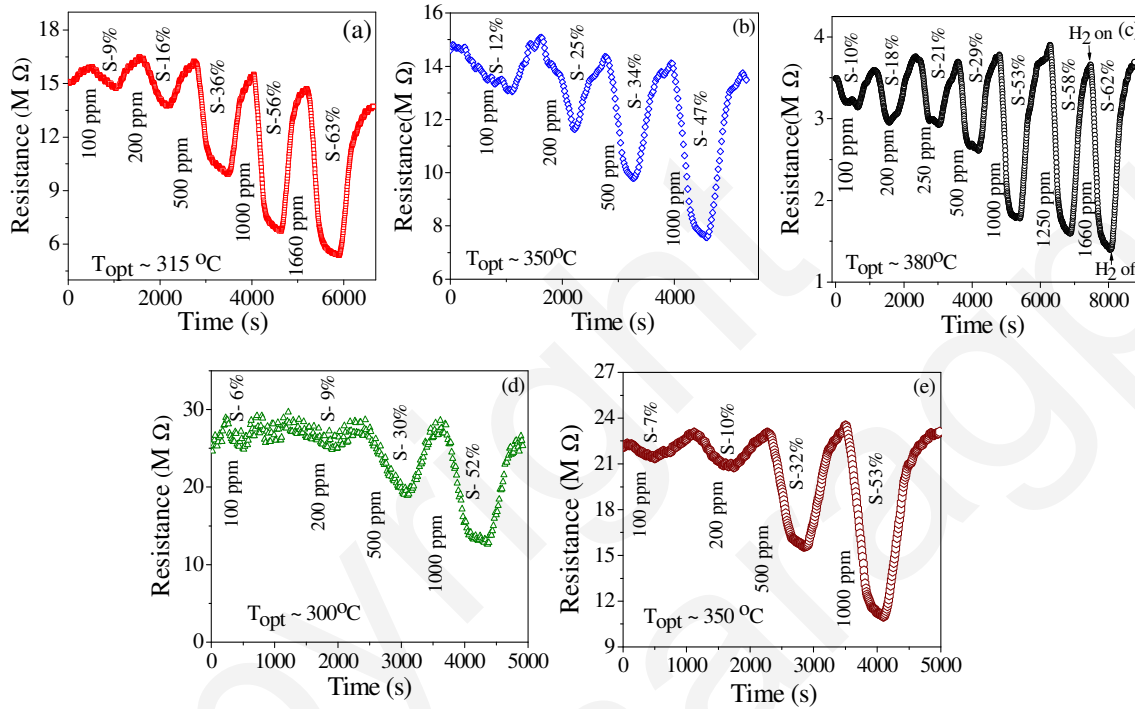


Fig. 3.8: Resistance transients recorded for (a) MgFe_2O_4 (b) $\text{Mg}_{0.75}\text{Zn}_{0.25}\text{Fe}_2\text{O}_4$ (c) $\text{Mg}_{0.5}\text{Zn}_{0.5}\text{Fe}_2\text{O}_4$ (d) $\text{Mg}_{0.25}\text{Zn}_{0.75}\text{Fe}_2\text{O}_4$ (e) ZnFe_2O_4 sensing elements towards the detection of various concentration of H_2 gas at their respective optimized operating temperature. The H_2 gas concentration and the respective response (%) are mentioned in the figures

It is interesting to note that these sensing elements are sensitive to low hydrogen concentration and the response percentage is increased with the increase in gas concentration. Among all these compositions, $\text{Mg}_{0.5}\text{Zn}_{0.5}\text{Fe}_2\text{O}_4$ exhibits superior sensing performance with marginal base line drift (see Fig. 3.8(c)). For 100 ppm hydrogen gas sensing, the response characteristics of all these ferrite compositions are compared in Fig. 3.9. The response (%) is estimated from the respective resistance transients for 100 ppm hydrogen sensing at respective optimized temperature. Note, that for each composition, response percent up to 5 minutes are compared. Clearly $\text{Mg}_{0.5}\text{Zn}_{0.5}\text{Fe}_2\text{O}_4$ sensor exhibits superior response as compared to other ferrite compositions.

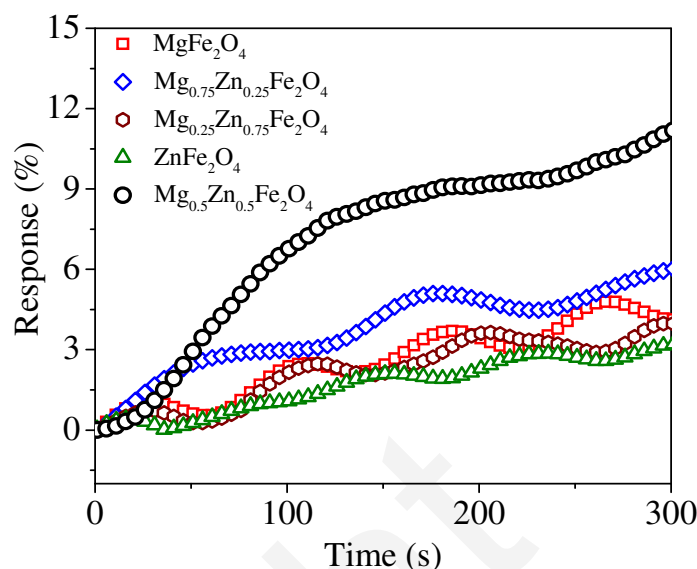


Fig. 3.9: Response (%) transient for $\text{Mg}_{1-x}\text{Zn}_x\text{Fe}_2\text{O}_4$ ($0.0 \leq x \leq 1.0$) sensing elements in presence of 100 ppm of H_2 measured for finite time (5 min) at their respective optimized operating temperature

In the present section, in order to yield improved gas sensing performance towards combustible gas sensing; nano-particles of $\text{Mg}_{1-x}\text{Zn}_x\text{Fe}_2\text{O}_4$ ($0.0 \leq x \leq 1.0$) have been synthesized using a PVA assisted wet chemical synthesis route. As described in this section, the synthesized materials are characterized in terms of their phase formation behavior, specific surface area and pore-size distribution of the synthesized particles, surface morphology of the sensing elements and combustible gas sensing characteristics. Through these integrated characterization scheme, we aim to understand the correlation among the structure of the gas sensing materials (at different length scale) and their gas sensing characteristics. As outlined in Chapter-2 (Sec. 2.3) we have highlighted the importance of nano-structured oxides to yield improved gas sensing properties. As combustible gas sensors, ferrite sensing elements have less studied as compared to conventional binary oxide based sensors (eg. SnO_2 , WO_3 , ZnO etc). As an effective alternative to these conventional sensing materials, ferrites should be cost effective, and exhibit superior response with faster response and recovery times. Additionally, these materials should be attractive for selective gas sensing and offer marginal base line drift during repeated response and recovery cycles. As mentioned earlier, the gas sensing characteristics are dependent on the material structure at different length scale; however,

limited attempts are made to delineate the structure property correlation. As presented earlier, it is difficult to synthesize phase pure $\text{Mg}_{1-x}\text{Zn}_x\text{Fe}_2\text{O}_4$ ($0.0 \leq x \leq 1.0$) solid solution, and a narrow (calcination) time-temperature window exists to yield phase pure ferrite. Only $\text{Mg}_{0.5}\text{Zn}_{0.5}\text{Fe}_2\text{O}_4$ particles are synthesized phase pure and for other ferrite compositions, impurity phase such as MgO , Fe_2O_3 are found to be phase separated. Some of these impurity phases themselves (e.g. Fe_2O_3) could sense reducing gas; however, in general they will increase the base resistance. Therefore, phase pure ferrite particles are required for gas sensing applications. The gas sensing characteristics are also influenced by the size of the primary particles and also the nature of pores (macro and meso) in the sensing elements. Viewing in this light we felt it reasonable to adopt alternate processing route to synthesize these sensing materials in phase pure form. For PVA assisted synthesis, a post annealing treatment is adopted to crystallize the desired cubic spinel phase. The post annealing is found to increase the crystallite size (see Table-3.1). To avoid the post annealing (that increases the particle size) ferrite materials need to be synthesized in ambient condition. Therefore to yield phase pure nano-crystalline cubic spinel ferrite under ambient condition, we have adopted a modified Pechini route. Since among all the ferrite compositions $\text{Mg}_{0.5}\text{Zn}_{0.5}\text{Fe}_2\text{O}_4$ yield better gas sensing characteristics, we have limited the particle synthesis only to this specific composition. In the following section, we have described the phase formation behavior, surface morphology and gas sensing characteristics of $\text{Mg}_{0.5}\text{Zn}_{0.5}\text{Fe}_2\text{O}_4$ particles synthesized using a modified Pechini route.

3.4. Phase Formation Behavior, Surface Morphology and Gas Sensing Characteristics of $\text{Mg}_{0.5}\text{Zn}_{0.5}\text{Fe}_2\text{O}_4$ Nano-particles Prepared Using Modified Pechini route

We have utilized a modified Pechini based chemical synthesis route to obtain phase pure $\text{Mg}_{0.5}\text{Zn}_{0.5}\text{Fe}_2\text{O}_4$ particles. Nitrate salts of magnesium, zinc, and iron are used as precursor. Citrate acid is used as chelating agent for the metal cations. Ethylene glycol is used for esterification to form a polymer resin. In this polymer resin magnesium, zinc and iron cations are distributed uniformly in stoichiometric proportions. When the resin is

continuously heated (~ 120 - 140 $^{\circ}\text{C}$) then an auto-combustion reaction is initiated and nano-crystalline $\text{Mg}_{0.5}\text{Zn}_{0.5}\text{Fe}_2\text{O}_4$ particles are obtained in very short time. The thermal and IR characteristics of the polymer resin are described in the following section. This is followed by the description of the phase formation behavior and pore-size distribution of the synthesized powder and microstructure of the sensing elements. Finally, the gas sensing characteristics of auto-combustion synthesized $\text{Mg}_{0.5}\text{Zn}_{0.5}\text{Fe}_2\text{O}_4$ particles are compared with $\text{Mg}_{0.5}\text{Zn}_{0.5}\text{Fe}_2\text{O}_4$ powder prepared by PVA assisted chemical synthesis route.

3.4.1. Thermal and FTIR Analyses

Figure 3.10(a) shows the combined DTA-TGA plots of the precursor gel prepared by the Pechini route (prior to the auto-combustion reaction to synthesize $\text{Mg}_{0.5}\text{Zn}_{0.5}\text{Fe}_2\text{O}_4$ particles). The FTIR spectra of the as prepared and $\text{Mg}_{0.5}\text{Zn}_{0.5}\text{Fe}_2\text{O}_4$ particles calcined at 300 $^{\circ}\text{C}$ and 600 $^{\circ}\text{C}$ are shown in Fig. 3.10(b). Two distinct exothermic peaks of the DTA plot (Fig. 3.10(a)) are attributed to the loss of water as well as organic species with comparatively lower boiling points (~ 180 $^{\circ}\text{C}$), and decomposition of the citrate complexes (~ 420 $^{\circ}\text{C}$). As shown in the TGA plot the sharp and subsequent gradual weight loss up to ~ 450 $^{\circ}\text{C}$ are related to the burnout of water and various organics and nitrate species.

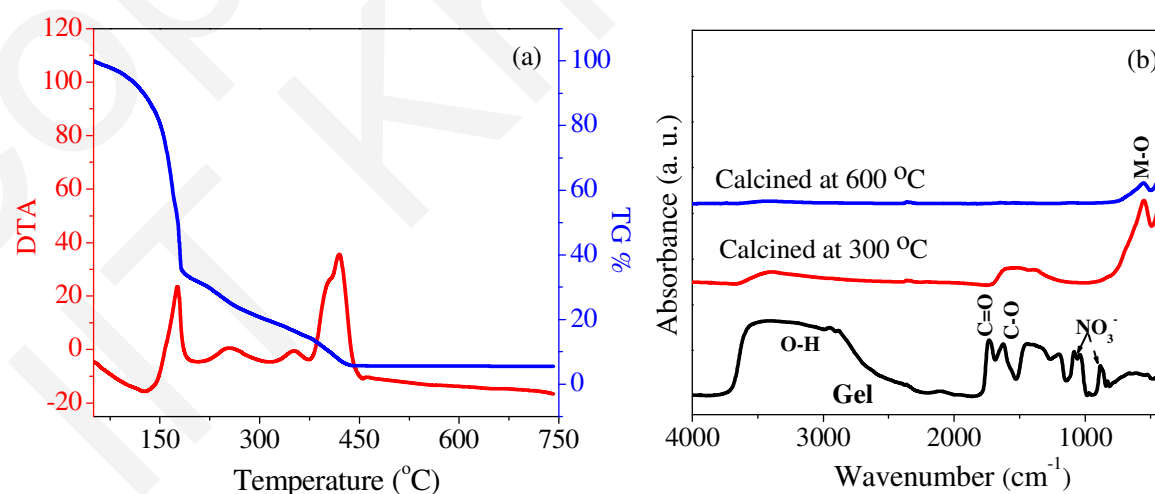


Fig. 3.10: (a) DTA-TGA plot of the $\text{Mg}_{0.5}\text{Zn}_{0.5}\text{Fe}_2\text{O}_4$ gel prepared using modified Pechini route (b) FTIR spectra of $\text{Mg}_{0.5}\text{Zn}_{0.5}\text{Fe}_2\text{O}_4$ gel (prepared using modified Pechini route) and calcined powders

No weight loss is detected beyond 450 °C. As shown in Fig. 3.10(b), the characteristic IR absorption peaks of the as prepared $\text{Mg}_{0.5}\text{Zn}_{0.5}\text{Fe}_2\text{O}_4$ gel at about 850 and 1350 cm^{-1} are assigned for NO_3^- , 3200-3400 cm^{-1} for OH^- , and 1550-1750 cm^{-1} for COO^- species. These peaks disappear when the gel is calcined at elevated temperature (~ 300 °C) and a peak (~ 552 cm^{-1}) which corresponds to the M-O bond emerges. The appearance of this peak is supportive to the formation of spinel phase at a temperature as low as 300 °C [24].

3.4.2. Phase Formation Behavior

Figure 3.11 shows the X-ray diffractograms of the as prepared and calcined (at 300 °C and 600 °C for 2 h in air) $\text{Mg}_{0.5}\text{Zn}_{0.5}\text{Fe}_2\text{O}_4$ powders prepared using auto-combustion route. As shown in the figure, most of the characteristics diffraction peaks are present in the as prepared powder. The crystallinity improves with the increase in calcination temperature. All these powders crystallize in cubic spinel structure without the formation of any other impurity phase(s). Rietveld refinement is performed for the powders calcined at elevated temperatures and the refined plots are also shown in Fig. 3.11. Table-3.2 compares the crystallite size and lattice parameters of $\text{Mg}_{0.5}\text{Zn}_{0.5}\text{Fe}_2\text{O}_4$ powders prepared using PVA assisted (MZFO-P) and auto-combustion (MZFO-C) synthesis routes. Inspecting Table-3.2 it is apparent that irrespective of the calcination temperature, powders prepared by auto-combustion route is phase pure, have smaller crystallite size with slightly reduced lattice parameters.

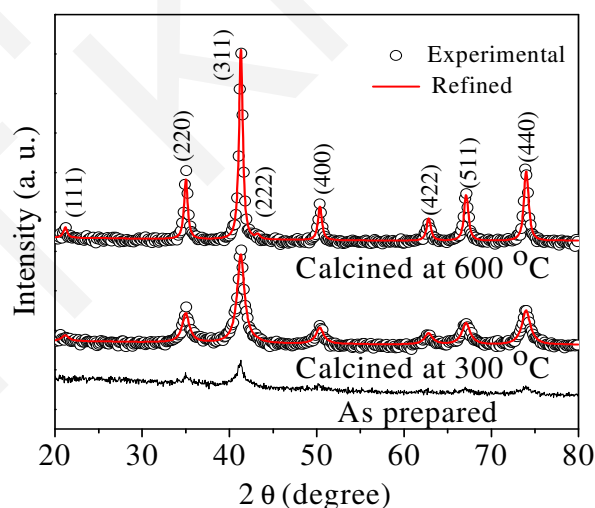


Fig. 3.11: X-ray diffractograms of the as prepared and calcined (at 300 °C and 600 °C for 2 h in air) $\text{Mg}_{0.5}\text{Zn}_{0.5}\text{Fe}_2\text{O}_4$ powders. The Rietveld refinement of the X-ray pattern (for calcined powders) are shown as solid line in the figure

Table-3.2: Comparison of phase purity, crystallite size and lattice parameters of $\text{Mg}_{0.5}\text{Zn}_{0.5}\text{Fe}_2\text{O}_4$ powders prepared using PVA assisted (MZFO-P) and auto-combustion (MZFO-C) synthesis routes

Sensor material	Phase (%)		Crystallite size (nm)		Lattice parameter (Å)	
	(Spinel: impurity phase)					
$\text{Mg}_{0.5}\text{Zn}_{0.5}\text{Fe}_2\text{O}_4$	300 °C	600 °C	300 °C	600 °C	300 °C	600 °C
PVA assisted synthesized (MZFO-P)	100: 0	62: 38	11	21	8.418	8.426
Pechini route synthesized (MZFO-C)	100: 0	100:0	7	16	8.390	8.40

3.4.3. Surface Morphology

Figure 3.12 shows (a) the TEM micrographs MZFO-C particles calcined at 400 °C, and (b) the FESEM micrograph of the sensor surface sintered at 600 °C for 2 h in air. As envisaged from the TEM micrographs, the particle size of MZFO-C particles are in the range of 10-15 nm. Similar morphology is also observed in powders calcined at 300 °C and as shown in Fig. 3.12(a) the calcined powders form soft agglomerate. The calcined powders are lightly pressed in the form of circular pellets and sintered at 600 °C for 2 h to form the sensing elements for gas sensing characterization. As shown in Fig. 3.12(b), marginal grain growth could not be avoided and the sensing surface has typical mesoporous surface morphology. The characteristic pore-size and pore-size distribution of the calcined powders are described in the next section.

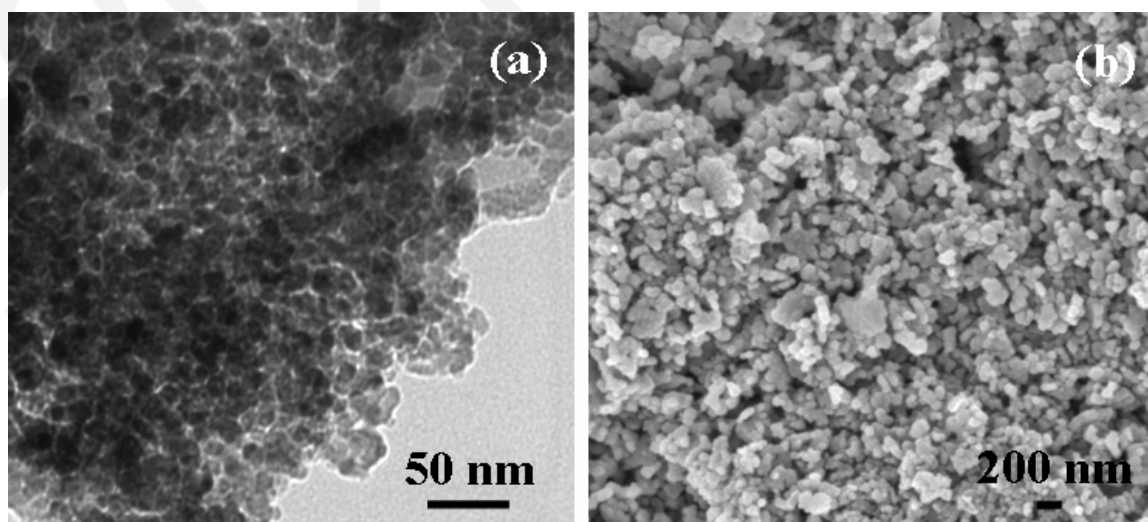


Fig. 3.12: (a) TEM image of the MZFO-C powder calcined at 400 °C for 2 h in air (b) FESEM image of the MZFO-C sensor sintered at 600 °C for 2 h in air

3.4.4. Pore-size and Pore-size Distribution

The nitrogen adsorption-desorption isotherm of MZFO-C particles (calcined at 600 °C for 2 h in air) is shown in Fig. 3.13. The isotherm is type-IV type exhibiting a typical H3 type hysteresis. The characteristic adsorption-desorption patterns supports the mesoporous nature of the synthesized particles. The estimated pore-size distribution is shown in the inset of Fig. 3.13. These particles have a bimodal distribution of meso-pores in the size range of 2-12 nm (narrower) and 12-45 nm (broader). The surface area of MZFO-C particles, calcined at 600 °C, is estimated to be $\sim 42 \text{ m}^2 \text{ g}^{-1}$.

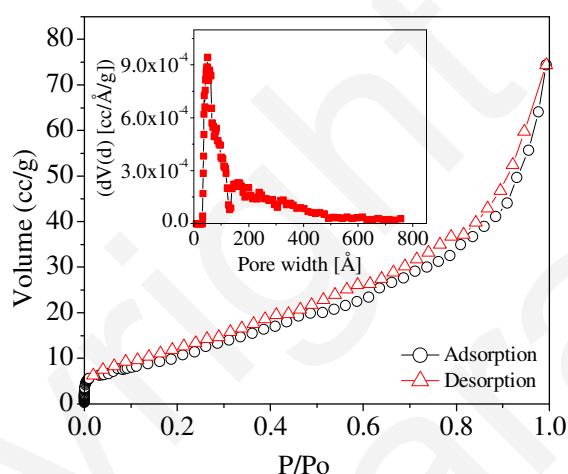


Fig. 3.13: Nitrogen adsorption-desorption isotherm for MZFO-C powder calcined at 600 °C for 2 h in air

In the preceding sections we have compared the phase formation behavior, structure/micro-structure, and nature of pores and pore-size distribution of MZFO powders prepared by PVA assisted (MZFO-P) and auto-combustion (MZFO-C) synthesis routes. It is demonstrated that auto-combustion prepared powders (MZFO-C) are phase pure with smaller crystallite as well as particle size, larger specific surface area, and meso-porous surface morphologies. All these characteristics are conducive to yield better gas sensing characteristics. In the following section we have described the gas sensing characteristics of MZFO-C powders and compared it with the sensing characteristics of MZFO-P particles wherever felt appropriate.

3.4.5. Comparison between the Gas Sensing Characteristics of $\text{Mg}_{0.5}\text{Zn}_{0.5}\text{Fe}_2\text{O}_4$ Nano-particles Synthesized Using PVA Assisted and Modified Pechini Based Chemical Routes

The sensing characteristics of the MZFO-C particles are investigated using hydrogen, carbon monoxide, methane and nitrous oxide as test gases. The response of the MZFO-C sensor is evaluated as a function of operating temperature and test gas concentration. Figure 3.14 compares the response (%) of (a) MZFO-C and (b) MZFO-P sensors at different operating temperatures in the range of 250-380 °C. The test gas concentration is kept fixed ~1660 ppm. Comparing Fig. 3.14(a) and (b), it is clear that irrespective of the operating temperature, for all these four test gases, MZFO-C sensors yield larger response as compared to MZFO-P sensing elements. Both these sensing elements show better response towards H_2 gas sensing, however, they have fairly good response towards other gases as well. The better response towards the detection of H_2 gas (as compared to CO, CH_4 , and N_2O) can be explained by considering the diffusion of gases through the meso-pores of the sensing element. The gas diffusion through the meso-porous sensor is controlled by Knudsen diffusion.

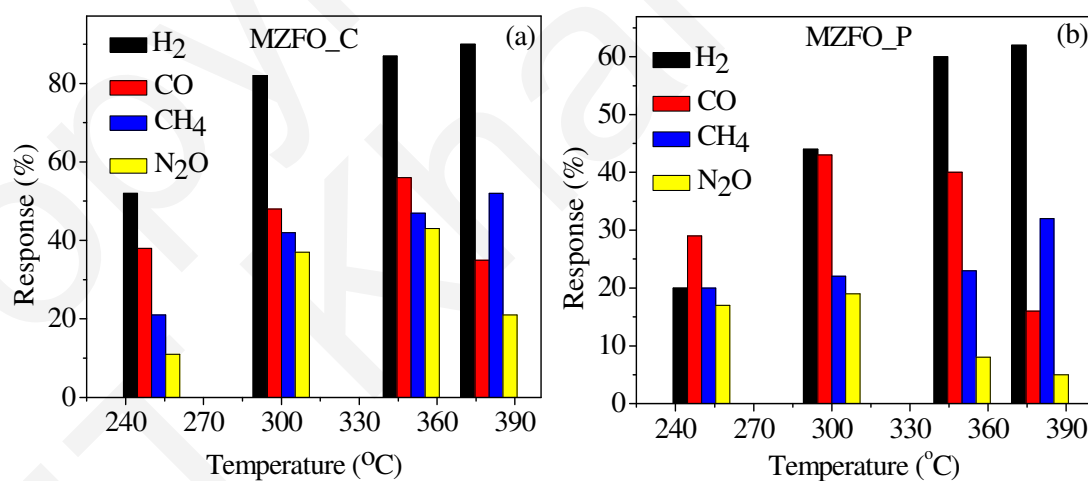


Fig. 3.14: Operating temperature dependence of H_2 (~ 1660 ppm) sensing response for (a) MZFO-C and (b) MZFO-P sensing elements

The Knudsen diffusion constant follows the following relation with the molecular weight of the respective test gas [25].

$$D_K = 4r/3\sqrt{(2RT/\pi M)} \quad (3.5)$$

where D_K is the Knudsen diffusion constant, T is the absolute temperature, R is the universal gas constant and M is the molecular weight of the gas. Having the lowest molecular weight, hydrogen gas has the largest diffusion constant among all the test gases. Faster diffusion of hydrogen in turn yields maximum response among all the test gases. Reviewing Fig. 3.14(a), the maximum response for hydrogen sensing is achieved at an operating temperature $\sim 380^\circ\text{C}$. For a wide range of hydrogen gas concentration

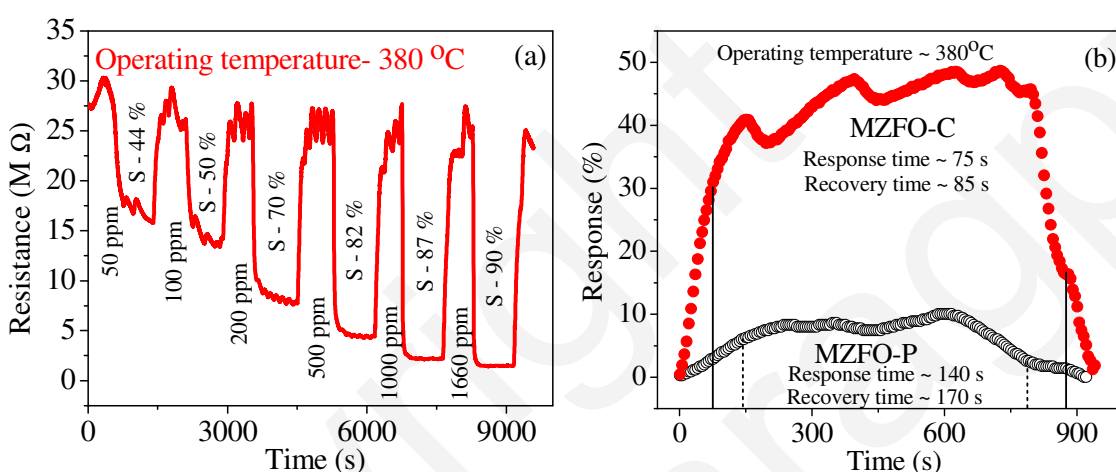


Fig. 3.15: (a) Resistance transients of MZFO-C sensing element in presence of various H_2 gas concentrations (50-1660 ppm) measured at 380°C . (b) Comparison between the response characteristics of MZFO-C and MZFO-P nano-particulate sensing elements towards 100 ppm H_2 gas sensing

(50-1660 ppm), Fig. 3.15(a) shows the resistance transients of MZFO-C sensing element measured at 380°C . The estimated response at each test gas concentration is marked in the figure. It is remarkable to note that MZFO-C nano-particulate sensing element exhibit excellent response ($S \sim 44\%$) even for very low concentration (~ 50 ppm) of test gas. Additionally, these sensor exhibits marginal resistance drift up on repeated response and recovery cycles. The response characteristics of MZFO-C and MZFO-P nano-particulate sensing elements towards 100 ppm hydrogen gas sensing are compared in Fig. 3.15(b). As shown in the figure, for MZFO-C particulate sensing elements, the response is markedly improved. The response and recovery times (time required for 63% change in resistance during the response or recovery) are also improved. Figure 3.16 compares the response characteristics of MZFO-C and MZFO-P nano-particulate sensors for hydrogen

and carbon monoxide gas sensing in a wide range of test gas concentrations. It is remarkable to note that for all these test gas concentrations, MZFO-C sensors exhibit superior response for combustible gas sensing.

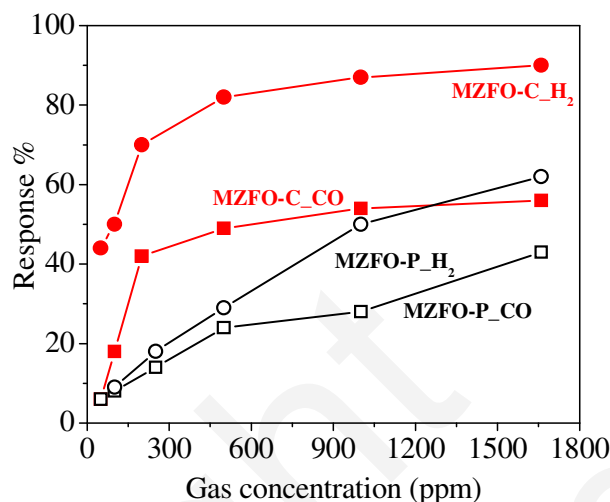


Fig. 3.16: Comparison between the response (%) of MZFO-C and MZFO-P nano-particulate sensors for the detection of various concentrations (50-1660 ppm) of H₂ and CO gases at operating temperature ~ 380 °C

For MZFO-C sensing elements, Fig. 3.17 shows the reproducibility for (a) hydrogen and (b) carbon monoxide gas sensing at ~350 °C. For both the cases the test gas concentration is kept fixed at 500 ppm. As shown in the figure, the response and recovery characteristics are repeatable and marginal base line drift is achieved upon repeated response and recovery cycles. We have repeated similar response and recovery cycles in a time interval of 1, 10, and 100 days. We have found that the response and recovery cycles are reproducible and these results demonstrate reasonably good stability of these sensing elements over extended period of time.

Table-3.3 summarizes the combustible gas sensing characteristics of all the cubic spinel ferrites synthesized using PVA assisted and auto-combustible modified Pechini based wet chemical synthesis routes. The test gas concentration is fixed to 1000 ppm and the gas sensing characteristics are measured at the respective optimized operating temperatures. As envisaged in the table, among all the synthesized sensing materials, MZFO-C sensing elements exhibit superior combustible gas sensing characteristics characterized by superior response and quick response and recovery times. However, the

optimized operating temperatures remain quite high and for these sensors the cross-selectivity could not be avoided.

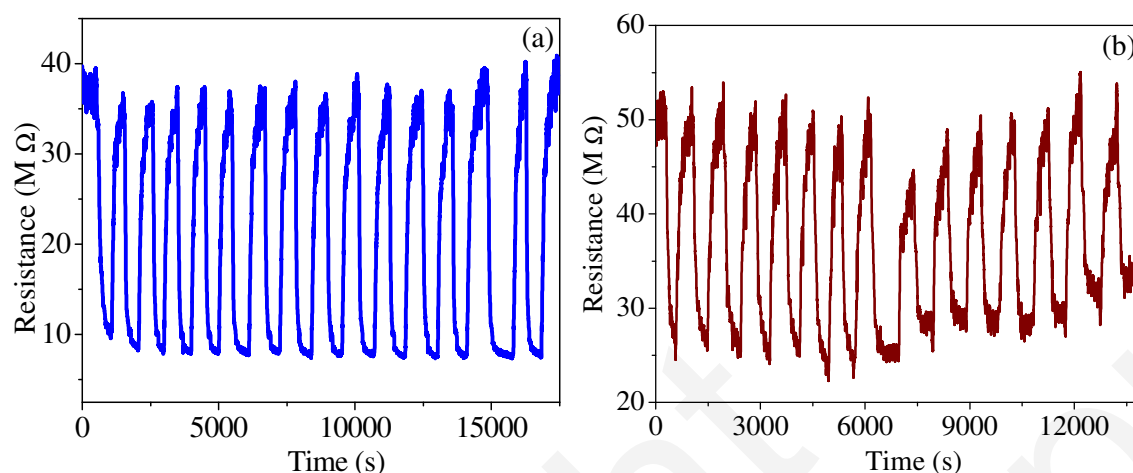


Fig. 3.17: Reproducibility of the gas sensing performance of MZFO-C sensors towards the detection of 500 ppm (a) H_2 and (b) CO gases at an operating temperature $\sim 350^\circ C$

Table-3.3: Comparison between the H_2 and CO sensing characteristics of $Mg_{1-x}Zn_xFe_2O_4$ ($0.0 \leq x \leq 1.0$) nano-particulate sensing elements

Composition (Synthesis route)	Sensor characteristics (measured at 1000 ppm gas concentration)							
	Response ($\Delta R/R_a$) %		T_{opt} ($^\circ C$)		Response time (s)		Recovery time (s)	
	H_2	CO	H_2	CO	H_2	CO	H_2	CO
$MgFe_2O_4$ (PVA assisted Wet chemical synthesis)	~56	~29	315	300	~170	~150	~190	~170
$Mg_{0.75}Zn_{0.25}Fe_2O_4$ (PVA assisted Wet chemical synthesis)	~47	~23	350	350	~250	~220	~265	~230
$Mg_{0.25}Zn_{0.75}Fe_2O_4$ (PVA assisted Wet chemical synthesis)	~52	~27	300	300	~240	~230	~250	~240
$ZnFe_2O_4$ (PVA assisted Wet chemical synthesis)	~53	~40	350	350	~230	~180	~250	~190
$Mg_{0.5}Zn_{0.5}Fe_2O_4$ (PVA assisted Wet chemical synthesis)	~53	~29	380	300	~165	~200	~200	~240
$Mg_{0.5}Zn_{0.5}Fe_2O_4$ (Citrate assisted Pechini route)	~87	~55	380	300	~30	~50	~40	~55

The superior gas sensing characteristics of Pechini derived particles can be traced down to the phase purity of the synthesized powders, smaller crystallite as well as particle size and uniform meso-porous surface morphology of the sensing elements. It is challenging to synthesize spinel ferrite particles at lower calcination temperature. Most ferrite powders are prepared by heat treatment of mixed oxides, hydroxides or carbonates at temperatures in the range of 600-1100 °C [26-27]. The kinetics of the solid-solid interactions during the formation of cubic spinel ferrites is a complex phenomenon and several models are developed in the literature to address this issue [28-29]. As revealed from these studies, first a thin film of MFe_2O_4 (M is the divalent metal cation of the ferrite composition) ferrite forms (at relatively lower temperature) and it covers the surfaces of reacting Fe_2O_3 grains. Formation of this film hinders the diffusion of divalent cations and eventually retards the formation of the ferrite phase. Higher calcination temperature is therefore necessary to expedite the diffusion of these divalent cations to form the desired ferrite phase without any impurity oxide phase/(s). Alternatively cation (viz. Li^{1+} , Zn^{2+} , Al^{3+} etc) doping is found to be beneficial to enhance the mobility of the constituent cation/(s) of the ferrite composition to form phase pure ferrites at relatively lower calcination temperature [30-31]. To be used as gas sensing materials, the phase pure cubic spinel must be synthesized at lower temperatures for two reasons: first, if formed at higher calcination temperature, substantial crystallite/particle growth may not be avoided. It is known that the response characteristics are markedly improved if the particle size is in the order of twice of the depletion layer width. Particle growth with calcination temperature would destroy this size effect. Second, low temperature synthesis would ensure the meso-porous particle morphology which is conducive to yield better response.

As described earlier, we have adopted a PVA assisted route to synthesize magnesium zinc ferrite particles for gas sensing application. It is known that in aqueous PVA solutions, many metals can be stabilized at the polymer surface via interaction with the hydroxyl group. Figure 3.18 shows the schematic of such metal ion stabilization through hydroxyl and chelated acetate groups. During drying, water evaporates and polymer chain come closer to each other and the viscosity of the solution is increased.

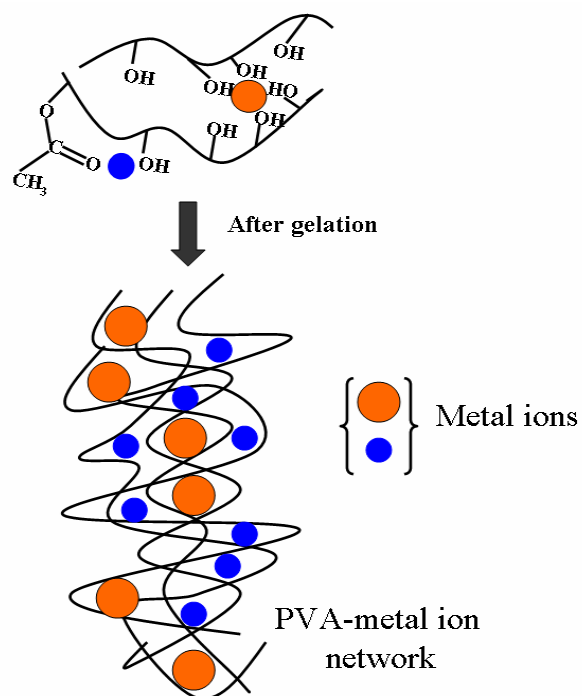


Fig. 3.18: Schematic diagram for the formation of PVA-metal ion network during the formation of gel in PVA assisted wet chemical synthesis process

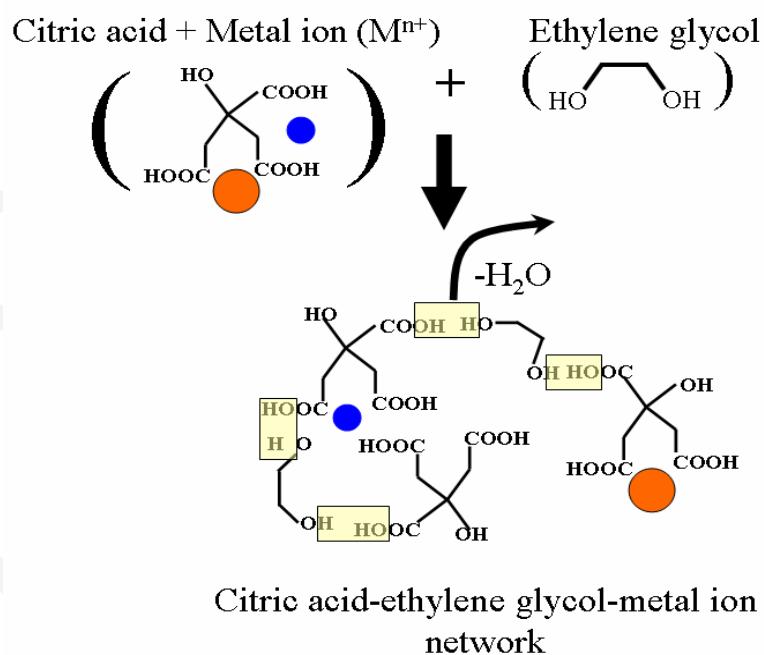


Fig. 3.19: Schematic diagram for the formation of citric acid-ethylene glycol-metal ion network during the formation of gel in the modified Pechini route

As shown schematically in Fig. 3.18, in dried gel, the free space between the polymer molecules shrink and chain entanglement causes a close polymer. At this stage, the mobility of the cation is greatly reduced and metal cations are distributed in stoichiometric ratio in the polymer-network. Up on calcining the polymer gel, phase pure spinel formation (without any impurity oxide phase precipitation) is expected. However, as reported earlier, PVA assisted synthesis could not yield phase pure $\text{Mg}_{0.5}\text{Zn}_{0.5}\text{Fe}_2\text{O}_4$ particles and MgO and Fe_2O_3 are phase separated during calcination.

Phase pure $\text{Mg}_{0.5}\text{Zn}_{0.5}\text{Fe}_2\text{O}_4$ particles could be synthesized using an auto-combustion synthesis route. In this modified Pechini based synthesis route, citric acid is used to chelate the metal cations. Polyethylene glycol is added into the chelated solution to initiate a poly-esterification reaction. The poly-esterification reaction result a polymerized resins that has the metal cations distributed uniformly is stoichiletric proportions. Figure 3.19 shows schematically the poly-esterification reaction when ethylene glycol is added to the citric acid chelated metal nitrate solution. The viscous gel upon poly-esterification is further heated to initiate auto-combustion reaction. During this auto-combustion citrate and nitrate act as fuel and oxidant respectively. As described earlier, the powder obtained by auto-combustion reaction has the highest degree of phase purity, narrower particle size distribution and larger specific surface area. Additionally, particle synthesized by auto-combustion route is found to yield nano-crystalline particles with meso-porous surface morphology. All these features contribute to yield better gas sensing performance of the $\text{Mg}_{0.5}\text{Zn}_{0.5}\text{Fe}_2\text{O}_4$ sensing elements prepared by auto-combustion synthesis route.

The precursor solution prepared by modified Pechini route is utilized to synthesize a variety of nano-structured $\text{Mg}_{0.5}\text{Zn}_{0.5}\text{Fe}_2\text{O}_4$ sensing elements. The work is described in the following sections.

3.5. Structural, Micro-structural and Gas Sensing Characteristics of $\text{Mg}_{0.5}\text{Zn}_{0.5}\text{Fe}_2\text{O}_4$ Nano-tubes

3.5.1. Phase Formation Behavior

The synthesis of embedded and isolated $\text{Mg}_{0.5}\text{Zn}_{0.5}\text{Fe}_2\text{O}_4$ nano-tubes has already been described in Chapter-2 (Sec. 2.3.2). Figure 3.20 shows the X-ray diffractograms of bare alumina template, and embedded $\text{Mg}_{0.5}\text{Zn}_{0.5}\text{Fe}_2\text{O}_4$ nano-tubes (inside the pores of anodized alumina template). As shown in the figure, the alumina template is amorphous, and the nano-tubes crystallize into phase pure cubic spinel structure.

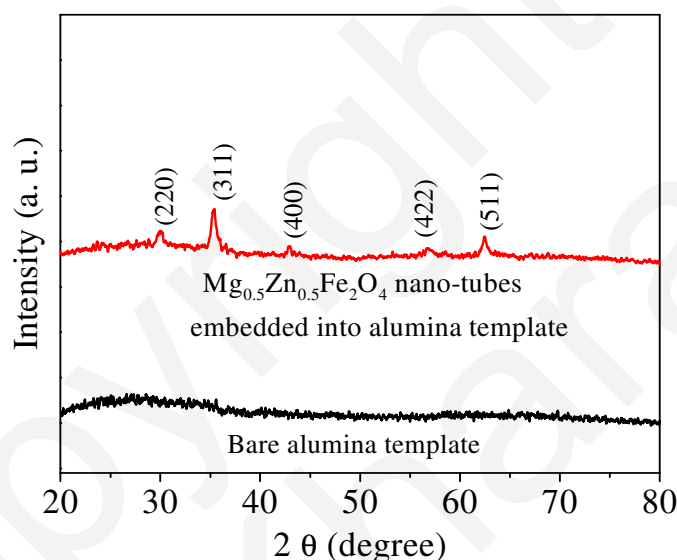


Fig. 3.20: X-ray diffractograms of bare alumina template and $\text{Mg}_{0.5}\text{Zn}_{0.5}\text{Fe}_2\text{O}_4$ nano-tubes embedded into alumina template

3.5.2. Surface Morphology

As described in details in Chapter-2, the $\text{Mg}_{0.5}\text{Zn}_{0.5}\text{Fe}_2\text{O}_4$ nano-tubes are dispersed into ethanol solvent after etching the alumina template and the suspended tubes are coated directly into fused quartz substrates. Figure 3.21(a)-(c) show the FESEM micrographs of these isolated nano-tubes at three different magnifications. As shown in Fig. 3.21(a) and (b), these tubes are entangled to each other and this would definitely help better transduction during gas sensing measurements. Also, as envisaged in the magnified image (Fig. 3.21(c)), the nano-tube is hollow and constitutes of innumerable tiny

crystallites. The EDS spectra of the nano-tube are presented in Fig. 3.21(d). Note, only the constituent elements (viz. Mg, Zn, Fe) of $\text{Mg}_{0.5}\text{Zn}_{0.5}\text{Fe}_2\text{O}_4$ are detected in the EDS spectra. It confirms that Al ion has not diffused into these nano-tubes during the repeated calcination and sintering steps.

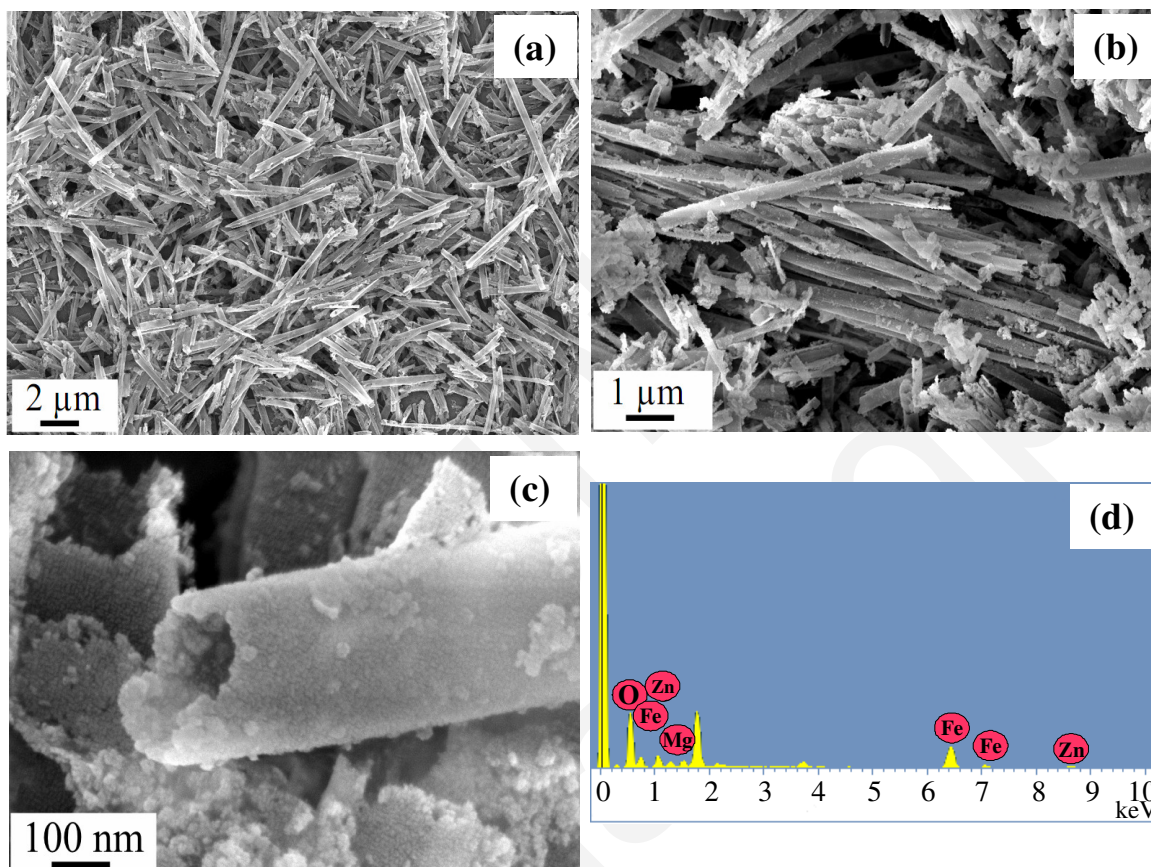


Fig. 3.21: FESEM image of the isolated $\text{Mg}_{0.5}\text{Zn}_{0.5}\text{Fe}_2\text{O}_4$ nano-tubes (coated on quartz substrates) at (a) low and (b) high magnifications. (c) Hollow nature of a single $\text{Mg}_{0.5}\text{Zn}_{0.5}\text{Fe}_2\text{O}_4$ nano-tube (d) EDS pattern of the $\text{Mg}_{0.5}\text{Zn}_{0.5}\text{Fe}_2\text{O}_4$ nano-tubes

The morphology of these isolated nano-tubes is further investigated using transmission electron microscopy (TEM) and recording its selected area electron diffraction (SAED) patterns. Figure 3.22(a) shows a bunch of nano-tubes. The magnified image of a single nano-tube is shown separately in Fig. 3.22 (b). The hollow nature of these nano-tubes is confirmed in Fig. 3.22(b). As shown in the enlarged micrograph, each single tube consists of several tiny particles. The SAED pattern (Fig. 3.22(c)) confirms the polycrystalline nature of these nano-tubes. Indexing this "ring-pattern" it is confirmed that these tubes are crystallized into cubic spinel structure.

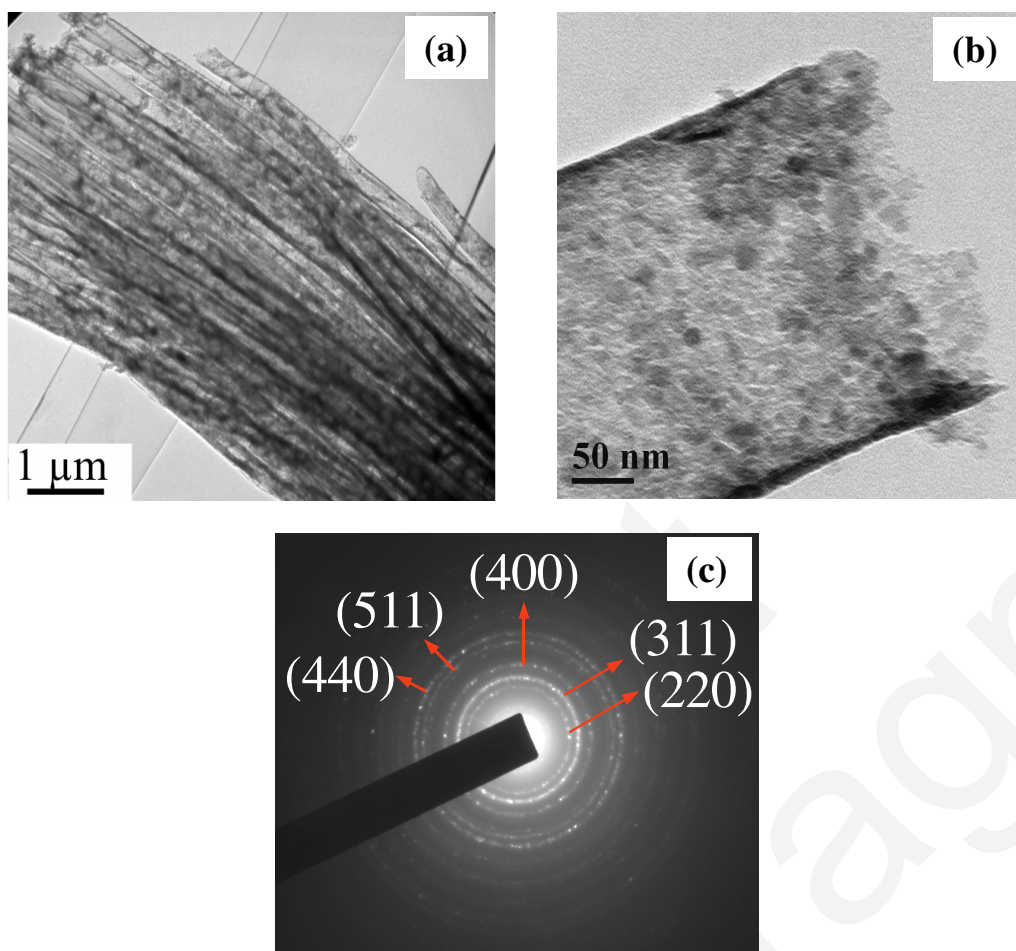


Fig. 3.22: TEM image of (a) bunch of $\text{Mg}_{0.5}\text{Zn}_{0.5}\text{Fe}_2\text{O}_4$ nano-tubes (b) single $\text{Mg}_{0.5}\text{Zn}_{0.5}\text{Fe}_2\text{O}_4$ nano-tube and (c) SAED pattern of the $\text{Mg}_{0.5}\text{Zn}_{0.5}\text{Fe}_2\text{O}_4$ nano-tube

3.5.3. Gas Sensing Characteristics of $\text{Mg}_{0.5}\text{Zn}_{0.5}\text{Fe}_2\text{O}_4$ Nano-tubes

We have investigated the gas sensing characteristics of both isolated and embedded $\text{Mg}_{0.5}\text{Zn}_{0.5}\text{Fe}_2\text{O}_4$ nano-tubes. The details of the fabrication of sensing elements and gas sensing measurements are described in Chapter-2 (Sec. 2.5). Figure 3.23 shows the response and recovery transients of embedded $\text{Mg}_{0.5}\text{Zn}_{0.5}\text{Fe}_2\text{O}_4$ nano-tubes for hydrogen gas sensing, measured at (a) 250 °C, (b) 300 °C, (c) 350 °C and (d) 380 °C. The hydrogen gas concentration for all these measurements is kept fixed at 1660 ppm. Irrespective of the operating temperature, the embedded nano-tube exhibits typical 'n'-type conduction (i.e. resistance decreases when the sensing elements are exposed to reducing gas). From the resistance transients, the estimated response (%) is found maximum at ~350 °C.

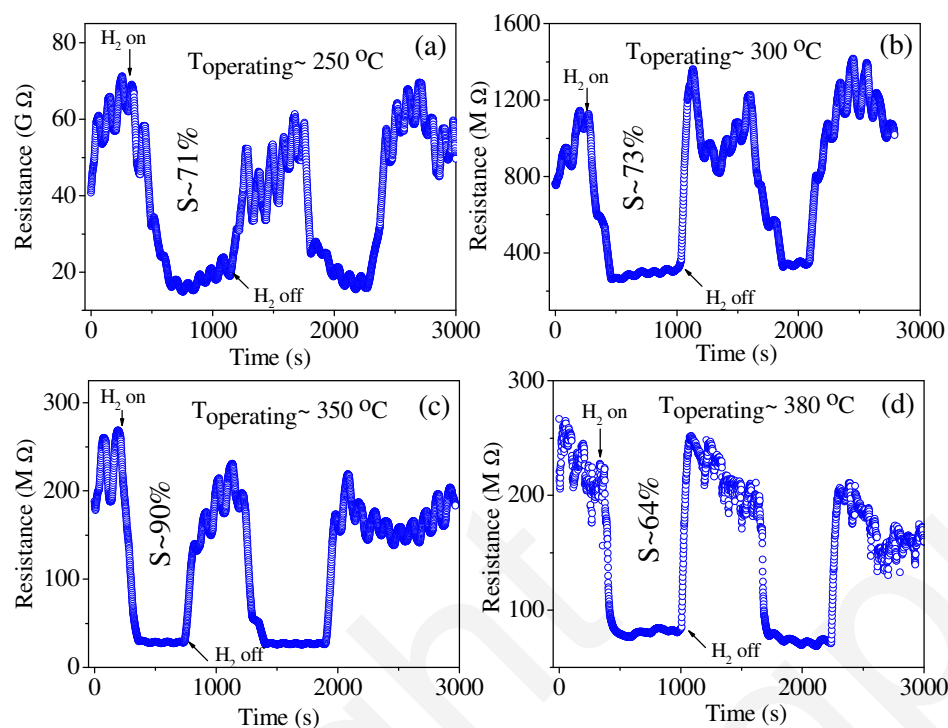


Fig. 3.23: Resistance transients of embedded $\text{Mg}_{0.5}\text{Zn}_{0.5}\text{Fe}_2\text{O}_4$ nano-tubes towards H_2 (~1660 ppm) sensing measured at (a) 250 °C, (b) 300 °C, (c) 350 °C and (d) 380 °C. The respective operating temperature ($T_{\text{operating}}$), response (S) (%) and H_2 on-off points are marked in the figure

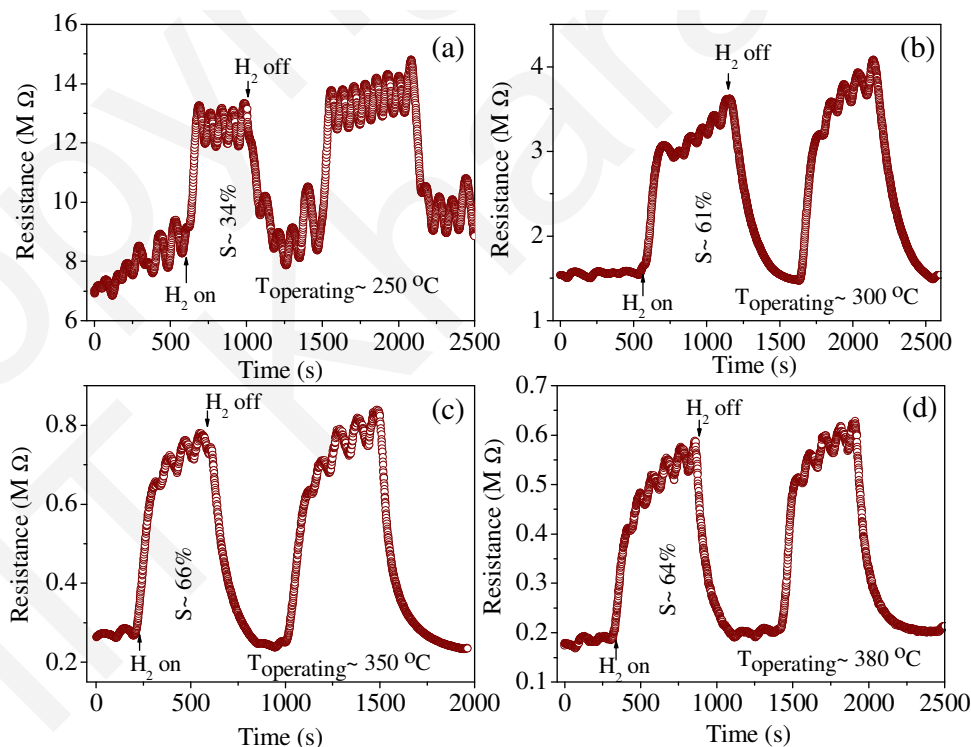


Fig. 3.24: Resistance transient of isolated $\text{Mg}_{0.5}\text{Zn}_{0.5}\text{Fe}_2\text{O}_4$ nano-tubes towards H_2 (~1660 ppm) sensing measured at (a) 250 °C, (b) 300 °C, (c) 350 °C and (d) 380 °C. The respective operating temperature ($T_{\text{operating}}$), response (S) (%) and H_2 on-off points are marked in the figure

Figure 3.24 shows the response and recovery transients of isolated $\text{Mg}_{0.5}\text{Zn}_{0.5}\text{Fe}_2\text{O}_4$ nano-tubes for hydrogen gas sensing, measured at (a) 250 °C, (b) 300 °C, (c) 350 °C and (d) 380 °C. Comparing, the resistance transients presented in Fig. 3.23 and 3.24, it is interesting to note that irrespective of the operating temperature the isolated nano-tubes exhibit typical 'p'-type conduction (i.e. resistance increases when the sensing elements are exposed to reducing gas). In case of isolated nano-tubes too the estimated response (%) is found to be maximized at ~350 °C.

At the optimized operating temperature ($T_{\text{opt}} \sim 350$ °C), Fig. 3.25 exhibits the hydrogen gas sensing characteristics (in a wide concentration range between 10-1660 ppm) of (a) embedded and (b) isolated $\text{Mg}_{0.5}\text{Zn}_{0.5}\text{Fe}_2\text{O}_4$ nano-tubes. In both these forms $\text{Mg}_{0.5}\text{Zn}_{0.5}\text{Fe}_2\text{O}_4$ sensing elements are capable to detect 10 ppm H_2 gas. As marked in the respective figures, the embedded nano-tubes exhibit better hydrogen response. Also irrespective of the test gas concentrations, the isolated nano-tubes exhibit 'p'-type conduction.

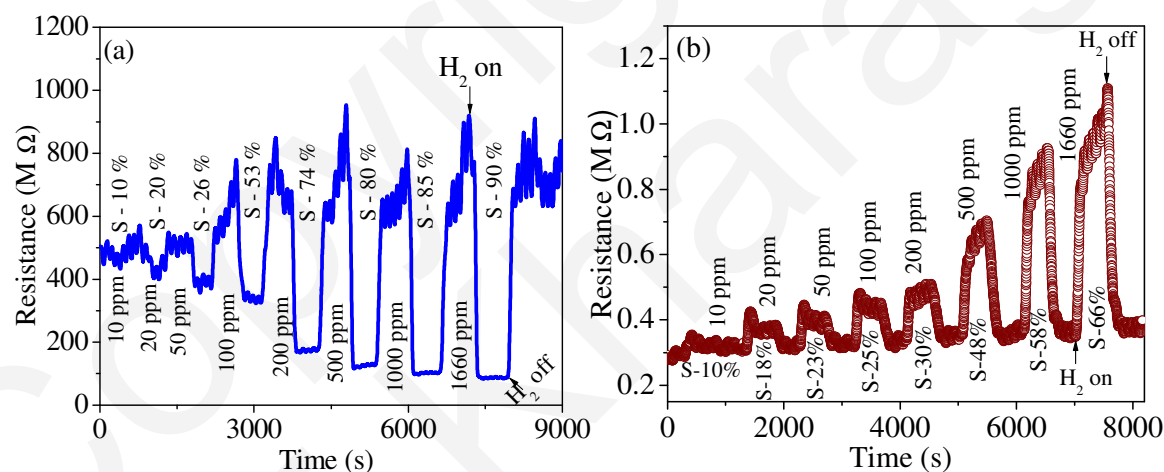


Fig. 3.25: Resistance transients of (a) embedded and (b) isolated $\text{Mg}_{0.5}\text{Zn}_{0.5}\text{Fe}_2\text{O}_4$ nano-tube sensors in presence of various hydrogen concentrations (10-1660 ppm) measured at ~350 °C. The H_2 concentrations and the respective response (S) (%) are mentioned in the figure

It is remarkable to note that irrespective of the type of test gas, embedded nano-tubes exhibit 'n'-type conduction whereas isolated nano-tube always exhibit 'p'-type conduction. Thus Fig. 3.26 exhibits the resistance transients for (a) CO and (b) N_2O gas sensing using embedded $\text{Mg}_{0.5}\text{Zn}_{0.5}\text{Fe}_2\text{O}_4$ nano-tubes. For both these cases typical 'n' type conduction is observed. Figure 3.27 shows the resistance transients (a) for CO gas sensing in a wide

range of gas concentrations and (b) N_2O gas sensing (1660 ppm) using isolated $\text{Mg}_{0.5}\text{Zn}_{0.5}\text{Fe}_2\text{O}_4$ nano-tubes. Note that for both these cases isolated nano-tubes exhibit 'p' type conduction.

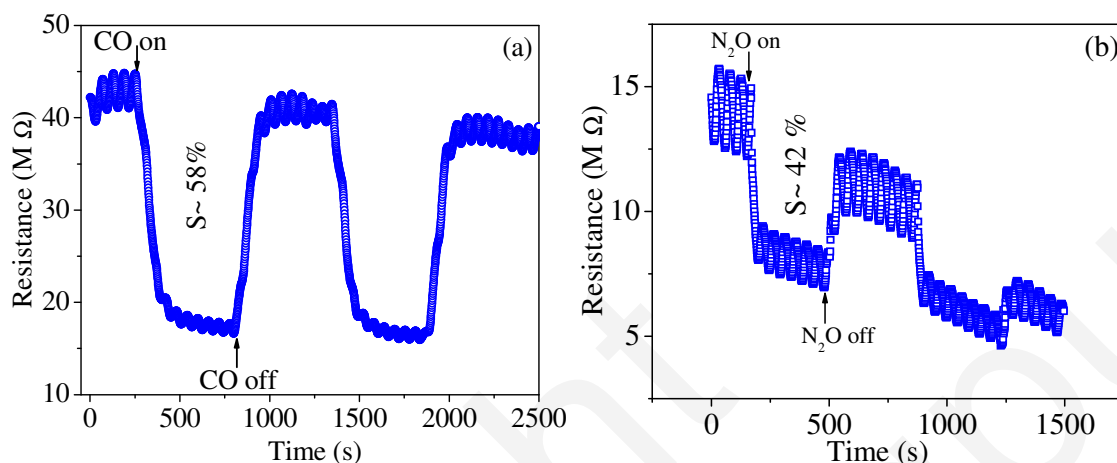


Fig. 3.26: Resistance transients of embedded $\text{Mg}_{0.5}\text{Zn}_{0.5}\text{Fe}_2\text{O}_4$ nano-tube sensor in presence of 1660 ppm of (a) CO and (b) N_2O gases measured at $\sim 350^\circ\text{C}$ and 380°C respectively. The respective response (S) (%) are mentioned in the figure

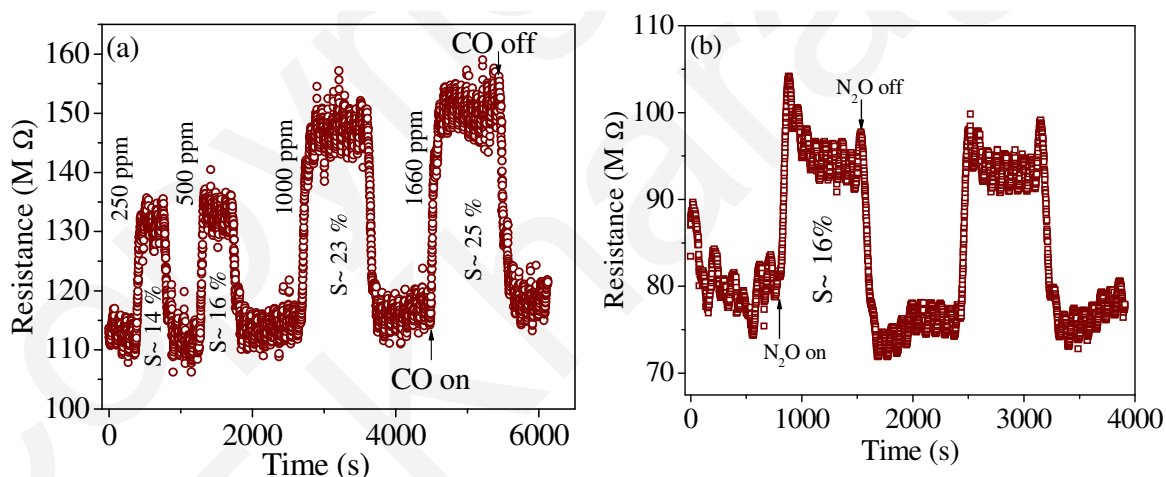


Fig. 3.27: Resistance transients of isolated $\text{Mg}_{0.5}\text{Zn}_{0.5}\text{Fe}_2\text{O}_4$ nano-tube sensor in presence of (a) CO (~ 250 -1660 ppm) and (b) N_2O (~ 1660 ppm) gases measured at ~ 250 and 300°C respectively. The respective response (S) (%) are mentioned in the figure

Summarizing the above results it is clear that irrespective of operating temperature, test gas concentrations and test gas types, embedded $\text{Mg}_{0.5}\text{Zn}_{0.5}\text{Fe}_2\text{O}_4$ nano-tubes exhibit 'n'-type conduction, whereas isolated nano-tubes exhibit 'p' type conduction characteristics. In the following section we have made an attempt to explain the observed behavior.

3.5.3.1. Origin of 'n' and 'p' type conduction in embedded and isolated $\text{Mg}_{0.5}\text{Zn}_{0.5}\text{Fe}_2\text{O}_4$ nano-tubes: Effect of surface morphology

The characteristic carrier reversal ('n' to 'p' and vice versa) of SMO based gas sensing materials are quite generic in nature and reported for a wide variety of materials for various types of gas sensing. Table-3.4 summarizes some of these results reported in recent literatures.

Table-3.4: Summary of the carrier inversion characteristics reported in literature

Sensor	Test gas	Measurement set-up	Observations made	Reference
Ni^{2+} doped TiO_2 thin film	Acetone, ethanol	Dynamic	The charge carrier changes from n to p type when TiO_2 is doped beyond 10% nickel	[32]
Fe^{3+} doped SnO_2 thick film	Oxygen	Dynamic	Undoped SnO_2 behaves as 'n' type conductor. Fe doped SnO_2 films exhibit 'p' type behavior. When the operating temperature is $> 400^\circ\text{C}$, conduction behavior changes again from 'p' to 'n' type.	[33]
ZnO nano-tubes	Nitrogen di oxide	Dynamic	Increase in operating temperature and NO_2 concentration change the conduction behavior of ZnO nano-tube from 'n' to 'p' type.	[34]
α -tellurium dioxide nano-wires	Ethanol	Dynamic	While sensing ethanol vapor, 'n' to 'p' type carrier conversion is reported at and beyond 500 ppm ethanol sensing. Up to 200 ppm ethanol, these nano-wires exhibit 'n' type gas sensing behavior.	[35]
TiO_2 nano-fibers	Nitrogen di oxide	Dynamic	While sensing NO_2 gas > 12.5 ppm, the charge carrier changes from 'n' to 'p' type. The n to p type inversion is facilitated by the high surface to volume ratio of the TiO_2 nano-fibers.	[36]
Pt coated SnO_2 nano-rods	Ethanol	Dynamic	The 'n' to 'p' type carrier inversion is explained to be due to the catalytic effect of Pt in changing the type (O^\cdot , O_2^\cdot , O_2^- etc) of ionosorbed oxygen	[37]
α - Fe_2O_3 thick film sensor	Carbon monoxide	Not mentioned	'n' to 'p' type carrier conversion is related to the concentration of adsorbed oxygen on the sensing surface.	[38]

As shown in Table-3.4, the carrier inversion has been reported for a variety of sensing materials (doped TiO_2 film, ZnO nano-tube, tellurium dioxide nano-wires, Pt coated

SnO₂ nano-rods, α -Fe₂O₃ thick film etc) for various types of gas sensing (acetone/ethanol, oxygen, nitrogen di oxide, ethanol, carbon mono oxide etc). However, as outlined in Table-3.4, the underlying mechanisms hypothesized for such carrier inversion is widely scattered. Reviewing the literatures presented in Table-3.4, the apparent reasons for the said carrier reversal is reported to be due to (i) aliovalent doping [32], (ii) aliovalent doping together with change in temperature [33], (iii) variation of test gas concentration and change in operating temperature [34-36], (iv) catalytic effect of noble metal coating on the sensing element [37] etc.

Interestingly, in the present case none of these factors seem to be responsible for the observed carrier reversal. Thus, in the present case we have not doped the sensing material, no noble metal coating is performed on the sensing materials, and the carrier reversal is observed irrespective of the test gas concentration, operating temperature and type of test gas. We feel that the surface morphology of the sensing elements plays an important role to control the carrier reversal. Figure 3.28 shows the schematic sensing elements of (a) embedded and (b) isolated Mg_{0.5}Zn_{0.5}Fe₂O₄ nano-tubes used for gas sensing. Since the nano-tubes are embedded into the pores of anodized alumina, oxygen can be chemi-adsorbed only in the inner surfaces of the hollow Mg_{0.5}Zn_{0.5}Fe₂O₄ nano-

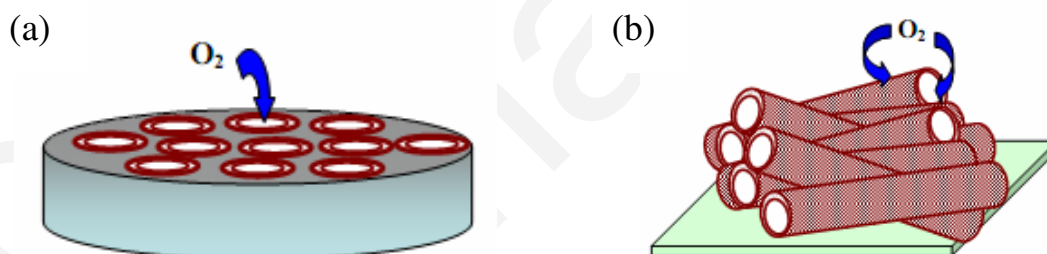


Fig. 3.28: Schematic of (a) embedded and (b) isolated tube based sensing elements

tubes. As compared to this larger surface is exposed in the isolated nano-tubes. Thus oxygen can be chemi-adsorbed both in the outer surface as well as in the inner surface of these isolated hollow Mg_{0.5}Zn_{0.5}Fe₂O₄ nano-tubes. In other words, for any fixed operating temperature, the concentration of chemi-adsorbed oxygen will always be higher in isolated nano-tubes as compared to its embedded counterpart. Figure 3.29 shows the magnified FESEM micrograph of isolated hollow Mg_{0.5}Zn_{0.5}Fe₂O₄ nano-tubes. Note that each single nano-tube constitutes innumerable tiny crystallites with average size ~10 nm.

As mentioned earlier, since oxygen can be chemi-adsorbed both in the inner as well as outer surface of these isolated nano-tubes, the crystallites may be electron depleted from both the surfaces.

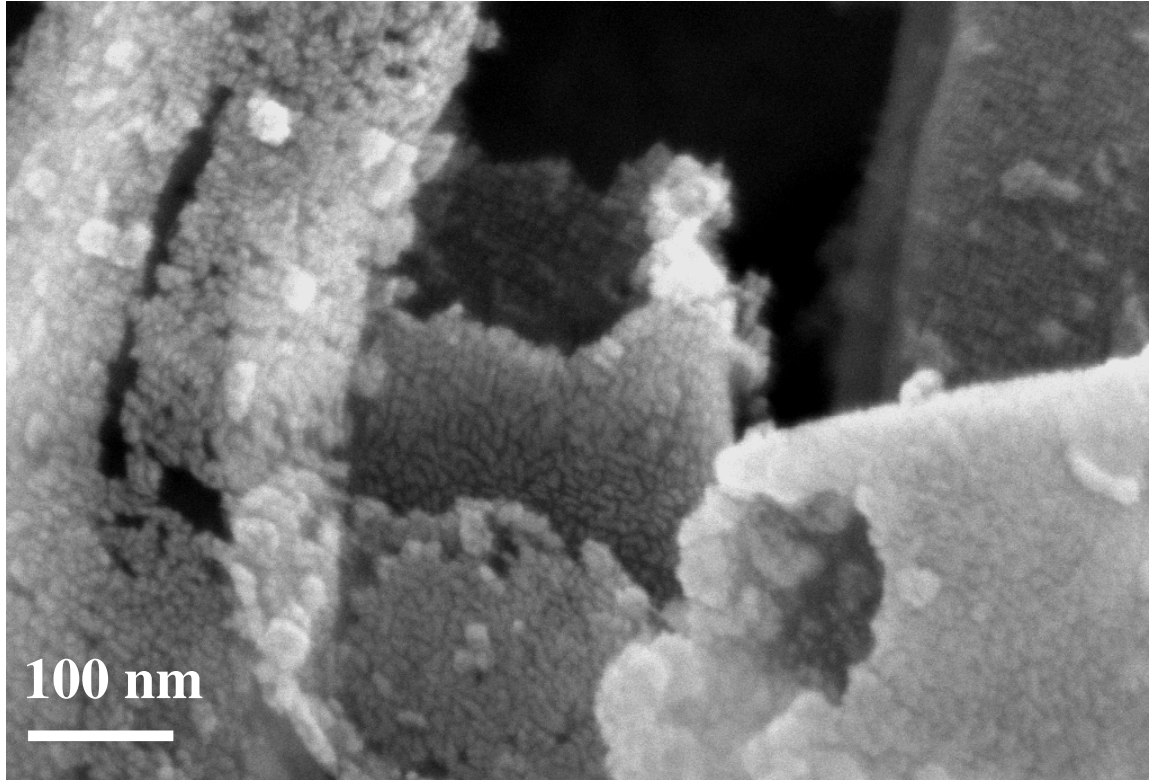
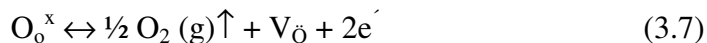


Fig. 3.29: Magnified FESEM micrograph of isolated hollow $\text{Mg}_{0.5}\text{Zn}_{0.5}\text{Fe}_2\text{O}_4$ nano-tubes. The micrograph shows that each tube consists of innumerable tiny crystallites

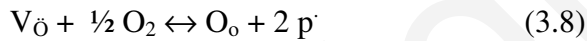
Normally the conductivity (σ) of a semiconducting material can be represented by the following relation

$$\sigma = -qn\mu_n + qp\mu_p \quad (3.6)$$

where n and p are the concentration of electron and hole respectively, q is the charge associated with the carrier and μ_n and μ_p are the mobility of electron and hole respectively. The parameters n , p , and their respective mobility are temperature dependent. For $\text{Mg}_{0.5}\text{Zn}_{0.5}\text{Fe}_2\text{O}_4$, the majority charge carriers are electrons, and donor trap level in the band gap is formed by oxygen vacancies [39]. The formation of oxygen vacancies may be represented by the following reaction



where, O_o^x , the oxygen atom from $Mg_{0.5}Zn_{0.5}Fe_2O_4$ lattice is lost as oxygen gas ($\frac{1}{2} O_2$ (g)), creating positively charged oxygen vacancies ($V_{\bar{O}}$) in $Mg_{0.5}Zn_{0.5}Fe_2O_4$ lattice. To maintain the charge neutrality, each $V_{\bar{O}}$ traps two electrons (e^-). The oxygen vacancies with trapped electrons act as donor level within the band gap. For low concentration of oxygen chemi-adsorption (in case of embedded nano-tubes) the sensing materials acts as 'n' type semiconductor. However, as mentioned earlier, since isolated nano-tubes have much larger surface to volume ratio, concentration of oxygen on the surface of the sensing materials is grossly increased. The available oxygen, apart from being chemi-adsorbed on the nano-tube surface, also incorporated into the intrinsic oxygen vacancies of the sensing material. The incorporation of oxygen (from the ambient) into the intrinsic oxygen vacancies (of $Mg_{0.5}Zn_{0.5}Fe_2O_4$) increase hole concentration on valance band and reaction can be represented by the following relation



We feel that in isolated $Mg_{0.5}Zn_{0.5}Fe_2O_4$ nano-tubes, the electron concentration becomes smaller than hole concentration ($n < p$), when they are exposed to air ambient at elevated temperature. In other words when oxygen is chemi-adsorbed on the surface of isolated nano-tubes, holes becomes the dominant charge carriers. During gas sensing, the chemi-adsorbed oxygen (on the nano-tube surface) would react with reducing gas (e.g. H_2) and this would release electrons which probably recombine with the holes (the initial dominant charge carriers). In other words, during gas sensing the hole concentration decreases resulting the increase of resistance with time.

The inversion of the dominant charge carrier (from n to p type) is thus solely dependent on the surface morphology of nano-structured $Mg_{0.5}Zn_{0.5}Fe_2O_4$ in the form of isolated nano-tube. Thus, in addition to their central role in gas sensing, engineering of the surface to volume ratio of these spinel ferrite may open up interesting possibilities to tailor their electronic conduction. In addition to 1-dimensional growth of $Mg_{0.5}Zn_{0.5}Fe_2O_4$ sensing elements, we have also synthesized them in 2-dimensional thin film form. The gas sensing characteristics of $Mg_{0.5}Zn_{0.5}Fe_2O_4$ thin films are described in the next section.

3.6. Structural, Micro-structural and Gas Sensing Characteristics of $\text{Mg}_{0.5}\text{Zn}_{0.5}\text{Fe}_2\text{O}_4$ Thin Films

As described in details in Chapter-2, the precursor sol prepared using a modified Pechini route is used to deposit $\text{Mg}_{0.5}\text{Zn}_{0.5}\text{Fe}_2\text{O}_4$ thin films on alumina substrates. As stated earlier, the primary objective is to investigate the gas sensing characteristics of two dimensional $\text{Mg}_{0.5}\text{Zn}_{0.5}\text{Fe}_2\text{O}_4$ sensing elements. First, we have studied the phase formation and micro-structure of the deposited thin films. Next, their gas sensing characteristics are investigated.

3.6.1. Structure and Surface Morphology of $\text{Mg}_{0.5}\text{Zn}_{0.5}\text{Fe}_2\text{O}_4$ Thin Films

Figure 3.30 shows the glancing angle X-ray diffractograms of $\text{Mg}_{0.5}\text{Zn}_{0.5}\text{Fe}_2\text{O}_4$ thin films coated on alumina substrates. For these films coating and firing cycles are repeated for 8, 15, and 45 times, and finally, these films are annealed at 600 °C for 2 h in air for crystallization. All these films are crystallized into desired cubic spinel phase without the formation of any other impurity phase/(s).

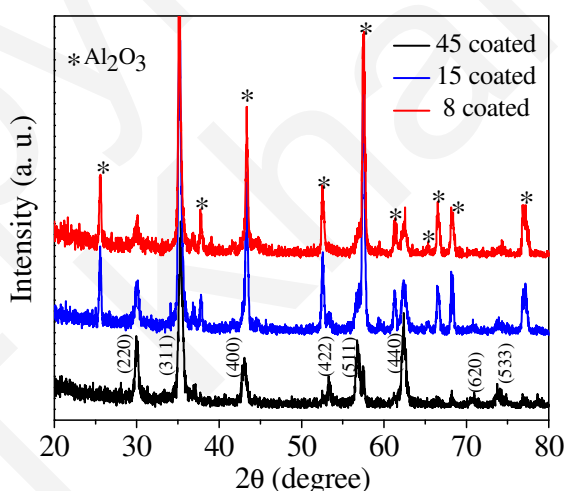


Fig. 3.30: X-ray diffractograms of $\text{Mg}_{0.5}\text{Zn}_{0.5}\text{Fe}_2\text{O}_4$ thin films annealed at 600 °C for 2 h in air

Figure 3.31 shows the surface morphologies of $\text{Mg}_{0.5}\text{Zn}_{0.5}\text{Fe}_2\text{O}_4$ thin films coated on alumina substrates for (a) 8, (b) 15, (c) 30, and (d) 45 times. The cross sectional morphology of 30 times coated film is shown in the inset of Fig. 3.31 (c). The typical

film thickness of 30 times coated films is measured to be $\sim 1.2 \mu\text{m}$. As envisaged from these micrographs, all these films exhibit dense and uniform microstructure. The grain size is found to be slightly increased with the increase in film thickness. The average grain size of the thickest film is estimated to be $\sim 20 \text{ nm}$. These micro-structures are very different from those reported for nano-particulate (bulk pellet) and 1-dimensional (nano-tubes) $\text{Mg}_{0.5}\text{Zn}_{0.5}\text{Fe}_2\text{O}_4$ sensing elements presented in earlier sections. Gold IDE electrodes are sputter deposited on the surface of these films and these electroded films are used as sensing elements for gas sensing measurements. The sensing characteristics of $\text{Mg}_{0.5}\text{Zn}_{0.5}\text{Fe}_2\text{O}_4$ thin films are described in the next section.

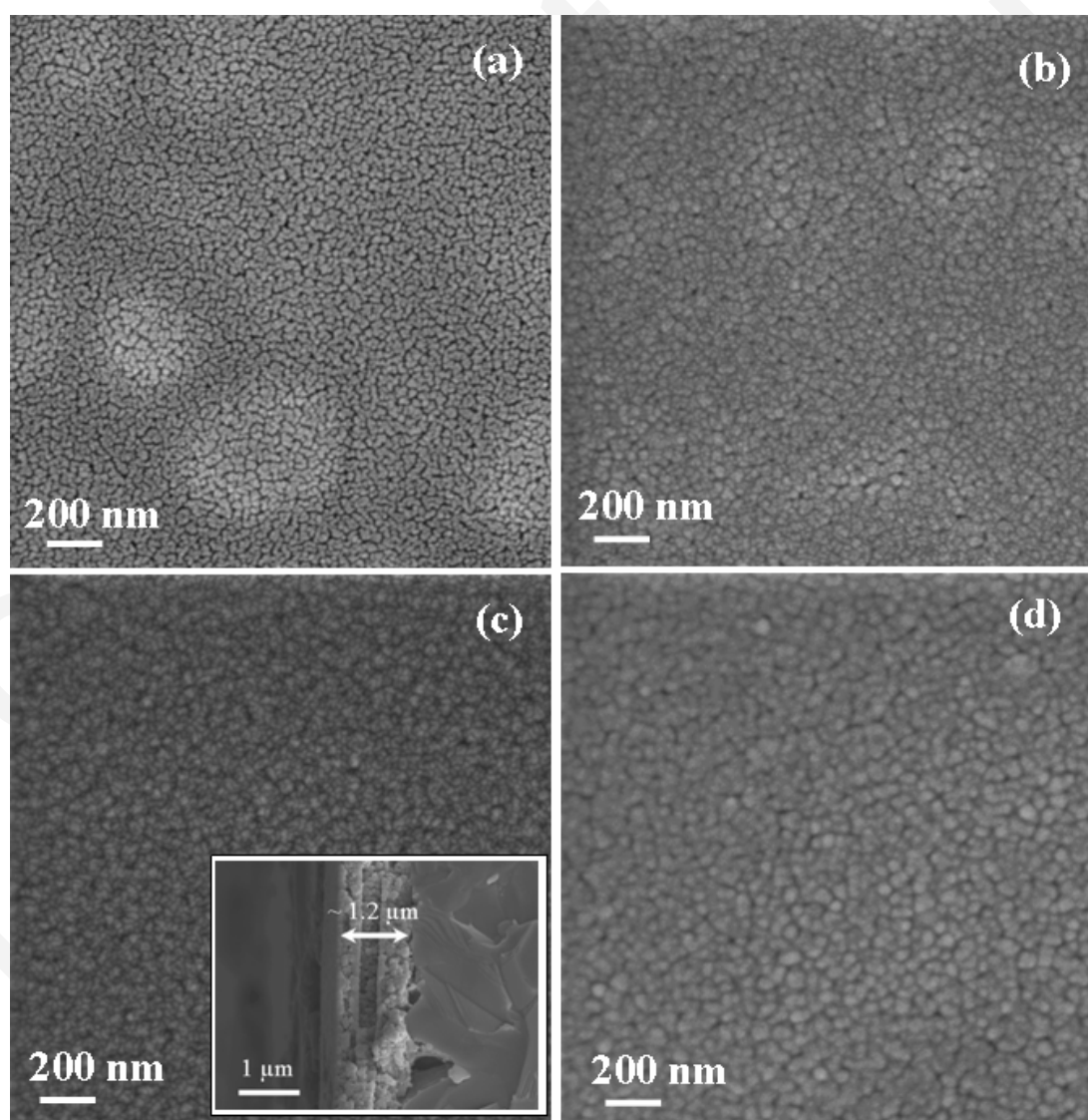


Fig. 3.31: Surface morphologies of $\text{Mg}_{0.5}\text{Zn}_{0.5}\text{Fe}_2\text{O}_4$ thin films spun coated on alumina substrates for (a) 8, (b) 15, (c) 30, and (d) 45 times and annealed at 600°C for 2 h in air. Inset of Fig. 3.31(c) shows the cross sectional morphology of 30 times coated film

3.6.2. Gas Sensing Characteristics of $\text{Mg}_{0.5}\text{Zn}_{0.5}\text{Fe}_2\text{O}_4$ Thin Films

We have first described the hydrogen gas sensing characteristics of $\text{Mg}_{0.5}\text{Zn}_{0.5}\text{Fe}_2\text{O}_4$ thin films. The hydrogen gas concentration is kept fixed ~ 1660 ppm, and the sensing characteristics of these films with different thicknesses are estimated maintaining the operating temperature in the range between 200 - 275 $^{\circ}\text{C}$. The resistance transients exhibit ‘n’ type behavior. The responses(S) for films (with different thicknesses) are calculated from the measured resistance transients and Fig. 3.32 shows the variation of response as a function of operating temperatures. It is shown that irrespective of the operating temperature, the response increases with film thickness up to 30 coating, however, it deteriorates in thicker (45 coating) films. The result is in line to the research works that report an optimum film thickness to yield maximum response [40-41]. Also, except the thinnest film (8 coating), the optimized operating temperature (T_{opt} , corresponding to the maximum response) for these films are estimated to be ~ 250 $^{\circ}\text{C}$. Comparing the sensing characteristics of nano-particulate and nano-tube based $\text{Mg}_{0.5}\text{Zn}_{0.5}\text{Fe}_2\text{O}_4$ sensors; it is observed that the T_{opt} is significantly lowered in thin film type sensing elements.

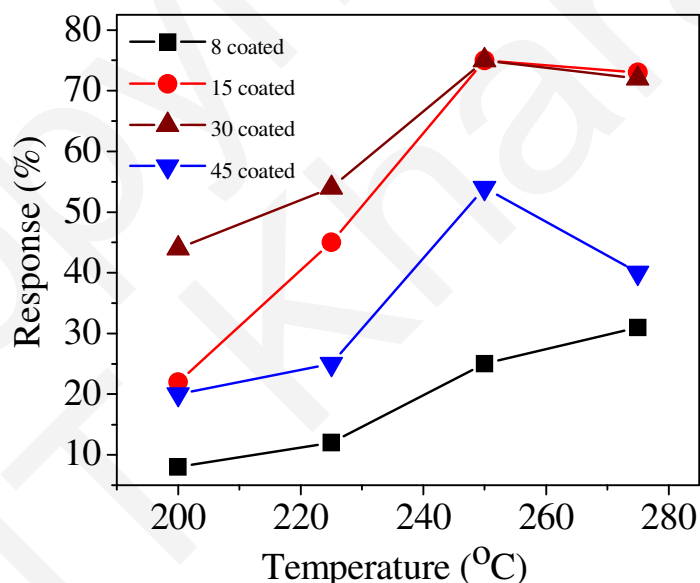


Fig. 3.32: Variation of response (%) of $\text{Mg}_{0.5}\text{Zn}_{0.5}\text{Fe}_2\text{O}_4$ thin films (8, 15, 30 and 45 times coated) towards the detection of 1660 ppm of H_2 gas as a function of operating temperature

At the optimized operating temperature (~ 250 $^{\circ}\text{C}$), the response during the gas sensing cycle is compared in Fig. 3.33. The response and recovery times, estimated from

the response transients of $\text{Mg}_{0.5}\text{Zn}_{0.5}\text{Fe}_2\text{O}_4$ films, are tabulated in the inset of Fig. 3.33. Note, 15 and 30 times coated films yield better response (%) in shorter response time. As tabulated in the inset, for all these films recovery time is more than the response. The longer recovery time could be due to the meso-porous nature of these thin films.

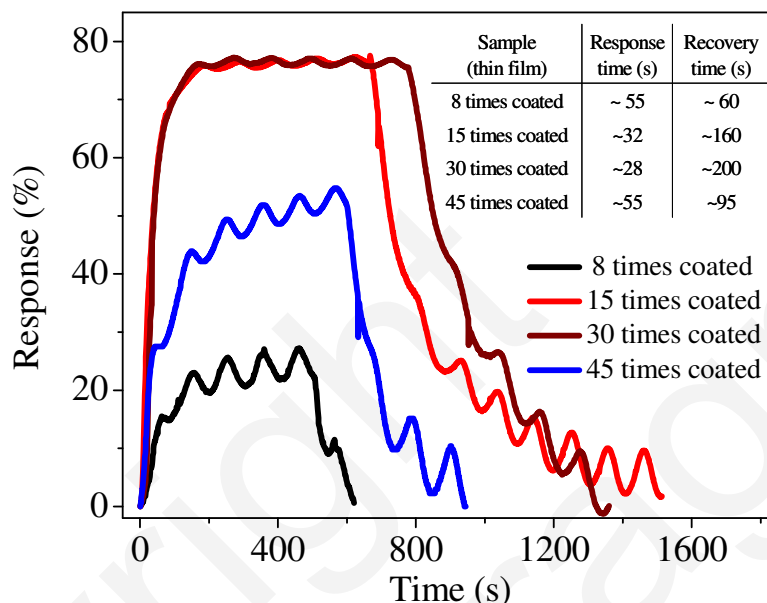


Fig. 3.33: Response transients of $\text{Mg}_{0.5}\text{Zn}_{0.5}\text{Fe}_2\text{O}_4$ films towards the detection of 1660 ppm of H_2 measured at $\sim 250^\circ\text{C}$

The resistance transients, measured during the response and recovery of hydrogen gas detection (in the concentration range between 20-1660 ppm), are shown in Fig. 3.34. The operating temperature is kept $\sim 250^\circ\text{C}$ and 15 times coated $\text{Mg}_{0.5}\text{Zn}_{0.5}\text{Fe}_2\text{O}_4$ film is used as sensing element. As shown in Fig. 3.34, the thin film is able to detect as low as 20 ppm hydrogen. Inspecting Fig. 3.34, the resistance drift is found to be more prominent in low concentration gas sensing. The issue of the drift in base resistance has been addressed in details in the next chapter. The response (S) %, and response/recovery times ($\tau_{\text{res}}/\tau_{\text{rec}}$) for hydrogen gas sensing (in a wide composition range between 20 to 1000 ppm) for 15 and 30 times coated $\text{Mg}_{0.5}\text{Zn}_{0.5}\text{Fe}_2\text{O}_4$ films are tabulated in Table-3.5. Note that the response time is systematically reduced with the increase in test gas concentration as well with the film thickness. No such systematic variation is observed for the estimated recovery times.

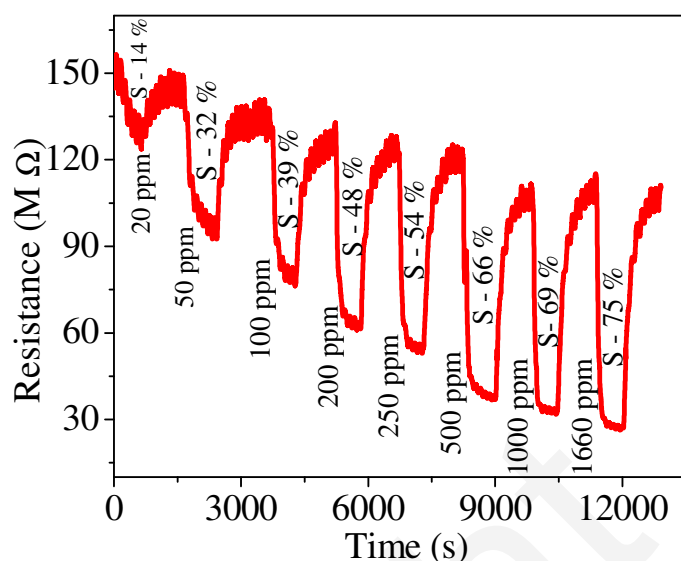


Fig. 3.34: Resistance transient of 15 times coated $\text{Mg}_{0.5}\text{Zn}_{0.5}\text{Fe}_2\text{O}_4$ thin film towards the detection of 20-1660 ppm of H_2 gas measured at $\sim 250^\circ\text{C}$

We have used 15 times coated $\text{Mg}_{0.5}\text{Zn}_{0.5}\text{Fe}_2\text{O}_4$ films to sense CO gas as well. The response (%) of this thin film towards the detection of 1660 ppm of CO as a function of operating temperature (in the range of $200\text{--}275^\circ\text{C}$) is shown in Fig. 3.35. The typical resistance transient recorded during the sensing of 1660 ppm of CO gas (at $\sim 225^\circ\text{C}$) is shown in the inset of Fig. 3.35.

Table-3.5: Values of response (%), response and recovery times estimated from the resistance transients of 15 and 30 times coated films during the detection of 20-1000 ppm of H_2 gas at operating temperature $\sim 250^\circ\text{C}$

Sensor (thin film)	H ₂ concentration (ppm)														
	20			50			100			500			1000		
	S (%)	τ_{res} (s)	τ_{rec} (s)	S (%)	τ_{res} (s)	τ_{rec} (s)	S (%)	τ_{res} (s)	τ_{rec} (s)	S (%)	τ_{res} (s)	τ_{rec} (s)	S (%)	τ_{res} (s)	τ_{rec} (s)
15 times coated	~14	~280	~215	~32	~150	~120	~39	~90	~115	~66	~55	~150	~69	~45	~150
30 times coated	---			~31	~70	~120	~40	~60	~110	~63	~35	~165	~69	~30	~175

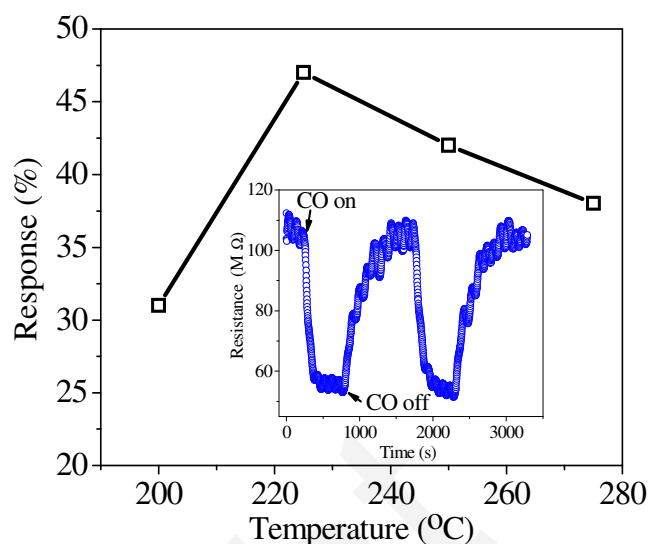


Fig. 3.35: Variation of response (%) of 15 times coated $\text{Mg}_{0.5}\text{Zn}_{0.5}\text{Fe}_2\text{O}_4$ thin film in presence of 1660 ppm of H_2 gas as a function of operating temperature. Inset shows the resistance transient recorded during sensing 1660 ppm of CO at 225 °C

From these sensing results we conclude that the optimized sensing temperature may be significantly reduced by using thin film type sensing elements. It is important to increase the porosity for better gas diffusion. This would in turn expedite the sensor recovery. More research effort is necessary to understand the combined effect of the grain size, porosity and thickness of these thin film sensing elements to their gas sensing characteristics. In the following section we have described the gas sensing performance of $\text{Mg}_{0.5}\text{Zn}_{0.5}\text{Fe}_2\text{O}_4$ hollow-sphere synthesized using hydrothermal route.

3.7. Structural, Micro-structural and Gas Sensing Characteristics of $\text{Mg}_{0.5}\text{Zn}_{0.5}\text{Fe}_2\text{O}_4$ Hollow Spheres

The details of the synthesis of $\text{Mg}_{0.5}\text{Zn}_{0.5}\text{Fe}_2\text{O}_4$ hollow-spheres (using spherical carbon template assisted hydrothermal synthesis route) have already been discussed in Chapter-2. In this section we have first described the IR analyses and surface morphology of the carbon templates and $\text{Mg}_{0.5}\text{Zn}_{0.5}\text{Fe}_2\text{O}_4$ hollow-spheres wherever appropriate. In the subsequent sections the structural, micro-structural and gas sensing characteristics of $\text{Mg}_{0.5}\text{Zn}_{0.5}\text{Fe}_2\text{O}_4$ hollow-spheres are described sequentially.

3.7.1. FTIR Analyses and Surface Morphology of the Carbon Templates

Figure 3.36 shows the FTIR spectra of the synthesized carbon templates and $\text{Mg}_{0.5}\text{Zn}_{0.5}\text{Fe}_2\text{O}_4$ hollow-spheres calcined at 600°C . As revealed from the spectra, the templates have organic hydrophilic (C=O, O-H) functional groups for metal cation attachments. The appearance of sharp M-O mode (at lower wave number) indicates the crystalline nature of the synthesized hollow-spheres.

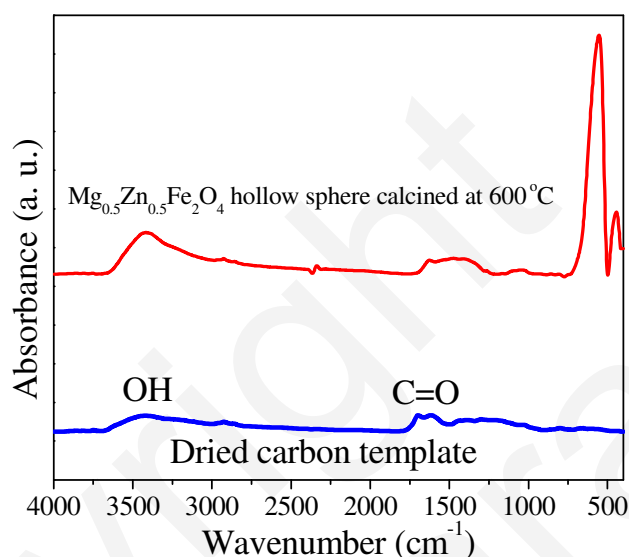


Fig. 3.36: FTIR spectra of as dried carbon templates and the calcined $\text{Mg}_{0.5}\text{Zn}_{0.5}\text{Fe}_2\text{O}_4$ hollow spheres (synthesized using spherical carbon template)

The morphology of the carbon templates are characterized using a field emission electron microscope. The FESEM micrographs of the carbon templates at lower and higher magnifications are shown in Fig. 3.37(a) and (b) respectively. As shown in Fig. 3.37, the diameters of the spherical carbon templates are in the range between 500-700 nm. As revealed from the magnified image (Fig. 3.37(b)), the surface of the templates is porous in nature and attached to each other. The porosity increases the surface area for better adhesion of metal cations during the hydrothermal synthesis of the hollow-spheres.

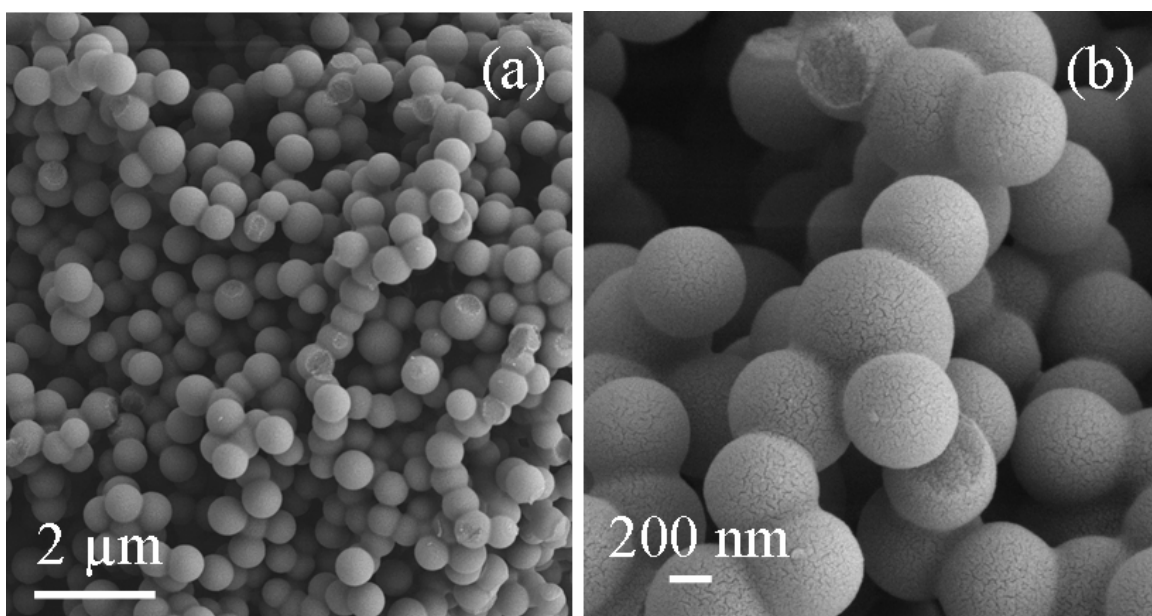


Fig. 3.37: FESEM image of synthesized spherical carbon templates at (a) low and (b) high magnification. The meso-porous surface of the templates are shown in the magnified image

3.7.2. Structural and Micro-structural Characteristics of $\text{Mg}_{0.5}\text{Zn}_{0.5}\text{Fe}_2\text{O}_4$ Hollow Spheres

Fig. 3.38 shows the X-ray diffraction pattern of the calcined $\text{Mg}_{0.5}\text{Zn}_{0.5}\text{Fe}_2\text{O}_4$ hollow-spheres. The spheres are crystallized into the desired cubic spinel phase. However, the formation of $\alpha\text{-Fe}_2\text{O}_3$, as an impurity phase, could not be avoided.

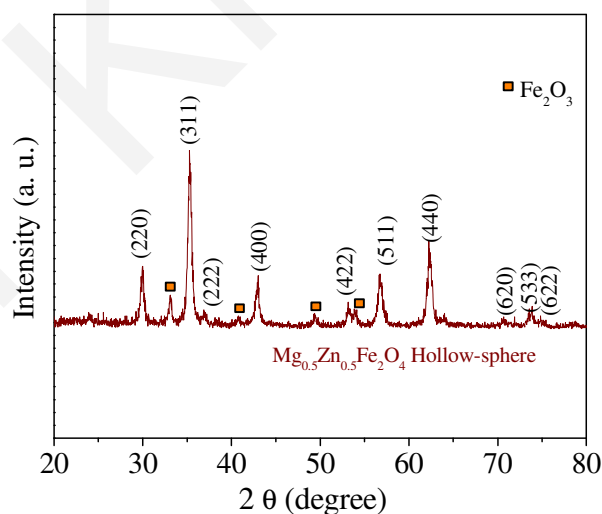


Fig. 3.38: X-ray diffractogram of $\text{Mg}_{0.5}\text{Zn}_{0.5}\text{Fe}_2\text{O}_4$ hollow spheres calcined at 600 °C for 2 h

Figure 3.39(a) shows the FESEM micrographs of the calcined hollow-spheres. As revealed in the micrograph, each sphere is composed of innumerable tiny crystallites less than about 20 nm average diameter. The shape of the hollow-sphere is dependent on the shape of the carbon templates. Since the carbon templates are attached to each other, we have found that most of the synthesized hollow-spheres are also joined to each other. The EDS spectra of these hollow-spheres are presented in Fig. 3.39(b). Note all the constituent elements of $\text{Mg}_{0.5}\text{Zn}_{0.5}\text{Fe}_2\text{O}_4$ are detected, and it is difficult to assign if the iron signal is for the impurity phase of spinel composition. Recall that the presence of iron is detected (as impurity phase) in the synthesized cubic spinel hollow-spheres.

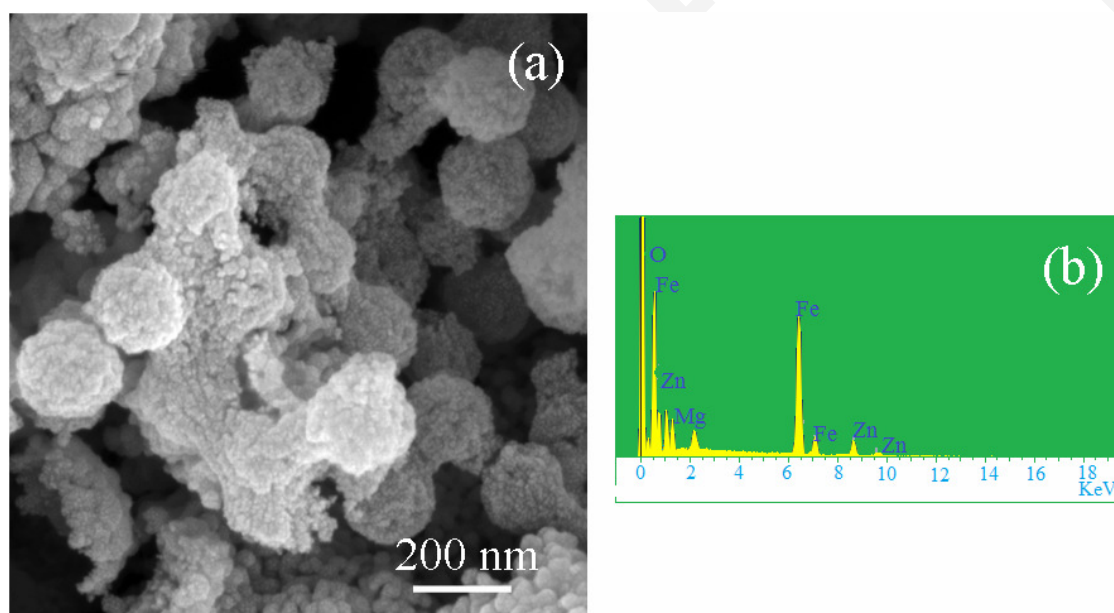


Fig. 3.39: (a) FESEM image (b) EDS spectra of the $\text{Mg}_{0.5}\text{Zn}_{0.5}\text{Fe}_2\text{O}_4$ hollow spheres calcined at 600 °C for 2 h

The hollow nature of these spheres is clearly demonstrated in the TEM micrographs. Figure 3.40 shows (a) the cluster of hollow-spheres, (b) the magnified image of a single hollow-sphere, (c) a partially formed hollow-sphere, and (d) the SAED pattern of these hollow-spheres. The TEM images confirm that each hollow-sphere consists of several nano-crystallites. Analyzing the SAED pattern we have confirmed the polycrystalline nature and cubic spinel structure of these hollow-spheres. In the following section we have described the gas sensing characteristics of the synthesized $\text{Mg}_{0.5}\text{Zn}_{0.5}\text{Fe}_2\text{O}_4$ hollow-spheres.

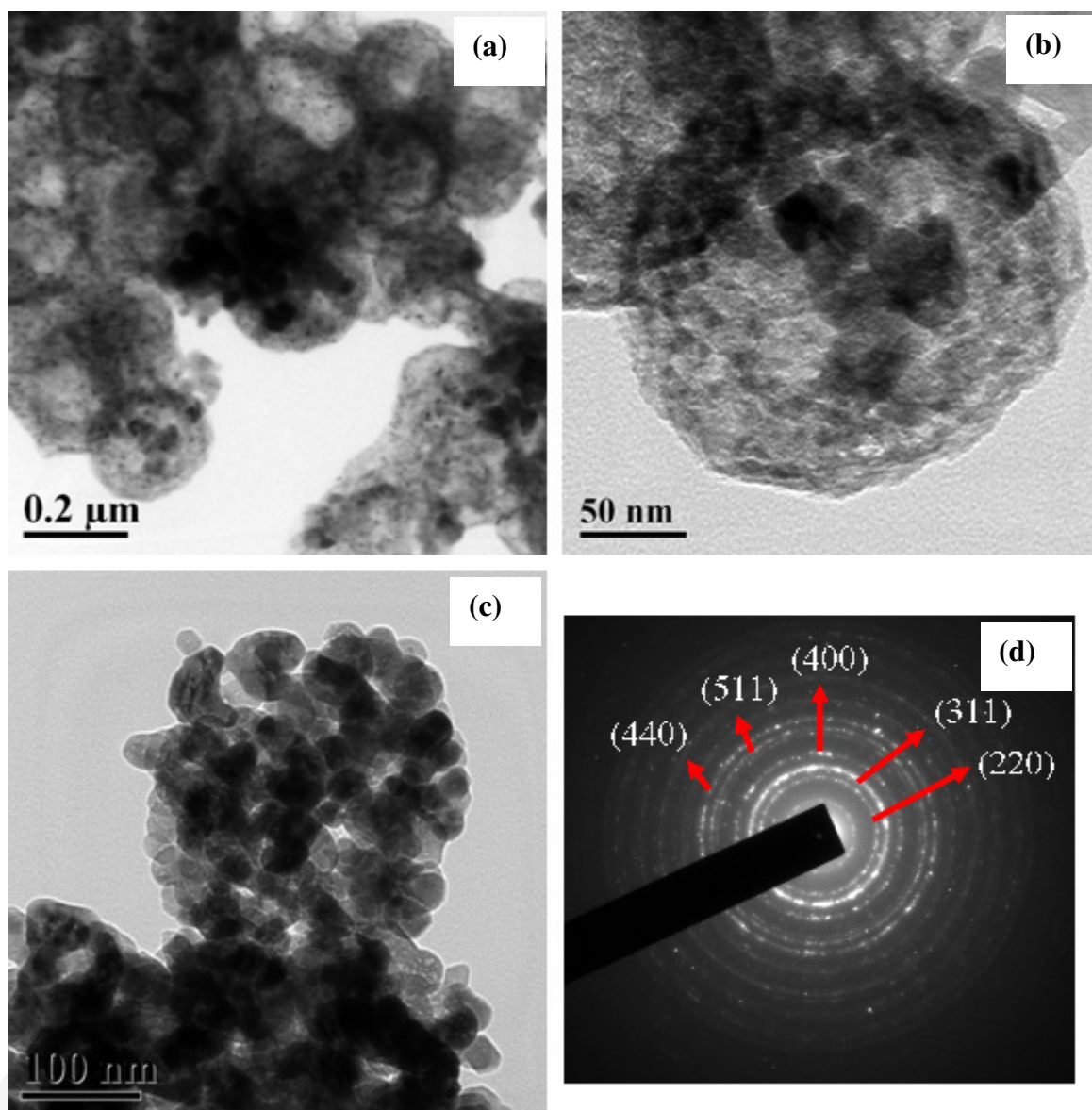


Fig. 3.40: TEM image of (a) the cluster of hollow-spheres, (b) the magnified image of a single hollow-sphere, (c) a partially formed hollow-sphere, and (d) the SAED pattern of these hollow-spheres

3.7.3. Gas Sensing Characteristics of $\text{Mg}_{0.5}\text{Zn}_{0.5}\text{Fe}_2\text{O}_4$ Hollow Spheres

Research efforts have been made to study the gas sensing characteristics of several conventional oxides in the form of hollow-spheres [13, 42]. However, very limited reports are available on the synthesis and gas sensing characteristics of spinel ferrite based hollow-spheres [43]. In the present section we have investigated the gas sensing characteristics of $\text{Mg}_{0.5}\text{Zn}_{0.5}\text{Fe}_2\text{O}_4$ hollow-spheres by varying the test gas concentration

and operating temperatures. Figure 3.41 shows the resistance transients for hydrogen gas sensing using $\text{Mg}_{0.5}\text{Zn}_{0.5}\text{Fe}_2\text{O}_4$ hollow-spheres. The test gas concentrations are varied in the range of 100-1000 ppm and the operating temperature is kept fixed at 300 °C. The response (%) at each gas concentration is marked in the figure. Although these hollow-spheres are sensitive to lower concentration of hydrogen detection (~100 ppm), we feel that the transduction characteristics need to be improved further. Marginal base-line drift is observed after repeated response and recovery.

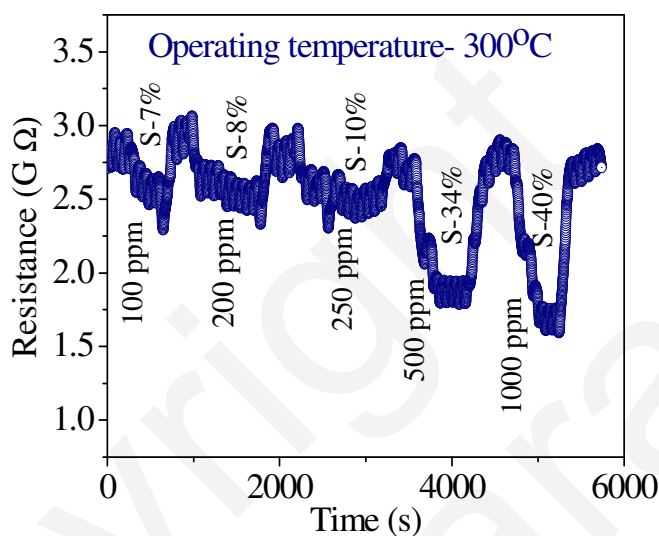


Fig. 3.41: Resistance transients of $\text{Mg}_{0.5}\text{Zn}_{0.5}\text{Fe}_2\text{O}_4$ hollow sphere sensors during H_2 gas sensing (100-1000 ppm). Transients are measured at ~ 300 °C.

As shown in Fig. 3.42 these hollow-spheres sense (a) N_2O and (b) CH_4 gas as well. The response characteristics of these hollow-spheres for four different gases (namely H_2 , CO , CH_4 and N_2O) are summarized in Fig. 3.43. The gas concentration is kept fixed ~1660 ppm and operating temperatures are varied in the range between 250-380 °C. Although these hollow-spheres have decent response at ~250 °C, the cross-selectivity among these gases remains a major problem. In the next section we have analyzed the relative merit and demerits of all the synthesized nano-structured oxides presented in the preceding sections.

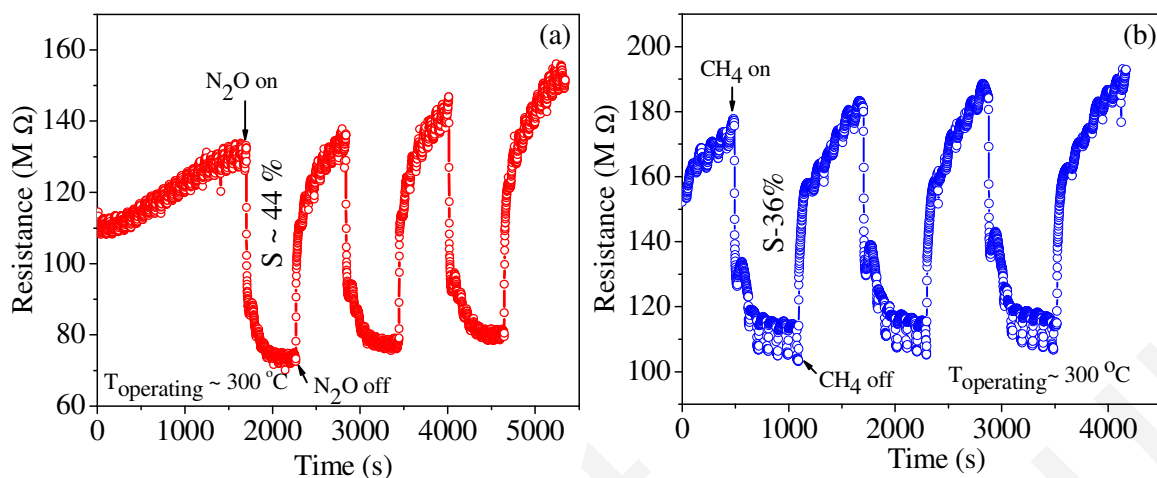


Fig. 3.42: Resistance transient of $\text{Mg}_{0.5}\text{Zn}_{0.5}\text{Fe}_2\text{O}_4$ hollow sphere based sensing element during sensing 1660 ppm of (a) N_2O and (b) CH_4 gas at operating temperature $\sim 300^\circ\text{C}$

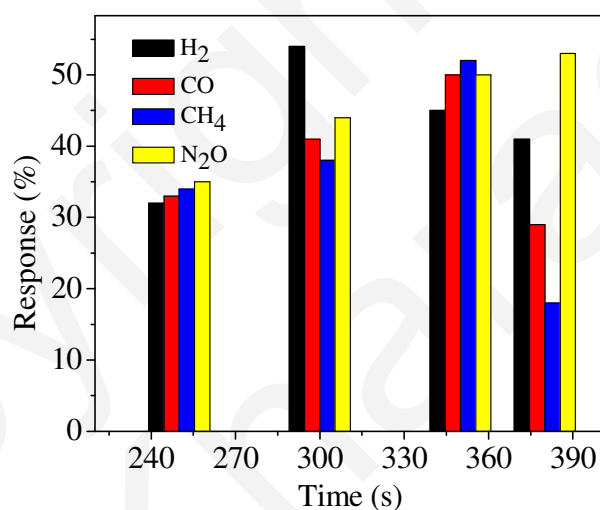


Fig. 3.43: Operating temperature dependence response (%) of $\text{Mg}_{0.5}\text{Zn}_{0.5}\text{Fe}_2\text{O}_4$ hollow sphere based sensing element towards the detection of ~ 1660 ppm H_2 , CO , CH_4 and N_2O gases

3.8. Pros and Cons of the Gas Sensing Characteristics of Tailor Made Spinel Nano-structures

After reviewing the results presented earlier in this chapter several questions come to our mind. The queries can be grouped as follows: (i) how the gas sensing performance of the spinel ferrites studied compare with their (conventional) binary oxide (e.g. SnO_2 , ZnO , WO_3 etc) counterparts? Keeping it straight, why should one seek for alternate gas

sensing materials? (ii) Theoretically, the positive effects of the nano-structured oxides towards their gas performances are well documented. However, the adaptability of these nano-structured oxides in making commercial sensing elements has not been tested adequately. This raises the question, even if the nano-structured oxide performs well in laboratory scale will they be commercially adapted in making sellable sensors? (iii) The cross-selectivity of the SMO based chemi-resistors towards various types of reducing gases remain a major research issue. It remains questionable if nano-structuring would make a particular sensing material selective for a specific gas sensing.

To address the first issue, we felt it necessary to compare the sensing performance of $\text{Mg}_{0.5}\text{Zn}_{0.5}\text{Fe}_2\text{O}_4$ (MZFO) spinel with the conventional oxides reported in recent literatures. Note that we have compared only hydrogen sensing performance. Fig. 3.44 shows the schematic of (a) MZFO pellet, (b) thin film and (c) embedded nano-tube, (d) isolated nano-tube, and (e) hollow-spheres with respective electrode configurations used for resistance measurements. The FESEM micrographs of these structures are shown respectively in Fig. 3.44(f) (pellet), (g) (thin film), (h) (embedded nano-tube), (i) (isolated nano-tube), and (j) hollow-spheres. The surface morphologies of these structures are distinctly different. Thus, as shown in Fig. 3.44(f), the bulk pellet ensures nano particulate nature with minimal MZFO grain growth. Moreover the sensor surface has both meso and macro-porous regions. The surface of MZFO thin film (Fig. 3.44(g)) is more compact and consists of nano-crystalline grains with uniform grain size distribution. Meso-porous regions are identified on the MZFO thin film surface. The porous natures of the embedded nano-tubes are clearly visible in Fig. 3.44 (h). The resistance transients of each of these nano-structures, measured upon exposing it to various concentration of hydrogen gas (10-1660 ppm) at elevated temperatures are shown in Fig. 3.44(k)-(o). Table-3.6 compares the hydrogen gas sensing performances of conventional oxides in different forms with the nano-structured $\text{Mg}_{0.5}\text{Zn}_{0.5}\text{Fe}_2\text{O}_4$ spinel elements summarized in Fig. 3.44. Inspecting Table-3.6, it is revealed that nano-structured spinel element has better gas detection limit and lower optimized operating temperature (T_{opt}) as compared to most of the conventional oxide nano-structures. There is a recent trend to use spinel and perovskite type oxides for gas sensing purpose. Use of these oxides is promoted to exploit the possibilities to make multi-functional gas sensors.

Material architecture

Morphology

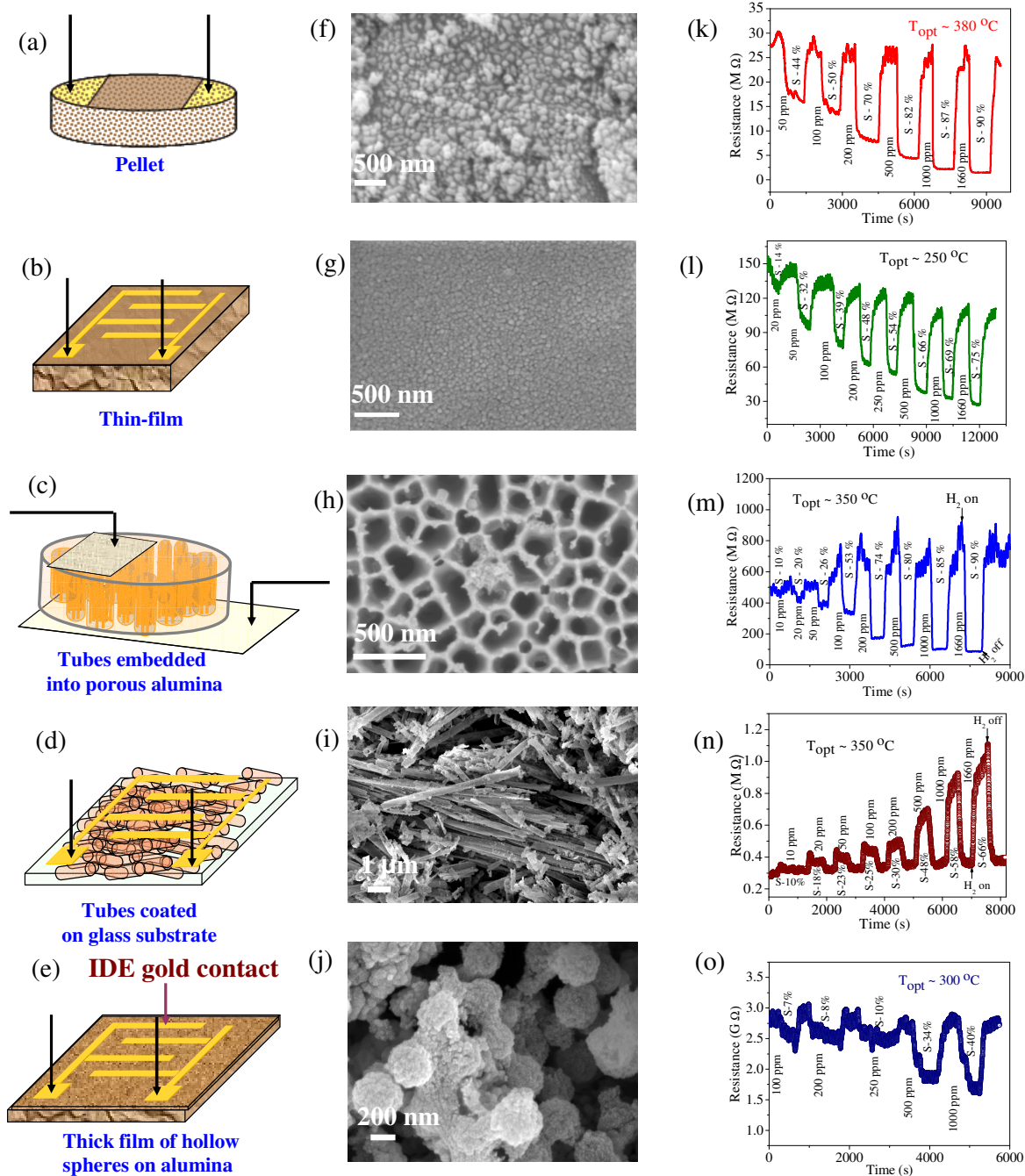
 H_2 sensing characteristics

Fig. 3.44: Schematic of $Mg_{0.5}Zn_{0.5}Fe_2O_4$ (a) pellet (b) thin film and (c) embedded nano-tube (d) isolated nano-tube (e) hollow sphere in the form of thick film with respective electrode configuration. The FESEM micrographs of (f) pellet (g) thin film (h) embedded nano-tubes (i) isolated nano-tubes (j) hollow sphere with respective resistance transients corresponding to hydrogen sensing at different gas concentrations for (k) pellet, (l) thin film and (m) embedded nano-tubes in anodized alumina templates (n) isolated nano-tubes and (o) hollow spheres

Table-3.6: Comparison of the H₂ sensing characteristics among the synthesized Mg_{0.5}Zn_{0.5}Fe₂O₄ sensing elements and conventional binary oxide based sensors

Sensing material	Architecture	Sensing set-up	H ₂ conc. (ppm)	T _{operating} (°C)	Response		Ref.
					R _a /R _g	ΔR/R _a	
SnO₂ Pt -SnO₂	Thin film	Dynamic	2500 2500	200 200	~2 ~6	[44]
SnO₂ Pd-SnO₂	Nanofibre	Static	100 100 (min^m 20)	320 280	~4 ~8.2	[45]
SnO₂ (by pyrolysis method) SnO₂ (by solution route)	Thick film	Dynamic	1000 1000	400 350	~19 ~60	[46]
SnO₂ SnO₂+Cr SnO₂+Cu SnO₂+Pd	Thick film	Static	200 200 200 200	400 400 400 350	~15 ~18 ~17 ~24	[47]
SnO₂ SnO₂-Pd (via impregnation) SnO₂-Pd (via direct solution method)	Thick film	Static	1000 (min^m 10)	300 275 250	~16 ~31 ~150	[48]
SnO₂ Al -SnO₂	Nanofibre	Static	100 (min^m 11.5) 100 (min^m 1.7)	340	~3.5 ~7.7	[49]
ZnO	Nanobelt	Dynamic	1000 (min^m 60)	385	~14	[50]
SnO₂ - carbon nano-tube	Film	Dynamic	100	100	~1.3	[51]
WO₃	Thin film	Dynamic	1000	300	~10	[52]
SnO₂	Nanowire	Dynamic	1000 (min^m 10)	300	~3.3	[53]
ZnO	Wire like thin films	Dynamic	200	200	~3	[54]
TiO₂/ WO₃	Thick film	Dynamic	200	200	~ 0.70	[55]
Mg_{0.5}Zn_{0.5}Fe₂O₄ <i>(by wet chemical)</i>	Pellet	Dynamic	1000 (min^m 50)	380	~11	~0.88	This work
	Embedded nano-tube		1000 (min^m 10)	350	~8	~0.87	
	Isolated nano-tube		1000 (min^m 10)	350	~2.4	~0.58	
	Thin film		1000 (min^m 20)	250	~3.3	~0.79	

Table-3.7 compares the H_2 sensing properties of the ferrites we have synthesized with the ones reported in literatures. Inspecting Table-3.7, it is clear that in most cases our synthesized compositions yield improved gas sensing performance. It is therefore fully justified to consider these ferrite compositions for gas sensing applications.

Table-3.7: Comparison of H_2 sensing characteristics of various cubic spinel ferrites with the synthesized $Mg_{1-x}Zn_xFe_2O_4$ ($0.0 \leq x \leq 1.0$) based sensing elements

Sensing material	Synthesis route	Morphology	Sensing set-up	Sensor characteristics			Ref	
				T _{opt} (°C)	Response			H ₂ (ppm)
					R _a /R _g	ΔR/R _a		
ZnFe ₂ O ₄	Molten salt	Thick film	Dynamic	250	~0.5	200	[56]
CuFe ₂ O ₄	Solid state reaction	Powder	Static	332	2	1000	[57]
CuFe ₂ O ₄ ZnFe ₂ O ₄ CoFe ₂ O ₄ NiFe ₂ O ₄	Chemical route	Thick film	Dynamic	250-400	≤0.4	[58]
CuFe ₂ O ₄ ZnFe ₂ O ₄ CdFe ₂ O ₄ MgFe ₂ O ₄	Chemical route	Thick film	Static	250 350 250 250	~10 ~05 ~20 ~08	6000	[59]
NiFe ₂ O ₄	Chemical route	Pellet	Dynamic	400	~ 0.2	200	[60]
MgFe ₂ O ₄	PVA assisted wet chemical route	Pellet	Dynamic	315	~2.6	~0.56	1000 (min ^m 100)	This work
Mg _{0.75} Zn _{0.25} Fe ₂ O ₄	-do-	Pellet	Dynamic	350	~1.8	~0.47	1000 (min ^m 100)	
Mg _{0.25} Zn _{0.75} Fe ₂ O ₄	-do-	Pellet	Dynamic	300	~2.1	~0.52	1000 (min ^m 100)	
ZnFe ₂ O ₄	-do-	Pellet	Dynamic	350	~ 2.1	~0.53	1000 (min ^m 100)	
Mg _{0.5} Zn _{0.5} Fe ₂ O ₄	-do-	Pellet	Dynamic	380	~2.2	~0.53	1000 (min ^m 100)	
Mg _{0.5} Zn _{0.5} Fe ₂ O ₄	Pechini route	Pellet	Dynamic	380	~11	~0.87	1000 (min ^m 50)	
Mg _{0.5} Zn _{0.5} Fe ₂ O ₄	-do-	Nano-tube embedded into alumina template	Dynamic	350	~8	~0.86	1000 (min ^m 10)	
Mg _{0.5} Zn _{0.5} Fe ₂ O ₄	-do-	Nano-tube coated on quartz	Dynamic	350	~2.4	~0.58	1000 (min ^m 10)	
Mg _{0.5} Zn _{0.5} Fe ₂ O ₄	-do-	Thin film	Dynamic	250	~3.3	~0.79	1000 (min ^m 20)	
Mg _{0.5} Zn _{0.5} Fe ₂ O ₄	Hydrothermal route	Hollow sphere coated on quartz	Dynamic	300	~1.7	~0.4	1000 (min ^m 100)	

The second issue is too complicated to answer in a straight forward way. Figure 3.45 (a) compares the response (%) as a function of operating temperature for a variety of nano-structured $\text{Mg}_{0.5}\text{Zn}_{0.5}\text{Fe}_2\text{O}_4$ sensing elements. The response (%) for 100 ppm hydrogen gas sensing for various nano-structured $\text{Mg}_{0.5}\text{Zn}_{0.5}\text{Fe}_2\text{O}_4$ sensing elements are compared in Fig. 3.45(b). Inspecting Fig. 3.45, it is clearly demonstrated that indeed the gas sensing performance is largely dependent on nano-structuring of the oxide sensing elements. Thus, as shown in Fig. 3.45(a), T_{opt} is found to be grossly reduced in $\text{Mg}_{0.5}\text{Zn}_{0.5}\text{Fe}_2\text{O}_4$ thin films. Also as shown in Fig. 3.45 (b), for low concentration H_2 sensing, the embedded nano-tube exhibit much better response characteristics as compared to the other nano-structures. Even if these nano-structured materials have improved gas sensing performance, at this stage, it is difficult to predict about their commercial acceptance. Usually the nano-structured electrodes have larger surface resistance as compared to the conventional oxide nano-structures. For commercial sensors this would increase the sensor power. Synthesis of these nano-structures for large scale production is also a challenging task.

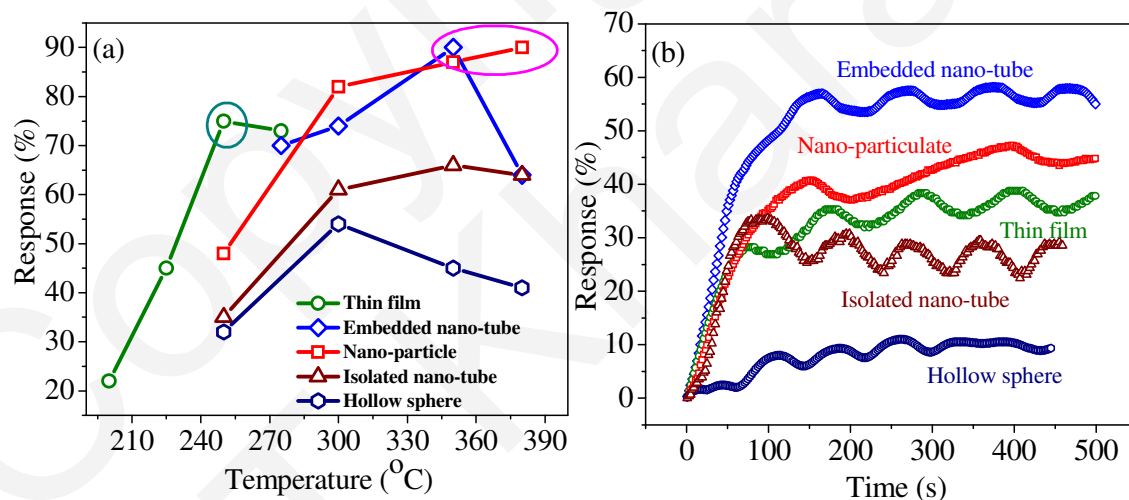


Fig. 3.45: (a) Variation of response (%) of $\text{Mg}_{0.5}\text{Zn}_{0.5}\text{Fe}_2\text{O}_4$ based nano-structured sensing elements as a function of operating temperature towards the detection of 1660 ppm of H_2 gas. (b) response transient of $\text{Mg}_{0.5}\text{Zn}_{0.5}\text{Fe}_2\text{O}_4$ based nano-structured sensing elements towards the detection of 100 ppm of H_2 gas

The cross-selectivity could not be avoided in any of these nano-structured spinel electrodes. We have addressed the cross-selectivity issue of SMO based sensing elements separately in Chapter-4 and 5.

3.9. Summary and Conclusions

We have optimized the precursor chemistry and heat treatment schedule to synthesize nano-crystalline $\text{Mg}_{1-x}\text{Zn}_x\text{Fe}_2\text{O}_4$ ($0.0 \leq x \leq 1.0$) powders using PVA assisted wet chemical synthesis route. Among these compositions, it is reported that only $\text{Mg}_{0.5}\text{Zn}_{0.5}\text{Fe}_2\text{O}_4$ (MZFO) particles can be synthesized phase pure [(cubic spinel, without the formation of any other impurity phase/(s))] by calcining it at a temperature as low as 300 °C. The powders are nano-crystalline (~ 20 nm) and having meso-porous surface morphologies. Among all the solid solution compositions, $\text{Mg}_{0.5}\text{Zn}_{0.5}\text{Fe}_2\text{O}_4$ sensing elements exhibit superior gas sensing characteristics in terms of response, response/recovery time and marginal base line drift.

Further improvement of the gas sensing characteristics of $\text{Mg}_{0.5}\text{Zn}_{0.5}\text{Fe}_2\text{O}_4$ elements are achieved using powders synthesized by a citrate assisted self combustion Pechini route. The improvement in gas sensing characteristics of Pechini route derived powders are explained to be due to their comparatively larger specific surface area and uniform pore-size distribution leading to better gas diffusion.

Using a modified Pechini route, we have synthesized $\text{Mg}_{0.5}\text{Zn}_{0.5}\text{Fe}_2\text{O}_4$ in the form of nano-tube (embedded in anodized alumina, and isolated) and thin films. Additionally, using a spherical carbon template assisted hydrothermal synthesis route we have also synthesized $\text{Mg}_{0.5}\text{Zn}_{0.5}\text{Fe}_2\text{O}_4$ hollow-spheres. We have reported a charge carrier reversal from n to p type in MZFO isolated nano-tubes. The inversion of charge carrier is explained to be solely dependent on the surface morphology of isolated $\text{Mg}_{0.5}\text{Zn}_{0.5}\text{Fe}_2\text{O}_4$ nano-tubes. In case of hydrogen sensing, we have reported that the embedded nano-tubes are sensitive enough for lower concentration (~10 ppm) hydrogen gas sensing. An excellent hydrogen response (~90%) is achieved for particulate as well as embedded nano-tube sensors at higher operating temperatures (≥ 350 °C). The temperature corresponding to the maximum response (~75%) is significantly reduced (~250 °C) for MZFO thin film sensors. For all these nanostructures, response and recovery times are estimated for various H_2 gas concentrations. Although the nano-tubes embedded in anodized alumina template exhibit promising hydrogen sensing characteristics, further research is needed to reduce the base resistance and operating temperature corresponding to the maximum response.

Reference

- [1] Korotcenkov, G., (2007), Metal Oxides for Solid State Gas Sensors: What Determines Our Choice?, *Materials Science and Engineering B*, Vol.139, pp. 1-23.
- [2] Han, N., Chai, L., Wang, Q., Tian, Y., Deng, P. and Chen, Y. (2010), Evaluating the Doping Effect of Fe, Ti and Sn on Gas Sensing Property of ZnO, *Sensors and Actuators B*, Vol.147, pp. 525-530.
- [3] Ionescu, R., Hoel, A., Granqvist, C.G., Llobet, E. and Heszler, P. (2005), Ethanol and H₂S Gas Detection in Air and in Reducing and Oxidizing Ambience: Application of Pattern Recognition to Analyse the Output Form Temperature Modulated Nanoparticles WO₃ Gas Sensors, *Sensor and actuators B*, Vol. 104, pp. 124-131.
- [4] Cadena, G.J., Riu, J. and Rius, F.X. (2007), Gas Sensors Based on Nanostructured Materials, *The Analyst*, Vol. 132, pp.1083-1099.
- [5] Gong, J.S., and Chen, J.Q. (2008), Micromachined Sol-Gel Carbon Nanotube/SnO₂ Nanocomposite Hydrogen Sensor, *Sensors and Actuators B*, Vol. 130, pp. 829-835.
- [6] Zhu, H., Gu, X., Zuo, D., Wang, Z., Wang, N. and Yao, K. (2008), Microemulsion Based Synthesis of Porous Zinc Ferrite Nanorods and its Application in a Room-Temperature Ethanol Sensor, *Nanotechnology*, Vol. 19, pp. 405503 (5).
- [7] Kamble, R.B. and Mathe, V. L. (2008), Nanocrystalline Nickel Ferrite Thick Film as an Efficient Gas Sensor at Room Temperature, *Sensors and Actuators B*, Vol. 131, pp. 205-209.
- [8] Zhang, G., Li, C., Cheng, F. and Chen, J. (2007), ZnFe₂O₄ Tubes: Synthesis and Application to Gas Sensors with High Sensitivity and Low-Energy Consumption, *Sensors and Actuators B*, Vol.120, pp. 403-410.
- [9] Simon, U., Sanders, D., Jockel, J. and Brinz, T. (2005), Setup for High Throughput Impedance Screening of Gas Sensing Materials, *Journal of Combinatorial Chemistry*, Vol. 7, pp. 682–687.
- [10] Jun, J.H., Yun, J., Cho, K., Hwang, I.S., Lee, J.H. and Kim, S. (2009), Necked ZnO Nanoparticle Based NO₂ Sensors with High and Fast Response, *Sensors and Actuators B*, Vol.140, pp. 412-417.
- [11] Senguttuvana, T.D., Srivastava, V., Tawal, J.S., Mishra, M., Srivastava, S. and Jain, K. (2010), Gas Sensing Properties of Nanocrystalline Tungsten Oxide Synthesized by Acid Precipitation Method, *Sensors and Actuators B*, Vol.150, pp. 384-388.
- [12] Gerlitza, R.A., Benkstein, K.D., Lahr, D.L., Hertz, J.L., Montgomery, C.B., Bonevich, J.E., Semancik, S. and Tarlov, M.J. (2009), Fabrication and Gas Sensing Performance of Parallel Assemblies of Metal Oxide Nanotubes Supported by Porous Aluminum Oxide Membranes, *Sensors and Actuators B*, Vol.136, pp. 257-264.

-
- [13] Moon, H.G., Shim, Y.S., Su, D., Park, H.H., Yoon, S.J. and Jang, H.W. (2011), Embossed TiO₂ Thin Films with Tailored Links between Hollow Hemispheres: Synthesis and Gas-Sensing Properties, *The Journal of Physical Chemistry C*, Vol. 115, pp. 9993-9999.
- [14] Cheng, Z.X., Ren, X.H., Xu, J.Q. and Pan, Q.Y. (2011), Mesoporous In₂O₃: Effect of Material Structure on the Gas Sensing, *Journal of Nanomaterials*, Article ID 654715, (6).
- [15] Varghese, O.K. and Grimes, C.A. (2003), Metal Oxide Nanoarchitectures for Environmental Sensing, *Journal of Nanoscience and Nanotechnology*, Vol. 3, pp. 277-293.
- [16] Zhang, G.Y., Guo, B. and Chen, J. (2006) MCo₂O₄ (M=Ni, Cu, Zn) Nanotubes: Template Synthesis and Application in Gas Sensors, *Sensors and Actuators B*, Vol. 114, pp. 402-409.
- [17] Waldron, R.D. (1955), Infrared Spectra of Ferrites, *Physics Review*, Vol. 99, pp. 1727-1735.
- [18] Ladgaonkar, B.P., Kolekar, C.B. and Vaingankar A.S. 2002, Infrared Absorption Spectroscopic Study of Nd³⁺ Substituted Zn-Mg Ferrites, *Bulletin of Materials Science*, Vol. 25, pp. 351-354.
- [19] Srinivasan, T.T., Srivastava, C.M., Venkataramanin, N. and Patni, M.J. Infrared Absorption in Spinel Ferrites, *Bulletin of Materials Science*, Vol. 6, pp. 1063-1067.
- [20] Sing, K.S.W., Everett, D.H., Haul, R.A.W., Moscou, L., Pierotti, R.A., Rouquerol, J. and Siemieniewska, T. (1985), Reporting Physisorption Data for Gas/ Solid Systems with Special Reference to the Determination of Surface Area and Porosity, *Pure and Applied Chemistry*, Vol. 57, pp. 603-619.
- [21] Zhao, H., Li, Y., Yang, L. and Wu, X. (2008), Synthesis, Characterization and Gas Sensing Property for C₂H₅OH of SnO₂ Nanorods, *Materials Chemistry and Physics*, Vol. 112, pp. 244-248.
- [22] Aifan, C., Xiaodong, H., Zhangfa, T., Shouli, B., Ruixian, L. and Chiun, L.C. (2006), Preparation Characterization and Gas Sensing Properties of SnO₂-In₂O₃ Nanocomposite Oxides, *Sensors and Actuators B*, Vol. 115, pp. 316-321.
- [23] Biswas, S.K., Pramanik, P. (2008), Studies on the Gas Sensing Behaviour of Nanosized CuNb₂O₆ towards Ammonia, Hydrogen and Liquefied Petroleum Gas, *Sensors and Actuators B*, Vol. 133, pp. 449-455.
- [24] Yue, Z., Guo, W., Zhou, J., Gui, Z. and Li, L. (2004), Synthesis of Nanocrystalline Ferrites by Sol Gel Combustion Process: The Influence of pH Value of Solution, *Journal of Magnetism and Magnetic Materials*, Vol. 270, pp. 216-223.
- [25] Tiemann, M. (2007), Porous Metal Oxides as Gas Sensors, *Chemistry-A European Journal*, Vol. 13, pp. 8376-8388.
-

-
- [26] Kirk, R.E. and Othmer, D. (1984), Encyclopedia of Chemical Technology, New York, Wiley, Vol 9, 3rd Edition.
- [27] Zenger, M. (1994), Modern Ferrite Technologies and Products, International Journal of Materials and Product Technology, Vol. 9, pp 265-272.
- [28] Barba, A., Orts, M.J., Sanchez, E. and Clausell, C. (2000), Kinetic Model Applicable to Synthesis of $(\text{Cu}_{0.25}\text{Ni}_{0.25}\text{Zn}_{0.5})\text{Fe}_2\text{O}_4$ Ferrite, British Ceramic Transaction, Vol. 99, pp. 53-56.
- [29] Korswaimy, L.K. and Sharma, M.M. (1984), Heterogeneous Reactions Analysis Examples and Reactor Design, New York, Wiley, 1st Edition.
- [30] El-shobaky, H.G. (2000), Solid-Solid Interactions between ZnO and Fe_2O_3 as influenced by Al_2O_3 doping, Thermochim Acta, Vol. 343, pp.145-150.
- [31] El-shobaky, H.G. and Radwan, N.R.E. (2003), Investigation of Solid-Solid Interactions in NiO/ Fe_2O_3 System Doped with ZnO, Thermochimica Acta, Vol. 398, pp. 223-231.
- [32] Wisitsoraat, A., Tuantranont, A., Comini, E., Sberveglieri, G. and Wlodarski, W. (2009) Characterization of n-type and p-type Semiconductor Gas Sensors Based on NiO_x Doped TiO_2 Thin Films, Thin Solid Films, Vol. 517, pp. 2775-2780.
- [33] Galatsis, K., Cukrov, L., Wlodarski, W., McCormick, P., Kalantarzadeh, K., Comini, E. and Sberveglieri, G. (2003), p- and n-type Fe-Doped SnO_2 Gas Sensors Fabricated by the Mechanochemical Processing Technique, Sensors and Actuators B, Vol. 93, pp. 562-565.
- [34] Wang, J.X., Sun, X.W., Yang, Y. and Wu, C.M.L. (2009), N-P Transition Sensing Behaviors of ZnO Nanotubes Exposed to NO_2 Gas, Nanotechnology, Vol. 20, pp. 465501 (4).
- [35] Siciliano, T., Tepore, A., Micocci, G., Genga, A., Siciliano, M. and Filippo, E. (2009), Transition from n-to p-Type Electrical Conductivity Induced by Ethanol Adsorption on Tellurium Dioxide Nanowires. Sensors and Actuators B., Vol.138, 207-213.
- [36] Kim, D., Rothschild, A., Lee, B.H., Kim, D.Y., Jo, S.M. and Tuller, H.L. (2006) Ultrasensitive Chemiresistors Based on Electrospun TiO_2 Nanofibers, Nano Letters, Vol. 6, pp. 2009-2013.
- [37] Xue, X.Y., Zhao, H.C., Chen, Y.J., Ma, C.H., Xing, L.L., Wang, Y.G. and Wang, T.H. (2010), Abnormal Gas Sensing Characteristics Arising from Catalyzed Morphological Changes of Adsorbed Oxygen, Nanotechnology, Vol. 21, pp. 065501 (5).
- [38] Gurlo, A., Barsan, N., Oprea, A., Sahm, M., Sahm, T. and Weimar, U. An n-to p-Type Conductivity Transition Induced by Oxygen Adsorption on $\alpha\text{-Fe}_2\text{O}_3$, Applied Physics Letters, Vol. 85, pp. 2280-2282.
- [39] Anjum, S., Jaffari, G.H., Rumaiz, A.K., Rafique, M.S. and Shah, S.I. (2010), Role of Vacancies in Transport and Magnetic Properties of Nickel Ferrite Thin Films, Journal of Physics D: Applied Physics, Vol. 43, pp. 265001 (7).
-

-
- [40] Korotcenkov, G. and Cho, B.K. (2009), Thin Film SnO_2 Based Gas Sensors: Film Thickness Influence, *Sensors and Actuators B*, Vol. 142, pp. 321-330.
- [41] Choe, Y. S. (2001), New Gas Sensing for SnO_2 Thin Film Gas Sensors Fabricated by Using Dual Ion Beam Sputtering. *Sensors and Actuators B*, Vol. 77, pp. 200-208.
- [42] Yin, X.M., Li, C.C, Zhang, M., Hao, Q.Y., Liu S., Li, Q.H., Chen, L.B. and Wang, T.H.(2009), SnO_2 Monolayer Porous Hollow Spheres as a Gas Sensor, *Nanotechnology*, Vol. 20, pp. 455503 (6).
- [43] Li, Z., Lai, X., Wang, H., Mao, D., Xing, C. and Wang, D. (2009), General Synthesis of Homogeneous Hollow Core-Shell Ferrite Microspheres, *The Journal of Physical Chemistry C*, Vol.113, pp. 2792-2797.
- [44] Ramgir, N.S., Hwang, Y.K., Jhung, S.H., Mulla, I.S. and Chang, J.S. (2006), Effect of Pt Concentration on the Physiochemical Properties and CO Sensing Activity of Meso Structured SnO_2 , *Sensors and actuators B*, Vol. 114, pp. 275-282.
- [45] Zhanga, H., Li, Z., Liu, Li., Xu, X., Wanga, Z., Wang, W., Zheng, W., Dong, B. and Wang, C. (2010), Enhancement of Hydrogen Monitoring Properties Based on Pd- SnO_2 Composite Nanofibers, *Sensors and Actuators B*, Vol.147, pp.111-115.
- [46] Hieda, K., Hyodo, T., Shimizu, Y. and Egashira, M. (2008) Preparation of Porous Tin Dioxide Powder by Ultrasonic Spray Pyrolysis and Their Application to Sensor Materials, *Sensors and Actuators B*, Vol.133, pp. 144-150.
- [47] Zeng, W., Liu, T., Liu, D. and Han, E.(2011), Hydrogen Sensing and Mechanism of M-Doped SnO_2 ($M = \text{Cr}^{3+}$, Cu^{2+} and Pd^{2+}) Nanocomposite, *Sensors and Actuators B*, (in Press), doi:10.1016/j.snb.2011.08.008.
- [48] Zhao, J., Wang, W., Liu, Y., Ma, J., Li, X., Du, Y. and Lu, G. (2011) Ordered Mesoporous Pd/ SnO_2 Synthesized by a Nanocasting Route for High Hydrogen Sensing Performance, *Sensors and Actuators B*, (in Press), doi:10.1016/j.snb.2011.08.035.
- [49] Xu, X., Sun, J., Zhang, H., Wang, Z., Dong, B., Jiang, T., Wang, W., Li, Z. and Wang, C., Effects of Al Doping on SnO_2 Nanofibers in Hydrogen Sensor, *Sensors and Actuators B*, (in Press), doi:10.1016/j.snb.2011.08.072.
- [50] Sadek, A.Z., Chooapun, S., Wlodarski, W., Ippolito, S.J. and Kalantarzadeh, K. (2007), Characterization of ZnO Nanobelt-Based Gas Sensor for H_2 , NO_2 , and Hydrocarbon Sensing, *IEEE Sensors Journal*, Vol. 7, pp. 919-924.
- [51] Yang, M., Kim, D.H., Kim, W.S. Kang, T.J., Lee, B.Y., Hong, S., Kim,Y.H. and Hong, S.H.(2010), H_2 Sensing Characteristics of SnO_2 Coated Single Wall Carbon Nanotube Network Sensors, *Nanotechnology*, Vol. 21, pp. 215501 (7).
- [52] Shen,Y., Yamazaki, T., Liu, Z., Meng, D., Kikuta, T. and Nakatani, N. (2009), Influence of effective surface area on gas sensing properties of WO_3 sputtered thin films, *Thin Solid Films*, Vol. 517, pp. 2069-2072.
-

-
- [53] Wang, B., Zhu, L. F., Yang, Y. H., Xu, N. S. and Yang G. W. (2008), Fabrication of a SnO₂ Nanowire Gas Sensor and Sensor Performance for Hydrogen, *Journal of Physical Chemistry C*, Vol.112, pp.6643-6647.
- [54] Hwang, C., (2009) Synthesis and Hydrogen Gas Sensing Properties of ZnO Wirelike Thin Flms, *Journal of Vacuum Science and Technology A*, Vol. 27, pp.1347-1351.
- [55] Chaudhari, G.N., Bende, A.M., Bodade, A.B., Patil, S.S. and Sapkal, V.S. (2006), Structural and Gas Sensing Properties of Nanocrystalline TiO₂:WO₃-Based Hydrogen Sensors, *Sensors and Actuators B*, Vol. 115, pp. 297-302.
- [56] Darshane, S.L., Deshmukh, R.G., Suryavanshi S.S. and Mullah, I.S., (2008), Gas-Sensing Properties of Zinc Ferrite Nanoparticles Synthesized by the Molten-Salt Route, *Journal of American Ceramic Society*, Vol. 91, pp. 2724-2726.
- [57] Sun, Z. Liu, L., Jia, D.Z. and Pan, W. (2007), Simple Synthesis of CuFe₂O₄ Nanoparticles as Gas-Sensing Materials, *Sensors and Actuators B*, Vol. 125, pp.144-148.
- [58] Reddy, C.V.G., Manorama, S.V. and Rao, V.J. (2000), Preparation and Characterization of Ferrites as Gas Sensor Materials, *Journal of Materials Science Letters*, Vol. 19, pp. 775-778.
- [59] Chen, N.S., Yang, X.J., Liu, E.S. and Huang, J.L. (2000), Reducing Gas-Sensing Properties of Ferrite Compounds MFe₂O₄ (M= Cu, Zn, Cd and Mg), *Sensors and Actuators B*, Vol. 66, pp. 178-180.
- [60] Darshane, S.L., Suryavanshi, S.S. and Mulla, I.S. (2009), *Ceramic International*, Nanostructured nickel ferrite: A liquid petroleum gas sensor,

Chapter-4

KINETIC ANALYSES OF RESISTANCE/ CONDUCTANCE TRANSIENTS OF FERRITE BASED SENSING ELEMENTS

4.1. Introduction

The present chapter deals with the analyses of resistance/conductance transients recorded during the response and recovery of gas sensing measurements. As described in Chapter-1, the principle of semiconducting metal oxide (SMO) gas sensors are based on the change of the surface resistance when exposed to reducing/ oxidizing gases. It has been demonstrated that irrespective of the n or p type oxide, the resistance of the sensor in air (R_a) changes in exposure to a reducing gas finally to attain steady state value (R_g). In most of the gas sensing studies, the response (%) (S) of the sensing element is usually measured from the temperature and gas concentration dependence of the sensor resistances (R_a , R_g) under equilibrium condition using either the relation $S=R_a/R_g$ or $S=(R_a-R_g)/R_a$ [1-4]. Analyses of the transient of initial sensor resistance in air (R_a) to its steady state value (R_g) during gas sensing have grossly been overlooked in most of the reports [5-7]. The correlation among the measured resistance transients and the adsorption, desorption, diffusion and interaction of gases is a complicated issue and not been fully understood. The factors such as adsorption/ desorption of gases, diffusion and interaction are in turn dependent on the composition of the sensor material, morphology of the sensing surface, operating temperature and gas concentration. Collectively all these factors influence the resistance transients during response and recovery. To correlate the resistance/ conductance change of the sensing element with the sequential surface

reactions among the adsorbed gas molecules and sensing surface, the kinetics of adsorption/ desorption as well as interaction of gases with the sensing surface need to be investigated. We feel that kinetic analysis of the resistance/conductance transient during gas sensing could provide valuable insight to the gas sensing mechanism operative to spinel sensors. Available literature reports on the analyses of resistance/ conductance transients fail to provide a comprehensive interrelation between the structure and gas sensing performance, especially for spinel based gas sensors [8-10]. In the present chapter for spinel based gas sensors, the kinetics of the response as well recovery behavior has been investigated through the analyses of respective conductance transients (during gas response and recovery) using Langmuir adsorption isotherm [11-13]. The variation of relaxation times during response and recovery as a function of gas concentration and temperature has been studied and the underlying mechanism/(s) controlling the gas sensing behavior of sensing elements are discussed. Prior to describe the modeling of the response and recovery transients of spinel based gas sensors, we have described the salient features of gas-solid interaction in the following section.

4.2. Salient Features of Gas-Solid Interaction during Gas Sensing

As reported in several research reports, the reaction mechanism for the sensing of reducing gas by an ‘n’ type semiconductor can be summarized as follows [9, 14]. In a first step, at elevated temperature, oxygen is physi-adsorbed in the sensor surface followed by the electron transfer from the semiconducting oxide to adsorbed oxygen to form chemical bond between the adsorbed oxygen and the semiconducting oxides. These reactions are described in Eqn. 4.1 and 4.2 respectively



The exact nature of chemiadsorbed oxygen is subject to debate and depending on the temperature of adsorption; oxygen may be of atomic or molecular origin. When the sensor is exposed to reducing gas ambient, the reducing gas is (physi) adsorbed on the sensor surface (Eqn. 4.3) and react with the pre-adsorbed oxygen according to the

reaction (Eqn. 4.4) and the product (RO_{gas}) escapes (Eqn. 4.5) when flushed further with air.



Out of these reactions the physi-adsorption of oxygen as well as reducing gas (Eqn. 4.1 and 4.3) are fast. On the other hand the reaction between the adsorbed gas and oxygen (Eqn. 4.4) is a slow process and therefore is the rate determining step for the response kinetics. Similarly for recovery (when reducing gas is turned off) out of reaction mentioned in Eqn. 4.2 and Eqn. 4.5, the later determines the rate of recovery kinetics. Since the chemi-adsorption of oxygen (molecular or atomic anionic species) over sensing surface form an electron depleted layer at the grain surface, these will lead to the formation of potential barrier for grain to grain electron migration. At a temperature T , the conductance of the sensor is determined by the barrier height through the well known Schottky relation

$$G(t) = G_0 \exp^{(-eV_s/kT)} \quad (4.6)$$

where eV_s is the Schottky barrier and k is the Boltzmann constant.

When the sensor is exposed to reducing gas, it reacts with chemiadsorbed oxygen species (see Eqn. 4.4), resulting the lowering of potential barrier which leads to the increase in conductance.

For the chemi-adsorption, a molecule will have to loose adequate amount of energy after the interaction with the sensing surface. The adsorption phenomenon of oxygen over sensing surface can be described using Lennard Jones diagram for non-activated adsorption (for trajectory A-D) shown schematically in Fig. 4.1 [15]. According to Lennard Jones diagram for oxygen adsorption, not all gas (oxygen) molecules approaching towards the sensing surface will be readily adsorbed. When the oxygen molecules with very high kinetic energy interact with the sensing surface (assuming the

motion of the oxygen molecules only from Z direction), these may reflect back from the sensing surface by two interaction pathways (i) without losing any energy (elastic collision shown in trajectory A) or (ii) gaining more energy (inelastic collision shown in trajectory B). The molecules with relatively low kinetic energy can not lose enough energy after colliding with the sensing surface and generally these are physisorbed on it (trajectory D). These physisorbed oxygen molecules will have to cross an energy barrier to fall in the potential well and thereby be chemisorbed on the surface (see Fig. 4.1). In order to fall directly into the chemisorption well the molecule will have to

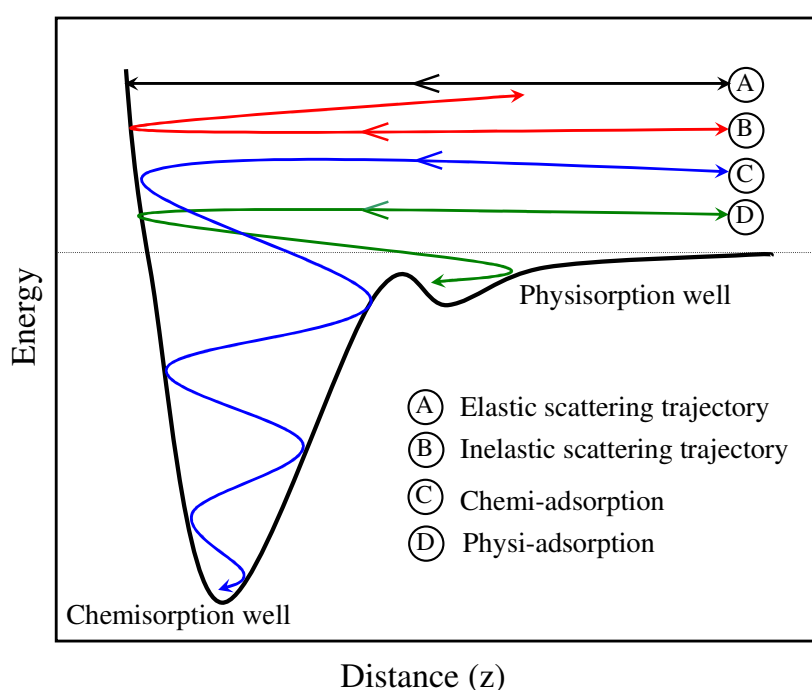


Fig. 4.1: Lennard Jones diagram for non activated gas adsorption

lose sufficient energy after the interaction with the sensor surface (trajectory C). It has been found that for a semiconducting oxide sensor, the chemisorption of oxygen increases when the sensing surface is heated to an optimized temperature. When heated beyond this optimized temperature the oxygen molecules are desorbed from the sensing surface. Additionally, with the rise in sensor temperature the physisorbed molecules also gain sufficient energy to cross the potential barrier and chemisorb on the sensing surface. When the surface temperature is raised to sufficiently higher temperature, the probability of desorption of the highly energetic oxygen molecules

predominate. Therefore, for each sensing surface there is an optimum temperature for the maximum chemi-adsorption of oxygen molecules. During gas sensing the reducing gas (R_{gas}) reacts with the chemiadsorbed oxygen (O_{ad}) molecules to form oxidized reaction product (RO_{ad}). There are several possible mechanisms hypothesized for the formation of the reaction product (RO_{ad}) [15]. The most common reaction mechanism is known as Langmuir-Hinshelwood mechanism where the gas molecules (e.g. R_{gas} and O_2) first adsorb (on the sensing surface) and then collide and form reaction product (e.g. RO_{ad}). In another mechanism known as Elay-Rideal mechanism, the reducing gas (e.g. R_{gas}) directly react with the pre-adsorbed gas (e.g. O_{ad}) and form the reaction product (e.g. RO_{ad}) which escapes directly in gas phase. Whatever be the mechanism, the formation of RO_{ad} is dependent on the kinetic energy of R_{gas} molecules and the heat of formation of the respective surface reactions. With the increase of test gas concentration, generally the formation of RO_{ad} expedites and as result the sensor response is increased. The generalized reaction sequence [Eqn. 4.1- 4.5] should cumulatively be reflected in the measured resistance transients during response and recovery of the gas sensing. In most of the gas sensing studies, the response (%) of the sensing elements is usually measured in the equilibrium condition. The dynamics of the gas sensing process (viz. surface oxidation/ reduction, electron exchange, desorption of the reaction product etc. is overlooked when the sensor characteristics is estimated from the resistance measurement under equilibrium condition. For ferrite based gas sensing materials there is an urgent need to undertake a detailed investigation on the resistance/ conductance transients in order to better understand the gas sensing kinetics through gas-solid interaction. In the subsequent sections the gas-solid interaction is investigated for MgFe_2O_4 (MFO), $\text{Mg}_{0.5}\text{Zn}_{0.5}\text{Fe}_2\text{O}_4$ (MZFO) and ZnFe_2O_4 (ZFO) nano-particulate sensing elements. The surface morphology and preliminary gas sensing characteristics of these sensing elements prepared by PVA assisted and Pechini routes are already reported in Chapter-3.

4.3. Experimental

MgFe₂O₄ (MFO), and ZnFe₂O₄(ZFO) nano-crystalline powders are synthesized using PVA assisted wet chemical synthesis route. Mg_{0.5}Zn_{0.5}Fe₂O₄ nano-crystalline powders are synthesized using both PVA assisted (MZFO-P) and citric acid and ethylene glycol assisted Pechini routes (MZFO-C). The ZnO nano-crystalline powders are also prepared using a chemical precipitation route. These powders are mixed with a few drop of PVA solution (10 %) as binder and pressed in the form of thin circular discs (thickness ~0.1 mm and diameter ~12 mm) using a hydraulic press. The pellets are sintered in a two step process; first, it is fired at 400 °C for 1 h for the removal of binder followed by sintering at 600 °C for 2 h in air. The above heat treatment ensures minimal particle growth, necking between particles, sufficient handling strength and porous nature of the sensing element. For the electrical measurements, one of the surfaces of the sensing elements are sputter coated with planar gold stripes of 7mm length, 3 mm wide and separated from each other by 4mm. A dynamic flow gas sensing measurement set-up (developed in our laboratory) is used to measure the resistance transients (for response and recovery) as a function of temperature and test gas concentration. Pre-diluted (concentration ~ 10000 ppm in diluted N₂) H₂ and CO are used as test gas. For resistance measurements, spring loaded probes (fixed in the reactor unit) are connected to the surface contacts coated on these sensing elements. The probes are connected to an electrometer (6517A, Keithley Instruments, USA) which acts as a source-measure unit for resistance measurements. The mass flow controllers (MFCs) (M100B, MKS instruments, USA) and electrometer are interfaced with a PC equipped with RS-232 interface, GPIB card (National Instruments, USA) and Labview 8.5 (National Instruments, USA) software. For the resistance measurements a fixed voltage is applied to the planar electrodes and the surface current is measured by the electrometer. In the voltage range between 1-5 V, an Ohmic behavior is observed and from the measured current, resistance is calculated [11].

4.4. Modeling the Conductance Transients during Response and Recovery

The preliminary gas sensing characteristics of the nano-particulate MgFe₂O₄ (MFO), PVA and Pechini route derived Mg_{0.5}Zn_{0.5}Fe₂O₄ (MZFO-P and MZFO-C respectively),

and ZnFe_2O_4 (ZFO) sensing elements have already been described in Chapter-3 (Sec. 3.2). The typical response recovery transients (for H_2 sensing at various test gas concentrations) for ZFO sensing element is shown in Fig. 4.2. The typical surface morphology of the ZFO sensing element is shown in the inset of Fig. 4.2.

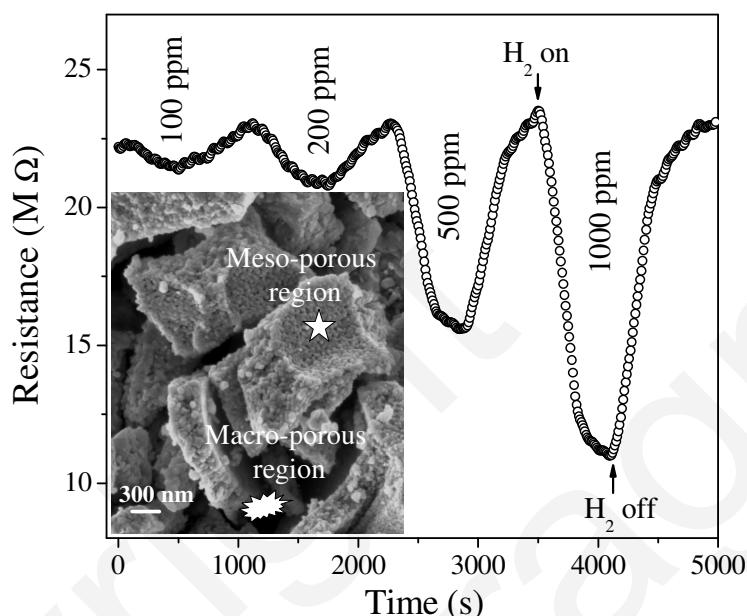


Fig. 4.2: Resistance transient of zinc ferrite sensor at various hydrogen concentrations. Inset shows the SEM micrograph of zinc ferrite sensing element sintered at 600 °C for 2 h in air. Regions with macro and meso-pores are marked in the picture

Out of the reaction sequence outlined in Sec. 4.2, the physi-adsorption of oxygen as well as reducing gas (Eqn. 4.1 and 4.3) are fast, on the other hand the reaction between the adsorbed gas and oxygen (Eqn. 4.4) is a slow process and therefore is the rate determining step for the response kinetics. Similarly for recovery (when reducing gas is turned off) out of reaction mentioned in Eqn. 4.2 and 4.5, the later determines the rate of recovery kinetics. Assuming the adsorption of the oxygen molecule on the sensing surface is governed by an 1-d attractive force (only from z direction) of the chemi-adsorption potential, and there is no inter-molecular interaction among them, the adsorption kinetics can be analyzed by modeling the resistance/ conductance transients using Langmuir adsorption isotherm. In accordance to the presumption of Langmuir adsorption isotherm monolayer coverage of gases over sensing surfaces we have modeled

the conductance transient (during response and recovery process) of some of the selected synthesized sensing materials [11-13]. The work is described in details as follows

4.4.1. Derivation of the Response and Recovery Conductance Transients Based on Langmuir Adsorption Isotherm

As mentioned earlier, since Eqn. 4.4 is the rate limiting process of sensor response, it is assumed that the formation of RO_{ad} will be in proportion to the concentration of the reducing gas. If monolayer coverage of reducing gas is assumed at constant temperature (T), then assuming Langmuir adsorption kinetics, the rate of formation of RO_{ad} ($\sim \theta$) can be written as follows

$$d\theta/dt = k_a(1-\theta)P_{R_{gas}} - k_d\theta \quad (4.7)$$

where k_a and k_d are the forward and backward rate constant for the formation of RO_{ad} and $P_{R_{gas}}$ is the partial pressure of test gas. Integration of Eqn. 4.7 with the boundary condition, at $t=0$, $\theta=0$ yields

$$\theta = [(k_a P_{R_{gas}})/(k_a P_{R_{gas}} + k_d)][1 - \exp^{-(k_a P_{R_{gas}} + k_d)t}] \quad (4.8).$$

The equation can be simplified as

$$\theta = [(K_1 - k_d)/K_1][1 - \exp^{-(K_1 t)}] \quad (4.9)$$

$$\text{where } K_1 = k_a P_{R_{gas}} + k_d \quad (4.10)$$

The forward adsorption rate coefficient k_a can be defined as [10]

$$k_a = (S_0 N_0 K_0)/(2\pi MRT)^{1/2} \exp^{(-E_A/RT)} \quad (4.11)$$

where S_0 is the surface area of the adsorbed gas, K_0 is the condensation coefficient, E_A is the activation energy for adsorption, N_0 is the Avogadro's number and R is universal gas constant. The backward desorption rate coefficient (k_d) is given by

$$k_d = v \exp^{(-E_d/RT)} \quad (4.12)$$

where ν is the frequency of oscillation of adsorbed gas molecule and E_d is the activation energy for backward desorption. Using relation (4.11) and (4.12), Eqn (4.10) can be written as

$$K_1 = P_{R_{\text{gas}}} (S_0 N_0 K_0) / (2\pi MRT)^{1/2} \exp^{(-E_A/RT)} + \nu \exp^{(-E_d/RT)} \quad (4.13)$$

Now defining $S_0 N_0 K_0 / (2\pi MRT)^{1/2} = \nu / b_0$ note b and b_0 have a dimension of pressure and K_1 has a dimension of $(\text{time})^{-1}$.

$$\text{where } b = b_0 \exp^{(-Q/RT)} \quad (4.14)$$

$$\text{and } Q = E_d - E_A \text{ is the heat of adsorption} \quad (4.15)$$

Putting these values Eqn. 4.13 becomes

$$K_1 = \nu [(P_{R_{\text{gas}}} / b_0) \exp^{(-E_A/RT)} + \exp^{(-E_d/RT)}] \quad (4.16)$$

Now upon simplification using Eqn 4.14 and 4.15, Eqn. (4.9) can be written as

$$\theta = [P_{R_{\text{gas}}} / (P_{R_{\text{gas}}} + b)] [1 - \exp^{-(K_1 t)}] \quad (4.17)$$

From Eqn. 4.17 when $t \rightarrow \infty$ then

$$\theta = \theta_0 = [P_{R_{\text{gas}}} / (P_{R_{\text{gas}}} + b)] \quad (4.18)$$

Defining $K_1 \sim 1/\tau_1$, θ can be written as

$$\theta = \theta_0 (1 - \exp^{(-t/\tau)}) \quad (4.19)$$

As outlined earlier, assuming the linear functional dependence between $\theta(t)$ and $G(t)$, the conductance transient for response ($G(t)_{\text{response}}$) (assuming single adsorption site) is given by

$$G(t)_{\text{response}} = G_0 + G_1 [1 - \exp^{(-t/\tau_1^{\text{response}})}] \quad (4.20)$$

where G_0 is the base resistance of the sensing material.

For recovery kinetics, from Eqn. 4.5 one can write

$$d\theta/dt = -k_D\theta \quad (4.21)$$

where k_D is the rate constant for recovery process

Integrating Eqn. 4.21 with the boundary condition at $t = 0$, $\theta = 1$ one gets

$$\theta = \theta_0 \exp^{(-k_D t)} \quad (4.22)$$

Accordingly, the conductance recovery is given by

$$G(t)_{\text{recovery}} = G_0' + G_1' \exp^{(-t/\tau_1^{\text{recovery}})} \quad (4.23)$$

Attempts are made to fit the (response) conductance transients with a single site Langmuir isotherm (Eqn. 4.20). The fits are poor with typical $R^2 \sim 0.70$. On the other hand the curve fit well with R^2 value > 0.95 when two adsorption sites are assumed with modified $G(t)_{\text{response}}$ given by the following equation

$$G(t)_{\text{response}} = G_0 + G_1[1 - \exp^{(-t/\tau_1^{\text{response}})}] + G_2[1 - \exp^{(-t/\tau_2^{\text{response}})}] \quad (4.24)$$

where τ_1^{response} and τ_2^{response} are the relaxation times for two energetically different adsorption sites 1 and 2 respectively.

Assuming two desorption site model, the recovery transient is fitted using the following equation.

$$G(t)_{\text{recovery}} = G_0' + G_1' \exp^{(-t/\tau_1^{\text{recovery}})} + G_2' \exp^{(-t/\tau_2^{\text{recovery}})} \quad (4.25)$$

The justification for the assumption of two adsorption sites can be understood as follows. Since the synthesized particles are lightly pressed and sintered at low temperature, it is assumed that the sensing element contains both macro-pores (between the secondary particles) and meso-pores (within the primary particles).

As revealed in the typical micrograph of MZFO-P sensing element (Fig. 4.3), the surface of the sensor consists with both macro-porous (> 50 nm) and meso-porous (2-50 nm) regions. Similar morphological features are also observed in ZFO sensing element (see inset of Fig. 4.2). As described in Chapter-3, molecular gas diffusion is probable in macro-pores whereas Knudsen diffusion may be operative through the meso-pores. For the adsorption of gases over these sensing surfaces these macro and meso-porous regions can act like two energetically different sites.

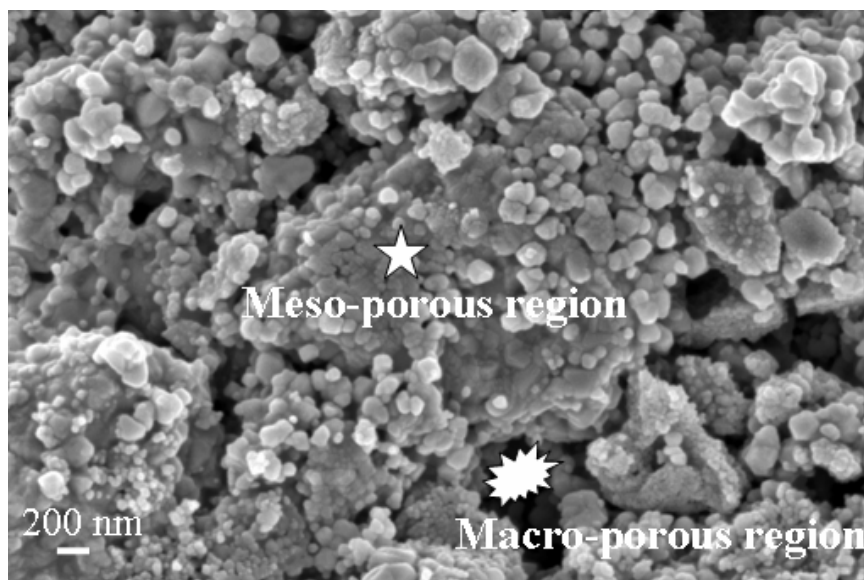


Fig. 4.3: Surface morphology of MZFO-P sensing element showing macro and meso-porous regions

4.4.2. Non-Linear Fitting of Response and Recovery Transients

The response and recovery conductance transients for the synthesized MFO, MZFO-P and ZFO sensing elements at various H_2 and CO gas concentrations (ranging 100 ppm to 1660 ppm) in the operating temperature range between 250-380 °C are fitted using Eqn. 4.24 and Eqn.4.25 respectively. The typical fitting of the response and recovery conductance transients of MFO, MZFO-P and ZFO sensing elements (prepared using PVA assisted wet chemical synthesis routes) for H_2 and CO gas sensing (500 ppm) at their respective optimized operating temperatures are shown in Fig. 4.4 (a)-(c) respectively. The kinetic parameters, estimated from the fitted response and recovery conductance transients for the detection of H_2 and CO gases are tabulated in Table-4.1 and 4.2 respectively. As shown in Table-4.1, we have estimated the values of G_0 (initial conductance of the sensor during response), $G_1, 2$ (change of the conductance during response process in two adsorption sites) and $\tau_{1, 2}$ (characteristic relaxation times for response process in two adsorption sites). Similarly from the fitting of the recovery transients we have estimated $G'_0, G'_1, G'_2, \tau_1^{\text{recovery}}, \tau_2^{\text{recovery}}$ for H_2 and CO sensing using MFO, MZFO-P, and ZFO sensors and these parameters are tabulated in Table-4.2.

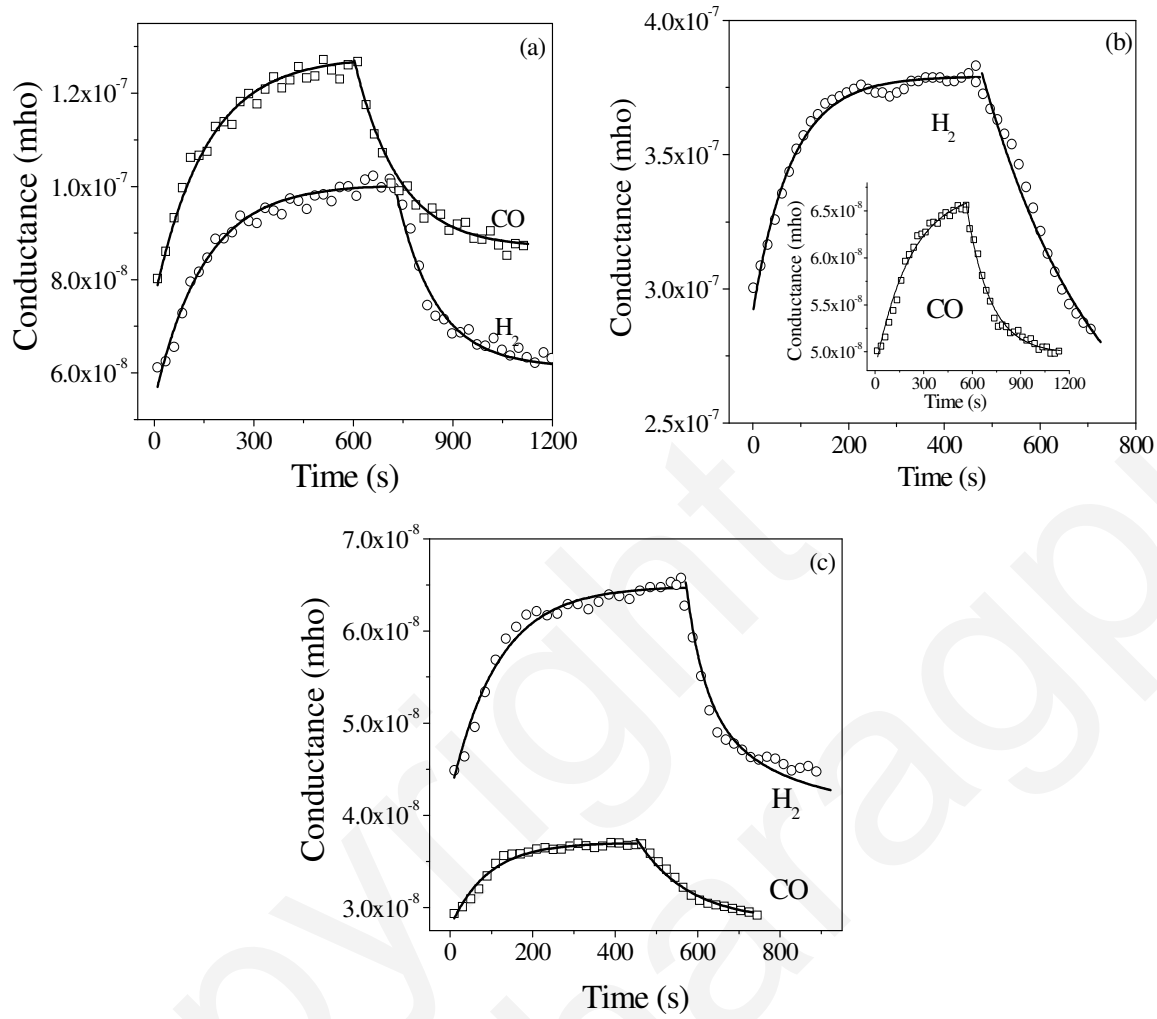


Fig. 4.4: The response and recovery conductance transients for (a) MgFe_2O_4 (b) $\text{Mg}_{0.5}\text{Zn}_{0.5}\text{Fe}_2\text{O}_4$ and (c) ZnFe_2O_4 sensing elements for H_2 and CO gas sensing (~ 500 ppm) at respective optimized operating temperature. The symbols are experimental data points, and the solid lines correspond the response and recovery, fitted according to Eqn. 4.24 and Eqn. 4.25 respectively

Table-4.1: Fitted parameters for the response kinetics for H_2 and CO (~ 500 ppm) gas sensing using MgFe_2O_4 , $\text{Mg}_{0.5}\text{Zn}_{0.5}\text{Fe}_2\text{O}_4$ and ZnFe_2O_4 sensing elements

Sensing materials	τ_1^{response} (s)		τ_2^{response} (s)		G_0 (mho) $\times (10^{-8})$		G_1 (mho) $\times (10^{-8})$		G_2 (mho) $\times (10^{-8})$	
	H_2	CO	H_2	CO	H_2	CO	H_2	CO	H_2	CO
MFO	155	158	144	155	5.40	7.56	2.4	2.61	2.3	2.60
MZFO-P	83	221	75	223	29.1	4.86	4.5	0.9	4.3	0.96
ZFO	141	88	124	93	4.23	2.78	1.2	0.47	1.1	0.45

Table-4.2: Fitted parameters for the recovery kinetics for H₂ and CO (~ 500 ppm) gas sensing using MgFe₂O₄, Mg_{0.5}Zn_{0.5}Fe₂O₄ and ZnFe₂O₄ sensing elements

Sensing materials	τ_1^{recovery} (s)		τ_2^{recovery} (s)		G_0' (mho) $\times (10^{-8})$		G_1' (mho) $\times (10^{-8})$		G_2' (mho) $\times (10^{-8})$	
	H ₂	CO	H ₂	CO	H ₂	CO	H ₂	CO	H ₂	CO
MFO	142	157	105	145	6.25	7.95	2.0	1.95	2.5	2.02
MZFO-P	249	144	246	146	23.2	4.98	7.9	0.85	7.7	0.86
ZFO	42	126	199	128	4.21	2.82	1.3	0.48	1.4	0.48

By fitting the experimental data we have estimated the response and recovery times for these sensing elements. Depending on the adsorption sites, both for H₂ and CO gas sensing the response and recovery times found to be different. Probably the differences in the response and recovery times for two different sites (1 and 2) are related to the macro and meso-porous regions of the sensor surface. We have studied the variation of these kinetic parameters with (i) temperatures (ii) test gas concentration and (iii) test gas type. The results are described in subsequent sections.

4.4.3. Variation of the Response and Recovery Time Constants with Sensor Operating Temperatures

When the kinetics of sensor response is controlled by adsorption/desorption process then the temperature dependence of the response time constant (τ) can be described by the following relation [10-11]

$$\tau^{\text{response}} = \tau_0^{\text{response}} \exp^{[(E_A+Q)/2kT]} \quad (4.26)$$

where E_A+Q is the activation energy for the adsorption of reducing gas. From a linear fit between $\ln \tau^{\text{response}}$ vs $1000/T$; the activation energy (E_A+Q) can be estimated from its slope. Similarly, for the recovery process the time constants (both for site 1 and 2 (τ_1^{recovery} , τ_2^{recovery})) follow following relation

$$\tau^{\text{recovery}} = \tau_0^{\text{recovery}} \exp^{[(E_D)/2kT]} \quad (4.27)$$

where E_D is the activation energy for desorption of RO_{ad} to RO_{gas} . The activation energy for desorption of RO_{ad} can be estimated from the slope of the linear variation of $\ln \tau^{recovery}$ vs $1000/T$. For MFO, MZFO-P, and ZFO sensing elements, Fig. 4.5-4.7 show the temperature variation of (a) $\tau^{response}$ and (b) $\tau^{recovery}$ (both for site 1 and 2) estimated from the fitting of conductance transients for H_2 and CO gas (~1660 ppm) sensing. From the slopes of the linear fit of the plots (shown in Fig. 4.5- 4.7) one can estimate the respective activation energies for the adsorption of H_2 , CO gases and desorption of their oxidized product. Table-4.3 summarizes the value of activation energies for the adsorption of H_2 , CO gases and desorption of the water and carbon dioxide molecules from the respective sensing surfaces. As shown in Table-4.3, the values of activation energies of adsorption of H_2 and CO gases, as well as desorption of H_2O and CO_2 molecules are estimated to be within the range between 0.1-0.8 eV. Lower are the activation energies for adsorption of test gases (e.g. H_2 and CO) and desorption of reaction product (e.g. H_2O and CO_2 from the sensing surface), better will be their gas sensing characteristics. The estimated average activation energies for site 1 and site 2 are in close agreement to those reported in the literatures for other semiconducting gas sensing materials [16-17]. However, exclusively for ferrite based sensor materials, we have not found any such data corresponding to the adsorption of test gas and desorption of reaction product.

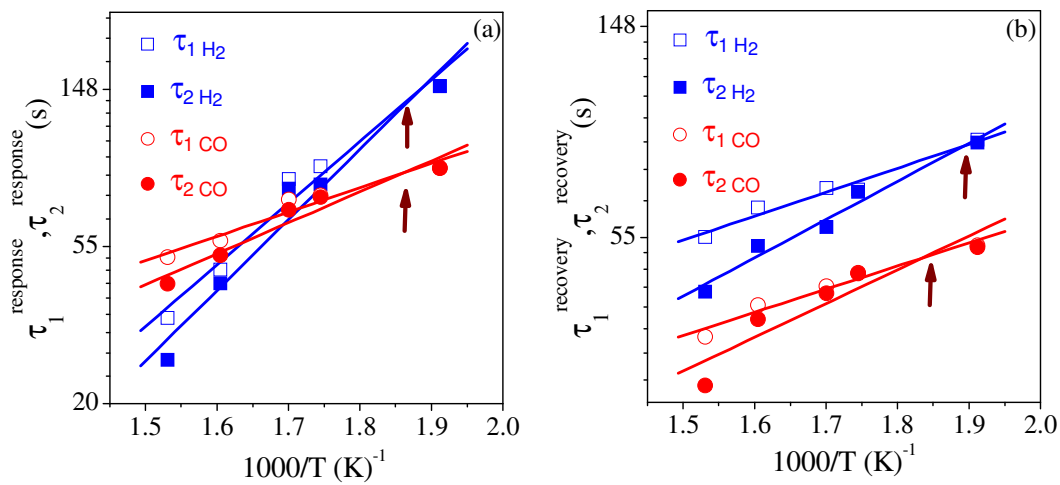


Fig. 4.5: Temperature variation in the (a) response and (b) recovery time constants for $MgFe_2O_4$ sensor at a fixed H_2 and CO gas concentration (1660 ppm)

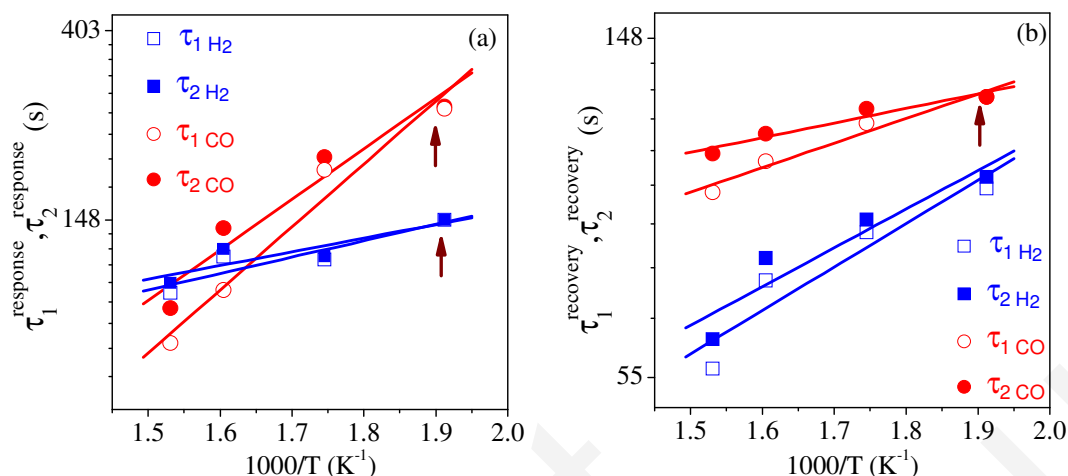


Fig. 4.6: Temperature variation in the (a) response and (b) recovery time constants for $\text{Mg}_{0.5}\text{Zn}_{0.5}\text{Fe}_2\text{O}_4$ sensor at a fixed H_2 and CO gas concentration (1660 ppm)

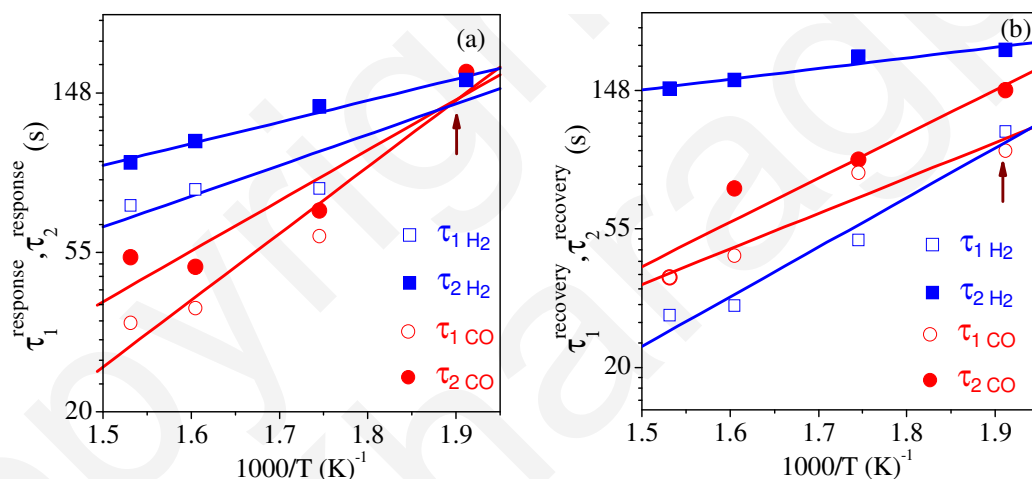


Fig. 4.7: Temperature variation in the (a) response and (b) recovery time constants for ZnFe_2O_4 sensor at a fixed H_2 and CO gas concentration (1660 ppm)

Table-4.3: Estimated activation energies (both for site 1 and site 2) for adsorption and desorption during H_2 and CO gas sensing using ferrite sensing elements

Sensing Material	Activation energy for adsorption of H_2 gas (eV)			Activation energy for desorption of H_2O vapor (eV)			Activation energy for adsorption of CO gas (eV)			Activation energy for desorption of CO_2 gas (eV)		
	site 1	site 2	average	site 1	site 2	average	site 1	site 2	average	site 1	site 2	average
MFO	0.68	0.77	0.73	0.20	0.31	0.26	0.27	0.34	0.32	0.19	0.28	0.24
MZFO-P	0.15	0.12	0.14	0.22	0.19	0.21	0.57	0.46	0.52	0.12	0.07	0.1
ZFO	0.33	0.23	0.28	0.62	0.13	0.38	0.72	0.55	0.64	0.44	0.55	0.5

As revealed in the Table-4.3, for any of these sensing element, the activation energies for adsorption/ desorption of test gas and reaction product differ appreciably between two sites (site 1 and 2). The difference in activation energies could be due to the difference in surface morphology of the sensing surface (micro porous or meso-porous regions) or it may be related to the difference in the nature of chemiadsorbed oxygen species. In the temperature range between 250-380 °C, it is more likely both atomic as well as molecular oxygen species are chemiadsorbed on the sensor surface [8]. Probably both surface morphological features and the nature of chemi-adsorbed oxygen influence the adsorption-desorption characteristics.

In light of the above analyses, we are making an attempt to comment on the nature of site 1 and site 2 corresponding to the different adsorption sites in these sensing elements. Note that for MFO sensing elements (as shown in Fig. 4.5) during H₂ and CO sensing, as compared to site 1, site 2 always exhibits faster response as well as recovery kinetics ($\tau_1^{\text{response}}, \tau_1^{\text{recovery}} > \tau_2^{\text{response}}, \tau_2^{\text{recovery}}$). However for MZFO-P and ZFO sensing elements, it is apparent that for T>250 °C, the response kinetics corresponding to site 1 is faster as compared to that of site 2 ($\tau_1^{\text{response}}, \tau_1^{\text{recovery}} < \tau_2^{\text{response}}, \tau_2^{\text{recovery}}$). As envisaged from Fig. 4.5-4.7, response and recovery times (for site 1 and site 2) for H₂ and CO sensing varies in a complicated way with operating temperature (T). For MZFO-P and ZFO sensing elements, the response and recovery times for site 1 (irrespective of the gas type) are always faster. The reverse is true for MFO sensing element. As indicated in Table-4.3, the activation energies for gas adsorption/ desorption (for site 1 and 2), are dependent on the slopes of the curves shown in Fig. 4.5-4.7. Close inspection of the data plotted in Fig. 4.5-4.7 reveals an intersection point (at lower temperature) below which the characteristic relation between the response and recovery time constants for site 1 and 2, observed at higher temperature is just reversed. Note that within the range of the measurement temperature, such intersection is observed for all the studied sensing materials during the detection of H₂ and CO gases (marked by small arrow in Fig. 4.5-4.7). Similar feature has also been reported in the literature for binary oxide sensor to describe the effect of humidity to the sensor response time. It is reported that the temperature corresponding to the intersection points depend on the type of sensor material and various other factors

[17]. Comparing the H₂ sensing characteristics of the ferrite sensors, with conventional oxide sensors one can find that the activation energies both for the adsorption of H₂ gas and desorption of the oxidized product (H₂O) is comparatively lower. For H₂ gas sensing it is therefore attractive to use ferrite sensors. The variation of the kinetic parameters with test gas concentration is described in the following section.

4.4.4. Variation of the Estimated Fitted Parameters with Test Gas Concentration: Addressing the Selectivity Issue

If Langmuir adsorption isotherm is indeed followed in ferrite based sensors, then for site 1 and 2, the following relations should be obeyed [10]

$$G_1 / (1 - G_1) = C_g / b_1 \quad (4.28) \text{ and}$$

$$G_2 / (1 - G_2) = C_g / b_2 \quad (4.29)$$

here it is assumed that $P_{\text{Rgas}} \sim C_g$ at low gas concentration and b_1 and b_2 are related to the respective heat of adsorption Q_1 and Q_2 through the relation.

$$b_{1\text{or}2} = b_0 \exp^{(-Q_{1\text{or}2}/RT)} \quad (4.30)$$

where b_0 (a constant) has a unit of pressure, T is the temperature and R is universal gas constant.

For a typical ZFO nano-particulate sensor Fig. 4.8 shows the plots of $G_1/(1-G_1)$, $G_2/(1-G_2)$ vs. C_{H_2} (at $T \sim 350^\circ\text{C}$). Indeed such plots (passing through origin) are linear in nature. The slope of these curves corresponds to the inverse of b_1 and b_2 which are related to the heat of adsorptions for site 1 and 2 respectively (see Eqn. 4.30). Following Eqn. 4.30, had the values of b_0 known, one can calculate Q_1 and Q_2 . No attempt is being made at present to estimate Q_1 and Q_2 , however, for a particular gas (say CO), the fact that b_1 and b_2 values are different (0.99×10^{11} Pa, and 0.88×10^{11} Pa for site 1 and 2) it can be assumed that two different adsorption sites are operative in ZFO sensor surface. For H₂, the values of b_1 and b_2 for site 1 and 2 (0.44×10^{11} Pa and 0.41×10^{11} Pa respectively) differ significantly as compared to CO. For these ferrite based sensing elements, the

characteristic relaxation times (τ) (estimated from the fitting of response transients during gas (H_2 , CO) sensing) also vary with test gas concentration (C_g) according to the following relation

$$\tau = \tau_0 C_g^{-\beta} \quad (4.31)$$

where τ_0 and β are the fitting constants.

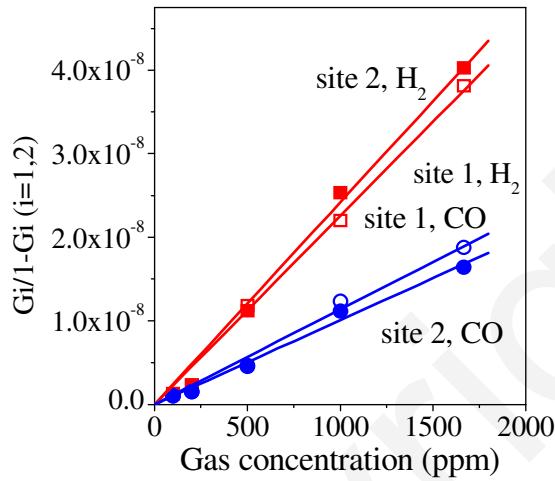


Fig. 4.8: For $ZnFe_2O_4$ sensor variation of $G_i/(1-G_i)$, $G_2/(1-G_2)$ vs test gas (H_2 and CO) concentration at constant operating temperature ($\sim 350^\circ C$)

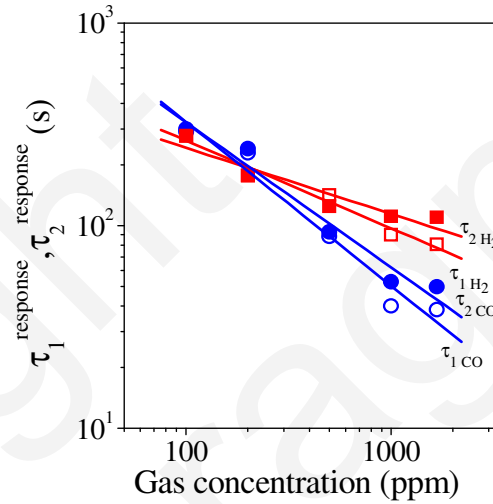


Fig. 4.9: Variation in the response time constants with test gas (H_2 and CO) concentration at constant operating temperature ($\sim 350^\circ C$)

For ZFO sensor, Fig. 4.9 shows the $\log \tau$ vs. $\log C_g$ plots for H_2 and CO gases (temperature is kept constant at $\sim 350^\circ C$). As shown in the figure, for both the gases in a wide concentration range the linear relation is maintained, however, the coefficient β is different for these two gases. Thus for two different adsorption sites 1 and 2, for CO the values of β are 0.80 and 0.71 respectively which is different than the β values of site 1 and 2 for H_2 gas (0.43 and 0.48 respectively).

Based on the results presented above, we have argued that from the analyses of the conductance transients during response and recovery process one can recognize different gas type. From the analyses of the conductance transients of the sensing elements, it is demonstrated that for the semiconducting oxide based sensing elements, depending on the chemical nature, size of the molecules etc, each gas has a characteristic reactivity,

response and recovery time constants. Due to the fact that the chemical reaction of the gas with the sensing surface can produce intermediate products and that each part of the reaction process is time dependent, the gas adsorption and desorption reaction of this effect can be followed to identify the type of the gas. Therefore, we felt that for a discrete gas sensor, the kinetic parameters (as a function of operating temperature and gas concentration) estimated from the fitting of the response and recovery conductance transients, could be beneficial for the identification and monitoring the detection of a specific gas.

For a discrete gas sensor (say ZFO sensor) as discussed earlier the activation energies (estimated from the variation of relaxation times with the sensor operating temperature) for response and recovery of test gases, the b values (related to heat of adsorption of gases on sensor surface), β values (related to the variation of relaxation times with gas concentration) are specific for a gas type. For ZFO sensor the activation energy for adsorption and desorption, b and β values for the detection of H_2 and CO gases are tabulated in Table-4.4. As envisaged from the Table-4.4, for ZFO sensor, the activation

Table-4.4: Estimated activation energies for adsorption desorption, b and β values for hydrogen and carbon monoxide sensing using zinc ferrite sensing element

Gas	Activation energy (eV) for response		Activation energy (eV) for recovery		$b \times 10^{11}$ (Pa)		β	
	Site1	Site 2	Site1	Site 2	Site1	Site 2	Site1	Site 2
H_2	0.33	0.23	0.62	0.13	0.44	0.41	0.43	0.48
CO	0.72	0.55	0.44	0.55	0.99	0.88	0.80	0.71

energies, b and β values differ significantly with the type of gas (H_2 or CO). Since each gas, depending on its reactivity, size of the molecules etc has characteristic features of adsorption and desorption, the analyses of the conductance transients (which reflects the electrical output of the gas adsorption and desorption) of the sensing element could be useful to estimate the selectivity of these sensors [18].

For real time situation, addressing the selectivity by analyzing the kinetic parameters would be a complicated task. Therefore, to address the selectivity issue of these discrete chemi-resistor type sensors, we have utilized noise spectra analyses as well as pattern recognition algorithm. The noise analyses are described in the subsequent section of this

chapter whereas the pattern recognition results are presented in Chapter-5. While analyzing the resistance/ conductance spectra, some interesting features are observed. Similar features are also reported in existing literatures, however either nothing is said explicitly about them [19-20], or the cited explanations are hand waiving [21-22]. In the next section, first we have summarized these features. In the subsequent sections attempts are made to analyze these features to provide the plausible explanation of their occurrence.

4.5. Characteristic Features Observed in Resistance Transients

A number of interesting features are observed in the recorded resistance/ conductance transients of the binary and spinel oxide based nano-structured sensing materials. These characteristic features are summarized in Fig. 4.10. Fig. 4.10(a) shows the resistance transients of MZFO-P sensing element for CO gas sensing in the concentration range 100-1000 ppm. The CO gas sensing characteristics of ZnO sensing element is shown in Fig. 4.10(b). Comparing the resistance transients of Fig. 4.10(a) and (b), significant base resistance drift is observed in ZnO sensing element, however, no such drift is there in MZFO-P sensing element. The occurrence of such drift is due to incomplete recovery of ZnO sensing element. Another interesting feature is shown in the inset of Fig. 4.10(b). As shown in the inset of Fig. 4.10(b), when plotted in expanded time scale, regular sinusoidal pattern is detected both in response and recovery cycles. Similar sinusoidal pattern is also detected in response and recovery resistance transients for some other sensing elements investigated in the present work. For n-type semiconducting oxide based reducing gas sensors, ideally, during response, resistance should decrease monotonously, whereas during recovery a continuous increase of resistance is expected. In contrast to this, as shown in the inset of Fig. 4.10(b), at reduced time scale, the resistance fluctuates, whereas in extended time duration the resistance change is as expected for response (decreasing trend) and recovery (increasing trend). Figure 4.10(c) and (d) show the H₂ sensing characteristics of Mg_{0.5}Zn_{0.5}Fe₂O₄ embedded (in AAO template) and isolated nano-tube respectively. As marked in the respective figures, both in response and recovery transients, ‘spike’ like features are detected. In addition to these sporadic spikes a typical p-type semiconducting characteristics is also observed in

$\text{Mg}_{0.5}\text{Zn}_{0.5}\text{Fe}_2\text{O}_4$ isolated tubes (Fig. 4.10(d)). In contrast, $\text{Mg}_{0.5}\text{Zn}_{0.5}\text{Fe}_2\text{O}_4$ embedded nano-tubes behave like typical n-type semiconducting oxide. These features have already been discussed in Chapter-3. In the remaining part of Chapter-4, we have made an attempt to understand the nature and origin of these features based on the reaction sequence of gas adsorption and desorption of the reaction products. In the following section we have investigated the base line drift characteristics for MZFO-P and ZnO sensing elements.

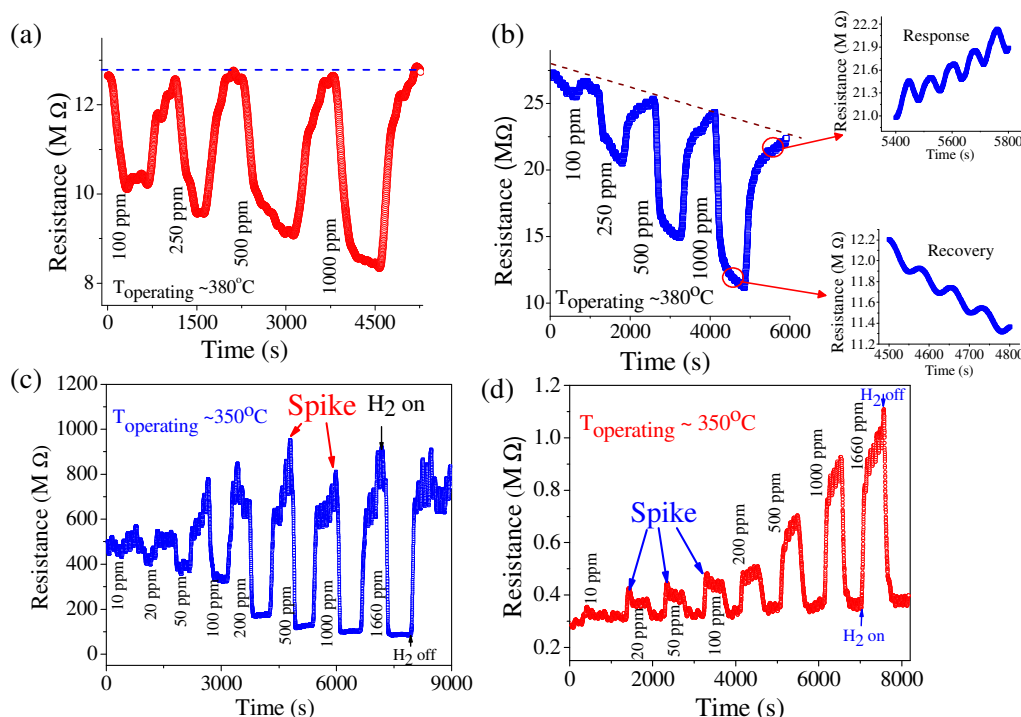


Fig. 4.10: Typical response and recovery transients of (a) nano-particulate $\text{Mg}_{0.5}\text{Zn}_{0.5}\text{Fe}_2\text{O}_4$, (b) nano-particulate ZnO, for CO sensing in the concentration range 100-1000 ppm (c) embedded $\text{Mg}_{0.5}\text{Zn}_{0.5}\text{Fe}_2\text{O}_4$ nano-tube (in porous alumina), and (d) isolated $\text{Mg}_{0.5}\text{Zn}_{0.5}\text{Fe}_2\text{O}_4$ nano-tube (coated on fused quartz substrate) for H_2 gas sensing in the concentration range between 10-1660 ppm. Figure 4.10 (a) and (b) compare base line drift characteristics. The inset of Fig. 4.10 (b) shows sinusoidal noise behavior. Fig. 4.10 (c) and (d) present typical spike like features in response and recovery transients. The isolated $\text{Mg}_{0.5}\text{Zn}_{0.5}\text{Fe}_2\text{O}_4$ tubes exhibit p-type sensing behavior

4.5.1. Investigations on the Irreversible and Reversible Type Gas Sensing in Oxide Gas Sensors

While analyzing the resistance transients of MZFO-P and ZnO sensing elements (Fig. 4.10(a) and (b)) two important features have been identified. In the first instance, when the sensing elements are exposed to reducing gas, the measured resistance never gets saturated for prolonged exposure (of the sensing element) in the test gas environment. Similarly, up on recovery, the original base resistance of the sensing element (i.e. resistance measured prior to the exposure in the test gas environment) is not fully recovered even if the sensor element is exposed in ambient air for long time (Fig. 4.10(b)). In the second instance, during response the resistance quickly gets saturated when the sensor is exposed briefly to test gas environment. Also during recovery, the base resistance is fully recovered when the sensor is flushed with ambient air (Fig. 4.10(a)). The sensing characteristics of first type are termed as irreversible whereas the second type is termed as reversible type gas sensing. Comparing Fig. 4.10(a) and (b), it is observed that MZFO-P and ZnO sensing elements exhibit reversible and irreversible type gas sensing respectively. The type of gas sensing has significant influence on the sensing characteristics of commercial gas sensors. For such gas detector reversible type gas sensing elements are desirable where quick sensing (small response time) as well as rapid (small recovery time) and complete recovery (no base line drift) is achieved. The use of reversible type gas sensor would also simplify the electronic circuitry of the sensing module where, due to the occurrence of appreciable base line drift, often the use of an additional comparator circuit becomes necessary. Usually the response (%) of commercial gas sensor varies linearly with the concentration of test gas. If marginal base line drift is achieved up on repeated sensing and recovery, then up on suitable calibration a discrete gas sensing element can be also used as a gas analyzer. Reversible type gas sensor would also simplify the commonly used pattern recognition protocols to make selective gas sensors [23]. The irreversible and reversible type gas sensing is a generic phenomenon observed in a wide spectrum of gas sensing materials used to detect a variety of test gases. Table-4.5 tabulates the type of sensing materials, test gas, nature of gas detection and plausible mechanism to explain the underlying mechanism that control the irreversible and reversible type gas sensing.

Table-4.5: Overview of the reversible and irreversible type gas sensing reported in various types of gas sensing materials. (The abbreviated terms mentioned in the table are: DMMP- dimethyl methylphosphonate; TTF–TCNQ- Tetrathiafulvalene tetracyanoquinodimethane; m-CNT- multiwall carbon nano-tubes; Ppy- polypyrrole)

Sensing material	Test gas	Type of gas sensing	Plausible mechanism cited	Ref
Single-walled carbon nano-tube (SWNT) networks	DMMP	Reversible gas sensing is achieved using vacuum in conjunction with IR radiation during recovery	Complete recovery is explained to be due to the good interconnection among the SWNT and their contact with gold electrode.	[24]
TTF–TCNQ thin film	NO ₂	Irreversible	Hypothesized that NO ₂ gas molecules are either absorbed or reacted with the sensing material to form reaction products. Thereby gas molecules are immobilized within the film to result irreversible type response	[25]
m-CNT/ NaClO ₄ /Ppy composite	C ₂ H ₅ OH	Irreversible without m-CNT. With the increase in m-CNT contents gas sensing turns reversible.	Irreversible response is due to strong chemical bond formation between the O atom of ethanol and H atom of Ppy. CNT ('n-type semiconductor) donates electrons to Ppy and wakens the O-H bond resulting reversible type sensing.	[26]
Nanostructured WO _{3-x}	H ₂ O	In the form of platelets irreversible type. Reversible type sensing in the form of nano-wires	The reversible gas sensing characteristics of nano-wires are postulated to be due to their reactive nature (due to the increased concentrations of point defects) and porous surface morphology	[27]
PPy- (PF ₆) film	NH ₃	Irreversible type gas sensing	Irreversible response is due to strong chemical bond formation between the NH ₄ ⁺ ion and PF ₆ ⁻ ion added to Ppy.	[28]
Meso-porous silicon	NO ₂	Irreversible, however, with ageing turns reversible	During ageing, surface passivation of the sensing element by native oxygen leads to reversible gas sensing.	[29]
Carbon nano-tube	NH ₃	Both irreversible as well as reversible type sensing	Reversible when NH ₃ is physisorbed whereas in case of chemisorption of NH ₃ irreversible type sensing occurs. The chemisorption is promoted during prolonged exposure of the sensing elements to test gas.	[30]
TiO _{2-x} thin film	O ₂	Irreversible under static and partially reversible during dynamic gas sensing measurements	A two stage reaction mechanism between oxygen and sensing material is proposed to explain the type of gas sensing. The first stage is dominated by chemisorption of oxygen (promotes reversible sensing) whereas in the second stage thin film gets oxidized which results irreversible type gas sensing.	[21]

Reviewing Table-4.5 it is apparent that the irreversible and reversible type sensing is observed in a wide spectrum of sensing materials (carbon nano-tube, polymer, ceramic oxide etc) for a variety of test gas (NO_2 , NH_3 , H_2O , O_2 , $\text{C}_2\text{H}_5\text{OH}$, DMMP (nerve gas simulating agent) etc) detection [21, 24-30]. The proposed mechanism controlling these types of sensing are scattered and most of the instances seems to be pure hand waiving. For ceramic oxide gas sensors hardly there is any effort made to systematically study such gas sensing phenomena to develop a general consensus between the structure property relationships. We have investigated the type of gas sensing phenomena operative in simple binary (e.g. ZnO) and cubic spinel (e.g. $\text{Mg}_{0.5}\text{Zn}_{0.5}\text{Fe}_2\text{O}_4$) type gas sensing materials for combustible (e.g. CO , H_2) gas sensing. As mentioned earlier, we have found that irreversible type gas sensing is dominant in ZnO sensing elements, whereas for MZFO-P sensors, typical reversible type gas sensing is observed.

We have demonstrated that the type of gas sensing is related to the nature of adsorption of carrier as well as the test gas and desorption of the reaction product from the sensing surface. For ZnO sensing elements, Fig. 4.11 shows the resistance transients for (a) H_2 and (b) CO gas sensing in the concentration range of 100-1000 ppm.

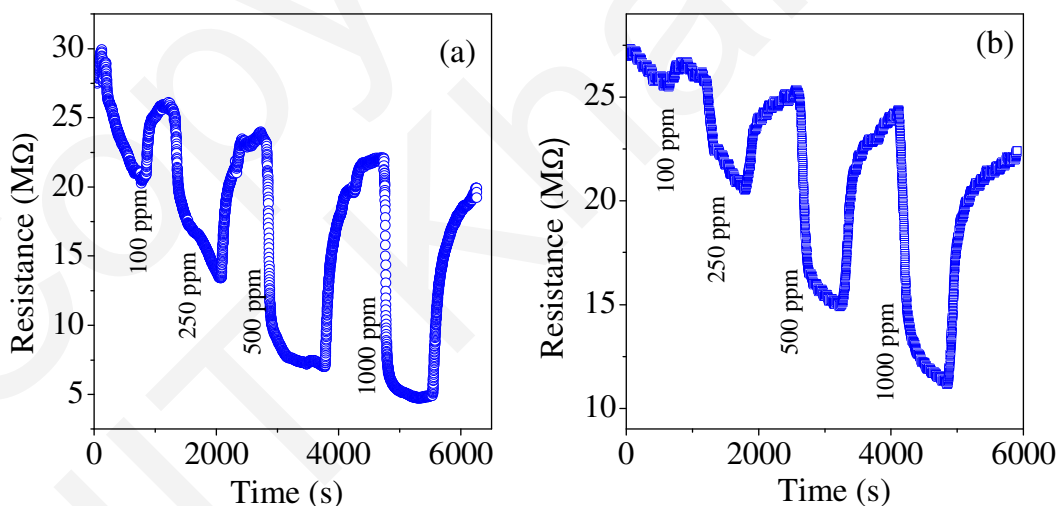


Fig. 4.11: Response and recovery resistance transients of ZnO sensing element recorded for (a) H_2 and (b) CO gas sensing in the concentration range of 100-1000 ppm at operating temperature $\sim 380^\circ\text{C}$

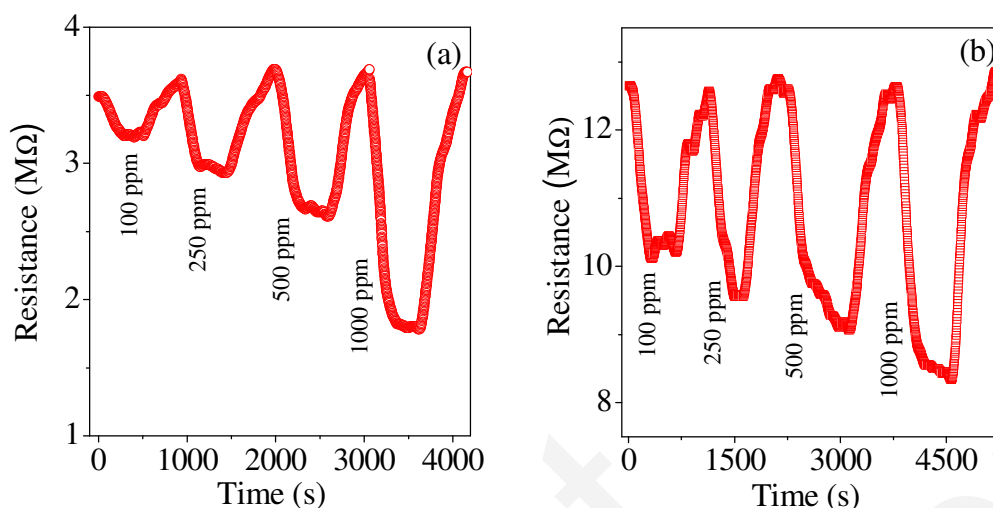


Fig. 4.12: Response and recovery resistance transients of $\text{Mg}_{0.5}\text{Zn}_{0.5}\text{Fe}_2\text{O}_4$ (MZFO-P) sensing element recorded for (a) H_2 and (b) CO gas sensing in the concentration range of 100-1000 ppm at operating temperature $\sim 380^\circ\text{C}$

Similarly, for MZFO-P sensing elements, the resistance transients for H_2 and CO gas sensing (100-1000 ppm) are shown in Fig. 4.12(a) and (b) respectively. Comparing the recorded resistance transients of these two sensing elements we have identified remarkable differences. The salient features of ZnO sensing elements are stated as follows:

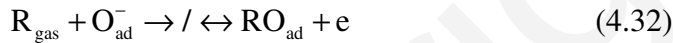
- (i) Both for H_2 and CO gas sensing, the response (%) increases with the increases in gas concentration.
- (ii) The transient response does not saturate, also the base resistance is partially recoverable.
- (iii) Irrespective of the test gas concentration continuous base line drift is observed.

In a similar way, for magnesium zinc ferrite sensing elements the salient features of resistance transients are as follows

- (i) Similar to ZnO sensing elements, both for H_2 and CO gas sensing, the response (%) increases with the increase in the test gas concentration.
- (ii) The response transients saturate and the base resistance is fully recoverable.
- (iii) Irrespective of the test gas concentrations, only nominal drift of base resistance is observed.

4.5.1.1. Mechanism of irreversible gas sensing

To investigate the dynamics of reversible and irreversible type gas sensing process, we have modeled the resistance transients of ZnO and MZFO-P sensors. The mechanism of irreversible and reversible gas sensing is presented as follows: Through Eqn. 4.1-4.5 we have already summarized the simplified and commonly accepted reaction mechanism for sensing of reducing gas by an n type semiconductor. Using these simplified reaction schemes, it is difficult to explain the subtle differences in the response and recovery transients as itemized above for ZnO and MZFO-P sensing elements. In line to a model developed for carbon nano-tube sensors [31] we presume that the key step that control the irreversible/ reversible type resistance transients lies in the way the reducing gas (R_{gas}) reacts with the chemi-absorbed oxygen (O_{ad}^-) to form the reaction product RO_{ad} . Thus the following reaction is important to decide the nature of irreversible or reversible the resistance transients.



The proposed oxidation reaction sequence is schematically illustrated in the following energy diagram (Fig. 4.13). The energy diagram is based on a surface reaction mechanism (Langmuir-Hinshelwood) where both reactants are first adsorbed on the sensing surface and then they collide to form the reaction products. In Fig. 4.13 'A'

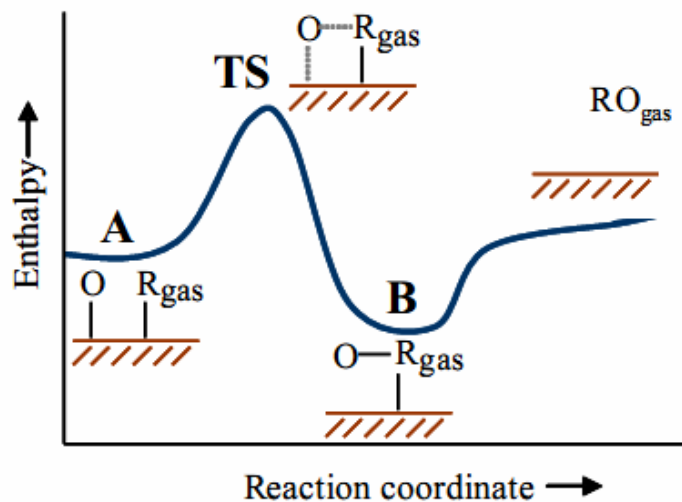


Fig. 4.13: Schematic diagram for Langmuir- Hinshelwood reaction mechanism

denotes adsorption of the test gas and the chemiadsorbed oxygen on the sensing surface. In order to react with the chemiadsorbed oxygen, the test gas must cross the energy barrier (TS) to form the reaction product RO_{ad} (denoted as B). In other words, surpassing the activation barrier, the physi-adsorbed test gas (R_{gas}) (with concentration C_g) is chemically bonded with O_{ad}^- to produce surface adsorbed oxidized product (RO_{ad}).

We have assumed that on the sensor surface, the site fraction ϕ , is covered by O_{ad}^- . On the available blank space reducing gas (R_{gas}) is adsorbed and subsequently reacts with O_{ad}^- in immediate vicinity to form reaction product RO_{ad} . The oxidation reaction is represented by the following relation



The forward rate constant of the above equation is defined as k_a . Considering the number of active sites on the sensor surface is conserved, one can write [31]

$$\phi (\sim [O_{ad}^-]) + RO_{ad} \text{ (occupied initially by } R_{gas}) = F\phi \text{ (total available sites)} \quad (4.34)$$

While writing Eqn. 4.34, it is tacitly assumed that the reaction product (RO_{ad}) occupies the same sites where the reducing gas molecules (R_{gas}) were adsorbed initially. It is assumed that $F\phi$ is a function of the sensor surface temperature and, for a fixed surface temperature the number of total surface sites remains constant. As mentioned earlier, formation of RO_{ad} is considered to be the rate determining step for the response kinetics of the sensor under consideration. Therefore, the response (%) of the sensor is directly proportional to the concentration of oxidized product $[RO_{ad}]$. Considering Eqn. 4.33 is the rate determining step, therefore, the rate of sensor response can be described by the following relation:

$$d[RO_{ad}]/dt = k_a [O_{ad}^-] R_{gas} \quad (4.35)$$

Rewriting Eqn. 4.33 in terms of respective site occupancies

$$d[RO_{ad}]/dt = k_a [F\phi - RO_{ad}] C_g \quad (4.36)$$

where $[R_{gas}] \sim C_g$, Solving Eqn. 4.36 one can write (The analytical steps for this solution is given in Appendix-2)

$$[RO_{ad}](t) = F\phi(1 - \exp^{-[k_a C_g t]}) \quad (4.37)$$

The maximum response corresponds to the situation when all the active sites ($F\phi$) are occupied by the reaction product (RO_{ad}). Therefore the response transient ($S(t)$) can be expressed by the following relation.

$$S(t) = S_{\max}(1 - \exp^{-[k_a C_g t]}) \quad (4.38)$$

Eqn. 4.38 can also be written as

$$S(t) = S_{\max}(1 - \exp^{-[t/\tau_{\text{irrev}}]}) \quad (4.39)$$

where $\tau_{\text{irrev}} = 1/k_a \cdot C_g$ is referred as characteristic response time for irreversible type gas sensing. Physically the response time is defined as the time required for the sensor to yield 63 % of its maximum response (%). Fig. 4.14 shows the time dependence of the response of ZnO sensor for (a) H_2 and (b) CO gas sensing.

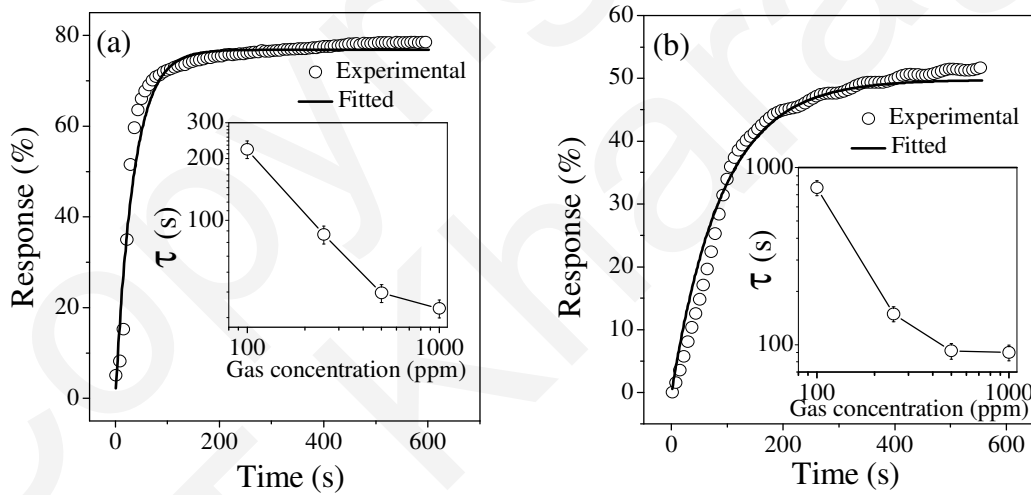


Fig. 4.14: For ZnO sensing elements the response transients for (a) H_2 and (b) CO gas sensing. The operating temperature and test gas concentration is kept at $\sim 380^\circ\text{C}$ and 1000 ppm respectively. The solid lines correspond to best fitted curve based on Eqn. 4.39. The inset shows the variation of response time with test gas concentrations

Based on Eqn. 4.39, typical non-linear fit of the response vs time data for H_2 and CO gas sensing of ZnO sensor is also shown in respective figures as solid lines. Similar fittings are also performed for other gas concentrations and the variation of the estimated τ_{irrev} vs gas concentration is shown at the inset of the respective figures. As shown in the inset,

the response time is reduced systematically with the increase of the gas concentration for irreversible type gas sensing. From Eqn. 4.39 it is clear that for irreversible sensing the maximum response is achieved when the parameters k_a , C_g or $t \rightarrow \infty$. Irrespective of the operating temperature the response as well as the resistance transients of zinc oxide sensing elements follows the irreversible sensing characteristics. Thus for CO sensing Fig. 4.15(a) shows the response (%) (S) plot as a function of time (t) for ZnO sensing elements measured at different operating temperatures (T) in the range of 250-370 °C. These transients are recorded keeping the test gas (CO) concentration (C_g) fixed at ~ 1660 ppm. For any fixed measurement time (say ~900s, as denoted by the dotted line), with the increase of operating temperature (T), clearly the forward rate constant (k_a) is increased resulting $S \rightarrow S_{\max}$ as $T \rightarrow T_{\max}$ (where T_{\max} is the maximum operating temperature). Also, as predicted in Eqn. 4.39, for a fixed operating temperature, $S \rightarrow S_{\max}$ as measurement time $t \rightarrow t_{\max}$. Fig. 4.15(b) illustrates the effect of CO gas concentration (C_g) on the response for irreversible type gas sensing. Thus, as predicted correctly in Eqn. 4.39, with the increase in C_g , $S \rightarrow S_{\max}$ within finite time.

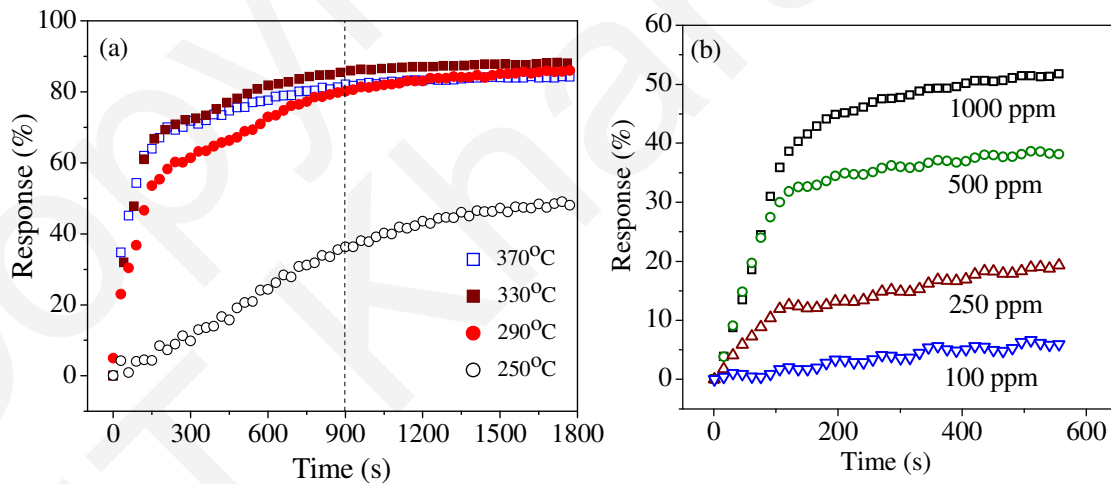


Fig. 4.15: (a) Response (%) transients of ZnO elements for CO sensing measured at different operating temperatures. The gas concentration is kept fixed ~ 1660 ppm. (b) Response (%) transients of ZnO elements for CO sensing at different gas concentrations. The operating temperature is kept fixed at ~ 380 °C

Assuming a Langmuir Hinselwood type of surface reaction; through the above analyses we have established that the response transients of ZnO sensing elements follow the irreversible gas sensing characteristics. It has again been demonstrated that for

irreversible sensing the base resistance is partially recoverable within finite time. Now we will describe the plausible physical phenomena occur during the recovery for irreversible gas sensing. We felt surface morphology of the sensing elements is found to play a major role in deciding the type of gas sensing.

The surface morphology of the ZnO sensing element (shown in Fig. 4.16(a)) represents the dense microstructure which poses difficulties for gas diffusion. The recorded BET isotherm (type IV isotherm with H3 nature of hysteresis as presented in Fig. 4.16(b)) is indicative to the irreversible uptake of adsorbates molecule. As per IUPAC guidelines for irreversible adsorption, the adsorbate molecules can not be removed from the adsorbent surface easily and external driving force (e.g. out gassing at higher temperature [32]) is required to desorb the gases.

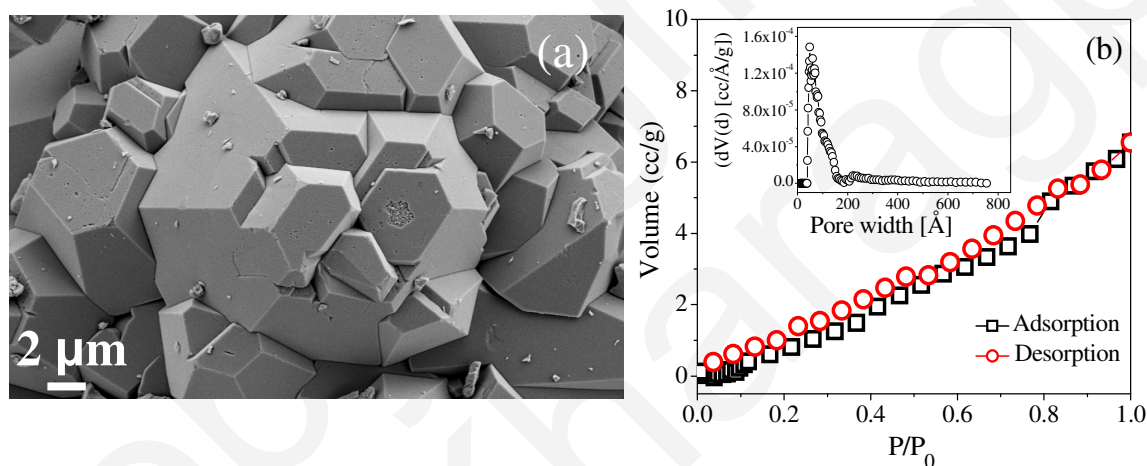


Fig. 4.16: The surface morphology of lightly pressed (a) ZnO sensor sintered at 600 °C for 2 h in air (b) The BET adsorption isotherm of ZnO powders calcined at 600 °C for 2 h in air. The corresponding dV (d) vs pore width plots are shown in the inset of respective figure

In the present case, during gas sensing, the reducing gas molecules are adsorbed to the surface as well as within slit-like pores in ZnO sensing element. As detailed above, during response the test gas is oxidized to form RO_{ad} , however, the oxidized product entrapped in tiny pores do not get desorbed easily. Therefore, in the ZnO sensing elements the initial base resistance does not get fully recovered. However, for CO (1660 ppm) sensing over ZnO sensing elements at different operating temperature (shown in Fig. 4.17), with the progressive rise in sensor operating temperature, the oxidized product

is desorbed more and as a result recovery is systematically improved. In the following section, we have analyzed the reversible type gas sensing phenomenon.

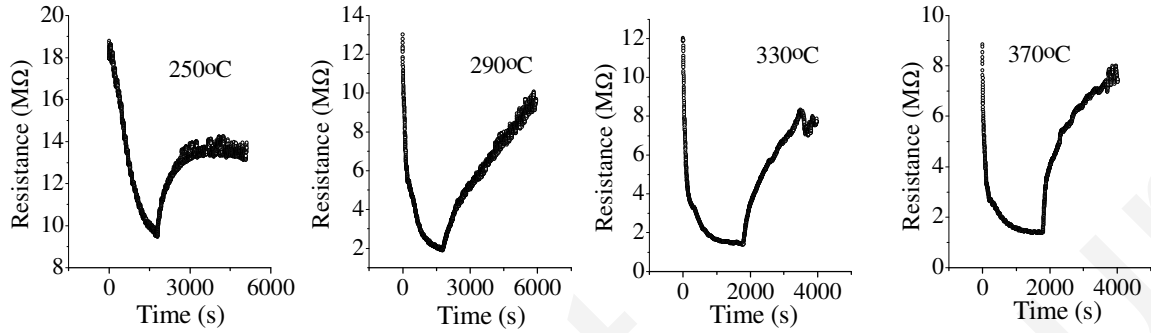


Fig. 4.17: Resistance transients for response and recovery during CO gas (~ 1660 ppm) sensing using ZnO sensing elements at different operating temperatures

4.5.1.2. Mechanism of reversible gas sensing

As outlined earlier, for MZFO-P sensing elements, the resistance transients are markedly different than the ZnO sensors. The operative sensing mechanism (for MZFO-P sensors) is hypothesized to be reversible type and the following relation (Eqn. 4.40) seems to be operative



Thus in case of reversible gas sensing there is an equal probability for the formation as well as dissociation of the oxidized product (RO_{ad}). We assume the equilibrium constant of the above reaction as K and the forward and reverse rate constant as k_a and k_a/K respectively. For such reversible reaction one can write [31]

$$d[RO_{\text{ad}}]/dt = k_a [O_{\text{ad}}^-] C_g - k_a / K [RO_{\text{ad}}] \quad (4.41)$$

Rewriting Eqn. 4.41 in terms of respective site occupancies

$$d[RO_{\text{ad}}]/dt = k_a [F\phi - RO_{\text{ad}}] C_g - k_a / K [RO_{\text{ad}}] \quad (4.42)$$

Solving the Eqn. 4.42 one can write (The analytical steps for this solution is given in Appendix-3)

$$RO_{ad}(t) = F\phi\{C_g K / (1 + C_g K)\} (1 - \exp^{-\{(1+C_g K/K)k_a t\}}) \quad (4.43)$$

Following similar analogy provided for Eqn. 4.37, Eqn. 4.43 can also be written as

$$S(t) = S_{max} \{C_g K / (1 + C_g K)\} (1 - \exp^{-\{(1+C_g K/K)k_a t\}}) \quad (4.44)$$

Assuming $1 + C_g K \approx C_g K$ we can approximate Eqn. 4.44 as

$$S(t) = S_{max} [1 - \exp^{(-t/\tau_r)}] \quad (4.45)$$

The response (%) vs time data for H₂ and CO gas sensing (for the gas concentration ranging 100-1000 ppm) are fitted to Eqn. 4.45 and from the non-linear best fit reversible response time constant (τ_r) is estimated for each test gas concentration.

Following Eqn. 4.45, the characteristic response time (τ_r) in case of reversible gas sensing can be expressed as

$$\tau_r = (1/k_a) \times [K / (1 + C_g K)] \quad (4.46)$$

$$\text{Now } \lim_{C_g \rightarrow 0} \tau_r = \lim_{C_g \rightarrow 0} (1/k_a) \times [K / (1 + C_g K)] = K / k_a \quad (4.47)$$

So, in case of reversible gas sensing at a fixed operating temperature and diluted test gas limit, the characteristic response time constant should be independent of test gas concentration. Fig. 4.18 shows the response (%) (S) vs time (t) plot for (a) hydrogen and (b) carbon monoxide test gas sensing using MZFO-P sensing element. A typical response (%) (S) vs time (t) plot for 1000 ppm CO sensing and the best fitted curve (according to Eqn. 4.45) is shown in Fig. 4.19. Similar fittings are also done for all the test gas concentrations both for hydrogen and carbon monoxide sensing and from the best fit, response time for reversible gas sensing (τ_r) is estimated. The variation of τ_r with test gas (hydrogen and carbon monoxide) concentration is shown in the inset of Fig. 4.19. As expected, indeed we have found that in case of reversible sensing the response time constant is almost independent of test gas concentration. Following the reversible type gas sensing model, as shown in respective resistance transients for hydrogen and carbon monoxide gas sensing (Fig. 4.12(a) and (b)), the response transients are quickly saturates

(irrespective of the test gas concentrations) soon after the respective response time constants.

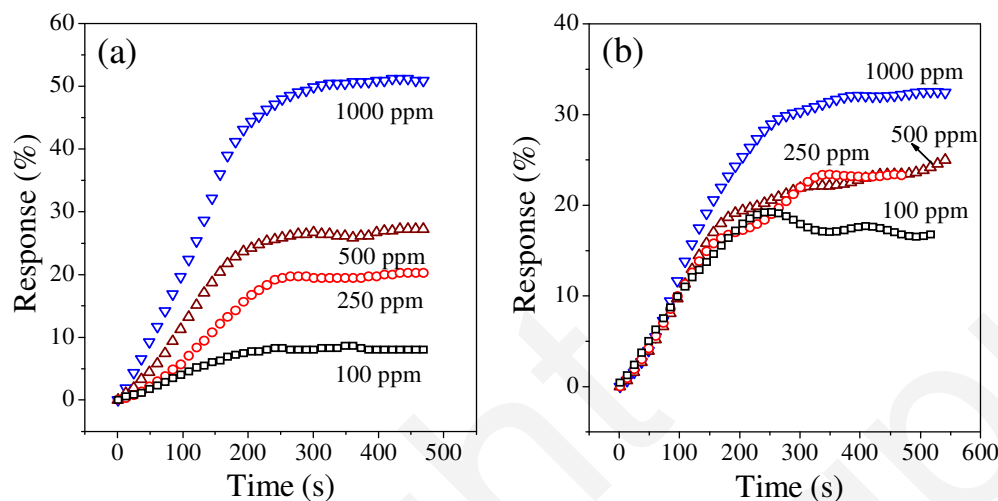


Fig. 4.18: Response (%) transients for (a) H₂ and (b) CO gas sensing using Mg_{0.5}Zn_{0.5}Fe₂O₄ (MZFO-P) sensing elements. The gas concentrations are varied in the range of 100-1000 ppm. The operating temperature is kept fixed at ~ 380 °C

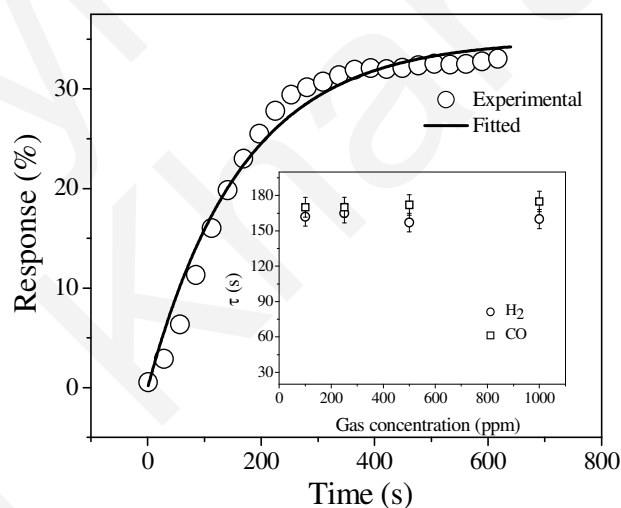


Fig. 4.19: For Mg_{0.5}Zn_{0.5}Fe₂O₄ (MZFO-P) sensing element, the response (%) transient for 1000 ppm CO gas sensing measured at ~ 380 °C. The solid line corresponds to the best fitted curve based on Eqn. 4.45. The inset shows the variation of response time with test gas (H₂ and CO) concentrations

In contrast to irreversible type, for reversible type gas sensing, as mentioned earlier (see Fig. 4.12(a) and (b)) the base resistance is fully recovered. Similar to that mentioned in case of irreversible type gas sensing, for reversible gas sensing too the rate limiting step

for recovery is the desorption of the oxidized product (RO_{ad}). As reported earlier, the MZFO-P sensing elements are characterized with meso-porous surface morphology with broad pore size distribution. Probably the meso-porous structure of the MZFO-P sensing element (shown in Fig. 4.20) is conducive to better desorption of the oxidized product yielding better recovery as compared to the ZnO sensing elements with relatively denser surface morphology. As a result the MZFO-P sensing elements exhibit complete recovery irrespective of the test gas concentration.

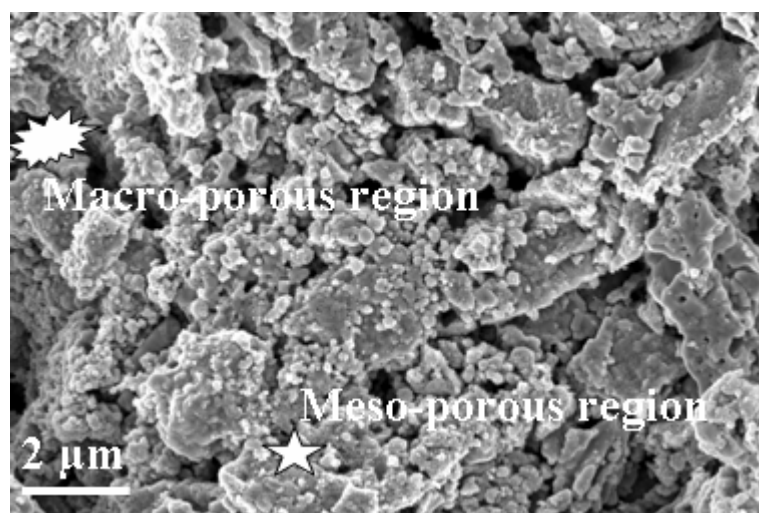


Fig. 4.20: Micrograph of $Mg_{0.5}Zn_{0.5}Fe_2O_4$ (MZFO-P) sensing element sintered at 600 °C for 2 h in air

The salient features of irreversible and reversible gas sensing as emerges from the analyses presented in Sec. 4.5.1.1 and 4.5.1.2 are summarized as follows.

The base resistance is partially recovered in case of irreversible sensing whereas for reversible sensing it is fully recovered. Fitting the response transients it is revealed that for irreversible type gas sensing the response time is systematically reduced with the increase in test gas concentration. In contrast, within the range of test gas concentration studied in this work, response time is found to be independent of gas concentration for reversible gas sensing. Additionally, the response saturates quickly for reversible gas sensing, whereas it takes long time to yield saturation in response for irreversible gas sensing. The recovery characteristics of ZnO and MZFO-P sensing elements are correlated with their respective surface morphologies. The relatively denser surface morphology of ZnO is argued to be responsible for irreversible sensing behavior. On the

other hand, the meso-porous surface morphology of MZFO-P is claimed to be conducive for reversible gas sensing. The other characteristic features observed in the measured resistance transients during gas sensing are investigated in the following sections.

4.5.2. Periodic Undulation of the Resistance Transients during Response and Recovery

As outlined in Sec. 4.5, for some sensing elements, we have observed sinusoidal variation in the resistance transients both during response and recovery (see inset of Fig. 4.10(b)). Such sinusoidal variation is more prominent when the resistance transients equilibrate either in test gas or in air environment. A literature search reveals that occurrence of similar sinusoidal variation is quite generic in nature and not limited only to semiconducting oxide based sensors. Table-4.6 summarizes the literatures that report the occurrence of similar sinusoidal variation in resistance transients.

Table-4.6: Overview of the noisy resistance transients observed for variety of gas sensors during detection of various test gases

Sensor	Test gas	Set-up	Comment/ plausible explanation	Reference
TGS SnO ₂ sensor (Figaro Engineering, Osaka)	CO	Static	Oscillation in the transient could be due to the adsorption-desorption of gases and influenced by temperature. The pattern of the oscillation changes with the temperature	[33]
Tin oxide hollow sphere	Ethanol	Dynamic	No explanation provided for the occurrence of noise in the resistance transient	[6]
Carbon nano-tube/ SnO ₂ nano composite	H ₂	Dynamic	No explanation provided	[19]
Palladium/ polypyrrole nanocomposite	NH ₃	Static	No explanation provided	[34]
Indium oxide nano wire	H ₂ S	Dynamic	No explanation provided	[35]
General model on the noise observed in metal oxide based gas sensors	General oxidizing or reducing gases	The exact reason for resistance fluctuation is not clear. The adsorption –desorption of gases and the change of carrier density and mobility during gas sensing are related to the noise.	[36]

Note that the observed behavior is quite generic in nature, and reported for a wide array of sensing materials (nano-structured semiconducting oxides, carbon nano-tube- SnO_2 , Pd-polypyrrole based nano-composites, etc), type of test gas (reducing, oxidizing, volatile organics etc) and both for dynamic and static gas sensing measurements. As tabulated in Table-4.6, either no explanation is offered for the observed behavior or the reason/(s) are cited are widely scattered. Interestingly, in some selected reports the oscillating feature of the resistance transients during the sensing of various test gas are analyzed and it has been predicted that using noise spectroscopy a single discrete sensor can be used efficiently to detect the test gas selectively [37-38], The origin of resistance undulation is related mainly to three factors namely (i) dynamic adsorption-desorption of gas molecules, (ii) diffusion of adsorbed molecules on the sensor surface and (iii) current flowing through the potential barrier at grain boundaries. Additionally temperature fluctuation during sensing measurement can also lead to resistance fluctuations [39]. Probably all the above factors contribute to the resistance fluctuation during response and recovery and it is complicated to separate out the individual contribution of these factors.

We feel that the factors namely adsorption-desorption of gas molecules together with the planner diffusion of the gas molecules on the sensor surface have dominant effect on the observed resistance undulation. To further investigate the resistance undulation, we have studied the effect of operating temperature on the characteristic resistance fluctuation of MZFO-C sensor ($\text{Mg}_{0.5}\text{Zn}_{0.5}\text{Fe}_2\text{O}_4$ sensor prepared using Pechini route) that senses H_2 (1660 ppm). Figure 4.21 shows the response and recovery transients measured at (a) 250 °C, (b) 300 °C, (c) 350 °C and (d) 380 °C. From Fig. 4.21, it is apparent that the resistance undulation is progressively reduced with the increase in the operating temperature. We are now making an attempt first to explain the observed behavior and then to further analyze the noise spectra to address the selectivity issue of MZFO-C discrete gas sensor. Assuming the adsorption of the gas molecule is governed only by the attractive force of the chemi-adsorption potential in z direction and there is no inter-molecular interaction between the adsorbed molecules, the adsorption kinetics has been modeled earlier using Langmuir adsorption isotherm. Later, using the Lennard Jones potential diagram we have reported that the adsorption ability of the gas molecule (over the sensing surface) will depend on the kinetic energy of the gases.

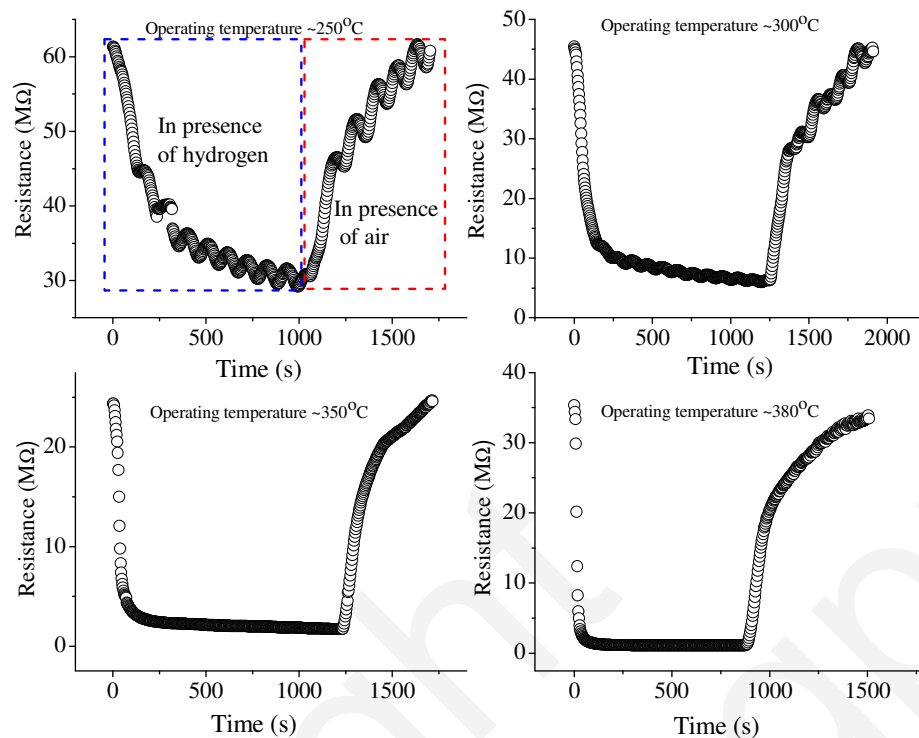


Fig. 4.21: Response and recovery transients for $\text{Mg}_{0.5}\text{Zn}_{0.5}\text{Fe}_2\text{O}_4$ (MZFO-C) sensor during detection of 1660 ppm of H_2 at (a) 250 °C, (b) 300 °C, (c) 350 °C and (d) 380 °C

Thus only the oxygen molecules having a requisite kinetic energy (marked as the sticking trajectory C shown in Fig. 4.1) will be chemisorbed on the sensing surface. The oxygen molecules, however, may not lose virtually all their energy in their first encounter with the SMO surface.

Surface dangling bonds

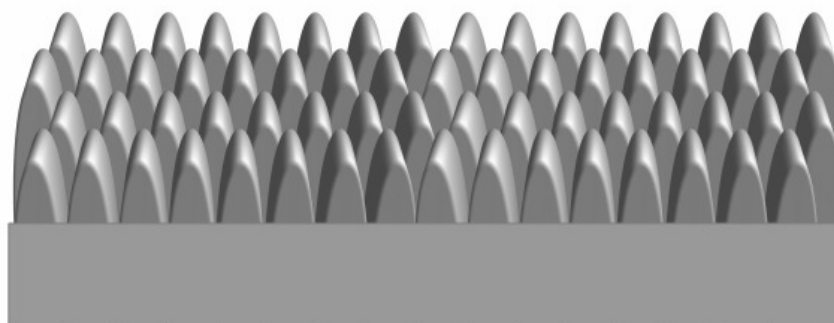


Fig. 4.22: Schematic of the adsorption sites on the sensing surface

In other words, the approaching oxygen molecules may not be chemi-adsorbed instantly on the sites where they land. Similarly, the test gas molecules also may not immediately react with the pre-adsorbed oxygen in their first encounter. The interaction in which a molecule sticks to the surface/ or reacts with the surface adsorbed molecules in its first encounter is termed as direct interaction. However, in real situation, usually the gas molecules are adsorbed on the surface (/interact with the pre-adsorbed oxygen molecules) through an indirect interaction pathway. As schematically shown in Fig. 4.22, there are different adsorption sites on the sensor surface and energy barriers separate them from each other. In case of an indirect interaction pathway, (where the energy of the adsorbate gas molecules are larger than what is required for direct interaction and chemi-adsorption for example) adsorbate gas molecules may hop from one binding site to another crossing the energy barrier. The diffusion of gas molecules across the barriers is driven by uniform 2D potential and therefore is expected to be governed by following Arrhenius equation [15]

$$D = D_0 \exp (-E_{\text{dif}}/ RT) \quad (4.48)$$

where D is the diffusion coefficient, D_0 the diffusion pre-factor and E_{dif} is the activation energy for diffusion. With the rise of surface temperature of the sensing element, the diffusion of the gas molecules (e.g. oxygen) across the diffusion barrier will be easier and at sufficiently high temperature (such that $RT \gg E_{\text{dif}}$) the adsorbate translates freely across the surface, following a Brownian type motion. In other words, at high temperature, the gases are bound in the z direction (i.e not desorbed) but free to move along X and Y directions. In view to this, the features presented in Fig. 4.22 can be explained as follows. When the sensing element is kept in air at elevated temperature, the adsorption of the oxygen molecules takes place on the sensor surface. After the saturation of the sensing surface with the adsorbed oxygen, the diffusion phenomenon will be predominant due to the steric repulsion of the gas molecules (sensor is kept in dynamic flow of gases) as well as unavailability of the adsorption sites. When the reducing gas is introduced initially they react with the adsorbed oxygen however, during saturation of the sensor response, the diffusion phenomenon predominates. The origin of resistance undulation is thought to be related to factors such as dynamic adsorption-desorption as

well as diffusion of adsorbed molecules on the sensor surface. As shown in Fig. 4.21, clearly the resistance undulation minimizes with the increase in sensor operating temperature. The resistance undulation feature is analyzed further as follows.

As mentioned above, the nature of chemical environment (air or test gas) influences the surface resistance and its undulation as the adsorbed gas molecules change the mobility and free carrier densities [39]. To address the selectivity of semiconducting oxide based gas sensors, usually a sensor array is used in which is individual sensor is having maximum response (%) towards a particular gas. Such arrangement would make the sensor system expensive and a bit unreliable for practical applications. Recently, fluctuation enhanced gas sensing, based on the analyses of resistance/ conductance fluctuation during gas sensing is proposed to be a viable tool to address the selectivity issue [37, 40]. It is proposed that in the equilibrium state during gas sensing (corresponding to almost constant absolute resistance/ conductance value with said undulation), the adsorption and desorption of gas molecules becomes a stationary stochastic process. Therefore the resistance undulation also becomes a stationary stochastic process. Practically, we have applied a fixed bias voltage (2 V) across the planner electrode on the sensor surface and from the measured current; resistance is calculated from the Ohm's law. The probable sources of the resistance noise are already outlined earlier. It is well known that the power spectrum of resistance noise is a good indicator of the change in chemical environment in gas sensing and therefore can be used for selective gas sensing [37]. The power density spectrum ($S_G(f)$) of the noise of any measured physical quantity has superimposed thermal and $1/f$ like noise [41]. In the equilibrium state, we presume that $1/f$ like noise predominates and the noise power P

$$(P = \int_{f_1}^{f_2} S_G(f) df, \text{ where } f_1 \text{ and } f_2 \text{ are low frequency limits}) \propto f^{-\gamma} \text{ where } \gamma \text{ is the frequency}$$

exponent of the gas type. The log-log plot of power (P) vs frequency (f) should yield a straight line and from the slope frequency exponent (γ) can be estimated. Fig. 4.23 shows the two consecutive conductance transients recorded during (a) H_2 (b) CO (c) CH_4 gas sensing using MZFO-C sensing elements. The gas concentration and operating temperature is kept fixed at ~ 500 ppm and $350^\circ C$. The power spectrum has been estimated from the measured conductance transients (during response process) using

Origin-8 software [<http://www.OriginLab.com>]. Fig. 4.24 shows the log-log plot of power vs frequency.

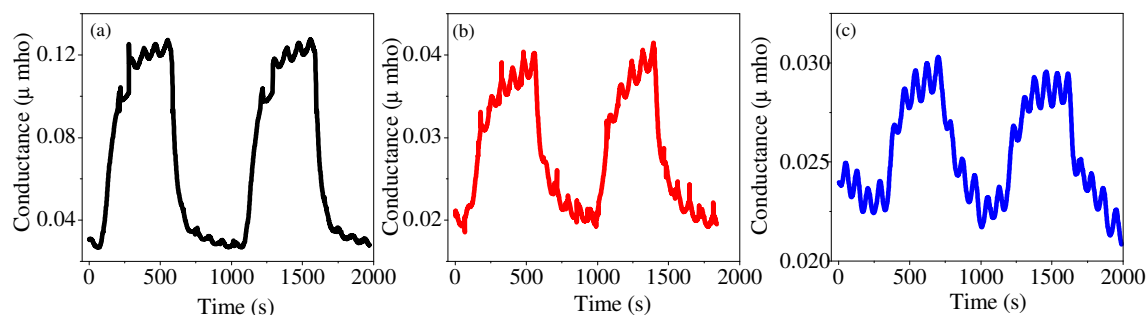


Fig. 4.23: Conductance transients recorded for (a) H₂ (b) CO (c) CH₄ gas (500 ppm) sensing using Mg_{0.5}Zn_{0.5}Fe₂O₄ (MZFO-C) sensing elements at ~350 °C

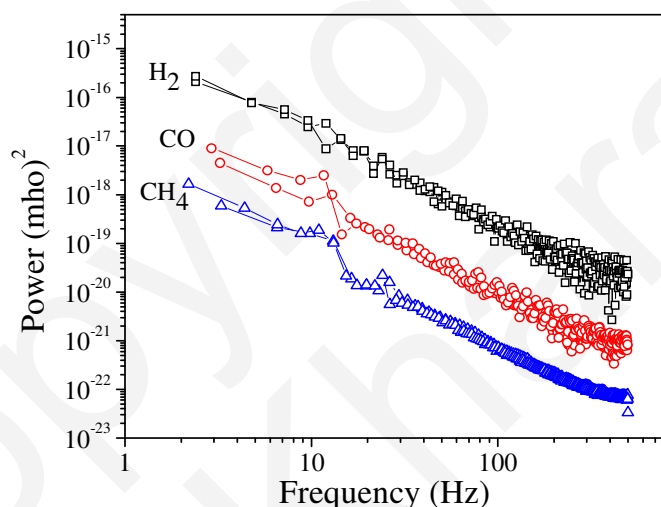


Fig. 4.24: The power spectrum of conductance noise for hydrogen, carbon monoxide and methane gas sensing estimated from the respective conductance transients

As shown in the figure, for each individual gas, the frequency dispersion of power, derived from each individual response transient of the conductance are clustered together and well separated from each other. For methane gas sensing, the power spectrum is found to be saturated at high frequency (> 200 Hz). As mentioned earlier, especially in low frequency region (< 100 Hz), indeed a linear relationship exist between $\log P$ vs $\log f$ plots for all these gases. For clarity typical plots for methane, carbon monoxide and hydrogen sensing is shown separately in Fig. 4.25. From the linear fit (dashed lines), the

exponent γ is estimated. As marked in the figure, the characteristics corner frequency (f_r) is denoted by the frequency where the power starts to saturate.

For CO and H₂ gas sensing, characteristic f_r is found to be different. For each of these gases, the average values for low frequency magnitude of power, γ and f_r are tabulated in the inset of Fig. 4.25. The data clearly show that power spectrum ‘finger print’ is sensitive enough to indicate at least that these gases are different.

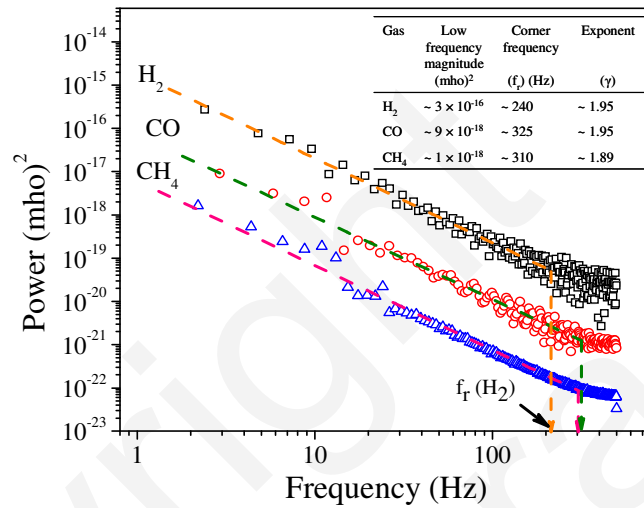


Fig. 4.25: Linear fit (dashed line) of log power vs log frequency for hydrogen, carbon monoxide and methane gas sensing. The exponent γ and corner frequency (f_r) is estimated from the linear fit. The low frequency magnitude of power, γ and f_r for H₂, CO and CH₄ gas sensing is shown at the inset

In the next section we have described the investigation details of spike-like noise just prior to the response and recovery transients.

4.5.3. Spike-Like Features in Resistance Transients

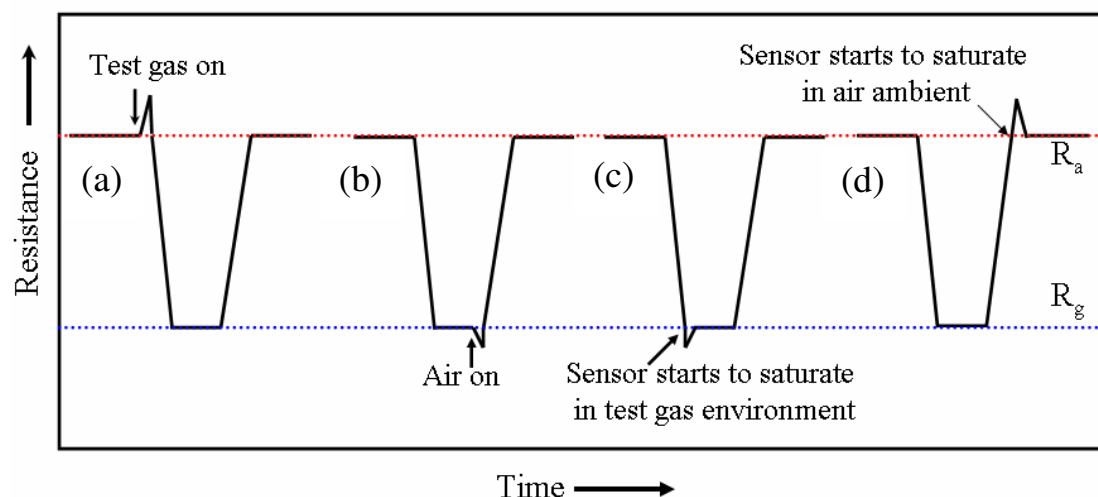
As outlined in Sec. 4.5, another interesting observation is the occurrence of ‘spike’ like features in the resistance transient of the sensing elements. The feature is not limited to the ferrite based sensors, but observed in various other semiconducting oxide based sensors as well. Table-4.7 summarizes some of the literature reports that describe the occurrence of such feature during gas sensing measurements.

Table-4.7: Overview of the spike like features reported for various sensing materials during the detection of a variety of test gases

Sensor	Test gas	Set-up	Comment/ plausible explanation	Reference
Ce, W, Zn, Sb doped Ga ₂ O ₃ thin films	O ₂	Dynamic	The sensors doped with Sb and W exhibit an initial spike when exposed to the analyte gas. No explanation has been given for the origin of these spikes.	[42]
Graphene	NH ₃ , CO, H ₂ O, NO ₂	Static	The observed spikes survive for few minutes and generally are irreproducible. No explanation has been given for the origin of spikes.	[43]
SnO ₂ hollow spheres	Ethanol	Static	The occurrence of spikes in the resistance transients are overlooked	[20]
ZnO-nano-wire based quartz crystal microbalance sensor	NH ₃	Dynamic	Spikes arise when NH ₃ is introduced in the sensing chamber. The occurrence of spike is related to the sudden mass increment due to NH ₃ adsorption on sensor surface.	[22]
Reduced graphene oxide	NH ₃	Static	Spike arises when ammonia is exposed to the sensor. It is attributed to the unsteadiness of the gas flow when the chemical environment is changed from one gas to another.	[44]

Reviewing these reports it is felt that the origin of these spikes is not very well understood. The spike like features can be grouped into two categories. As shown in Fig. 4.26(a) and (b), Category-I spikes appear when air ambient is switched to test gas or vice versa. Category-II spikes appear when resistance transients starts to saturate either in test gas or in air ambient (Fig. 4.26(c) and (d) respectively). In other words for Category-I spikes the chemical environment is changed around the sensor surface, however, for Category-II spikes, chemical environment around the sensor surface remains unaltered. For Mg_{0.5}Zn_{0.5}Fe₂O₄ hollow spheres, Category-I and II type spikes are shown in Fig. 4.27 (a) and (b) respectively. These transients are measured during H₂ gas (~1660 ppm) sensing at 300 °C and 350 °C respectively. The inset of Fig. 4.27(a) and (b) show these

two types of spike separately. At present, the underlying mechanism controlling the occurrence of these spikes is not clear.



As discussed in the preceding section, in equilibrium condition gas molecules hop from one binding site to another on the sensor surface. The resistance undulation observed in the equilibrium state in test gas (H_2) environment (see Fig. 4.27(a)) is related to dynamic adsorption-desorption as well as diffusion of H_2 molecules on the sensor surface. When the sensor is flushed with air, the hopping H_2 molecules instantly form

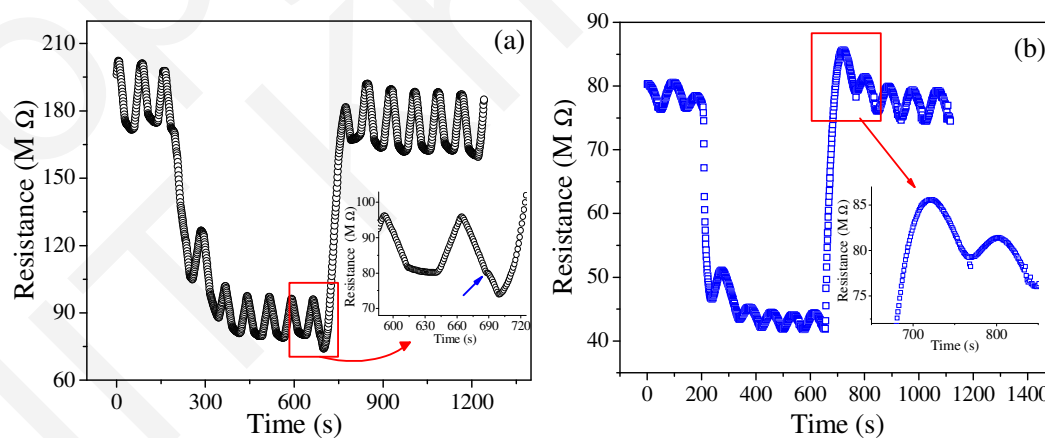


Fig. 4.27: Different types of spike recorded for H_2 sensing using $Mg_{0.5}Zn_{0.5}Fe_2O_4$ hollow spheres (a) Category-I and (b) Category-II. The spikes for each category are enlarged in the inset of respective figures

oxidized product. Probably this leads to sudden decrease in resistance resulting a spike (marked in Fig. 4.27(a)). After this, oxygen is chemi-adsorbed on the sensor surface and resistance starts to increase with time. As shown in Fig. 4.27(b), Category-II spike appears just prior to attain the equilibrium condition (in air environment). The occurrence of this kind of spikes is thought to be due to kinetically favored chemi-adsorption of oxygen species. To better understand these features, the characteristics of the spikes should be studied systematically at different gas concentration as well as by varying sensor operating temperatures.

4.6. Summary and Conclusions

The n-type semiconducting spinel ferrite ceramics exhibit good response towards a variety of gases including carbon monoxide, hydrogen, methane and nitrous oxide. We have already reported in Chapter-3 that as compared to other spinel ferrites, wet chemical synthesized magnesium zinc ferrite exhibit superior gas sensing performances towards these gases. The present chapter deals with the analyses of resistance/conductance transients during the response and recovery of gas sensing measurements.

At the beginning of this chapter a brief description has been provided on the generalized gas-solid interaction. It is argued that for spinel ferrite sensors the adsorption of the reducing gas and desorption of its oxidized products are the rate limiting processes for response and recovery of the gas sensor respectively. The response and recovery transients of conductance for spinel ferrite sensing elements towards hydrogen and carbon monoxide gas sensing are modeled using Langmuir adsorption kinetics with two active adsorption sites in the sensing elements. These two active sites are the macro- and meso-porous regions of the sensing elements as identified in their scanning electron micrographs. It is found that for both the adsorption sites, at constant temperature T , Langmuir adsorption isotherm behavior is obeyed. We have reported that at constant temperature, response time constants follow an inverse power relation to the test gas concentration ($\tau \propto C_{\text{gas}}^{-\beta}$). When the kinetics of sensor response is controlled by adsorption/desorption process then the temperature dependence of the response and recovery time constants follow an Arrhenius relation with sensor operating temperature.

From the best fitted response and recovery time constants, we have estimated the corresponding activation energies of the adsorption and desorption of gases. For carbon monoxide and hydrogen gases, the corresponding activation energies for adsorption and desorption are found to be distinctly different. It is recommended that since each gas, depending of its reactivity, size of the gas molecules, etc has characteristic activation energies for adsorption and desorption, kinetic analyses of resistance transient during response and recovery might be beneficial to address the selectivity issue of these gas sensing materials.

A number of interesting features are observed in the recorded resistance/conductance transients of the binary and spinel oxide based nano-structured sensing materials. The identified features are (i) drift in the base resistance upon repeated response and recovery cycles, causes mainly due to the unsaturated resistance transients during response and recovery, (ii) response and recovery transients with sinusoidal noise, and (iii) occurrence of spike-like features in the recorded transients. We have made an attempt to understand the nature and origin of these features based on our developed hypothesis on the reaction sequence of gas absorption and desorption of the reaction products.

Little or marginal base resistance drift of metal oxide sensor is desirable during repeated response and recovery cycles. However, due to the partial recovery, often significant drift in base resistance is reported. The resistance transient is termed reversible in case of complete recovery; otherwise it is termed irreversible when partial recovery is occurred. As for example, for hydrogen and carbon monoxide gas sensing we have demonstrated distinct reversible and irreversible resistance transients for magnesium zinc ferrite and zinc oxide sensing elements respectively. The corresponding response transients for these sensing elements are modeled using Langmuir-Hishelwood reaction mechanism and the characteristic response times are estimated. It is found that for irreversible transients the response time is dependent on the test gas concentration; however, for reversible transients it (the response time) is almost independent to the gas concentration. Finally, it is concluded that the irreversible and reversible nature of gas sensing is related to the dense and open type surface morphology respectively.

The occurrences of the sinusoidal noise in the response and recovery transients in some of the synthesized nanostructures are explained to be due to nature of surface diffusion of the gas molecules in these structures. The power spectrum of resistance noise is proposed to be a good indicator of the change in chemical environment in gas sensing and therefore can be used for selective gas sensing using a single discrete sensor. It is demonstrated that for each individual gas (viz. H_2 , CO , and CH_4), the frequency dispersion of power (derived from each individual response transient of the conductance), are clustered together and well separated from each other. By linear fitting of log-power vs log-frequency plots we have estimated the characteristic corner frequency, frequency exponent and low frequency magnitude of power for each of the above three gas sensing measurement. By analyzing the estimated values of the above parameters it is concluded that power spectrum 'finger print' is sensitive enough to selectively detect these three gases. The spike like features in the resistance transients during response and recovery are detected either during the change of chemical environment surrounding the sensor surface or just prior attaining the equilibrium state during response or recovery. Attempts are made to explain these features based on our understanding of gas-solid interaction during reducing gas sensing using nano-structured cubic spinel ferrite sensing elements.

Reference

- [1] Liu, Y.L., Liu, Z.M., Yang, Y., Yang H.F., Shen, G.L. and Yu, R.Q. (2005), Simple Synthesis of MgFe_2O_4 Nanoparticles as Gas Sensing Materials, *Sensors and Actuators B*, Vol. 107, pp. 600-604.
- [2] Liao, L., Lu, H.B., Li, J.C., He, H., Wang, D.F., Fu, D.J. and Liu, C. (2007), Size Dependence of Gas Sensitivity of ZnO Nanorods, *The Journal of Physical Chemistry. C*, Vol.111, pp.1900-1903.
- [3] Eriksson, J., Khranovskyy, V., Soderlind, F., Kall, P.O., Yakimova, R., Spetz, A.L. (2009), ZnO Nanoparticles or ZnO Flms: A Comparison of the Gas Sensing Capabilities, *Sensors and Actuators B*, Vol. 137, pp. 94-102.
- [4] Ramgir, N.S., Hwang, Y.K., Jhung, S.H., Mulla, I.S. and Chang, J.S. (2006), Effect of Pt Concentration on the Physicochemical Properties and CO Sensing Activity of Mesoporous SnO_2 , *Sensors and Actuators B*, Vol.114, pp. 275-282.
- [5] Choi, Y.J., Hwang, I.S., Park, J.G., Choi, K.J., Park, J.H. and Lee, J.H. (2008), Novel Fabrication of an SnO_2 Nanowire Gas Sensor with High Sensitivity, *Nanotechnology*, Vol.19, pp. 095508 (4).
- [6] Yin, X.M., Li, C.C, Zhang, M., Hao, Q.Y., Liu S., Li, Q.H., Chen, L.B. and Wang T.H.(2009), SnO_2 Monolayer Porous Hollow Spheres as a Gas Sensor, *Nanotechnology*, Vol. 20, pp. 455503 (6).
- [7] Carotta, M.C., Cervi, A., Natale, V., Gherardi, S., Giberti, A., Guidi, V., Puzzovio, D., Vendemiati, B., Martinelli, G., Sacerdoti, M., Calestani, D., Zappettini, A., Zha, M. and Zanotti, L. (2009), ZnO Gas Sensors: A Comparison between Nanoparticles and Nanotetrapods Based Thick films, *Sensors and Actuators B*, Vol.137, pp.164–169.
- [8] Korotcenkov, G., Ivanov, M., Blinov, I. and Stetter, J.R. (2007), Kinetics of Indium Oxide Based Thin Film Gas Sensor Response: The Role of “Redox” and Adsorption/Desorption Processes in Gas Sensing Effects, *Thin Solid Films*, Vol. 515, pp.3987-3996.
- [9] Aygun, S. and Cann, D. (2005), Response Kinetics of Doped CuO/ZnO Heterocontacts, *The Journal of Physical Chemistry B*, Vol.109, pp. 7878-7882.
- [10] Hu, H., Trejo, M., Nicho, M.E., Saniger, J.M. and Valenzuela, A.G. (2002), Adsorption Kinetics of Optochemical NH_3 Gas Sensing with Semiconductor Polyaniline Films, *Sensors and Actuators B*, Vol. 82, pp.14-23.
- [11] Mukherjee, K. and Majumder, S.B., (2009), Analyses of Response and Recovery Kinetics of Zinc Ferrite as Hydrogen Gas Sensor, *Journal of Applied Physics*, Vol.106, pp. 064912 (9).
- [12] Mukherjee, K. and Majumder, S.B., (2010), Reducing Gas Sensing Behavior of Nano-Crystalline Magnesium-Zinc Ferrite Powders, *Talanta*, Vol. 81, pp.1826-1832.

-
- [13] Mukherjee, K., Bharti, D.C. and Majumder, S.B. (2010), Solution Synthesis and Kinetic Analysis of the Gas Sensing Characteristics of Magnesium Ferrite Particles, *Sensors and Actuators B*, Vol.146, pp. 91-97.
- [14] Darshane, S.L., Deshmukh, R.G., Suryavanshi, S.S. and Mullah, I.S. (2008), Gas Sensing Properties of Zinc Ferrite Nanoparticles Synthesized by the Molten Salt Route, *Journal of American Ceramic Society*, Vol. 91, pp. 2724-2726.
- [15] Kolasinski, K.W. (2008), *Surface Science: Foundations of Catalysis and Nanoscience*, West Chester University, USA, John Wiley and Sons Ltd., Second Edition.
- [16] Korotcenkov, G., Brinzari, V., Golovanov, V. and Blinov, Y. (2004), Kinetics of Gas Response to Reducing Gases of SnO₂ Flms, Deposited by Spray Pyrolysis, *Sensors and Actuators B*, Vol. 98, pp. 41-45.
- [17] Korotcenkov, G., Brinzari, V., Stetter, J.R., Blinov, I. and Blaja, V. (2007), The Nature of Processes Controlling the Kinetics of Indium Oxide-Based Thin Film Gas Sensor Response, *Sensors and Actuators B*, Vol.128, pp. 51-63.
- [18] Mukherjee, K. and Majumder, S.B. (2010), Analyses of Conductance Transients to Address the Selectivity Issue of Zinc Ferrite Gas Sensors, *Electrochemical and Solid State Letters*, Vol.13, pp. J25-J27.
- [19] Gong, J., Sun, J. and Chen, Q. (2008), Micromachined Sol-Gel Carbon Nanotube/ SnO₂ Nanocomposite Hydrogen Sensor, *Sensors and Actuators B*, Vol.130, pp. 829-835.
- [20] Tan, Y., Li, C., Wang, Y., Tang, J. and Ouyang, X. (2008), Fast-Response and High Sensitivity Gas Sensors Based on SnO₂ Hollow Spheres, *Thin Solid Films*, Vol. 516, pp. 7840-7843.
- [21] Rothschild, A., Edelman, F., Komem, Y. and Cosandey, F. (2000), Sensing Behavior of TiO₂ Thin Films Exposed to Air at Low Temperatures, *Sensors and Actuators B*, Vol. 67, pp. 282-289.
- [22] Wang, X., Zhang, J. and Zhu, Z. (2006), Ammonia Sensing Characteristics of ZnO Nanowires Studied by Quartz Crystal Microbalance, *Applied Surface Science*, Vol. 252, pp. 2404-2411.
- [23] Bermak, A., Belhouari, S.B., Shi, M. and Martinez, D. (2006), Pattern Recognition Techniques for Odor Discrimination in Gas Sensor Array, *Encyclopedia of Sensors*, Vol. X, pp. 1-17.
- [24] Wang, Y., Zhou, Z., Yang, Z., Chen, X., Xu, D. and Zhang, Y. (2009), Gas Sensors Based on Deposited Single-Walled Carbon Nanotube Networks for DMMP Detection, *Nanotechnology*, Vol. 20, pp. 345502 (8).
- [25] Liao, J.Y. and Ho, K.C. (2008), A Study of Partially Irreversible Characteristics in a TTF-TCNQ Gas Sensing System, *Sensors and Actuators B*, Vol.130, pp. 343-350.
-

-
- [26] Wu, R.J., Huang, Y.C., Yu, M.R., Lin, T.H. and Hung, S.L. (2008), Application of m-CNTs/ NaClO₄/Ppy to a Fast Response Room Working Temperature Ethanol Sensor, *Sensors and Actuators B*, Vol. 134, pp. 213-218.
- [27] Tison, Y., Stolojan, V., Watts, P.C.P, Cox, D.C., Chen, G.Y. and Silva, S.R.P. (2007), Gas Sensing Properties of Vapour-Deposited Tungsten Oxide Nanostructures, *Microscopy of Semiconducting materials*, Vol.120, pp. 281-284.
- [28] Kemp, N.T., Kaiser, A.B., Trodah, H.J., Chapman, B., Buckley, R.G., Partridge, A.C. and Foot, P.J.S. (2006), Effect of Ammonia on the Temperature Dependent Conductivity and Thermopower of Polypyrrole, *Journal of Polymer Science: Part B: Polymer Physics*, Vol. 44, pp.1331-1338.
- [29] Pancheri, L., Oton, C.J., Gaburro, Z., Soncini, G. and Pavesi, L. (2004), Improved Reversibility in Aged Porous Silicon NO₂ Sensors, *Sensors and Actuators B*, Vol. 97, pp. 45-48.
- [30] Ong, K.G., Zeng, K. and Grimes, C.A. (2002), A Wireless Passive Carbon Nanotube-Based Gas Sensor, *IEEE Sensors Journal*, Vol. 2, pp. 82-88.
- [31] Lee, C.Y. and Strano, M.S. (2005), Understanding the Dynamics of Signal Transduction for Adsorption of Gases and Vapors on Carbon Nanotube Sensors, *Langmuir*, Vol. 21, pp. 5192-5196.
- [32] Sing, K.S.W., Everett, D.H., Haul, R.A.W., Moscou, L., Pierotti, R.A., Rouquerol, J. and Siemieniewska, T. (1985), Reporting Physisorption Data for Gas/ Solid Systems with Special Reference to the Determination of Surface Area and Porosity, *Pure and Applied Chemistry*, Vol. 57, pp. 603-619.
- [33] Nakata, S., Kato, Y., Kaneda, Y. and Yoshikawa, K. (1996), Rhythmic Chemical Reaction of CO on the Surface of a SnO₂ Gas Sensor, *Applied Surface Science*, Vol.103, pp. 369-376.
- [34] Hong, L., Li, Y. and Yang M. (2010), Fabrication and Ammonia Gas Sensing of Palladium/Polypyrrole Nanocomposite, *Sensors and Actuators B*, Vol.145, pp. 25-31.
- [35] Zeng, Z., Wang, K., Zhang, Z., Chen, J. and Zhou W. (2009), The Detection of H₂S at Room Temperature by Using Individual Indium Oxide Nanowire Transistors, *Nanotechnology*, Vol. 20, pp. 045503 (4).
- [36] Gomri, S., Seguin, J.L. and Aguir, K. (2005), Modeling on Oxygen Chemisorption-Induced Noise in Metallic Oxide Gas Sensors, *Sensors and Actuators B*, Vol.107, pp. 722-729.
- [37] Kish, L.B., Vajtai, R. and Granqvist, C.G. (2000), Extracting Information from Noise Spectra of Chemical Sensors: Single Sensor Electronic Noses and Tongues, *Sensors and Actuators B*, Vol. 71, pp. 55-59.
- [38] Kish, L.B., Li. Y., Solis J.L., Marlow, W.H., Vajtai, R., Granqvist, C.G., Lantto, V., Smulko, J.M. and Schmera, G. (2005), Detecting Harmful Gases Using Fluctuation-Enhanced Sensing, *IEEE Sensors Journal*, Vol. 5, pp.671-676.
-

- [39] Gomri, S., Seguin, J.L., Guerin, J. and Aguir, K. (2008), A Mobility and Free Carriers Density Fuctuations Based Model of Adsorption-Desorption Noise in Gas Sensor, *Journal of Physics D: Applied Physics*, Vol. 41, pp. 065501 (11).
- [40] Solis, J.L., Seeton, G., Li, Y. and Kish, L.B. (2003), Fluctuation-Enhanced Sensing with Commercial Gas Sensors, *Sensors and Transducers Magazine*, Vol. 38, pp.59-66.
- [41] Solis, J.L., Kish, L.B., Vajtai, R., Granqvist, C.G., Olsson, J., Schnurer, J. and Lantto, V. (2001), Identifying Natural and Artificial Odours Through Noise Analysis with a Sampling-and-Hold Electronic Nose, *Sensors and Actuators B*, Vol. 77, pp. 312-315.
- [42] Li, Y., Trinchì, A., Wlodarski, W., Galatsis, K. and Kalantarzadeh, K. (2003), Investigation of the Oxygen Gas Sensing Performance of Ga_2O_3 Thin Flms with Different Dopants, *Sensors and Actuators B*, Vol. 93, pp. 431-434.
- [43] Schedin, F., Geim, A.K., Morozov, S.V., Hill E.W., Blake, P., Katsnelson, M.I. and Novoselov, K.S. (2007), Detection of Individual Gas Molecules Adsorbed on Graphene, *Nature Materials*, Vol. 6, pp. 652-655.
- [44] Lu, G., Ocola, L.E. and Chen, J. (2009), Reduced Graphene Oxide for Room-Temperature Gas Sensors, *Nanotechnology*, Vol. 20, pp. 445502 (9).

Chapter-5

PART-I: CROSS SELECTIVITY OF MAGNESIUM ZINC FERRITE SENSING ELEMENT: USE OF PATTERN RECOGNITION TECHNIQUES

PART-II: DEVELOPMENT OF PROTOTYPE MAGNESIUM ZINC FERRITE COMBUSTIBLE GAS SENSOR

5.1. Introduction

The cross-selectivity restricts the adaptability of semiconducting metal oxide based gas sensors mostly in economic gas alarm system for domestic and industrial applications. Various strategies with limited success has been attempted to address the cross-selectivity issue of semiconducting gas sensors. These strategies can be grouped into three major categories: First, during gas sensing, the nature of the transient resistance response at different operating temperature depends on the type of test gas under investigation. This is due to the fact that sensor operating temperature modulates the adsorption/desorption kinetics of the test gas on the sensing surface resulting characteristics resistance transient specific to the respective gas type [1-2]. Second, various catalyst: semiconducting oxide combinations have been used to improve the sensitivity of the respective oxide towards specific gas [3-4]. As for example, as compared to CO, CH₄ gases, WO₃: Pd sensor is found to be more sensitive and thereby termed selective towards NO_x gas sensing [4]. Third, noise spectroscopy analyses of conductance transient have been adopted to address the selectivity issue [5]. In this case the estimated corner frequency and low frequency magnitude is demonstrated to be

specific for a given gas type in the analysis. The limited success of the above techniques to address the cross-selectivity issue can be traced down to the use of expensive precursor material for sensor synthesis, costly equipment and laboratory procedure which is non conducive to yield continuous monitoring for any practical application.

From the studies on gas sensing characteristics of a discrete magnesium zinc ferrite nano-structured sensing materials (discussed in Chapter-3 and 4), it is apparent that though the sensing materials exhibit higher response towards the detection of hydrogen gas but the cross-selectivity with other gases (CO, CH₄, N₂O) could not be avoided. In Chapter-4 we have demonstrated that the kinetic analyses of the resistance/ conductance transients could be beneficial to address the selectivity issues of the gas sensors. However, in real time situation, it is difficult to comment on the selectivity based on the estimated variation of the kinetic parameters on the gas concentration and operating temperature. Thus, for a hand-held sensor functioning at a fixed operating temperature, addressing the selectivity based on such kinetic analyses is inconvenient, and may not be useful to readily detect a particular gas type. As described in details in Chapter-4, in spite of this drawback to use it for addressing the selectivity issue, kinetic analyses of a discrete nano-structured oxide sensor are fruitful to investigate the gas sensing mechanism, and to understand the interrelation between the sensor structure and gas sensing characteristics including sensitivity, response/recovery time, and stability.

Usually, in order to generate a separate pattern corresponding to different gas type, a sensor array is needed which makes the gas sensing system complicated and expensive. As detailed in Chapter-4, analyses of the noise spectra (of the measured resistance / conductance transients of the sensing elements during gas sensing) could be a viable alternative for selective gas sensing using a discrete sensor. Such fluctuation enhanced sensing is able to generate a complex pattern using a single discrete sensor. The most promising application for this approach could be realized through the development of an economic portable electronic nose system with low power consumption. However, as we concluded in the preceding chapter, to realize of such electronic nose, the fluctuation enhanced sensing of a single discrete element (in different gas environments) should be studied in details as a function of the sensor operating temperature and gas concentration.

As another viable alternative to the above techniques, in the present chapter, we have further addressed the cross-selectivity issue of magnesium zinc ferrite sensors by analyzing the characteristics features of the conductance transients using pattern recognition algorithm. Pattern recognition techniques are widely adopted as a multivariate statistical tool which has drawn considerably attention in analyzing various experimental data (chromatographic, spectroscopic, spectrometric, spectro-photometric, etc.) for a variety of application including but not limited to profiling, authentication, detection of adulteration, finger-printing, food quality assessment, data interpretation, etc [6].

The experimental work is described in two parts. In PART-I we have described the experimental results addressing the cross-selectivity of magnesium zinc ferrite sensing elements towards reducing gas sensing using pattern recognition techniques. Finally, in PART-II of this chapter, we have described the development and performance of a Taguchi type combustible gas sensor prototype using $\text{Mg}_{0.5}\text{Zn}_{0.5}\text{Fe}_2\text{O}_4$ (prepared using modified Pechini route) (MZFO-C) nano-particulate sensing materials.

PART-I

5.2. Feature Extraction and Pattern Recognition Methods

In this section first we have reviewed various methods used to extract important features from the response transients of chemi-resistor type temperature modulated gas sensors. Next we have reviewed various pattern recognition algorithms that use these features to recognize and quantify the test gases also mixture of test gases.

5.2.1. Feature Extraction Technique

Fast Fourier transform (FFT): In the semiconducting oxide based gas sensors the features of the resistance/ conductance transients are mostly extracted using FFT. The Fourier analysis is a mathematical technique to transform the time based signal to frequency based one. The process of Fourier analyses is represented as

$$F(\omega) = \int_{-\infty}^{+\infty} f(t) \exp(-i\omega t) dt \quad (5.1)$$

where the Fourier transform $F(\omega)$ is the sum over all time of the signal $f(t)$ multiplied by a complex exponential. The complex exponential can be broken down to real and imaginary sinusoidal components. The results of the transform are the Fourier coefficients $F(\omega)$. In transforming the signal the time information is lost. As outlined in Chapter-4, the experimental resistance/conductance transients contain various transitory characteristics including drift, sinusoidal modulation, sporadic spikes etc. Unfortunately, Fourier transform can not detect these features efficiently. If on the other hand the signal does not change much with time then this drawback is of less significance. As an effective alternative, wavelet analyses yield both frequency and temporal information and the details of wavelet transform is provided next.

Wavelet transform (WT): Wavelet analysis is the breaking up of a signal into shifted and scaled versions of the original wavelet. Wavelet transform is of three different types namely the continuous wavelet transform (CWT), discrete wavelet transform (DWT) and wavelet packets transform (WPT). The continuous wavelet transforms is defined as the sum over the total time of the signal multiplied by scaled, shifted versions of the wavelet function. In the discrete wavelet transform the total time domain of the sensor signal (viz. recorded during response/ recovery during gas sensing) is not monitored at a fixed rate rather a windowing technique with different-sized regions is employed. Wavelet packets are used to analyze frequency change in a signal over time; however, the results are not very smooth.

For acquiring low-frequency information DWT allows long duration windows, whereas, shorter windows are used for the accurate acquisition of high-frequency information. DWT automatically modifies the size of the windows depending on the signal being analyzed. As the wavelets of the signal are discretely sampled, both temporal and frequency information of the signal are obtained in this feature extraction technique. Different types of wavelet families (e.g. Haar wavelets, Daubechies wavelets etc) are used in the DWT based feature extraction. Among these, the Daubechies family is most popular and has all the desirable properties including orthogonality, approximation quality, redundancy and numerical stability [7]. Fig. 5.1 shows the schematic of the

sequential steps performed during the decomposition (upto 3rd level) of an input signal using DWT.

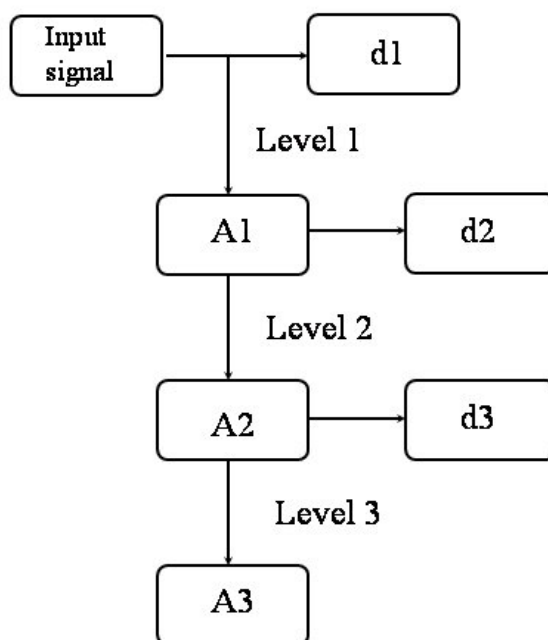


Fig. 5.1: Schematic of the three level decomposition of the discrete wavelet transformation

As shown in the schematic, the input signal is first decomposed into two parts: approximate coefficients (A: low frequency part) and detailed coefficients (d: high frequency part). The approximate coefficients are used in next level decomposition and in each of these levels detailed coefficients are discarded. Finally, after level 3, using approximate coefficients, the original signal can be reconstructed back without any distortion. Various pattern recognition techniques are reviewed in the following sections.

5.2.2. Pattern Recognition Algorithm

Pattern recognition algorithms are used extensively to discriminate the chemicals, hazard gases, aromas etc using sensor array based electronic nose and tongue. These pattern recognition algorithms are used to address the cross-selectivity issue of the semiconducting oxide gas sensors. Generally two types of algorithms, namely supervised and unsupervised, are adopted for this purpose. In supervised pattern recognition, first a discrimination model is developed. The model is then trained using known data which is finally verified by unknown samples. Discriminant factor analyses (DFA), linear

discriminate analyses (LDA), classification and regression trees (CART), partial least squares discriminate analysis (PLS-DA), and artificial neural networks (ANN) have been some of the most commonly used supervised algorithms. One of the drawbacks of these discriminating algorithms is that the unknown samples are always clustered into one of the given categories, even if they do not belong to any of them [6]

In the unsupervised algorithm the data are clustered based on the inherent similarities among the data-patterns. As the clustering of data is only based on the intrinsic feature of the patterns and no trained dataset are used as reference, the classification of various experimental data using unsupervised algorithm is a difficult problem. Using this algorithm the discrimination of closely varying dataset is reported to be poor and the component of the clusters are wide spread. The most common unsupervised algorithm used in the pattern recognition technique is principal component analysis (PCA). Some of the other unsupervised algorithms are projection pursuit (PP) [8], independent component analysis (ICA) etc [9-10]. Next we have described the important features of discriminate factor analyses and principle component analyses as commonly used supervised and unsupervised pattern recognition algorithms for gas sensor research.

Principle component analysis (PCA): As mentioned earlier PCA is an unsupervised pattern recognition algorithm. It is a statistical tool which converts a data set of possibly correlated variables (variables that carry most of the available information.) to a set of uncorrelated variables termed as principle components (PCs). To use the PCA in gas sensor research, first the sensor response values are converted using available feature extraction techniques such as FFT or DWT. The selected coefficients (correlated variables) of FFT and DWT are converted to principle component (PC_1 and PC_2) (uncorrelated variables) using PCA algorithm. The conversion is defined in such a way that the PCs contain the maximum data variance and orthogonal to each other. Further details of these analyses can be found elsewhere [11].

Discriminant factor analysis (DFA): It is a supervised pattern recognition algorithm i.e. the classes are predefined before one begins the analyses using an unknown set of data. It is apparent that the unknown set of data will fall in the specific predefined classes where it finds the most similar features. Discriminating axes are modified in such a way that optimum separation of the predefined classes is attained. Similar to the PCA, DFA

also forms new orthogonal coordinates using linear combination of the input variables. In DFA, the estimated factors are so arranged that minimize the variance within intra class and maximize the variance between inter classes. The minimization of variance between intra class and maximize the variance in inter classes leads to the optimal separation among intensified classes. In the present chapter, we have adopted feature extraction method of conductance transients in conjunction with pattern recognition algorithms to investigate the cross-selectivity of $\text{Mg}_{0.5}\text{Zn}_{0.5}\text{Fe}_2\text{O}_4$ (MZFO-C) sensing elements towards methane, carbon monoxide and hydrogen gases.

5.3. Experimental

Nano-crystalline phase pure $\text{Mg}_{0.5}\text{Zn}_{0.5}\text{Fe}_2\text{O}_4$ powders are synthesized using a self-combustion route described earlier in Chapter-3. The synthesized nano-crystalline $\text{Mg}_{0.5}\text{Zn}_{0.5}\text{Fe}_2\text{O}_4$ powders (MZFO-C) are pelletized and sintered at 600 °C for 2 h to form circular sensing elements. Planar gold electrodes are deposited on the surface of the sensing elements. The gas sensing performance of MZFO-C sensing elements are evaluated using a dynamic flow automated gas sensing measurement set up described earlier in Chapter-2. Hydrogen, methane and carbon monoxide are used as test gas and commercial air is used as carrier gas. We have utilized the fast Fourier transform (FFT) and discrete wavelet transform (DWT) to extract the important features of the measured conductance transients of MZFO-C sensors upon exposure to various reducing gases (H_2 , CO, CH_4) at ~350 °C. Selected coefficients from FFT and DWT analyses are used as input parameter in linear unsupervised (principal component analysis (PCA)) and supervised (discriminant factor analysis (DFA)) pattern recognition techniques. We have discussed relative merits and demerits of the used feature extraction methods and demonstrated the effectiveness of the dynamic pattern recognition techniques to discriminate these gases using a single MZFO-C sensing element.

The experimental procedure for pattern recognition analyses are as follows. First the optimized operating temperature corresponding to the maximum response (S, defined as $(R_a - R_g)/R_a$ where R_a and R_g are the surface resistance of the sensing materials measured in air and gas environment respectively) for each test gas (concentration ~500 ppm) is estimated. Then for each of this test gas, at least seven continuous responses and recovery

transients are recorded at the optimized operating temperature. After necessary data acquisition, the conductance transients are either fast Fourier transformed (FFT) or discrete wavelet transformed (DWT) using Labview® (Labview-8.5, National Instruments, USA) and MATLAB® (MATLAB 7.8.0.347-R2009a, MathWorks, USA) software. The linear unsupervised (PCA) as well as supervised pattern recognition analyses (DFA) are performed using commercial statistics analysis software (STATISTICA-9, StatSoft, USA) in conjunction with MATLAB®.

5.4. Results and Discussion

Fig. 5.2 shows the response and recovery conductance transients for (a) H_2 , (b) CO , (c) CH_4 (500 ppm) measured at 350 °C. Fig. 5.2(d) shows the response of these gases (1660 ppm) measured at different operating temperatures ranging 250-380 °C. Inspecting Fig. 5.2(a)-(c) marginal (Fig. 5.2(a)) to significant (Fig. 5.2(c)) conductance drift during

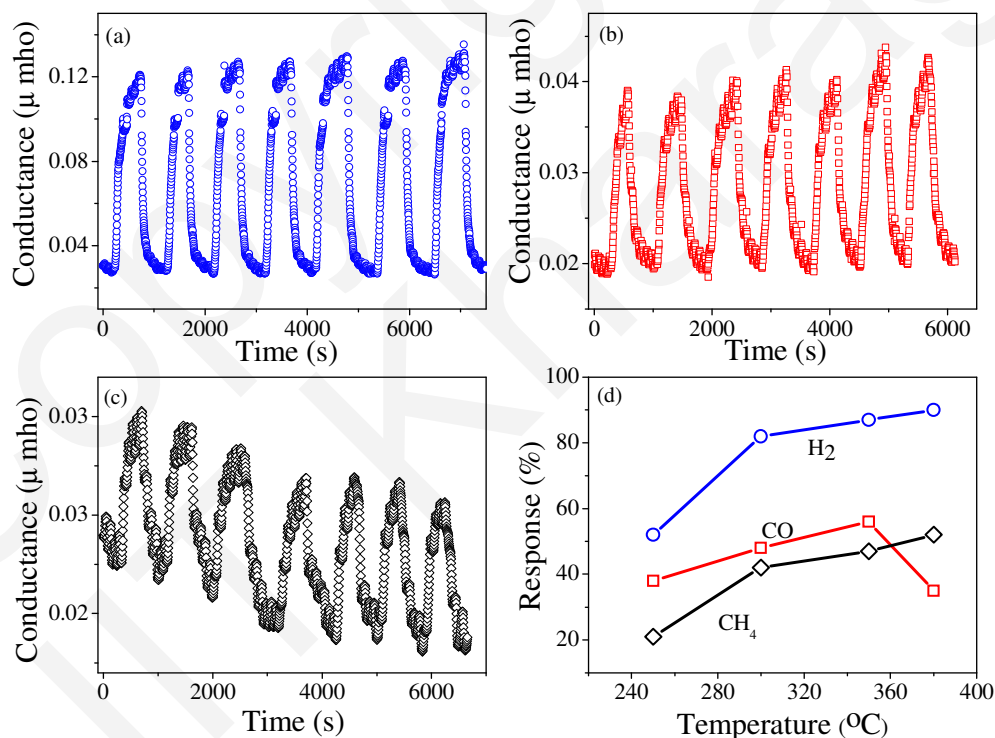


Fig. 5.2: Conductance transients during response and recovery of magnesium zinc ferrite (MZFO-C) particles for 500 ppm (a) hydrogen, (b) carbon monoxide, (c) methane sensing at the operating temperature ~ 350 °C. Fig. 5.2.(d) shows the temperature variation of response for the sensing of fixed concentration (1660 ppm) of gases

response and recovery is apparent and from Fig. 5.2(d) it is clear that the cross-selectivity of MZFO-C sensor cannot be avoided simply by modulating the operating temperature of these sensing elements.

5.4.1. Feature Extraction from the Conductance Transients

After acquiring at least seven transients for each of the above type of gas sensing, the conductance transients are either fast Fourier transformed (FFT) or discrete wavelet transformed (DWT) using Labview® (Labview-8.5, National Instruments, USA) and MATLAB® (MATLAB 7.8.0.347-R2009a, MathWorks, USA) software. The linear unsupervised (PCA) as well as supervised pattern recognition analyses (DFA) are performed using commercial statistics analysis software (STATISTICA-9, StatSoft, USA) in conjunction with MATLAB®. The sequence of the data analyses is summarized in Fig. 5.3. Through the fast Fourier transformation, the time domain conductance data is

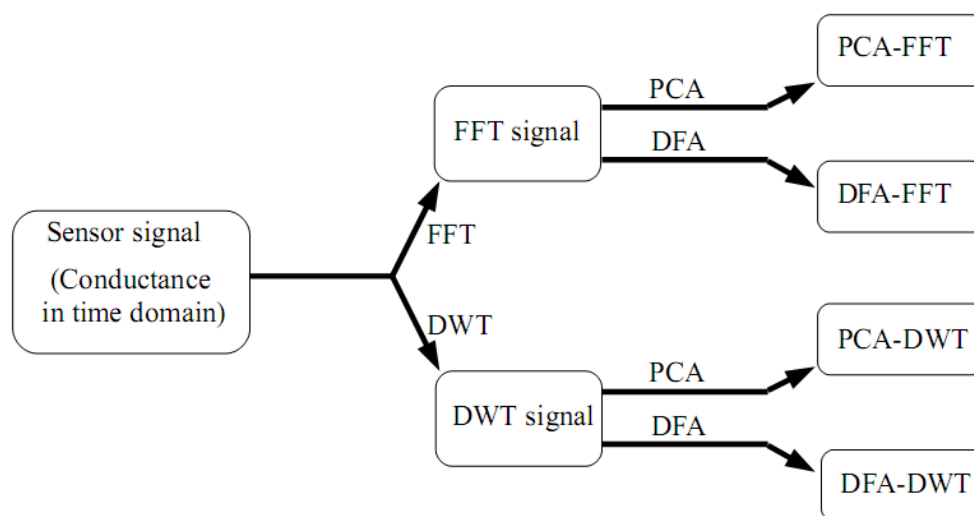


Fig. 5.3: Schematic of the sequence of the data analyses adopted for the pattern recognition algorithms

transformed into its frequency domain. The Fourier coefficients of the frequency domain data represent the contribution of sine and cosine function at each frequency. For each test gas used in the present investigation, similar FFT is performed on their respective conductance transients. It is known that the low amplitude harmonics (at relatively higher frequencies) are affected by noise. Therefore the low amplitude harmonics are

discarded and only the low frequency part of the transformed harmonics is used for further analyses. Fig. 5.4 shows the typical variation of the amplitude of the Fourier coefficients of 500 ppm methane conductance transient measured at 350 °C. The amplitude is estimated from the real and imaginary part of the Fourier coefficients shown in the inset of Fig. 5.4.

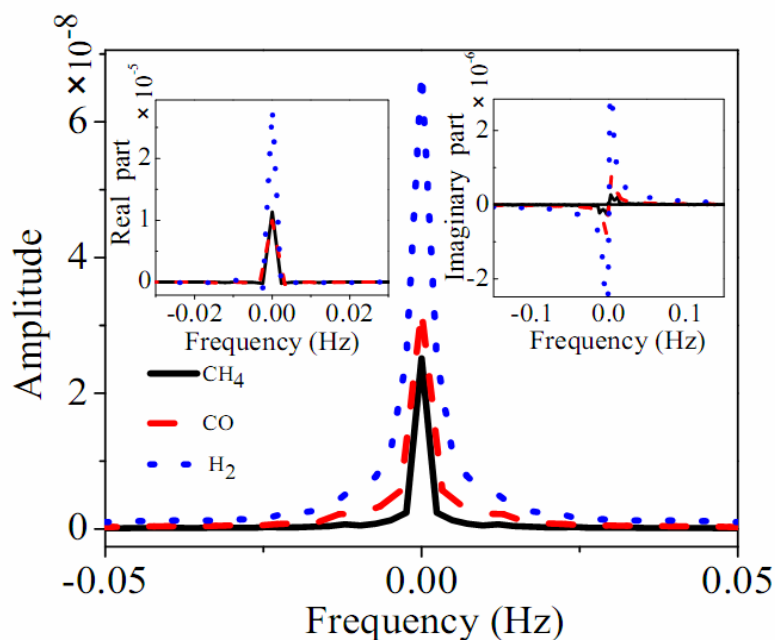


Fig. 5.4: Variation of the amplitude of the Fourier coefficients of 500 ppm methane conductance transient measured at 350 °C. The amplitude is estimated from the real and imaginary part of the Fourier coefficients shown in the inset

Finally, the amplitude of the first four frequency harmonics (with comparatively higher magnitude than its high frequency counterpart) for each test gas has been used for linear pattern recognition algorithms. In addition to FFT we have also performed discrete wavelet transform to extract both frequency and temporal information from the measured response conductance transients. Among the various available wavelet families we have selected Daubechies-four for the present analysis.

The typical decomposition of methane response (500 ppm) conductance transient is shown in Fig. 5.5(a)-(f). As outlined earlier (Fig. 5.1), the input signal is decomposed in 3 sequential levels. The respective approximated and detailed coefficients at each level (level 1-3) are shown in Fig. 5.5. After the final decomposition (level 3) the approximate

coefficients are considered as input data set for pattern recognition. To construct the DWT data matrix input we have selected 27-29 and 37-39 wavelet numbers of the approximated coefficients. The selection is based on the yield of maximum variance of the approximate coefficients for different gas types. The data matrices extracted from FFT and DWT analyses are used as input in already stated two pattern recognition techniques namely principal component analysis (PCA) and discriminant factor analysis (DFA).

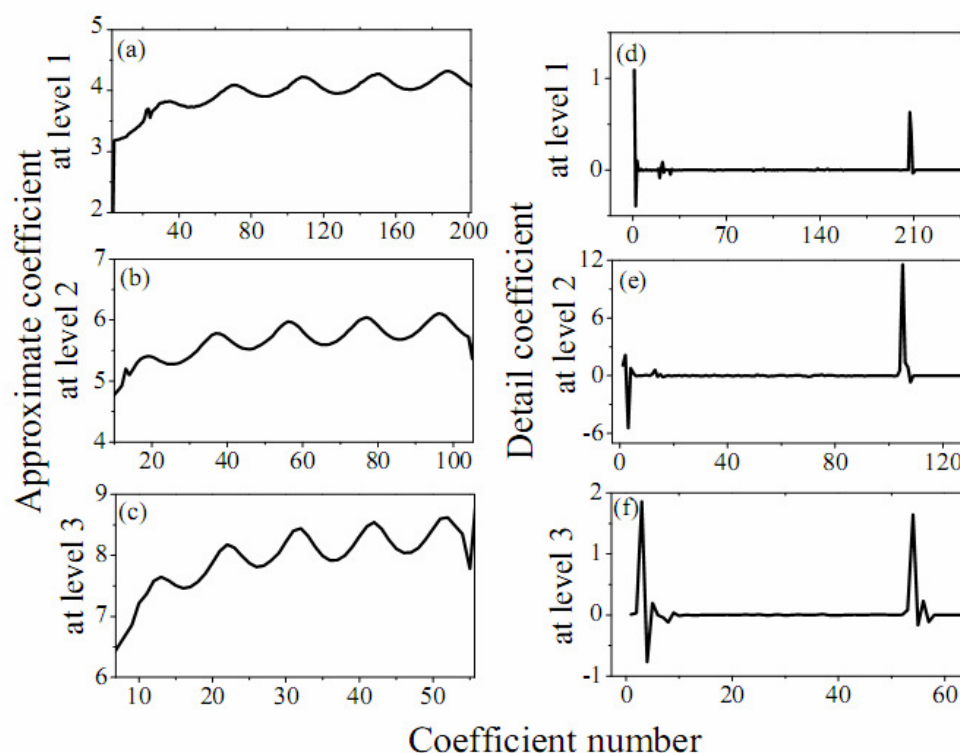


Fig. 5.5: For methane (500 ppm) conductance transient response, the extracted approximate coefficient from discrete wavelet transformation analyses for (a) level 1, (b) level 2, and (c) level 3. The extracted detailed coefficients for (d) level 1, (e) level 2 and (f) level 3

5.4.2. Pattern Recognition: Addressing the Selectivity of $\text{Mg}_{0.5}\text{Zn}_{0.5}\text{Fe}_2\text{O}_4$ Sensors

In order to perform the PCA using FFT coefficients the following steps are adopted. A typical FFT input data is a 4×21 matrix (first four Fourier coefficients and seven conductance transients for three different gases have been considered). Figure 5.6 (a) shows the plot of principal component 2 vs 1 (PC2 vs PC1 estimated from the principal

component analyses) for all the transients of three different gases. Similarly using the DWT we had generated 6×21 matrix (6 corresponds to selected approximate coefficients and for 3 different gases 7 transients have been considered). Using this matrix PCA has been performed and Fig 5.6 (b) shows the PC2 vs PC1 plots using DWT matrix as data input. As shown in Fig.5.6, for both type PCA analyses three types of gases form distinct clusters. Note that for PCA DWT combination (Fig. 5.6b); dispersion within CH_4 and CO is quite small as compared to hydrogen.

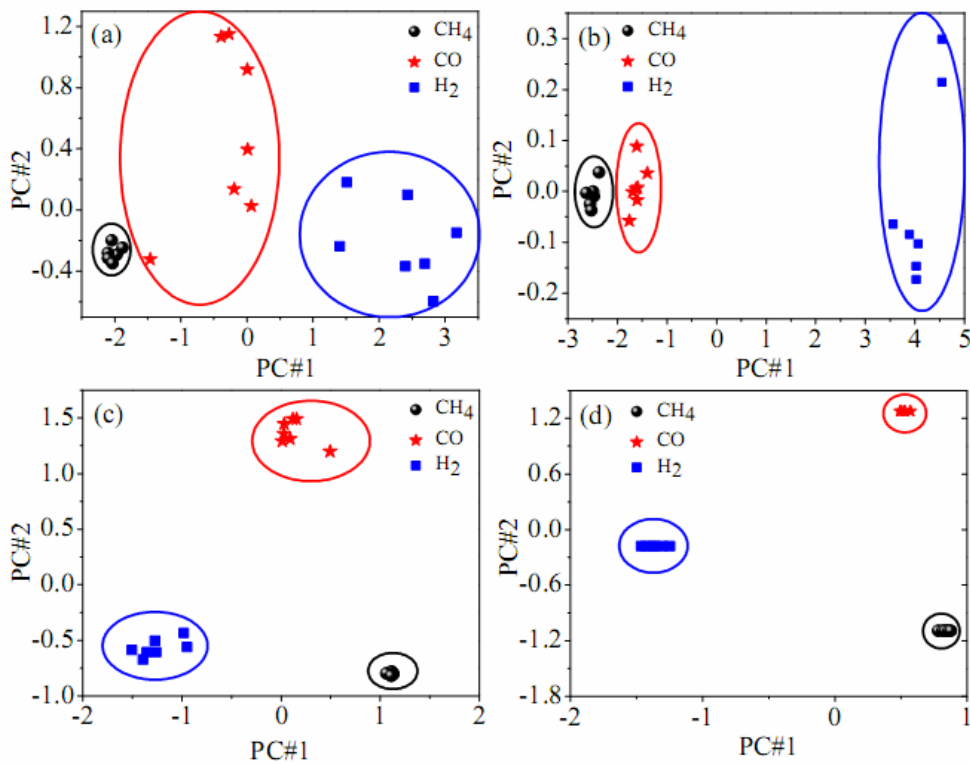


Fig. 5.6: Principal component analysis using (a) FFT and (b) DWT extraction parameter matrices and discriminant factor analyses using (c) FFT and (d) DWT extraction parameter matrices

Interestingly, as compared to PCA, much better gas discrimination is achieved using discriminant factor analysis (DFA). It is known that unlike PCA, DFA computes factors that minimize the variance within each class and thus the variance among different classes are maximized [8, 13]. As adopted in PCA pattern recognition, for DFA also we have used both FFT and DWT coefficients as input matrix. The results using FFT and DWT input parameters (for DFA pattern recognition) are shown in Fig. 5.6(c) and 5.6(d)

respectively. For all the three types of gases used in the present study, the dispersion among individual gas types is very low in DFA-DWT combined pattern recognition. Therefore DWT extraction in conjunction with DFA pattern recognition is superior to address the cross-selectivity in MZFO spinel sensors towards CH₄, CO, H₂ gas sensing.

The experimental work presented above is now summarized as follows: As envisaged in Fig. 5.2(d) it is clear that the synthesized MZFO-C sensing elements are more sensitive to hydrogen as compared to carbon monoxide and methane gas sensing. The cross-selectivity would pose serious problem towards their commercial adaptability for making, for example, hydrogen gas sensor. We have demonstrated that using pattern recognition technique one can differentiate hydrogen from the other two gases namely carbon monoxide and methane. Linear unsupervised (PCA) as well as supervised (DFA) pattern recognition techniques are used to differentiate the gas types. The data matrices extracted from FFT and DWT analyses of the conductance transients (recorded for H₂, CH₄, and CO gas sensing) are used as input parameter in the two pattern recognition techniques. The relative merit and demerit of these pattern recognition techniques are highlighted and it is recommended that DWT-DFA combination yield excellent results in differentiating the gas types used in the present study [13].

Through the experimental work presented so far in Chapter-3-5, we have demonstrated that (i) using chemical synthesis route we can synthesize various nano-structured oxide sensing elements, (ii) understand the interrelation between the structures (at different length scale) of the sensing element and their gas sensing characteristics, (iii) can relate the underlying physical mechanism controlling the gas sensing and its reflection to the recorded resistance transient during response and recovery, and (iv) address the cross-selectivity issue through kinetic/noise spectra analyses and pattern recognition techniques. Through the gained knowledge from these studies we are now in a position to build a prototype gas detector system and test its gas sensing characteristics. The details of the fabrication and testing of a Taguchi-type MZFO-C gas sensor is presented in the following section, at PART-II of this chapter.

PART-II

5.5. Development and Performance of a Taguchi Type $\text{Mg}_{0.5}\text{Zn}_{0.5}\text{Fe}_2\text{O}_4$ Sensor Prototype

The gas sensing characteristics of the sensing materials are characterized using a dynamic flow automated measurement unit (described in details in Chapter-2). In this system, controlling the flow rates of test and carrier gases we could precisely control the test gas concentration. The actual sensor is used mostly in a static flow environment. Therefore, the sensing characteristics of $\text{Mg}_{0.5}\text{Zn}_{0.5}\text{Fe}_2\text{O}_4$ based Taguchi sensor is also evaluated in a static flow gas chamber also developed in our laboratory. The prototype sensor development scheme has the following steps:

- Fabrication of a Taguchi-type sensing element using optimized $\text{Mg}_{0.5}\text{Zn}_{0.5}\text{Fe}_2\text{O}_4$ powders.
- Evaluation of the gas sensing characteristics of the sensing element using a resistance measurement circuitry developed in our laboratory
- Packaging of the sensing element and electronic circuitry into a single portable unit

We have used Pechini route derived nano-crystalline $\text{Mg}_{0.5}\text{Zn}_{0.5}\text{Fe}_2\text{O}_4$ (MZFO-C) particles to fabricate combustible gas sensor (targeting gas CO and H_2). In the following sections we have described the fabrication details and gas (H_2 and CO) sensing performance of Taguchi type $\text{Mg}_{0.5}\text{Zn}_{0.5}\text{Fe}_2\text{O}_4$ (MZFO-C) nano-particulate sensor prototype.

5.5.1. Fabrication of Taguchi Type Sensing Element

For the preparation of Taguchi type sensing element, the MZFO-C nano-particles (calcined at 600 °C for 2 h) are coated over an alumina tube (length- 4.5 mm and outer diameter-8 mm). Alumina is a cost effective chemically stable material having high thermal conductivity but poor electrical conductivity. These characteristics make it popular as a substrate for semiconducting oxide based gas sensors. To heat the sensor, a heating coil (nichrome) is inserted in the hollow tube and sealed using magnesia and

sodium silicate mixture as a sealing agent. The assembly described above is shown schematically in Fig. 5.7. To coat the sensing materials over the alumina tube first a suitable paste of the sensing material is prepared using N-methyl pyrrolidone (NMP) as solvent and polyvinylidene fluoride as binder. The paste is uniformly painted on the alumina tube and dried at 150 °C overnight. Once the coated layer is dried, as shown in Fig. 5.7, electrical contacts is made on the surface of the sensor using silver paste.

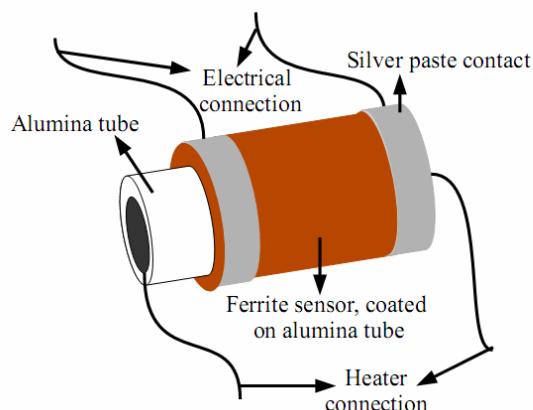


Fig. 5.7: Schematic of the Taguchi type ferrite gas sensing element

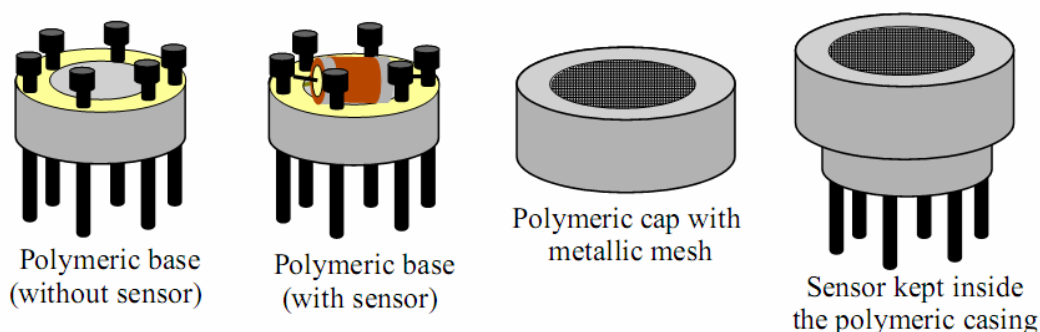


Fig. 5.8: Schematic design of the polymeric casing to hold the Taguchi type ferrite sensor

A nylon 106 based polymeric casing has been used to hold the electroded sensing element. The schematic of the polymeric holder (custom made by injection molding) is shown in Fig. 5.8. As shown in the figure the holder has two parts namely a base and a cap. The sensing element is kept in the cavity of the base. Two leads each from the heater and sensor electrodes (to measure the output voltage of the sensor) are connected with the pins embedded to the polymeric base. Note, out of the 6 connectors shown in Fig. 5.8, we have used 4 of them. A metallic mesh is provided on top of the cap to cover the sensing

element from external dust particles or shoots. The sensing element is connected to the electronic circuit module described below.

5.5.2. Resistance Measurement Circuitry

The electronic circuitry to measure the gas sensing characteristics of the semiconducting oxide based Taguchi type sensing element has also been developed in our laboratory. With this electronic circuitry, the gas sensing performance of the fabricated Taguchi type MZFO-C sensor can be measured. Figure 5.9 shows the (a) Taguchi type MZFO-C sensing element with resistance measurement circuitry and (b) photograph of the MZFO-C sensor. The basic resistance measurement circuit diagram is shown in Fig. 5.10(a). The circuit is connected to an in built power supply unit which provides both heater (V_H) and circuit voltage (V_C). To control the dc voltage, the power supply is equipped with full wave rectifiers and voltage regulator ICs (7815 and 7805). Varying the heater voltage one can control the sensor operating temperature. A variable resistor R_L (1 M ohm) has been connected in series to the sensing element to measure the output voltage (V_{out}) across it.

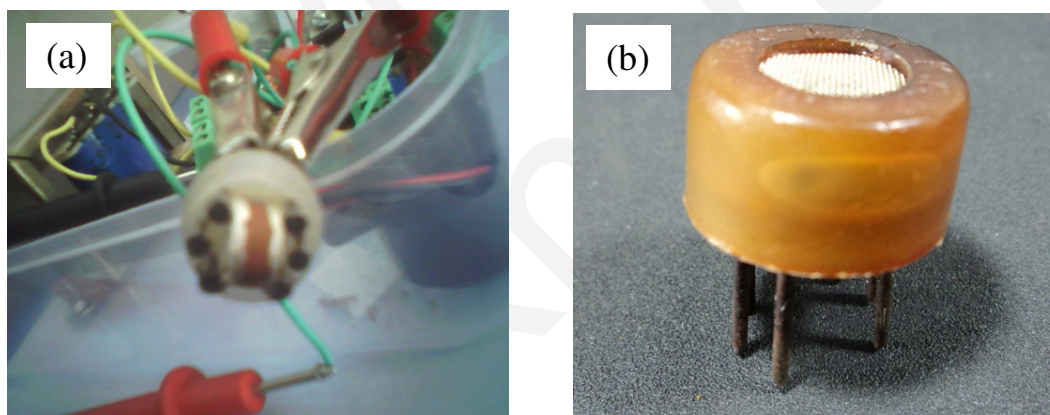


Fig. 5.9: (a) Photograph of Taguchi type actual $Mg_{0.5}Zn_{0.5}Fe_2O_4$ sensing element (b) photograph of the actual polymeric casing prepared using injection molding

The resistance R_L should be comparable with the sensor resistance. If the resistance R_L is very high than R_S , then the circuit voltage (V_C) will be dissipated through the sensing element. The output voltage (V_{out}) across the sensor R_L is related to the supplied circuit voltage (V_C) and resistance of the sensing element (R_S) by the following relation:

$$V_{out} = [R_L / (R_L + R_s)] \times V_C \quad (5.2)$$

The schematic of the actual circuit diagram (with relevant component marked) is shown separately in Fig. 5.10(b).

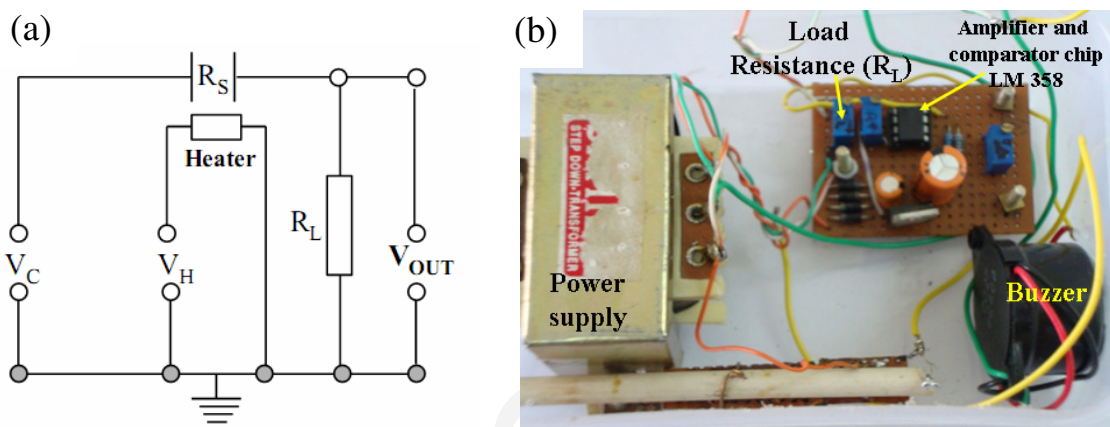


Fig. 5.10: (a) Schematic of the resistance measurement circuit diagram (b) photograph of the actual resistance measurement circuit developed in our laboratory

5.5.3. Evaluation of the Gas Sensing Characteristics

As mentioned earlier the gas sensing characteristics of the prepared Taguchi type MZFO-C sensing elements are evaluated using a static gas sensing set-up (shown in Fig. 5.11) developed in our laboratory. The chamber (volume ~6000 cc) is equipped with a gas inlet and outlet valve to inject the test gas and evacuate the test chamber respectively. A small fan is attached inside the test chamber to homogenize the injected test gas. The electrical connections from the fabricated Taguchi type sensing element are taken out of the chamber (using airtight feed-through) and connected to the electronic circuitry shown in the picture (Fig. 5.11 and also in Fig. 5.10(b)). To mimic the actual gas sensing, in the present measurement tests the fan inside the chamber is not used. After injection the gas diffuses inside the chamber and ultimately reaches to the sensor surface kept hot with a preset temperature. Thus the sensor (n type $Mg_{0.5}Zn_{0.5}Fe_2O_4$ (MZFO-C)) resistance decreases with time. The decrease in sensor resistance is detected by the increase of V_{out} with time. After prolonged exposure of the sensor in test gas (H_2 or CO) and subsequent data acquisition, the sensor is recovered by disconnecting the inlet and opening the outlet valve.

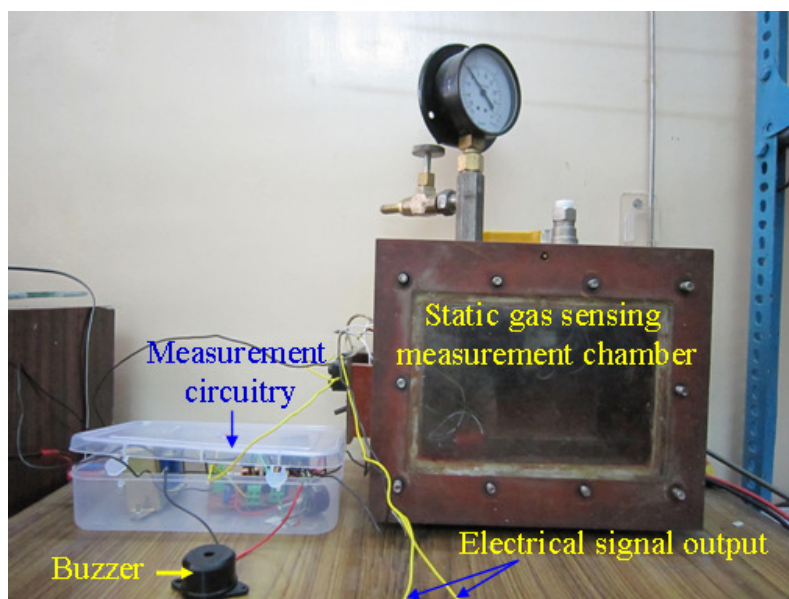


Fig. 5.11: Static gas sensing measurement set-up and measurement circuitry developed in our laboratory

The gas sensing performance of the Taguchi type MZFO-C sensor (kept at 200 °C) is measured in H_2 and CO gas exposure. Figure 5.12 shows the hydrogen sensing characteristics of MZFO-C sensor when (a) 300 cc and (b) 500 cc H_2 is injected in the static chamber. The voltage transient of the sensor in presence of CO gas (500 cc) is shown in Fig. 5.13. The test gas concentrations are 10,000 ppm diluted in N_2 . The gas ‘on’ state is marked as small up arrow (\uparrow) in figures. As shown in Fig. 5.12 and 5.13, the voltage transients of the sensor in presence of both H_2 and CO gases are noisy in nature. The poor transduction of the material in relatively low operating temperature may lead to such fluctuation in the voltage transient. Since polymer casing is used we could not further increase the operating temperature. However the sensing elements exhibit very good response towards the detection of H_2 and CO gases. The increase in the output voltage (V_{out}) during H_2 sensing is higher than the corresponding voltage change during CO sensing. For a particular gas (say H_2) the response of the sensor increases with the concentration of the test gases (see Fig. 5.12). As shown in Fig. 5.12(b), the recovery of the sensor is quite fast for H_2 sensing. For all these experiments marginal base line drift is detected (i.e. V_{out} in air ambient remains unaltered).

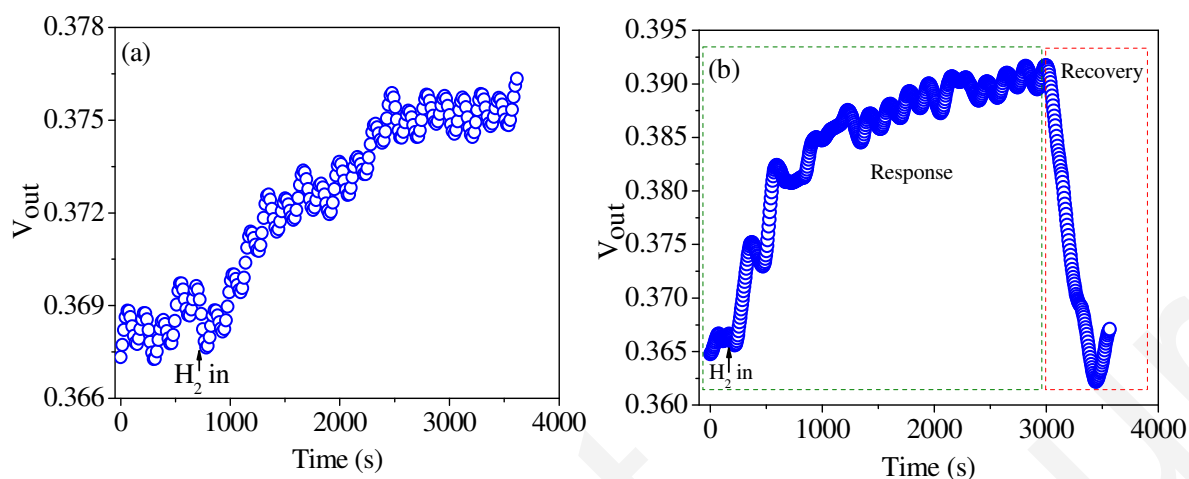


Fig. 5.12: Hydrogen sensing performance of Taguchi type $\text{Mg}_{0.5}\text{Zn}_{0.5}\text{Fe}_2\text{O}_4$ sensor in presence of (a) 300 cc (b) 500 cc of 10,000 ppm of H_2 (at $\sim 200^\circ\text{C}$)

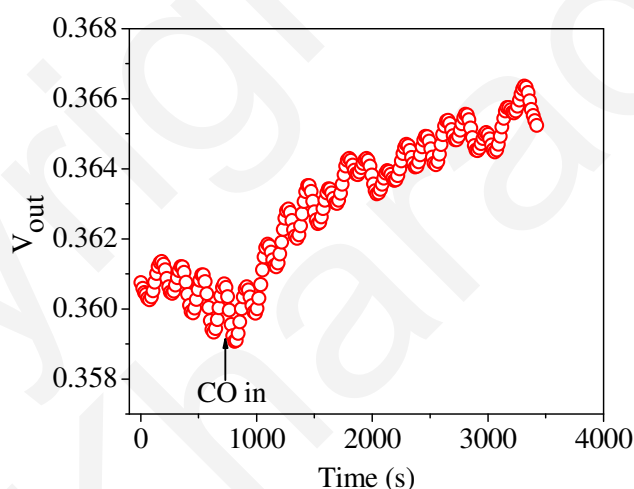


Fig. 5.13: Carbon monoxide sensing performance of Taguchi type $\text{Mg}_{0.5}\text{Zn}_{0.5}\text{Fe}_2\text{O}_4$ (MZFO-C) sensor in presence of 500 cc of 10,000 ppm of CO (at $\sim 200^\circ\text{C}$)

5.5.4. Packaging of the Prototype Ferrite Gas Sensor

The laboratory made prototype portable gas sensor is shown in Fig. 5.14. As shown it uses line voltage (230 V, 50 Hz) to operate. The combustible gas detector is equipped with LED lamps and audible alarm. One LED lamp act as power indicator and other one is detector. The sensing element is exposed to the open ambient (top cover is not shown). The prototype is tested as follows. H_2 gas is leaked in the vicinity of this prototype. The

gas is found to be almost immediately detected (30-50 s) by the LED detector and the audible alarm. The gas detection is repeated for a number of times within time frame span of several months.

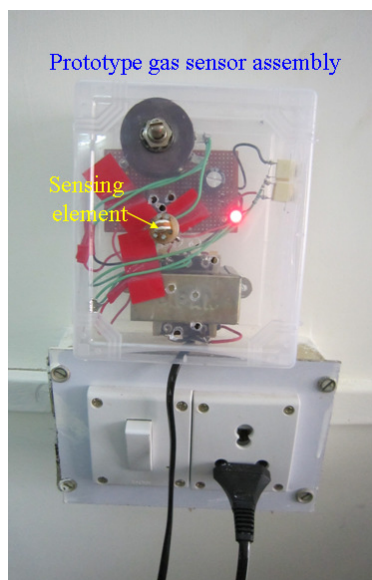


Fig. 5.14: Prototype combustible gas sensor using $\text{Mg}_{0.5}\text{Zn}_{0.5}\text{Fe}_2\text{O}_4$ (MZFO-C) sensing element

5.6. Summary and Conclusions

The present chapter is divided into two parts. In the first part (PART-I) we have described how the cross-selectivity issue of the magnesium zinc ferrite sensing element can be addressed by using pattern recognition techniques. The second part (PART-II) of the chapter deals with the description of making a prototype combustible gas sensor using nano-crystalline $\text{Mg}_{0.5}\text{Zn}_{0.5}\text{Fe}_2\text{O}_4$ as sensor material.

We have utilized the pattern recognition techniques to address the problem of cross-selectivity in magnesium zinc ferrite based sensor for selective detection of methane, carbon monoxide and hydrogen. For this purpose first Fourier transform (FFT) and discrete wavelet transform (DWT) are used to extract the important features of the measured conductance transients of $\text{Mg}_{0.5}\text{Zn}_{0.5}\text{Fe}_2\text{O}_4$ sensors upon exposure to H_2 , CO and CH_4 gases at $\sim 350^\circ\text{C}$. Selected coefficients from FFT and DWT analyses are used as input parameters in linear unsupervised (principal component analysis (PCA)) and supervised (discriminant factor analysis (DFA)) pattern recognition techniques. For both

type PCA analyses, three type of gases (CH_4 , CO and H_2) form distinct clusters. However for PCA-DWT combination dispersion within CH_4 and CO is quite small as compared to H_2 . Interestingly, as compared to principal component analysis (PCA), much better gas discrimination is achieved using discriminant factor analysis (DFA). We have discussed relative merits and demerits of the used feature extraction methods and demonstrated the effectiveness of the dynamic pattern recognition techniques to discriminate these gases using a single $\text{Mg}_{0.5}\text{Zn}_{0.5}\text{Fe}_2\text{O}_4$ sensing element.

Although the discriminant factor analysis suggesting the possibility to discriminate among the three gases, further research effort is needed to selectively sense a gas from a mixture of gases. In general the problem of identifying a single analyte from three probable analytes is much different than identify /and or quantify an individual gas type in any possible combination of these three analytes in a mixture. Therefore addressing the selectivity issue in a gas mixture is important. Moreover the calibration data are collected from multiple exposures to a single concentration for each gas; the results of the FFT and DWT might differ for different gas concentrations. It would be interesting to investigate if the features extracted using the various transforms be a functions of the concentrations of the calibration of the gases.

PART-II of the present chapter describes the fabrication details and combustible gas sensing characteristics of a Taguchi-type prototype sensor that uses process optimized magnesium zinc ferrite as sensing materials. An electronic circuit module is developed to evaluate the gas sensing characteristics of the sensing element kept inside a static gas chamber. To mimic the real time environment the static gas chamber is fabricated in our laboratory. It is demonstrated that that the fabricated sensing element can detect the presence of minute quantity of H_2 and CO gas. These sensing elements also exhibit stable and repeatable gas sensing performance with marginal base resistance drift up on repeated sensing and recovery cycles. Since the casing of the sensor element is polymer-made we limit the operating temperature maximum upto 200°C . Better sensor response is expected if sensor operating temperature is increased beyond 200°C .

Reference

- [1] Lee, A.P. and Reedy, B.J. (1999), Temperature Modulation in Semiconductor Gas Sensing, *Sensors and Actuators B*, Vol. 60, pp.35-42.
- [2] Fort, A., Gregorkiewitz, M., Machetti, N., Rocchi, S., Serrano, B., Tondi, L., Ulivieri, N., Vignoli, V., Faglia, G. and Comini, E. (2002), Selectivity Enhancement of SnO₂ Sensors by means of Operating Temperature Modulation, *Thin Solid Films*, Vol. 418, pp. 2-8.
- [3] Ramgir, N.S., Hwang, Y.K., Jhung, S.H., Mulla, I.S. and Chang, J.S. (2006), Effect of Pt Concentration on the Physiochemical Properties and CO Sensing Activity of Meso Structured SnO₂, *Sensors and Actuators B*, Vol. 114, pp. 275-282.
- [4] Penza, M., Martucci, C. and Cassano, G. (1998), NO_x Gas Sensing Characteristics of WO₃ Thin Films Activated by Noble Metals (Pd, Pt, Au) Layers, *Sensors and Actuators B*, Vol. 50, pp. 52-59.
- [5] Gomri, S., Seguin, S.L. and Aguir, K. (2005), Modeling on Oxygen Chemisorption Induced Noise in Metallic Oxide Gas Sensors, *Sensors and Actuators B*, Vol. 107, pp. 722-729.
- [6] Berrueta, L.A., Alonsosalces, R.M. and Heberger, K. (2007), Supervised Pattern Recognition in Food Analysis, *Journal of Chromatography A*, Vol.1158, pp. 196-214.
- [7] Ionescu, R., Llobet, E., Vilanova, X., Brezmes, J.E., Sueiras, J., Calderer, J. and Correig, X. (2002), Quantitative Analysis of NO₂ in the Presence of CO Using a Single Tungsten Oxide Semiconductor Sensor and a Dynamic Signal Processing, *The Analyst*, Vol. 127, pp. 1237-1246.
- [8] Friedman J.H. (1987), Exploratory projection pursuit, *Journal of the American Statistical Association*, Vol. 82, pp.249-266.
- [9] Comon, P. (1994), Independent Component Analysis, A New Concept?, *Signal Processing*, Vol. 36, pp. 287-314.
- [10] Bell, A.J. and Sejnowski, T.J. (1995), An Information Maximization Approach to Blind Separation and Blind deconvolution, *Neural Computation*, Vol. 7, pp. 1129-1159.
- [11] Joliffe, I.T. (1986), *Principle Component Analysis*, New York, Springer, Second Edition.
- [12] Ionescu, R., Hoel, A., Granqvist, C.G., Llobet, E. and Heszler, P. (2005), Ethanol and H₂S Gas Detection in Air an in Reducing and Oxidizing Ambience: Application of Pattern Recognition to Analyse the Output Form Temperature Modulated Nanoparticles WO₃ Gas Sensors, *Sensor and Actuators B*, Vol. 104, pp. 124-131.
- [13] Maity, A., Mukherjee, K. and Majumder, S.B. (2011), Addressing the Cross-Sensitivity of Magnesium Zinc Ferrite towards Reducing Gas Sensing Using Pattern Recognition Techniques, *Sensor Letters* (accepted, Editor decision SL1731968_1605)

Chapter-6

SUMMARY AND CONCLUSIONS

6.1. Summary of the Thesis Work

The primary objective of the present research is to prepare gas sensing material which would have high response to toxic and inflammable gases in low concentration range, good selectivity towards a particular gas, high stability as well as low operating temperature. So far significant research effort has been undertaken to improve the sensitivity, selectivity and stability of the sensing material as well as to design a smaller and inexpensive gas sensors. In the area of ceramic semiconducting oxide based gas sensor, a variety of oxide materials (simple binary oxides, ferrites, perovskites etc) has been studied by various research groups. From these studies simple binary oxides (SnO_2 , In_2O_3 , WO_3 , ZnO etc) as well as their cation modified counterparts emerge to be popular choice mainly due to their ease of preparation, good sensitivity and stable sensing performance towards reducing gases. Although less studied as compared to binary oxides; ternary and quaternary oxides have also been demonstrated to be efficient gas sensing materials and many of them exhibit pronounced selectivity towards specific gases. Viewing in light of these research reports, in the present work we have studied spinel oxides as alternative combustible gas sensing materials for commercial gas sensors. It is known that the gas sensing characteristics of semiconducting oxide sensors are dependent on their surfaces to volume ratio, grain size and morphology as well as the pore-size distribution of the sensing elements. We felt it important to study the

(synthesis) process induced modifications of these micro-structural features on the gas sensing performance. The executed research works are grouped as follows:

- We have developed a soft solution processing route which enable us to grow oxide ceramic nano-structures in the form of nano-powders (0-d), nano-tubes and rods (1-d), thin films (2-d), embedded nano-tubes in anodized alumina templates, and hollow spheres.
- The gas (CO, H₂, CH₄, N₂O) sensing characteristics of the synthesized oxides has been evaluated in various configuration which includes porous pellet, thick film of nano-tube on alumina substrate, thin film on alumina substrate, tubes embedded into porous alumina template, thick film of hollow spheres on fused quartz substrates.
- An automated dynamic flow measurement set up has been developed to evaluate the gas sensing characteristics of the above nano-structures.
- The gas sensing performances of the synthesized oxides are optimized in terms of response (%), response/recovery times, stability and selectivity. The adsorption and desorption characteristics of the test gases are investigated by analyzing the resistance transients during gas sensing. The activation energies of gas absorption and desorption, estimated from these kinetic analyses are found to be dependent of the type of the test gas.
- Building a low cost prototype gas sensor using the sensing elements with optimized gas sensing characteristics.

6.2. Conclusive Remarks

We have optimized the precursor chemistry and heat treatment schedule to synthesize nano-crystalline $\text{Mg}_{1-x}\text{Zn}_x\text{Fe}_2\text{O}_4$ ($0.0 \leq x \leq 1.0$) powders using PVA assisted wet chemical synthesis route. Among these compositions, it is reported that only $\text{Mg}_{0.5}\text{Zn}_{0.5}\text{Fe}_2\text{O}_4$ (MZFO) particles can be synthesized phase pure [(cubic spinel without the formation of any other impurity phase/(s)] calcining it at a temperature as low as 300 °C. The powders are nano-crystalline (~20 nm) and having meso-porous surface

morphologies. Among all the solid solution compositions, MZFO sensing elements exhibit superior gas sensing characteristics in terms of response (%), response/recovery time and marginal base line drift.

Further improvement of the gas sensing characteristics of $\text{Mg}_{0.5}\text{Zn}_{0.5}\text{Fe}_2\text{O}_4$ elements are achieved using powders synthesized by a citrate based self combustion Pechini route. The improvement in gas sensing characteristics of Pechini route derived powders are explained to be due to their comparatively larger specific surface area and uniform pore size distribution leading to better gas diffusion.

We have demonstrated that the change in surface morphology significantly influences the gas sensing characteristics of MZFO spinel ferrites. In case of hydrogen sensing, we have reported that the embedded nano-tubes are sensitive enough for lower concentration (~10 ppm) hydrogen gas sensing. An excellent hydrogen response (~90%) is achieved for particulate as well as embedded nano-tube sensors at higher operating temperatures ($\geq 350^\circ\text{C}$). The temperature corresponding to the maximum response (~75%) is significantly reduced (~250 $^\circ\text{C}$) for MZFO thin film sensors. For all these nano-structures, response and recovery times are estimated for various H_2 gas concentrations. Although the nano-tubes embedded in anodized alumina template exhibit promising hydrogen sensing characteristics, further research is needed to reduce the base resistance and operating temperature corresponding to the maximum response.

The gas sensing response (S) of the sensors is usually measured in the equilibrium condition (noting the resistance values when the chemi-adsorption of oxygen is complete (R_a) and test gas reacts completely with the absorbed oxygen (R_g)) using either the relation $S = R_a/R_g$ or $(R_a - R_g)/R_a$. Since the gas sensing mechanism involves surface oxidation/reduction, electron exchange and desorption of the reaction product, the dynamics of these process is completely overlooked when the sensor characteristics is estimated from the equilibrium conditions. In order to measure the kinetics of response and recovery, dynamic measurement protocol is adopted. We have analyzed the resistance/conductance transients during the response and recovery of gas sensing measurements.

The response and recovery transients of conductance for spinel ferrite sensing elements towards hydrogen and carbon monoxide gas sensing are modeled using Langmuir adsorption kinetics with two active adsorption sites in the sensing elements. These two active sites are the macro and meso-porous regions of the sensing elements as identified in their scanning electron micrographs. It is found that for both the adsorption sites, at constant temperature T , Langmuir adsorption isotherm behavior is obeyed. We have reported that at constant temperature, response time constants follow an inverse power relation to the test gas concentration ($\tau \propto C_g^{-\beta}$). When the kinetics of sensor response is controlled by adsorption/desorption process then the temperature dependence of the response and recovery time constants follow an Arrhenius relation with sensor operating temperature. From the best fitted response and recovery time constants, we have estimated the corresponding activation energies of the adsorption and desorption of gases. For carbon monoxide and hydrogen gases, the corresponding activation energies for adsorption and desorption are found to be distinctly different. It is recommended that since each gas, depending of its reactivity, size of the gas molecules, etc has characteristic activation energies for adsorption and desorption, kinetic analyses of resistance transient during response and recovery might be beneficial to address the selectivity issue of these gas sensing materials.

A number of interesting features are observed in the recorded resistance/conductance transients of the binary and spinel oxide based nano-structured sensing materials. The identified features are (i) drift in the base resistance upon repeated response and recovery cycles, causes mainly due to the unsaturated resistance transients during response and recovery, (ii) response and recovery transients with sinusoidal noise, and (iii) occurrence of spike-like features in the recorded transients. We have made an attempt to understand the nature and origin of these features based on our developed hypothesis on the reaction sequence of gas absorption and desorption of the reaction products.

Little or marginal base resistance drift of metal oxide sensor is desirable during repeated response and recovery cycles. However, due to the partial recovery, often significant drift in base resistance is reported. The resistance transient is termed reversible in case of complete recovery; otherwise it is termed irreversible when partial

recovery is occurred. As for example, for hydrogen and carbon monoxide gas sensing we have demonstrated distinct reversible and irreversible resistance transients for magnesium zinc ferrite and zinc oxide sensing elements respectively. The corresponding response transients for these sensing elements are modeled using Langmuir-Hishelwood reaction mechanism and the characteristic response times are estimated. It is found that for irreversible transients the response time is dependent on the test gas concentration; however, for reversible transients it (the response time) is almost independent to the gas concentration. Finally, it is concluded that the irreversible and reversible nature of gas sensing is related to the dense and open type surface morphology respectively.

The occurrences of the sinusoidal noise in the response and recovery transients in some of the synthesized nanostructures are explained to be due to nature of surface diffusion of the gas molecules in these structures. The power spectrum of resistance noise is proposed to be a good indicator of the change in chemical environment in gas sensing and therefore can be used for selective gas sensing using a single discrete sensor. It is demonstrated that for each individual gas (viz. H_2 , CO , and CH_4), the frequency dispersion of power (derived from each individual response transient of the conductance), are clustered together and well separated from each other. By linear fitting of log-power vs log-frequency plots we have estimated the characteristic corner frequency, frequency exponent and low frequency magnitude of power for each of the above three gas sensing measurement. By analyzing the estimated values of the above parameters it is concluded that power spectrum 'finger print' is sensitive to selectively detect these three gases.

The spike like features in the resistance transients during response and recovery are detected either during the change of chemical environment surrounding the sensor surface or just prior attaining the equilibrium state during response or recovery. Attempts are made to explain these features based on our understanding of gas-solid interaction during reducing gas sensing using nano-structured cubic spinel ferrite sensing elements.

We have utilized the pattern recognition techniques to address the problem of cross-selectivity in magnesium zinc ferrite based sensor for selective detection of methane, carbon monoxide and hydrogen. For this purpose first Fourier transform (FFT) and

discrete wavelet transform (DWT) are used to extract the important features of the measured conductance transients of $\text{Mg}_{0.5}\text{Zn}_{0.5}\text{Fe}_2\text{O}_4$ sensors upon exposure to H_2 , CO and CH_4 gases at $\sim 350^\circ\text{C}$. Selected coefficients from FFT and DWT analyses are used as input parameters in linear unsupervised (principal component analysis (PCA)) and supervised (discriminant factor analysis (DFA)) pattern recognition techniques. For both type PCA analyses, three type of gases (CH_4 , CO and H_2) form distinct clusters. However for PCA-DWT combination dispersion within CH_4 and CO is quite small as compared to H_2 . Interestingly, as compared to principal component analysis (PCA), much better gas discrimination is achieved using discriminant factor analysis (DFA). We have discussed relative merits and demerits of the used feature extraction methods and demonstrated the effectiveness of the dynamic pattern recognition techniques to discriminate these gases using a single $\text{Mg}_{0.5}\text{Zn}_{0.5}\text{Fe}_2\text{O}_4$ sensing element.

Finally, we have described the fabrication details and combustible gas sensing characteristics of a Taguchi-type prototype sensor that uses process optimized magnesium zinc ferrite as sensing materials. An electronic circuit module developed in our laboratory is used to evaluate the gas sensing characteristics of the sensing element kept inside a static gas chamber. To mimic the real time environment the static gas chamber is fabricated in our laboratory. It is demonstrated that that the fabricated sensing element can detect the presence of minute quantity of H_2 and CO gas. These sensing elements also exhibit stable and repeatable gas sensing performance with marginal base resistance drift up on repeated sensing and recovery cycles. The highlights of the present work are described in the following section.

6.3. Highlights of the Thesis Work

We have developed a generic wet chemical route to synthesize various nano-structured (e.g. nano-particle, thin film, nano-tube, embedded nano-tube, hollow spheres) binary, and spinel oxides. An automated dynamic flow measurement set up is developed to evaluate the gas sensing characteristics of the synthesized gas sensing materials. Through a systematic study we have established that the embedded nano-tube sensing elements exhibit better gas sensing performance among the other synthesized nano-

structures. Based on Langmuir adsorption isotherm kinetics we have successfully modeled the resistance transients (during response and recovery) and evaluated the relevant kinetic parameters including the activation energies of adsorption and desorption of relevant gases on the sensing elements. We have proposed that the analyses of the resistance transients could be useful to address the selectivity problem of these semiconducting gas sensors. Finally we have demonstrated the hydrogen sensing performance of the optimized spinel sensing elements by fabricating a Taguchi-type sensor prototype.

The highlights of the thesis work are itemized below.

- We have developed a soft solution processing route which enable us to grow oxide ceramic nano-structures in the form of nano-powders (0-d), nano-tubes and rods (1-d), thin films (2-d), embedded nano-tubes in anodized alumina templates, and hollow spheres. The sensing elements are characterized in terms of their phase formation behavior and microstructure evolution characteristics.
- In order to investigate the gas sensing characteristics of the synthesized oxides we have fabricated a dynamic flow automated gas sensing measurement set up. The synthesized oxides are characterized in terms of their response (S), response/recovery time, stability and cross-selectivity towards hydrogen, carbon monoxide, methane, and nitrous oxide gases.
- We have demonstrated that the gas sensing characteristics of these oxides are influenced by its structure at different length scales. Thus in nano-meter scale, the sensing characteristics are influenced by the crystallite size, intra-particle as well as inter-particle pore size and pore size distribution. At the level of micro-structure, the nature of surface morphology has dominant influence on the gas sensing characteristics. In device scale, the sensing characteristics are influenced by factors such as electrode material and its configuration, amplitude of applied voltage, temperature fluctuation during resistance measurement etc.
- Through the kinetic analyses of response and recovery transients we have commented on the nature of gas-solid interaction in these nano-structures that eventually control their sensing characteristics.

- The cross-selectivity issue of these nano-structured sensing elements is addressed by various feature extraction methods of the conductance transients in conjunction with pattern recognition algorithms.
- Finally, using process optimized spinel sensing elements we have fabricated Taguchi type sensor and demonstrated its performance towards hydrogen gas sensing.

6.4. Scope for Further Research

The present work is a systematic study to evaluate the gas sensing characteristics of magnesium zinc ferrite based sensing elements synthesized in various nano-structured forms. Based on the experimental findings of this research, the scope for further research is itemized as follows:

- Sensing elements should be synthesized in the form of thin/thick films. These elements should be equipped with an integrated heater to control its surface temperature precisely. Sensing elements in the form of a thin/thick film would have a defined thickness, and its grain size and porosity may be engineered to better understand the gas-solid interaction.
- Although the discriminant factor analysis suggests the possibility to discriminate a particular gas, further research effort is needed to selectively sense a gas from a mixture of gases. In general the problem of identifying a single analyte from a mixture analytes may be very different than to identify an individual gas type as has been done in the present study. Therefore addressing the selectivity issue in a gas mixture is important.
- Moreover the calibration data are collected from multiple exposures to a single concentration for each gas; the results of the FFT and DWT might differ for different gas concentrations. It would be interesting to investigate if the features extracted using the various transforms be a functions of the concentrations of the calibration of the gases.
- The gas sensing performance of the optimized sensing elements must be studied in static flow ambient in order to mimic the real time situation.

APPENDIX

Appendix-1: AUTOMATION OF THE MASS FLOW CONTROLLER UNIT AND DATA ACQUISITION SYSTEM

As mentioned in Chapter-2 (Sec. 2.2), we have developed a dynamic volume gas sensing set-up to measure the sensing characteristics (in terms of resistance change) of chemi-resistive gas sensors. The flow rates of test and carrier gases (inside the test chamber) are controlled by mass flow controllers and the resistance of the sensor is measured using a data acquisition system (electrometer) (6517A, Keithley Instruments, USA). We felt that to acquire the data fast (with high precision) and to avoid the trouble to manually control the gas flow rate, the electrometer and the mass flow controllers should be automated. Therefore, we have interfaced the mass flow control unit (PR4000, MKS instrument, USA) and the electrometer with a PC through RS 232 and GPIB interface respectively using Labview 8.5 (National Instruments, USA) software.

RS 232 is a standard port (proposed by the Instrument Society of America) available in most of the the instruments for serial communications. When an instrument interfaced with a PC using RS-232 interface, it transfers data at the rate one bit at a time. GPIB (general purpose interface bus) interface is another popular instrument communication which transfers data in parallel at the rate one byte (eight bits) at a time. The data transfer data for GPIB interface is faster than RS-232 interface.

Automation of the mass flow controller unit: As the double channel mass flow controller unit reads only the command and thereby controls the flow rate, it is equipped with simple RS-232 serial communication port. We have interfaced the mass flow controller unit with a PC (by matching the address, baud rate, parity of both the instrument and the PC) using RS-232 cable and LabView-8.5 software. The instrument driver for the controller is downloaded from <http://forums.ni.com/t5/LabVIEW/MKS-PR4000-CONTROLLER>. The communication between the PC and mass flow controller unit is attained using specific device commands available in the PR 4000 manual.

Automation of the data acquisition system: The data acquisition system (6517A, Keithley Instruments, USA) is equipped with both the RS-232 and GPIB interface port. However for the fast as well as parallel communication (data read and send message) we have interfaced the system using GPIB interface. For the integration of the electrometer with the PC, we have built the VI using LabView-8.5 software. Fig. 1 shows the block diagram and front panel of the VI developed for interfacing the electrometer with a PC.

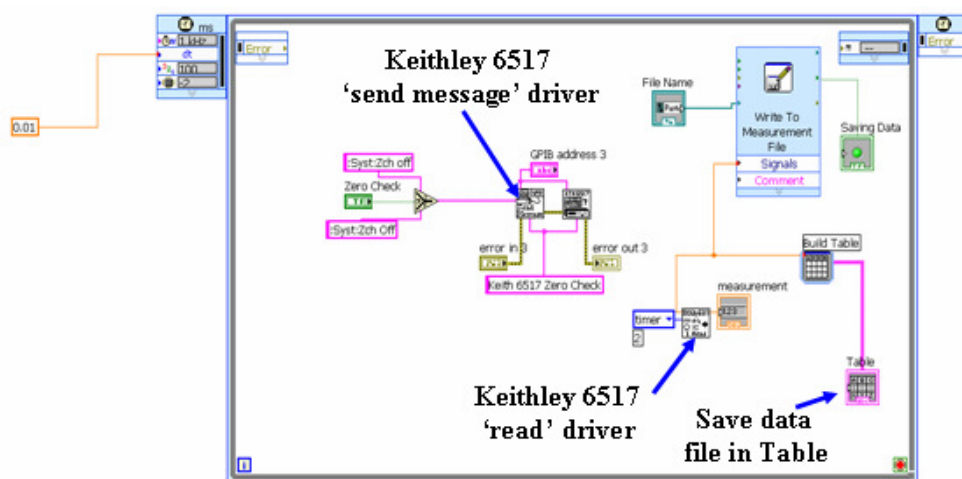


Fig. 1. Block diagram of the developed VI

As shown in the figure the required 'send message' and 'read' drivers (for Keithley 6517 series), are downloaded from <http://www.ni.com/downloads/idnet/> and used in the VI. For interfacing, the instrument the address, baud rate, parity of the PC and the instrument are matched. The VI is made to perform instrument specific tasks (e.g. auto zero, voltage source operate), acquire data and save in tabular form (as LVM file) in a PC. The front panel of the VI is shown in Fig. 2

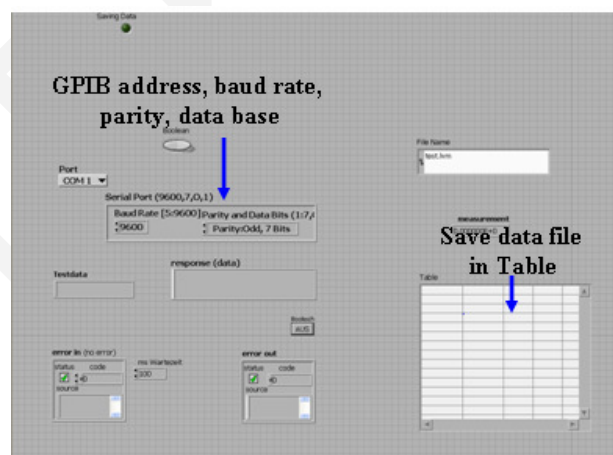


Fig. 2. Front panel of the developed VI

Appendix-2: SOLUTION OF EQN. 4.36

As mentioned in Chapter-4 (Sec. 4.5.1.1), the solution of Eqn. 4.36 is derived as follows.

Considering the reaction of reducing gas (R_{gas} , concentration C_g) with the adsorbed oxygen (O_{ad}^-) is irreversible type (as mentioned in the Eqn. 4.33 of the text), the rate of formation of surface adsorbed oxidized product (RO_{ad}) in irreversible gas sensing process (assuming $\phi \sim [O_{ad}^-]$ + RO_{ad} {occupied initially by R_{gas} } = $F\phi$ (total available sites)) can be written as

$$d[RO_{ad}]/dt = k_a[F\phi - RO_{ad}]C_g \quad (4.36)$$

Integrating Eqn. 4.36, one can write

$$\int d[RO_{ad}]/[F\phi - RO_{ad}] = \int k_a C_g dt \quad (4.36a)$$

Solving the Eqn. 4.36a we get

$$-\ln(F\phi - RO_{ad}) = k_a C_g t + c \quad (4.36b) \text{ where } c \text{ is integration constant}$$

When $t \rightarrow 0$; $RO_{ad} \rightarrow 0$ so $c = -\ln F\phi$

Now the Eqn. 4.36b can be rewritten as

$$-\ln(F\phi - RO_{ad}) = k_a C_g t - \ln F\phi \quad (4.36c)$$

Eqn. 4.36c can again be simplified as

$$\ln(1 - RO_{ad}/F\phi) = -k_a C_g t \quad (4.36d)$$

The concentration of $[RO_{ad}]$ as a function of time 't' can be written as

$$[RO_{ad}](t) = F\phi(1 - \exp^{-\{k_a C_g t\}}) \quad (4.37)$$

Appendix-3: SOLUTION OF EQN. 4.42

As stated in Chapter-4 (Sec. 4.5.1.2), the solution of Eqn. 4.42 is derived as follows.

Considering the reaction of reducing gas (R_{gas} , concentration C_g) with the adsorbed oxygen (O_{ad}^-) is reversible type (as mentioned in the Eqn. 4.40 of the text), then the rate of formation of surface adsorbed oxidized product (RO_{ad}) in reversible gas sensing process (assuming $\phi \sim [O_{ad}^-] + RO_{ad}$ {occupied initially by R_{gas} } = $F\phi$ (total available sites)) can be written as

$$\frac{d[RO_{ad}]}{dt} = k_a [F\phi - RO_{ad}] C_g - k_a / K [RO_{ad}] \quad (4.42)$$

$$\text{or, } \frac{d[RO_{ad}]}{k_a [F\phi] C_g - k_a [RO_{ad}] (C_g + 1/K)} = dt \quad (4.42a)$$

$$\text{or, } \frac{d[RO_{ad}]}{k_a (C_g + 1/K) \left\{ \frac{k_a [F\phi] C_g}{k_a (C_g + 1/K)} - [RO_{ad}] \right\}} = dt \quad (4.42b)$$

Eqn. 4.42b can be simplified as

$$\frac{d[RO_{ad}]}{\left\{ \frac{[F\phi] C_g}{(C_g + 1/K)} - [RO_{ad}] \right\}} = k_a (C_g + 1/K) dt \quad (4.42c)$$

Integrating Eqn. 4.42c, one can write

$$\int \frac{d[RO_{ad}]}{\left\{ \frac{[F\phi] C_g}{(C_g + 1/K)} - [RO_{ad}] \right\}} = k_a (C_g + 1/K) \int dt \quad (4.42d)$$

Solving the Eqn. 4.42d we get

$$-\ln \left\{ \frac{(F\phi) C_g}{(C_g + 1/K)} - [RO_{ad}] \right\} = k_a (C_g + 1/K) t + c \quad (4.42e)$$

When $t \rightarrow 0$; $RO_{ad} \rightarrow 0$ so $c = -\ln\left\{\frac{(F\phi)C_g}{(C_g + 1/K)}\right\}$

Putting the value of c in Eqn. 4.42e, one can write

$$-\ln\left\{\frac{(F\phi)C_g}{(C_g + 1/K)} - [RO_{ad}]\right\} = k_a (C_g + 1/K)t - \ln\left\{\frac{(F\phi)C_g}{(C_g + 1/K)}\right\} \quad (4.42f)$$

Now the Eqn. 4.42f can be written as

$$\ln\left[\frac{\frac{(F\phi)C_g}{(C_g + 1/K)}}{\left\{\frac{(F\phi)C_g}{(C_g + 1/K)} - [RO_{ad}]\right\}}\right] = k_a (C_g + 1/K)t \quad (4.42g)$$

Eqn. 4.42g can be written as

$$\ln\left[\frac{\left\{\frac{(F\phi)C_g}{(C_g + 1/K)} - [RO_{ad}]\right\}}{\frac{(F\phi)C_g}{(C_g + 1/K)}}\right] = -k_a (C_g + 1/K)t \quad (4.42h)$$

Eqn. 4.42h can be simplified as

$$1 - \frac{[RO_{ad}]}{\left\{\frac{(F\phi)C_g}{(C_g + 1/K)}\right\}} = \exp^{-k_a (C_g + 1/K)t} \quad (4.42i)$$

The concentration of $[RO_{ad}]$ as a function of time 't' can be written as

$$[RO_{ad}](t) = \left\{\frac{(F\phi)C_g}{(C_g + 1/K)}\right\} \{1 - \exp^{-k_a (C_g + 1/K)t}\} \quad (4.42j)$$

Eqn. 4.42j can be written as

$$[RO_{ad}](t) = \left\{\frac{(F\phi)C_g K}{(1 + C_g K)}\right\} \{1 - \exp^{-(1 + C_g K)/K k_a t}\} \quad (4.43)$$

CURRICULUM VITAE

KALISADHAN MUKHERJEE

Vill: Jhanka, P.O. + P.S.: Saltora

Dist: Bankura,

State: West Bengal, India, Pin: 722158

Ph: (91)9775552143

E-mail: kalisadhanm@yahoo.com/ kalisadhan@matsc.iitkgp.ernet.in

Proficiency:

Ph. D Research Experience (IIT Kharagpur, India) (~ 48 month): Wet chemical synthesis of nano-structured oxide materials; Materials characterization using thermal analyses (DTA, TGA) X-ray diffraction along with Rietveld analyses of XRD pattern, FTIR spectra, electron microscopy (SEM, TEM), N₂ adsorption isotherm analyses (BET) etc. **Data analyses; Writing research papers and project proposals; Software proficient with:** Origin, Maud, Labview etc.

Industrial Experience (Chembiotek, TCG Life Sciences Group, Kolkata, India) (~ 14 month): Synthesis of organic molecules (Experience on the familiar organic reactions viz: Suzuki, Heck, Grignard, Amide coupling, hydrogenation, microwave reaction etc); **Purification of organic molecules using various techniques (viz: column chromatography, biotage column, crystallization, distillation), Characterization of organic molecules (viz: NMR, GCMS, LCMS, FIAMS).**

Academic Records:

M. Sc in Chemistry: 75.01 % (1st class) (The University of Burdwan, 2006)

B. Sc in Chemistry: 60.60 % (1st class) (The University of Burdwan, 2004)

10 + 2 standard: 79.40 % (1st Division) (WBCHSE, 2000)

10th standard: 86.37 % (1st Division) (WBBSE, 1998)

Lectureship and NET (National Eligibility Test) (CSIR): June'06 and June'08

Future Research Concentrations:

- Sensorial Research (SMO, Electrochemical and Biosensor)
- Renewable Energy Sources (e.g. Solar Cell (DSSC))

International Journal Publications:

1. "Promising methane sensing characteristics of hydrothermal synthesized magnesium zinc ferrite hollow-spheres" **K. Mukherjee** and S. B. Majumder, *Scripta Materialia*, <http://dx.doi.org/10.1016/j.scriptamat.2012.06.025>.
2. "Synthesis process induced improvement on the gas sensing characteristics of nano-crystalline magnesium zinc ferrite particles" **K. Mukherjee** and S. B. Majumder, *Sensors and Actuators B*, 162 (2012) 229-236.
3. "Addressing the cross-sensitivity of magnesium zinc ferrite towards reducing gas sensing using pattern recognition techniques" A. Maity, **K. Mukherjee** and S. B. Majumder, *Sensor Letters* 10 (2012) 1-5.

4. "Hydrogen sensing characteristics over sol-gel assisted tailored structures of $\text{Mg}_{0.5}\text{Zn}_{0.5}\text{Fe}_2\text{O}_4$ " **K. Mukherjee** and S. B. Majumder, *Nanotechnology*, 21 (2010) 255504-255509.
5. "Reducing gas sensing behavior of nano-crystalline magnesium-zinc ferrite powders", **K. Mukherjee** and S. B. Majumder, *Talanta*, 81 (2010) 1826–1832.
6. "Solution synthesis and kinetic analyses of the gas sensing characteristics of magnesium ferrite particles", **K. Mukherjee**, D. C. Bharti and S. B. Majumder, *Sensors and Actuators B*, 146 (2010) 91-97.
7. "Wet chemical synthesis and gas sensing properties of magnesium zinc ferrite nano-particles", D. C. Bharti, **K. Mukherjee** and S. B. Majumder, *Materials Chemistry and Physics*, 120 (2010) 509–517.
8. "Analyses of conductance transients to address the selectivity issue of zinc ferrite gas sensors" **K. Mukherjee** and S. B. Majumder, *Electrochemical and Solid State Letters*, 13 (4) (2010) J25-J27.
9. "Analyses of response and recovery kinetics of zinc ferrite as hydrogen gas sensor", **K. Mukherjee** and S. B. Majumder, *Journal of Applied Physics* 106 (2009) 064912.
10. "Combustible gas sensing characteristics of chemical solution synthesized nano-crystalline magnesium ferrite spinel particles" **K. Mukherjee**, D. C. Bharti and S. B. Majumder, *Transaction of Indian Ceramic Society* 69 (3) (2010) 187-192.
11. "Kinetic and statistical analysis of the conductance transient to address the selectivity issue of the wet chemically synthesized tailored nanostructured ferrite gas sensors" **K. Mukherjee**, A. Maity, and S. B. Majumder, *AIP conference proceedings* 1362 (2011) 279-280.
12. "Synthesis of embedded and isolated $\text{Mg}_{0.5}\text{Zn}_{0.5}\text{Fe}_2\text{O}_4$ nano-tubes and investigation on their anomalous gas sensing characteristics" **K. Mukherjee** and S.B. Majumder, *Sensors and Actuators B* (under review).
13. "Investigations on the irreversible and reversible type gas sensing for zinc oxide and magnesium zinc ferrite gas sensors" **K. Mukherjee** and S. B. Majumder, *Analytica Chimica Acta* (under review).

Book Chapter:

1. "Conductance Transient Analyses in Metal Oxide Gas Sensors on the Example of Spinel Ferrite Gas Sensor" by **K. Mukherjee** and S. B. Majumder, *Chemical Sensors-Simulation and Modeling, Vol-2*, Editor- Ghenadii Korotcenkov, **Momentum press**, New Jersey 08904-2114, USA, book chapter (in press).

International Conference Presentations:

1. "Kinetic and statistical analysis of the conductance transient to address the selectivity issue of the wet chemically synthesized tailored nano-structured ferrite gas sensors" **K. Mukherjee**, A. Maity, S. B. Majumder, International Symposium on Olfaction and Electronic Nose, 2-5th May 2011, *New York, USA*.
2. "Anomalous gas sensing characteristics of embedded and isolated $\text{Mg}_{0.5}\text{Zn}_{0.5}\text{Fe}_2\text{O}_4$ nano-tubes" S.B. Majumder, **K. Mukherjee**, A. Maity, S. Basu, C. Lang, and M. Topic, A nature conference on Frontiers in Electronic Materials: Correlation Effects and Memristive Phenomena, 17-20th June 2012, *Aachen, Germany*.